U.S.NRC
United States Nuclear Regulatory Commission
Protecting People and the Environment

NUREG-2162

Weld Residual Stress Finite Element Analysis Validation: Part 1 – Data Development Effort

Office of Nuclear Regulatory Research

AVAILABILITY OF REFERENCE MATERIALS IN NRC PUBLICATIONS

NRC Reference Material

As of November 1999, you may electronically access NUREG-series publications and other NRC records at NRC's Public Electronic Reading Room at http://www.nrc.gov/reading-rm.html. Publicly released records include, to name a few, NUREG-series publications; *Federal Register* notices; applicant, licensee, and vendor documents and correspondence; NRC correspondence and internal memoranda; bulletins and information notices; inspection and investigative reports; licensee event reports; and Commission papers and their attachments.

NRC publications in the NUREG series, NRC regulations, and Title 10, "Energy," in the *Code of Federal Regulations* may also be purchased from one of these two sources.

1. The Superintendent of Documents
   U.S. Government Printing Office
   Mail Stop SSOP
   Washington, DC 20402–0001
   Internet: bookstore.gpo.gov
   Telephone: 202-512-1800
   Fax: 202-512-2250
2. The National Technical Information Service
   Springfield, VA 22161–0002
   www.ntis.gov
   1–800–553–6847 or, locally, 703–605–6000

A single copy of each NRC draft report for comment is available free, to the extent of supply, upon written request as follows:

Address: U.S. Nuclear Regulatory Commission
Office of Administration
Publications Branch
Washington, DC 20555-0001
E-mail: DISTRIBUTION.RESOURCE@NRC.GOV
Facsimile: 301–415–2289

Some publications in the NUREG series that are posted at NRC's Web site address http://www.nrc.gov/reading-rm/doc-collections/nuregs are updated periodically and may differ from the last printed version. Although references to material found on a Web site bear the date the material was accessed, the material available on the date cited may subsequently be removed from the site.

Non-NRC Reference Material

Documents available from public and special technical libraries include all open literature items, such as books, journal articles, transactions, *Federal Register* notices, Federal and State legislation, and congressional reports. Such documents as theses, dissertations, foreign reports and translations, and non-NRC conference proceedings may be purchased from their sponsoring organization.

Copies of industry codes and standards used in a substantive manner in the NRC regulatory process are maintained at—

The NRC Technical Library
Two White Flint North
11545 Rockville Pike
Rockville, MD 20852–2738

These standards are available in the library for reference use by the public. Codes and standards are usually copyrighted and may be purchased from the originating organization or, if they are American National Standards, from—

American National Standards Institute
11 West 42nd Street
New York, NY 10036–8002
www.ansi.org
212–642–4900

Legally binding regulatory requirements are stated only in laws; NRC regulations; licenses, including technical specifications; or orders, not in NUREG-series publications. The views expressed in contractor-prepared publications in this series are not necessarily those of the NRC.

The NUREG series comprises (1) technical and administrative reports and books prepared by the staff (NUREG–XXXX) or agency contractors (NUREG/CR–XXXX), (2) proceedings of conferences (NUREG/CP–XXXX), (3) reports resulting from international agreements (NUREG/IA–XXXX), (4) brochures (NUREG/BR–XXXX), and (5) compilations of legal decisions and orders of the Commission and Atomic and Safety Licensing Boards and of Directors' decisions under Section 2.206 of NRC's regulations (NUREG–0750).

U.S.NRC
United States Nuclear Regulatory Commission
Protecting People and the Environment

NUREG-2162

Weld Residual Stress Finite Element Analysis Validation: Part 1 – Data Development Effort

Manuscript Completed: February 2014
Date Published: March 2014

Prepared by:
Michael Benson, David Rudland, and Aladar Csontos

Michael Benson, NRC Project Manager

Office of Nuclear Regulatory Research

ABSTRACT

This report is aimed at prediction of weld residual stress (WRS) in safety-related nuclear components. WRS is a significant driving force for primary water stress corrosion cracking. As such, it is an important input to deterministic and probabilistic flaw growth calculations.

The U.S. Nuclear Regulatory Commission's objectives for this work include:

- Validate axisymmetric finite element modeling as a predictive tool for WRS, using robust experimental methods.
- Support the development of appropriate WRS/flaw evaluation review guidelines.
- Perform independent confirmatory research on industry guidance for executing WRS analysis.
- Assess and evaluate the adequacy of industry's mitigation activities where WRS minimization is necessary.
- Improve WRS finite element analysis predictive methodologies.
- Determine estimates for WRS uncertainty distributions, which are needed in probabilistic analyses.

This report describes WRS measurement methods and finite element modeling techniques for predicting WRS. The measurement and modeling efforts were performed on both small-scale scientific specimens and on large-scale prototypic mockups of in-service nuclear plant components. For example, Chapter 4 describes results from a double-blind finite element round robin, where international participants completed finite element models of a prototype pressurizer surge nozzle without access to the measurement data. Validation criteria for WRS models will be developed in future research efforts.

TABLE OF CONTENTS

Section **Page**

LIST OF FIGURES

LIST OF TABLES

Table **Page**

EXECUTIVE SUMMARY

The need to understand weld residual stress (WRS) in safety-related nuclear components began with the occurrence of intergranular stress corrosion cracking in boiling water reactors. Later, the discovery of primary water stress corrosion cracking (PWSCC) in pressurized water reactor dissimilar metal welds also demonstrated the need to understand the driving force for crack growth. Two prime examples of PWSCC in pressurized water reactors include:

(1) Cracking of Davis-Besse control rod drive mechanism nozzles in March 2002.
(2) Circumferential cracking in the Wolf Creek pressurizer nozzles in October 2006.

Advanced finite element analysis studies of PWSCC, which simulate natural crack growth by calculating the driving force along the entire crack front, showed that WRS was a significant input for flaw growth calculations. As part of the U.S. Nuclear Regulatory Commission's (NRC's) strategy for ensuring nuclear safety in PWSCC-susceptible components, a probabilistic fracture mechanics code is under development. The Extremely Low Probability of Rupture (xLPR) code will analyze rupture probabilities in piping systems approved for Leak-Before-Break. An understanding of WRS and proper characterization of the associated uncertainty is vital for determination of rupture probabilities and appropriate confidence bounds for primary piping systems.

In addition, a nuclear plant owner may seek relief from required inspection programs or repair/replacement activities in PWSCC-susceptible components. A deterministic flaw growth evaluation in many cases provides the necessary technical basis to support the relief request. Such evaluation requires review and approval by the NRC staff before relief is granted. These calculations necessitate an assumption of the WRS present in the system. Safety evaluations require that the NRC staff make an informed judgment of whether the assumed WRS is accurate or conservative.

Finite element simulations of WRS involve a two-step process: (1) calculating the temperature distribution in space and time with an assumed heat input model and (2) calculating the stress field resulting from the temperature history. The models considered in this work were two-dimensional axisymmetric; i.e., a moving heat source was not explicitly modeled. Potential sources of modeling uncertainty include the choice of heat input model, choice of strain hardening law, bead geometry, process sequence, material property inputs, and post-processing of results.

WRS measurement, which is a specialized field requiring specific expertise, involves calculating stress from measured deformation or strain. Techniques include diffraction-based and strain relief-based methods. Diffraction methods rely on measurement of crystallographic lattice spacing, along with a specified reference lattice spacing, as a measurement of strain. Strain relief techniques involve mechanical perturbation of the component that releases the stress field. Strains measured when the stress field is released are used to back-calculate the stress. Each technique has its own limitations and uncertainties, and these must be taken into account for proper experimental execution and interpretation of results.

Validation of WRS finite element models with experiments is not a straight-forward topic. Approaches have been developed by organizations outside the NRC, such as the R6 code established in Europe. Rather than addressing specific validation criteria for use at NRC, this

report discusses data collection efforts to support determining effective validation techniques and criteria. The development of validation criteria is left for future reports.

This work was performed under an addendum to the memorandum of understanding with the Electric Power Research Institute. It consisted of four research phases:

(1) Phase 1: Scientific Weld Specimens
(2) Phase 2a: Fabricated Prototypic Nozzle
(3) Phase 3: Pressurizer Nozzles from a Cancelled Plant
(4) Phase 4: Optimized Weld Overlay on a Cold Leg Nozzle

This research project found bulk WRS measurement techniques were significantly more reliable than surface techniques. Further, this project showed that across a wide range of groups, calculated WRS generally followed the profile shape of the measurements. However, the report identified significant analyst-to-analyst variability of calculated WRS values by up to ±200 MPa. In the future, establishing guidance on choice of strain hardening law (among other lessons learned) may reduce the observed scatter. This variability has a significant impact on calculations of the stress intensity factor, K_I, and time-to-leakage in deterministic flaw analyses. Therefore, future work will focus on developing numerical procedures that reduce analyst-to-analyst scatter.

ACKNOWLEDGMENTS

The authors would like to thank the following.

- Howard Rathbun and Matthew Kerr, both formerly at the U.S. Nuclear Regulatory Commission (NRC), for leading the Weld Residual Stress Validation Program. Much of the work presented in this document is a result of their technical and leadership efforts. Readers may refer to their publications on this topic [22], [23], [49].
- Paul Crooker of the Electric Power Research Institute (EPRI) and John Broussard of Dominion Engineering, Inc., for technical cooperation in the joint NRC-EPRI program.
- EPRI for the use of tables and figures from the Materials Reliability Program (MRP)-316 report.
- Lee Fredette and Paul Scott at Battelle Memorial Institute for their work on weld overlay finite element simulations.
- Pacific Northwest National Laboratory, Edison Welding Institute, and Richard Olson at Battelle Memorial Institute for Mockup Design/Fabrication.
- Engineering Mechanics Corporation of Columbus for providing material properties for the round robin finite element analysis effort.
- VEQTER, Ltd. of Bristol, United Kingdom, for deep hole drilling and incremental deep hole drilling measurements and the use of Figure 2-4.
- Hill Engineering, LLC of Rancho Cordova, CA, for contour measurements and the use of Figure 2-3.
- Ed Kingston of VEQTER, Ltd.; Adrian DeWald of Hill Engineering, LLC; and EPRI for useful technical comments on this report.
- Gary Stevens, Raj Iyengar, and Joshua Kusnick of the NRC Office of Nuclear Regulatory Research for supplying the historical information on primary water stress corrosion cracking found in Chapter 1.

ABBREVIATIONS

2-D	two-dimensional
AFEA	Advanced Finite Element Analysis
ANO	Arkansas Nuclear One
ASME Code	American Society of Mechanical Engineers Boiler and Pressure Vessel Code
BMI	bottom mounted instrument nozzle
BWR	boiling water reactor
C-1, C-3, C-4, and C-5	cylindrical specimen designations for phase 1 work
CS	carbon steel
DHD	deep hole drilling
DM	dissimilar metal
EPRI	Electric Power Research Institute
FE	finite element
FSWOL	full structural weld overlay
GTAW	gas tungsten arc welding
ID	inner diameter
iDHD	Incremental Deep Hole Drilling
IGSCC	intergranular stress corrosion cracking
KWO	mothballed Obrigheim Nuclear Power Plant
MOU	memorandum of understanding
MRP	Materials Reliability Program
NRC	United States Nuclear Regulatory Commission
NDE	nondestructive evaluation
OD	outer diameter
OWOL	optimized weld overlay
P-3, P-4, P-5, and P-6	plate specimen designations for Phase 1 Work
PWHT	post weld heat treat
PWR	pressurized water reactor
PWSCC	primary water stress corrosion cracking
SIA	Structural Integrity Associates
SONGS	San Onofre Nuclear Generating Station
SS	stainless steel

WE-3	Westinghouse three-loop plant
WRS	weld residual stress

UNIT CONVERSION

1 mm = 0.0394 in. = 3.281×10^{-3} ft

1 mm/s = 2.4 in./min

1 kg = 2.205 lb_m

T[R] = T[K]*9/5

1 MPa = 20.9 kip/ft^2

1 J/s = 3.414 BTU/hr

NOTATIONS

a	crack depth
d_{hkl}	interplanar spacing for lattice planes with Miller indices *hkl*
$d_{hkl,0}$	reference interplanar spacing
ε_{hkl}	lattice strain
E_{hkl}	*hkl*-specific modulus
hkl	Miller indices
θ	Bragg angle
K_I	Mode I stress intensity factor
R	outer radius
σ_{ii}	normal stress component
σ	general stress magnitude
$\overline{\sigma}$	mean stress
t	wall thickness
τ	time
ν_{hkl}	*hkl*-specific Poisson's ratio
x	through-thickness distance ID to OD
Q	power density (weld thermal model)
a_0	build-up time (weld thermal model)
C_1	parameter affecting heat input time (weld thermal model)
C_2	amplitude scaling parameter (weld thermal model)
S	welding speed (weld thermal model)
E	arc efficiency (weld thermal model)
V	welding voltage (weld thermal model)
A	welding current (weld thermal model)
K	pre-exponential (weld thermal model)
σ_m	axial membrane stress for operating loads
σ_b	axial bending stress for operating loads

1 REGULATORY PURPOSE

1.1 Environmentally Assisted Cracking Operating Experience

Shack [1] initiated an early study of weld residual stress (WRS) due to the occurrence of intergranular stress corrosion cracking (IGSCC) in boiling water reactor (BWR) stainless steel components. This particular degradation mechanism often involved sensitization in the heat affected zone of type-304 stainless steel welds. Later, primary water stress corrosion cracking (PWSCC) in pressurized water reactors (PWRs) raised the issue of WRS again. For both PWSCC and IGSCC, component susceptibility is thought to depend upon a combination of stress, material characteristics, and material environment.

In PWR coolant systems, nickel-based dissimilar metal (DM) welds are typically used to join low alloy steel components—including the reactor pressure vessel, steam generators, reactor coolant pump casings, and the pressurizer—to stainless steel piping. Figure 1-1 shows a cross-section of a representative nozzle-to-pipe connection, including the DM weld [1]-[3]. In Figure 1-1, the DM weld is indicated as "Alloy 82/182 Butt Weld." The DM weld is fabricated by sequentially depositing weld passes as molten metal that cools, solidifies, and contracts, retaining stresses that approach or exceed the material's yield strength.

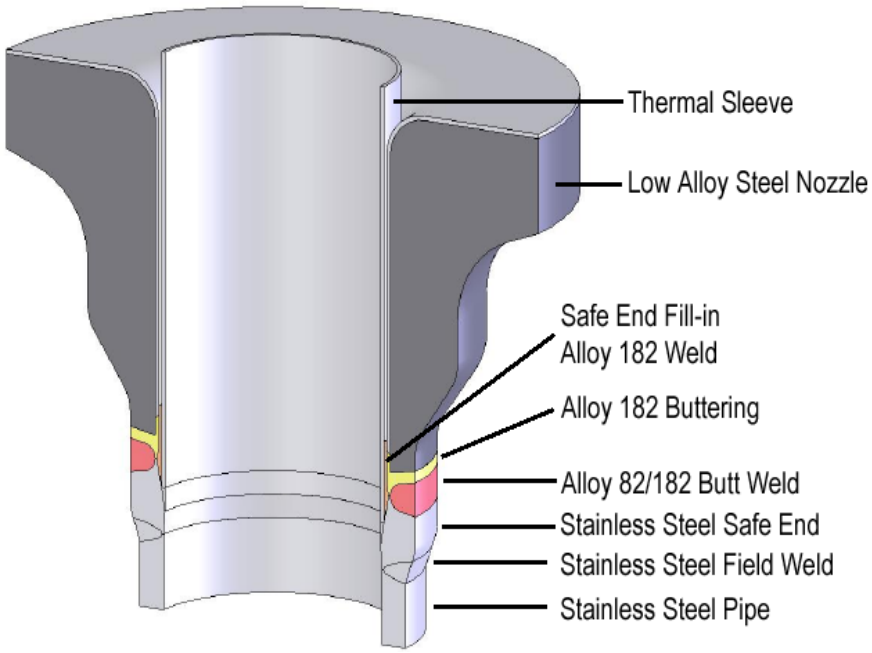

Figure 1-1 Representative Nozzle Cross Section

These DM welds are susceptible to PWSCC as an active degradation mechanism that has led to reactor coolant system pressure boundary leakage. Operational issues associated with PWSCC events include expanded outage work scope, unplanned shutdowns, and repair/replacement activities. If a utility chooses to seek temporary relief from required repairs or inspections, then the licensee prepares a flaw evaluation for U.S. Nuclear Regulatory Commission (NRC) review. If approved by the NRC, the flaw evaluation is only valid for a specified time period.

One major PWSCC event in the U.S. fleet is the Davis-Besse Nuclear Station upper head wastage incident on March 5, 2002. PWSCC in the control rod drive mechanism nozzles led to boric acid contact with the vessel upper head. The acid reacted with the carbon steel head, resulting in a cavity approximately 130-194 cm^2 in surface area and over 15 cm deep [4]-[6]. This event left the stainless steel cladding as the primary pressure boundary in that area. As a result of such cracking in vessel closure head penetration j-groove welds, WRS finite element simulations for that geometry have been performed and documented [7]. Furthermore, American Society of Mechanical Engineers Boiler and Pressure Vessel Code (ASME Code) Case N-729-1 provides volumetric inspection requirements for these j-groove welds. Independent confirmatory finite element analyses provided NRC staff with a technical basis for incorporating Code Case N-729-1 into NRC regulations [8]. Therefore, research on WRS has regulatory significance.

PWSCC has occurred in safety-related piping systems, as well. On October 13, 2006, the Wolf Creek Nuclear Operating Corporation performed inspections on pressurizer nozzle-to-safe end DM and safe end-to-pipe stainless steel butt welds [9]. These inspections identified five circumferential indications in the surge, relief, and safety nozzle-to-safe end DM butt welds that were attributed to PWSCC. These indications were the first occurrence of multiple and large circumferential indications in commercial PWRs. As a result of an NRC flaw evaluation scoping study that predicted little to no margin between leakage and potential rupture, the nuclear power industry conducted advanced finite element analysis (AFEA) [10]. This work took advantage of more realistic assumptions to address the NRC staff's concerns regarding the potential for rupture without prior evidence of leakage. The industry's and NRC staff confirmatory AFEA studies both demonstrated that through-wall axial weld residual stress profiles played a key role in whether the postulated PWSCC would grow through-wall to leakage or circumferentially to potential rupture characteristics.

Figure 1-2 and Table 1-1 through Table 1-3 provide a historical overview of select PWSCC events in domestic and international PWRs. Also in Table 1-1 through Table 1-3 are significant actions taken by the NRC and industry to deal with the PWSCC issue. One significant action is the issuance of Code Case N-770 by ASME in 2009. This Code Case spells out alternative inspection requirements to ASME Code Section XI for primary pressure boundary butt welds subject to PWSCC [11]-[12].

PWSCC in safety-related nuclear components has led to significant actions from both the NRC and the U.S. nuclear industry. This degradation mechanism is driven by tensile WRS and other applied loads. Hence, proper assessment of these stresses is essential to predict PWSCC flaw growth.

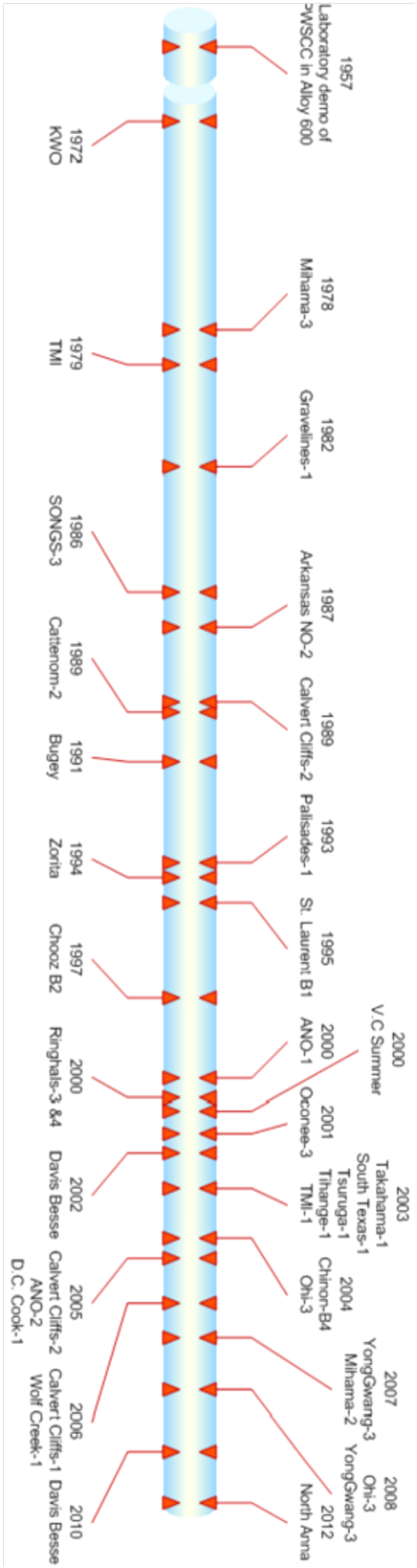

Figure 1-2 PWSCC Timeline

Table 1-1 Summary of Select PWSCC Events (page 1 of 3)

Event	Year	Plant	Description
1	1957	---	Susceptibility of Alloy 600 to IGSCC demonstrated in laboratory.
2	1972	KWO	First steam generator tube (secondary side) leakage/cracking.
3	1978	Mihama-3, PWR, WE-3	Control Rod Cluster Guide Tube Support Pins. Alloy X750. Replaced (Heat Treatment, Shot Peening, Design Change, Torque change).
4	1979	Three Mile Island-1	First steam generator tube (primary side) leakage/cracking.
5	1982	Gravelines-1	Control rod guide tube support pins. Alloy X750. Multiple events.
6	1986	SONGS-3	Pressurizer Relief Valve Instrumentation nozzle cracking.
7	1987	Arkansas Nuclear One-2	Pressurizer Heater Sleeve. Alloy 600.
8	1989	Cattenom-2 Calvert Cliffs-2	1300 MWe Pressurizer Nozzles. Alloy 600. Multiple events. Pressurizer heater penetration cracking.
9	1991	Bugey-3	CRDM nozzle. Alloy 600. First known case in 1991; multiple events.
10	1993	Palisades-1	Pressurizer power-operated relief nozzle. Alloy 600. First instance of PWSCC in a U.S. DM butt weld.
11	1994	Zorita	Many cracks (boundary segregation).
12	1995	Saint Laurent-B1	Steam generator water box. Alloy 82. Only known case of Alloy 82 cracking in France.
13	1997	Chooz-B2 ---	Electrical heaters. Type 316 SS. Multiple events. U.S. NRC Generic Letter 97-01, "Degradation of Control Rod Drive Mechanism Nozzle and Other Vessel Closure Head Penetrations," April 1, 1997.
14	2000	V.C. Summer ANO-1 Ringhals-3, -4 Oconee-1	"A", "B", and "C" hot leg pipe-to-RPV nozzle DM welds, "A" and "C" cold leg-RPV nozzle DM welds. Alloy 182/82. Spool piece replacement. Cracks at 6 small nozzles in RCPB piping. RPV outlet/RCS hot leg nozzle safe end dissimilar metal butt weld cracking in Alloy 82/182. CRDM J-groove weld cracking.
15	2001	Oconee-3	First circumferential wall crack starting at OD.
16	2002	Davis Besse-1 ---	CRDM Nozzle. Severe corrosion/wastage of RPV top head. Alloy 600. Replace head Alloy 690. NRC issues letter to ASME Code Subcommittee on Nuclear Inservice Inspection requesting that it re-evaluate inspection and corrective action requirements.

Table 1-1 Summary of Select PWSCC Events (page 2 of 3)

Event	Year	Plant	Description
17	2003	Takahama-1	Bottom Mounted Instrument (BMI) nozzle. Alloy 600. (ECT detected) Removed indication & WJP.
		South Texas-1	Bottom Mounted Instrument (BMI) nozzle. Alloy 600. Half nozzle repair Alloy 690, 152, 52.
		Tsuruga-2	Weld (Pressurizer relief valve nozzle). Weld Metal Alloy 132. (UT detected) Spool Piece Replacement (Alloy 690).
		Tihange-2	Pressurizer surge line nozzle (weld).
		Three Mile Island-1	Pressurizer Surge Nozzle (weld). Alloy 182/82.
18	2004	Chinon-B4	Partition plate of steam generator. Alloy 600. Multiple events.
		---	Materials Reliability Project (MRP) issues a recommendation letter to the industry.
		---	U.S. NRC issues Information Notice 2004-11, "Cracking in Pressurizer Safety and Relief Nozzles and in Surge Line Nozzle."
		---	U.S. NRC issues Information Notice 2004-01, "Inspection of Alloy 82/182/600 Materials Used in the Fabrication of Pressurizer Penetrations and Steam Space Piping Connections at Pressurized Water Reactors."
		Ohi-3	CRDM Nozzle (RPV Penetration). Weld Metal Alloy 132. Claddings (Alloy 690 type) - Replacement of RVH.
19	2005	Calvert Cliffs-2	Hot Leg Drain nozzle.
		---	ASME issues Code Case N-722, "Additional Examinations for PWR Pressure Retaining Welds in Class 1 Pressure Boundary Components Fabricated with Alloy 600/82/182 Materials, Section XI, Division 1"
		---	MRP issues MRP-139, "Materials Reliability Program: Primary System Piping Butt Weld Inspection and Evaluation Guideline (MRP-139)."
		ANO-2	Pressurizer Heater Sleeve.
		---	U.S. NRC requests ASME Code Section XI Subcommittee on Nuclear Inservice Inspection to take actions to develop improvements in volumetric examinations.
		D.C. Cook-1	Pressurizer Relief Valve Nozzle (weld). Alloy 182/82.
20	2006	Calvert Cliffs-1	Pressurizer Relief Nozzle, Hot Leg Drain Nozzle, and Surge Nozzle (weld). Alloy 182/82.
		Wolf Creek-1	Pressurizer Relief Valve Nozzle (weld). Alloy 182/82. Full structural weld overlay.
		Wolf Creek-1	Pressurizer Safety Injection Nozzle (weld). Alloy 182/82. Full structural weld overlay.
		Wolf Creek-1	Pressurizer Surge Nozzle (weld). Alloy 182/82. Full structural weld overlay.
		---	ASME issues Code Case N-740, "Dissimilar Metal Weld Overlay for Repair of Class 1, 2 and 3 Items."
		---	Industry and NEI developed an inspection plan for unmitigated pressurizer dissimilar metal butt welds that contain Alloy 82/182 material.

Table 1-1 Summary of Select PWSCC Events (page 3 of 3)

Event	Year	Plant	Description
21	2007	YongGwang-3	Steam Generator drain line nozzle. Alloy 600. Replace.

			U.S. NRC issues Confirmatory Action Letters to 27 nuclear plants in response to the 2006 Wolf Creek PWSCC indications.
		---	U.S. NRC acquires the St. Lucie-1 pressurizer that was removed from service in 2005.
		Mihama-2	Weld (Steam Generator Inlet Nozzle). Type 316 SS (IGSCC). Spool Piece Replacement (Alloy 690), USP.
22	2008	Ohi-3	Weld (RPV Outlet Nozzle). Weld Metal Alloy 82. Remove, STP inlay, Cladding (Alloy 690 type).
		---	EPRI issues MRP-2008-012, "Examination Results on Nozzles from removed St Lucie Pressurizer."
		YongGwang- 4	Steam Generator drain line nozzle. Alloy 600. Replace.
23	2009	---	ASME issues Code Case N-770, "Alternative Examination Requirements and Acceptance Standards for Class 1 PWR Piping and Vessel Nozzle Butt Welds Fabricated with UNS N06082 or UNS W86182 Weld Filler Material with or without Application of Listed Mitigation Activities"
24	2012	North Anna-1	Axially-oriented PWSCC cracking discovered in steam generator hot leg nozzle.

1.2 Flaw Growth Evaluations

ASME Code Section XI requires the application of nondestructive evaluation (NDE) techniques, such as ultrasonic testing, to assess the potential presence of flaws in safety-related components. If an indication is found in a nickel alloy DM weld, it is generally assumed to be a PWSCC crack. PWSCC cracks are not allowed in service, according to IWB-3430 of ASME Code Section XI (2008a) [13]. When nuclear plant owners decide to seek relief from required repair/replacement activities, they typically submit a fracture mechanics flaw evaluation to the NRC for review and approval. Flaw evaluations can also be used in cases where NDE inspection presents a hardship to the plant owner. A flaw is assumed to exist in the component in question, even without direct evidence of flaw, in these cases. In any event, flaw evaluations are good only for the length of time analyzed. Typically, PWSCC flaws are repaired during a subsequent refueling outage. Flaw evaluation procedures are described in IWB-3600 and Appendix C of ASME Code Section XI (also see Figure 1-3) [13].

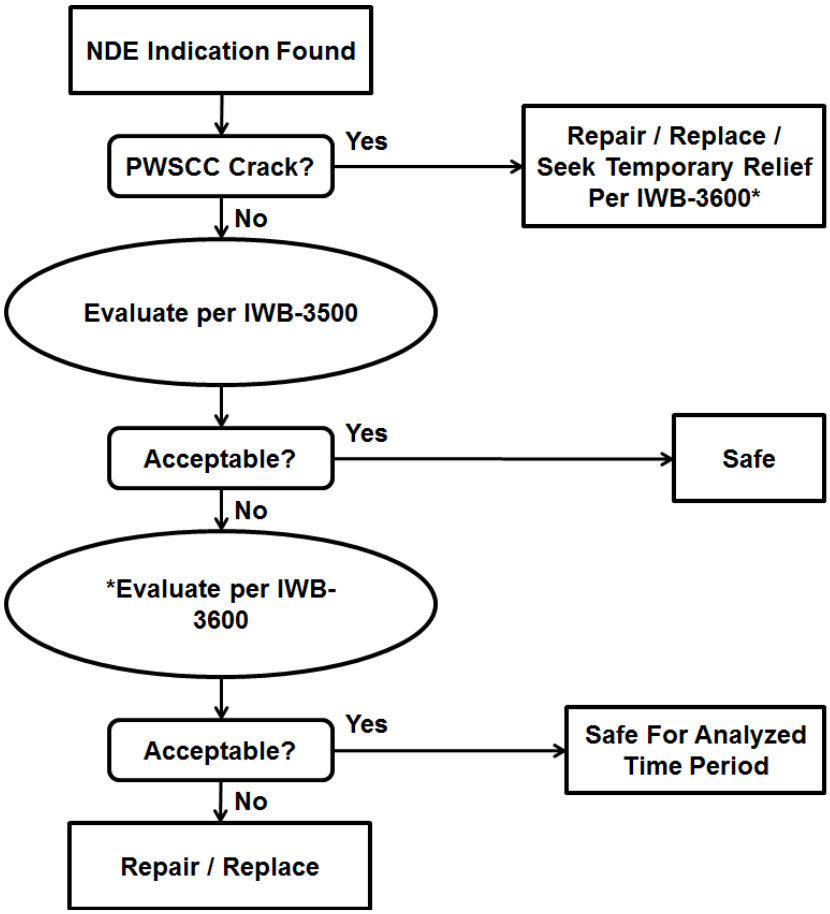

Figure 1-3 Flowchart for ASME Code Flaw Disposition

An IWB-3600 evaluation typically involves analyzing the found flaw with the measured dimensions. Other steps include calculating the stress intensity factor (K_I) at the surface point and deepest point of the crack front, estimating the PWSCC growth rate, advancing the crack in the length and depth dimensions, and performing a flaw stability calculation (see Figure 1-4).

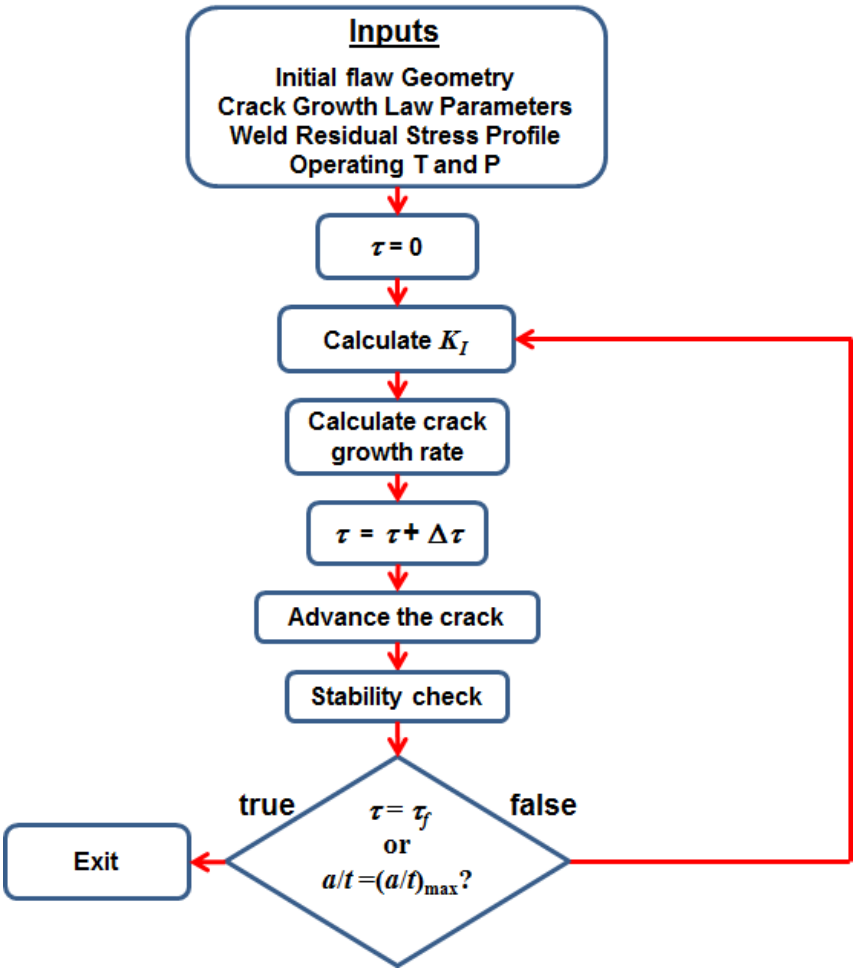

Figure 1-4 Flowchart for IWB-3600 Evaluation (τ = time, a = crack depth, t = thickness)

Methods for calculating K_I can be found in [14]-[17]. They involve different representations of the through-wall stress distribution that creates mode I loading on the crack. This stress distribution should include both operating loads and WRS. WRS input into these calculations may take a range of forms, from conservative and simple to refined and complicated, as indicated schematically in Figure 1-5.

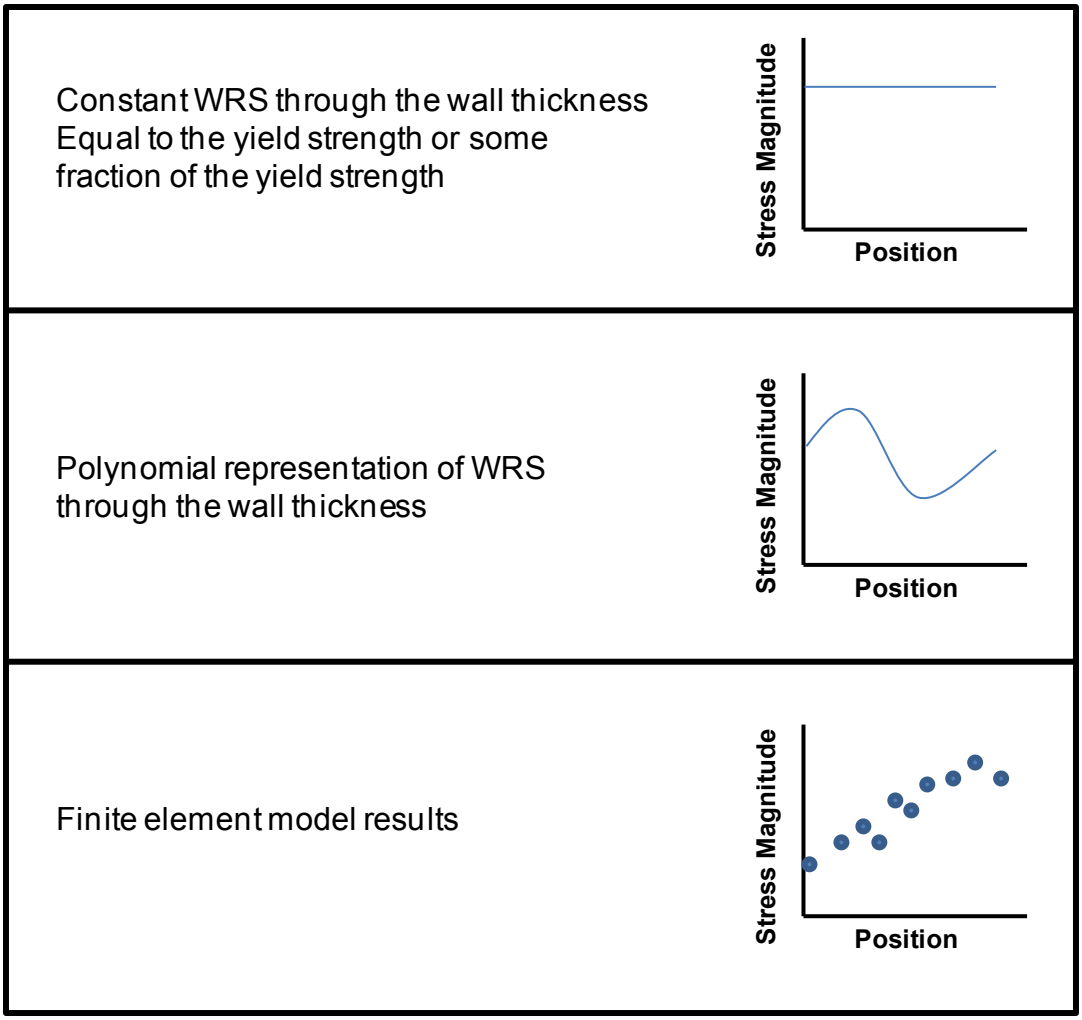

Figure 1-5 Schematic of Possible WRS Inputs in Flaw Growth Calculations

1.3 Uncertainties in WRS Input and Motivation of Research

Two documents, in particular, describe the NRC's regulatory response to the Wolf Creek event described in Section 1.1 and the motivation for the present work. The first is a March 5, 2007 letter from the NRC to the Nuclear Energy Institute [18]. This letter discussed eight points to be addressed in industry's AFEA work described in Section 1.1. The second is a March 22, 2007 letter from the NRC's Advisory Committee on Reactor Safeguards [19]. Both of these letters discussed the potential for uncertainty in WRS assumptions.

To address NRC staff concerns, the Electric Power Research Institute (EPRI) performed sensitivity analyses for flaw growth calculations [10]. Studies such as these have demonstrated the significant impact WRS assumptions have on flaw growth analyses. There are uncertainties involved with determining the actual WRS distribution in a field component. Uncertainties may include material property variability and unknowns associated with fabrication procedure. Recent improvements in computational efficiency have facilitated advances in WRS predictions, but no universally accepted guidelines for these analyses have been established. Also, it is necessary to benchmark analytical results with experiments, as in [20],[21]. The assumptions

and estimation techniques employed in finite element modeling vary from analyst to analyst, causing variability in the predicted residual stress profiles for a given weld.

Therefore, the NRC initiated a WRS analysis validation program. This program consisted of four phases, with each phase intended to investigate progressively more realistic service conditions [22]-[24]. The NRC and EPRI completed this project under an addendum to the memorandum of understanding (MOU), which is a legal document allowing the NRC Office of Nuclear Regulatory Research and EPRI to perform cooperative research. The MOU is authorized under Section 31 of the Atomic Energy Act and/or Section 205 of the Energy Reorganization Act.

The NRC staff's objectives in completing this research program included:

- Validate axisymmetric FE modeling as a predictive tool for WRS, using robust experimental methods.
- Support the NRC's Office of Nuclear Reactor Regulation in development of appropriate WRS/flaw evaluation review guidelines.
- Perform independent confirmatory research on industry guidance for executing WRS analysis.
- Assess and evaluate the near-term adequacy of industry's mitigation activities where WRS minimization is necessary.
- Improve WRS finite element (FE) analysis predictive methodologies.
- Determine estimates for WRS uncertainty distributions, which are needed in probabilistic analyses (e.g., xLPR Code – eXtremely Low Probability of Rupture [25],[26]).

This report is organized in the following manner. Chapter 2 describes WRS model validation techniques. Chapters 3-6 respectively cover the following four phases of the NRC/EPRI WRS Validation Program:

(1) Phase 1: Scientific Weld Specimens
(2) Phase 2a: Fabricated Prototypic Nozzles
(3) Phase 3: Pressurizer Nozzles from a Cancelled Plant
(4) Phase 4: Optimized Weld Overlay on a Cold Leg Nozzle

Each chapter describes fabrication of the mockups for WRS measurement, the measurement techniques employed, FE modeling efforts, and conclusions. Chapter 7 discusses implications of the findings in Chapters 3-6. Knowledge gaps and future work are also discussed at the end of the report.

2 WELD RESIDUAL STRESS VALIDATION TECHNIQUES

2.1 Validation Criteria

The three approaches to weld residual stress (WRS) estimation in flaw growth calculations shown in Figure 1-5 each represent various degrees of accuracy and conservatism. For instance, a constant WRS equal to the material yield strength is a highly conservative estimation. This approach does not require significant validation of the accuracy of the WRS input. Applying the more refined approach with finite element (FE) analysis may be more accurate, but it requires validation with experimental data. This line of reasoning is found, for instance, in the European R6 code for structural integrity assessments [21]. R6 specifies several criteria for a "High Standard of Validation," such as:

- Use of two diverse measurement techniques (i.e., the techniques are based upon different physics)
- Predicted and measured transient temperatures should match within ±10 percent.
- Predicted and measured fusion zone area should match within ±20 percent.
- Predicted and measured distortions should be compared, if available.
- Stress intensity factors based upon the predicted WRS profile should be greater than 95 percent of that calculated with the measured profile.

Electric Power Research Institute's (EPRI's) Materials Reliability Program (MRP)-287 report suggests a criterion of ±10 MPa$\sqrt{m}$ on stress intensity factor calculations. This report does not define or endorse any specific validation criteria. Rather, this report presents data that may be used to develop such criteria. Determination of validation criteria is left for future work. Sections 2.2 and 2.3 describe measurement and modeling approaches that were employed to gather the data.

2.2 Weld Residual Stress Measurement Techniques

The experimental determination of residual stresses involves measurements on a specimen to quantify physical changes in the material due to residual stress (e.g., variations in lattice spacing, or strain and deformation from material removal). The residual stress is calculated from the experimental data. The mathematical procedures for calculating stresses range from simple application of Hooke's Law in three dimensions to more sophisticated FE techniques.

The NRC and EPRI considered a wide variety of potential measurement techniques. Methods may vary based upon a number of factors. Table 2-1 provides an overview of the techniques considered and their characteristics. Certain techniques did not meet the needs of the project. For example, magnetic methods can only be used on ferromagnetic materials, and the Curie temperature of the nickel-chromium alloys of interest here is well below 0^{o}C. In the end, the residual stress measurement techniques applied in this work fell into two broad categories, according to the physics they are based upon: (1) diffraction-based methods and (2) strain relief-based methods.

Table 2-1 Summary of WRS Measurement Methods

Technique	Physical Basis	Penetration Depth
X-ray	Diffraction	μm's
Synchrotron X-ray	Diffraction	μm's - mm's
Neutrons	Diffraction	10s of mm's
Magnetic	Magnetism	mm's
Ultrasonic	Acoustic Wave Propagation	mm's
Center Hole Drilling	Strain Relief	mm
Ring Core	Strain Relief	mm's
Deep Hole Drilling	Strain Relief	10s - 100s of mm's
Sachs	Strain Relief	10s - 100s of mm's
Slitting/Contour	Strain Relief	10s - 100s of mm's
Block Removal and Surface Layering	Strain Relief	10s - 100s of mm's

2.2.1. Diffraction-Based Methods

Diffraction in general and diffraction for WRS measurement is introduced in engineering textbooks and elsewhere [27]-[31]. Fundamentally, diffraction measures crystal lattice interplanar spacings, d_{hkl}, as illustrated in Figure 2-1. To calculate strain, the measured d_{hkl} can be compared to a reference lattice spacing, $d_{hkl,0}$, according to Equation 2-1.

$$\varepsilon_{ii}^{hkl} = \frac{d_{hkl} - d_{hkl,0}}{d_{hkl,0}} \qquad \text{Equation 2-1}$$

where, ε_{ii}^{hkl} is the ii normal strain component. The exact method used to determine the reference lattice spacing varies from experiment to experiment. Typically in engineering components, the measurements are made in the assumed principal directions. After measurement of three (mutually-perpendicular) normal strain components, the calculation of normal stress is accomplished through application of Hooke's Law in three dimensions (Equation 2-2).

$$\sigma_{ii} = \frac{E_{hkl}}{1+\nu_{hkl}}\left[\varepsilon_{ii}^{hkl} + \frac{\nu_{hkl}}{1-2\nu_{hkl}}\left(\varepsilon_{11}^{hkl} + \varepsilon_{22}^{hkl} + \varepsilon_{33}^{hkl}\right)\right] \qquad \text{Equation 2-2}$$

where, σ_{ii} is the ii normal stress component, E_{hkl} is the hkl-specific modulus, and ν_{hkl} is the hkl-specific Poisson's ratio. Successful application of diffraction to residual stress measurement relies on appropriate scattering statistics. This means that the scattering volume should contain a relatively large number of randomly oriented grains. Elements in solid solution have an effect on d-spacings, so any effect of chemical concentration gradients should be accounted for and may lead to increased measurement uncertainty. The strains measured with diffraction are averaged over the scattering volume.

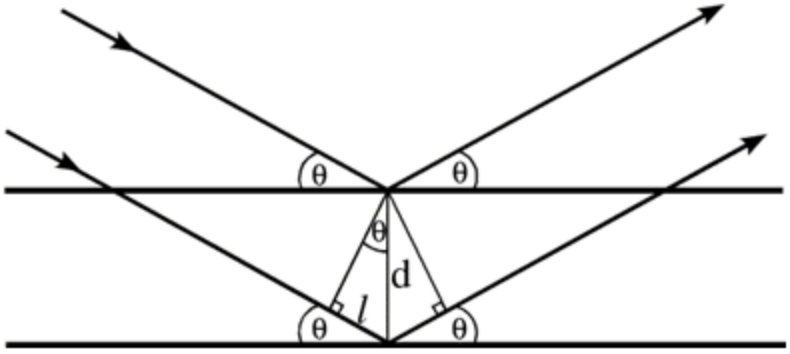

Figure 2-1 Measurement of Interplanar Spacings through Diffraction

X-ray and neutron diffraction were both investigated as potential measurement techniques. X-ray diffraction is considered to be a technique suitable for surface stress measurement, since the beam cannot penetrate into the bulk of the material. Neutron diffraction is considered suitable for bulk stress measurements in engineering materials. Neutron measurements can be made at two types of facilities: pulsed sources and reactor sources. Measurements at pulsed source facilities utilize a spectrum of wavelengths and time-of-flight techniques. A reactor source uses a single wavelength and scans through the Bragg angle, θ in Figure 2-1, to measure the diffraction pattern.

2.2.2. Strain Relief-Based Methods

Strain relief-based methods involve mechanically perturbing the specimen, thereby altering the existing stress field. Resulting strains or displacements are then measured. Calculation of stresses is often fairly sophisticated, involving finite element techniques [32]-[38]. These techniques are destructive or semi-destructive in nature.

Incremental slitting involves cutting the part along a linear path, as in Figure 2-2. At each increment of slitting, the strains are measured via strain gages. This technique can be appropriate for near-surface or through-thickness measurements. This technique provides the component of stress that is perpendicular to the cut along a linear path.

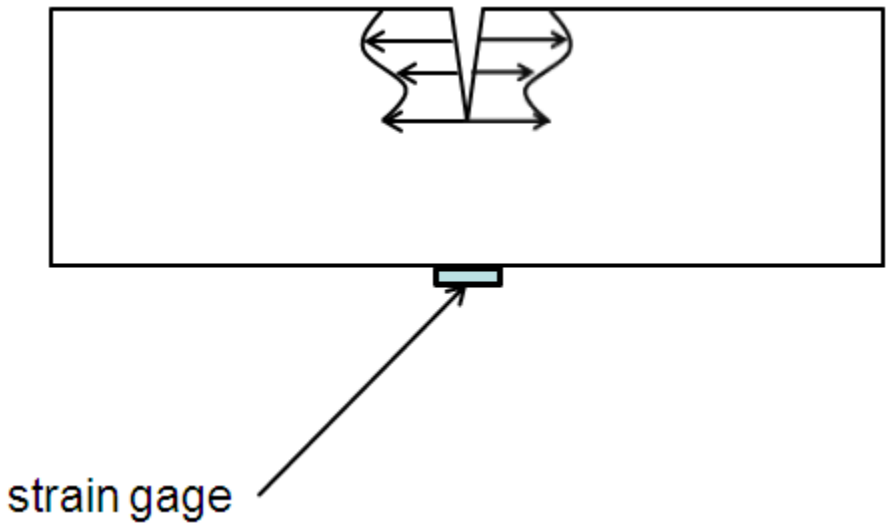

Figure 2-2 Incremental Slitting

The contour method (see Figure 2-3) involves complete sectioning of the component and measurement of surface deformation using a coordinate measuring machine. The original residual stress is determined through an inverse analysis using the measured surface deformation and a finite element model of the section. This technique provides spatial distribution of the stress over the entire cross-section of the cut. The component of the measured stress is perpendicular to the cutting plane. Due to the nature of the experiment, the contour method has difficulty resolving high stress gradients (e.g., surface stress variations due to machining) and may under-determine residual stress peaks in these situations. As with other mechanical techniques, the contour method assumes elastic material behavior and is susceptible to errors when stresses approach the material yield strength.

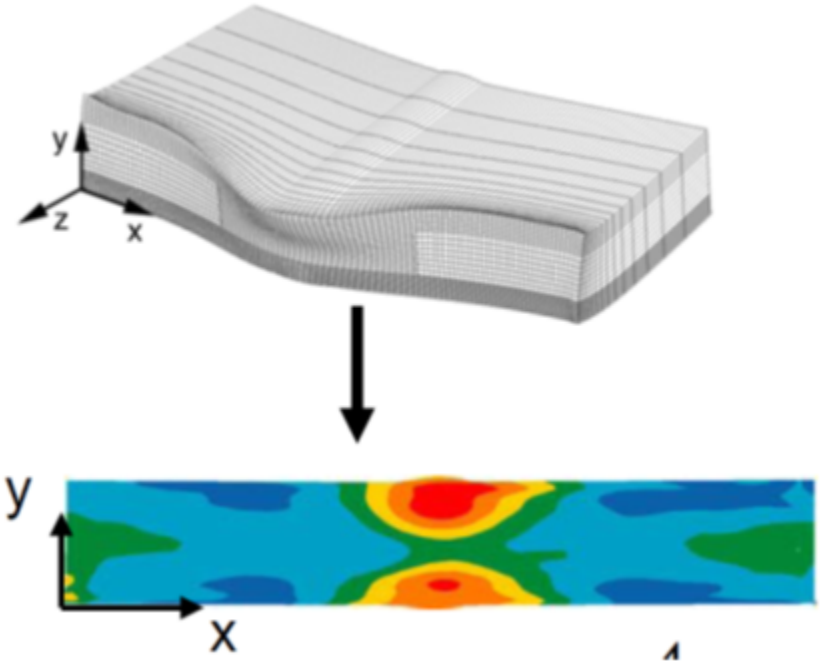

Figure 2-3 Contour Method (Courtesy: Hill Engineering, LLC)

Deep hole drilling (DHD) is illustrated in Figure 2-4. This technique for determining bulk stresses involves drilling a hole in the component and measuring the dimensions of the hole with an air probe. The drilled area is then trepanned using electro-discharge machining. The redistribution of residual stress due to trepanning affects the dimensions of the hole. A second air probe measurement of the hole provides the necessary information for residual stress determination. This measurement results in the spatial variation of three stress components (two normal and one shear) along the drilled path.

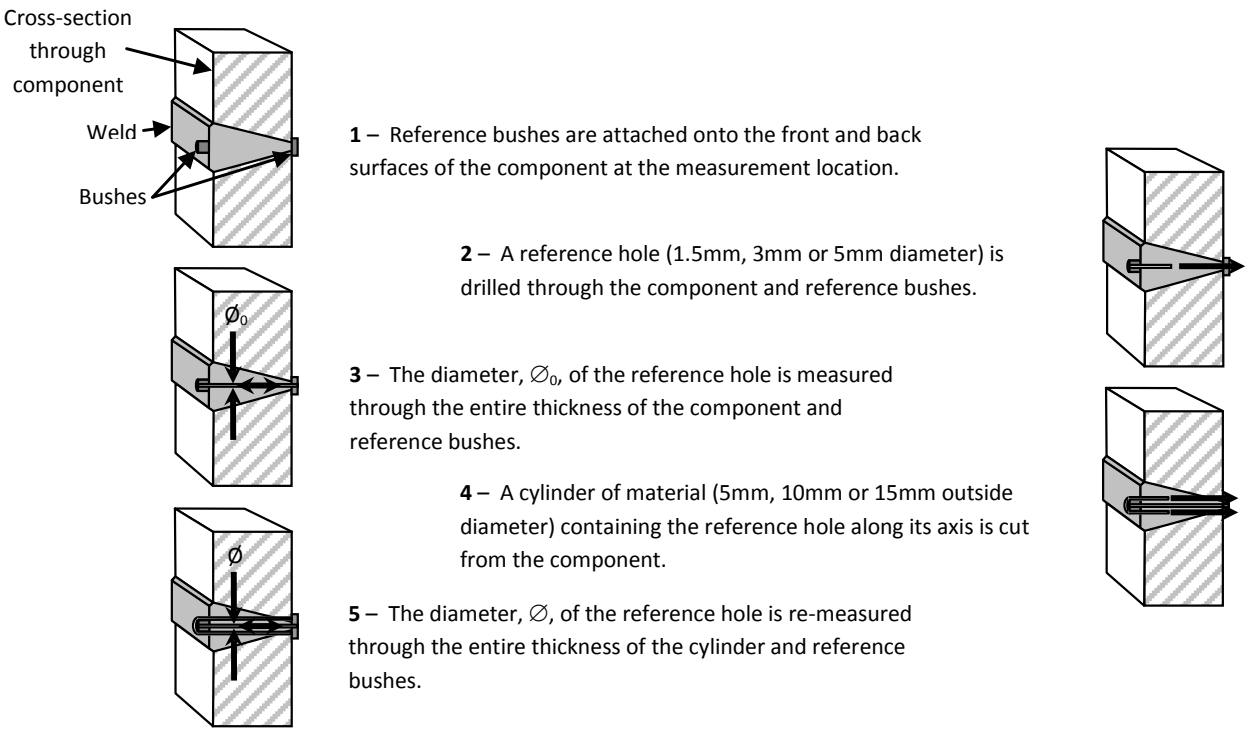

Figure 2-4 Deep Hole Drilling (Courtesy: VEQTER, Ltd.)

If residual stresses approach the material's yield strength, plastic deformation of the material when the drilled area is cut out can potentially affect DHD measurement results. A modification of the DHD method (Incremental DHD or iDHD), which incrementally cuts out the drilled area, temporarily stopping the plastic flow of material and measuring its affect with an air probe, was developed to produce more reliable results in high stress regions. The DHD measurements presented here were supplemented with the iDHD method in regions with high anticipated residual stresses.

2.3 Finite Element Modeling Techniques

2.3.1. Overview

The two-dimensional (2-D) FE models employed in this work were sequentially-coupled thermal-mechanical models. Using this approach, the transient heat transfer analysis (thermal model) was conducted to calculate the temporal and spatial distribution of temperature. This temperature distribution/history was then mapped to the structural analysis that calculated the stress field as a function of time (mechanical model). The 2-D models were either axisymmetric or generalized plane strain, depending on the geometry of the part being modeled.

2.3.2. Thermal Model

The thermal model calculates the temperature distribution in space and time, based upon the input material properties and the welding heat input model. Several methods exist to model the heat input during welding [39]. In a heat source model the total energy input as a function of time (J/s) accounts for the heat input from the welding torch. The 2-D nature of the models applied in this work means that a moving heat source is not modeled. Rather, the weld bead,

with its associated spatially-distributed heat flux, is applied across the entire surface of the part simultaneously. However, one method is based on a moving heat source model originally developed by Goldak [40] and modified for 2-D axisymmetric geometry [41]-[43]. In this model, the power density, Q [W/mm^2], is modeled as an exponential increase and decrease with time (Equation 2-3).

$$Q = K \exp\left\{ -\frac{[\tau - (1 + a_0)]^2}{a_0^2} \right\} \text{ for } \tau > 1 + a_0$$

$$Q = K \exp\left\{ -\frac{[\tau - (1 + a_0)]^2}{a_1^2} \right\} \text{ for } \tau \leq 1 + a_0 \qquad \text{Equation 2-3}$$

where, $K = \dfrac{C_2 \times E(p) \times V(p) \times A(p)}{a_0 + a_1}$, $a_0 = \dfrac{C_1}{S(p)}$, and $a_1 = \dfrac{2}{S(p)}$.

The user-specified weld parameters for this heat input model are defined as follows.

- $S(p)$ = weld speed for pass p
- $E(p)$ = arc efficiency for pass p
- $V(p)$ = voltage for pass p
- $A(p)$ = current for pass p
- τ = current time in seconds

Build up time and arrival time are given by:

- buildup time = a_0
- arrival time = $1 + a_0$

C_1 [mm] affects the duration over which the heat is applied, and C_2 is a dimensionless amplitude scaling parameter. Table 2-2 lists the material property inputs used in the thermal model.

Table 2-2 Material Properties for Thermal Model

Description	Dependencies
Density	Constant
Latent Heat	Constant
Solidus Temperature	Constant
Liquidus Temperature	Constant
Thermal Conductivity	Function of Temperature
Specific Heat	Function of Temperature

While Equation 2–3 approximates heating and cooling cycles that are experienced due to a moving heat source, the 2-D axisymmetric models employed in this work do not explicitly model a moving weld arc. Other commonly-used heat models may have similar, but not identical, exponential forms [39].

An alternative simplified approach to Equation 2-3 is to specify a constant heat flux with time over the weld bead elements. In either case, conduction to the adjacent elements and convection to the surroundings was modeled. The calculated transient temperatures can be compared to thermocouple data to calibrate thermal model parameters. While the chosen heat input model is often applied over a single weld bead, analysts may choose to "lump" a number of beads together and apply the heat over the entire lumped area. This approach requires careful calibration of the heat input model and may introduce uncertainties in the results [39].

2.3.3. Mechanical Model

The mechanical model calculates stress and strain based upon the temperature distribution determined by the thermal model. While exact methods vary from analyst to analyst, material property inputs for the structural model may include:

- coefficient of thermal expansion
- elastic modulus
- strain hardening law
- flow stress as a function of plastic strain
- creep law
- annealing temperature

Many of these parameters are a function of temperature.

During plastic deformation most metals harden, requiring increasing load to cause further plastic deformation. The chosen strain hardening law defines how hardening behavior is calculated in the FE model. Example hardening laws include: elastic-perfectly plastic, isotropic hardening, kinematic hardening, and mixed isotropic-kinematic hardening [39]. For isotropic hardening, the yield surface expands upon plastic deformation, such that the yield stress in tension is always equal to the yield stress in compression. The yield surface translates in the kinematic model, meaning that the yield stress is different in tension and compression. Real materials exhibit both isotropic and kinematic hardening behavior during deformation (mixed hardening). Development of hardening laws may require extensive material testing.

Creep properties may be used to simulate stress relaxation during post weld heat treating (PWHT). Typically, the nozzle buttering on the carbon or low alloy steel nozzle is heat treated prior to service, so it is useful to simulate this step. For some FE software packages, the annealing temperature input causes all existing plastic strains to be analytically removed upon reaching that temperature.

2.3.4. Additional FE Modeling Details

For cylindrical geometry discussed in this report, the elements used in the thermal model were axisymmetric, diffusive heat transfer elements. Plane strain elements were used for the plate geometry. The mesh was fine at the weld passes and in the adjacent regions, where high stress and temperature gradients were expected. The mesh was allowed to coarsen away from those areas for computational efficiency. The boundary conditions varied, depending upon the geometry and type of constraint in the physical system. The thermal model allowed heat convection along the entire surface of the assembly. For the mechanical model in axisymmetric cases, one node in the nozzle region (see Figure 1-1) away from the welds was restrained from

displacing parallel to the nozzle axis. Potentially, more than one node could be similarly restrained, without appreciably affecting the results [39].

The thermal model consisted of transient heat transfer steps for each weld pass. The mechanical model consisted of transient static response steps for each weld pass. Transient static response steps with time-dependent material behavior were required to simulate stress relaxation during heat treatment.

2.4 WRS Validation Conclusions

Chapter 2 provided a discussion of techniques for developing validation criteria for WRS FE simulations. Conclusions are as follows.

- While validation criteria have been proposed by other organizations, the NRC has not developed specific criteria for WRS model validation as of publication of this document.
- Validation criteria can potentially be based upon stress intensity factors, fusion zone area, root-mean-square differences between measurement and model results, and a combination of these and other quantities.
- Diffraction measurements are based upon changes in crystal lattice spacings relative to a chosen reference lattice spacing.
- Strain relief measurements are based upon measurements of strain and/or deformation when the dimensions of the material are physically altered.
- For WRS measurement, two independent measurements that are based upon different physics (e.g., a diffraction measurement and a strain relief measurement) have been recommended to obtain confidence in measurement techniques.
- The FE techniques considered in this study include mostly 2-D models, so a moving heat source is not explicitly modeled.
- The thermal model can simulate heat input during welding based upon previously-developed equations for moving arc analyses. A less sophisticated approach may involve holding weld bead elements at a certain temperature for a given time, while any temperature decrease is based solely upon conduction and convection.
- The mechanical model calculates strains (and stresses) based upon the temperature fields calculated in the thermal model.
- Several approaches are available to account for strain hardening material behavior, including: isotropic, kinematic, mixed, and elastic-perfectly plastic.

3 PHASE 1: SCIENTIFIC WELD SPECIMENS

3.1 Introduction

Phase 1 of the weld residual stress (WRS) Validation Program focused on small specimens that were not representative of nuclear plant components. Two geometries were considered: a grooved plate and a cylinder with a butt weld in the center. The purpose of Phase 1 was to efficiently develop knowledge of WRS measurement and modeling techniques. Discussion of the Phase 1 work can also be found in the Electric Power Research Institute's (EPRI's) Materials Reliability Program (MRP)-316 report [45].

3.2 Specimen Fabrication

3.2.1. Flat Plate Specimens

Six flat plates were fabricated as shown in Figure 3-1. Two of those plates were used for material property characterization, while the other four were designated for WRS measurement. The plate material was 304L stainless steel (UNS S30403), and the deposited weld metal was Alloy 82 (UNS N06082). Nominal chemistry of these two materials is shown in Table 3-1 and Table 3-2 [46], [47].

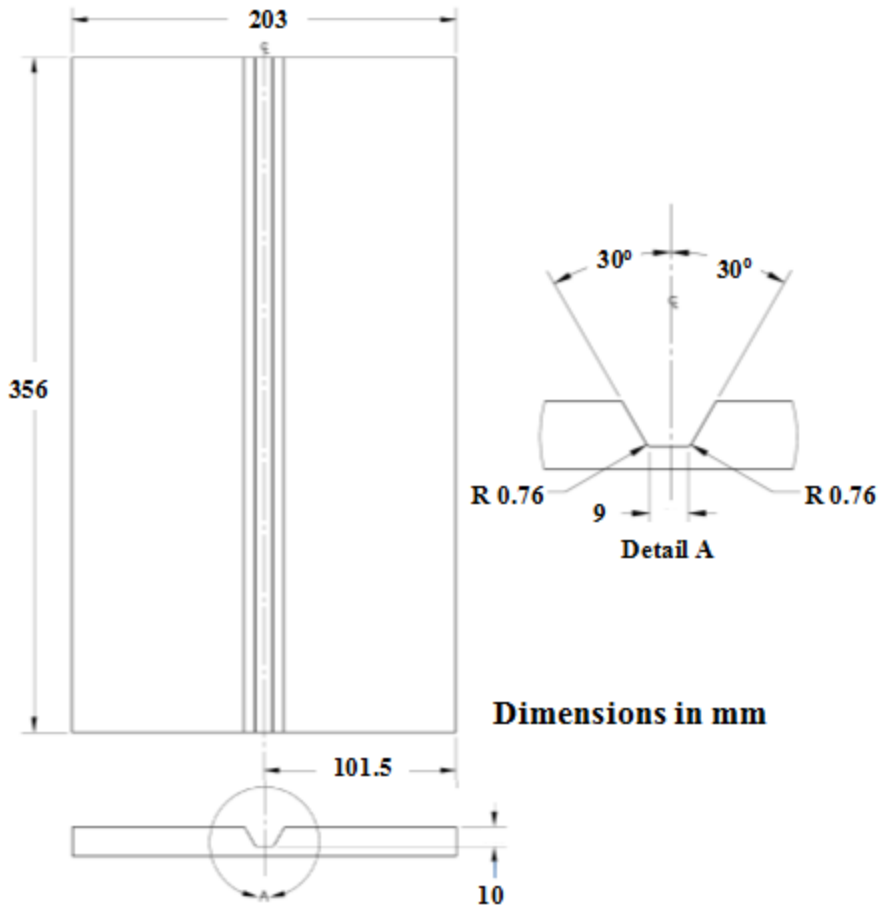

Figure 3-1 Flat Plate Geometry (Courtesy: EPRI)

Table 3-1 Chemical Composition of 304L Stainless Steel [46]

C	Mn	P	S	Si	Cr	Ni	N
0.03	2.00	0.045	0.030	0.75	18.0-20.0	8.0-12.0	0.10

Table 3-2 Chemical Composition of Alloy 82 [47]

C	Mn	Fe	P	S	Si	Cu	Ni	Ti	Cr	Nb + Ta
0.10	2.5-3.5	3.0	0.03	0.015	0.50	0.50	67.0 min	0.75	18.0-22.0	2.0-3.0

The welding method for depositing filler metal in the groove was automated gas tungsten arc welding. The different plate specimens were designated P-3, P-4, P-5, and P-6, with welding parameters listed in Table 3-3. All weld passes were started on the same side of the plate. Restraint was applied during welding by an aluminum backing plate loaded by Belleville washers with linear force/displacement behavior. The weld and restraint geometry is illustrated in Figure 3-2. The bolts in the restraint were preloaded to account for differential thermal expansion between the plate and fixture materials. Thermocouple data was collected during welding, and bead geometry was measured using laser profilometry between passes. Example data from thermocouples and laser profilometry are shown in Figure 3-3 and Figure 3-4, respectively.

Table 3-3 Welding Parameters for Plate Studies (Courtesy: EPRI)

ID	Variable Tested	No. of Passes	Current (A)	Voltage (V)	Travel Speed (mm/s)	Wire Feed Speed (mm/s)	
						Root Passes	Remaining Passes
P-3	Plate Base Case	11	275/225	11.5	2.5	32	41
P-4	Decrease Travel Speed	7	275/225	11.5	1.5	32	41
P-5	Increase Current and Wire Feed Rate	7	375/325	11.8	2.5	58	58
P-6	Decrease Current and Wire Feed Rate	23	175/125	10.8	2.5	17	17

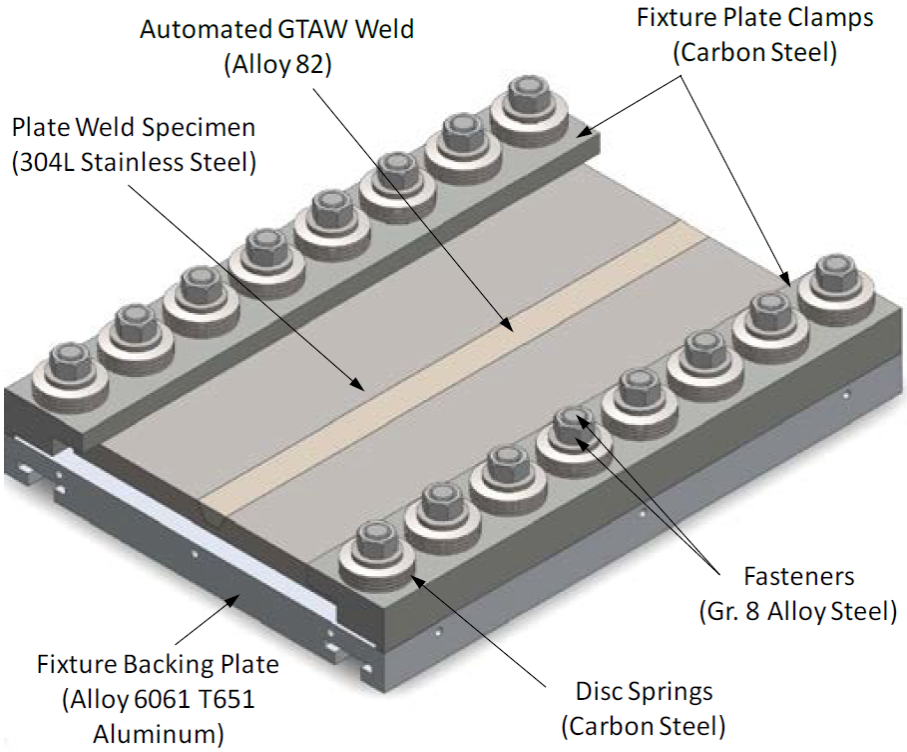

Figure 3-2 Welding Restraint for Plate Specimen (Courtesy: EPRI)

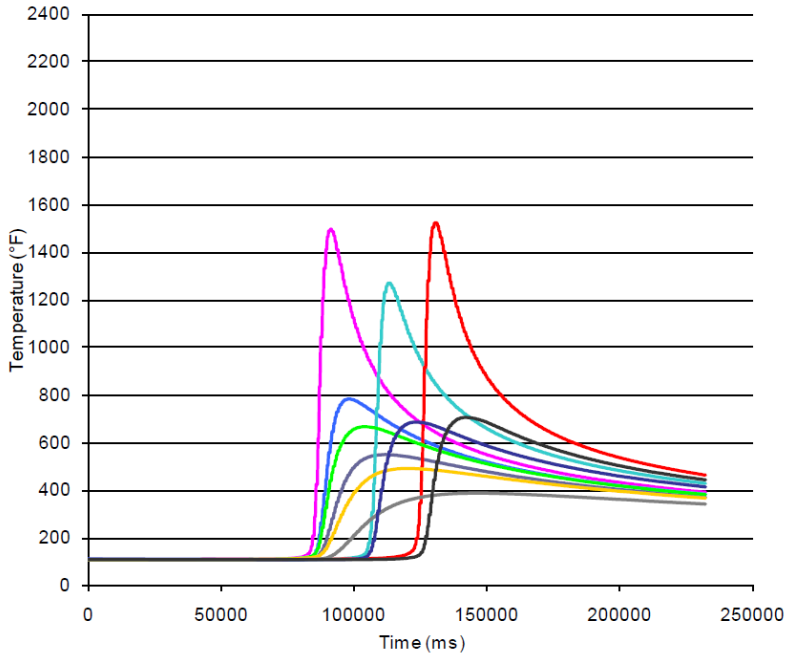

Figure 3-3 Example Thermocouple Data (Courtesy: EPRI)

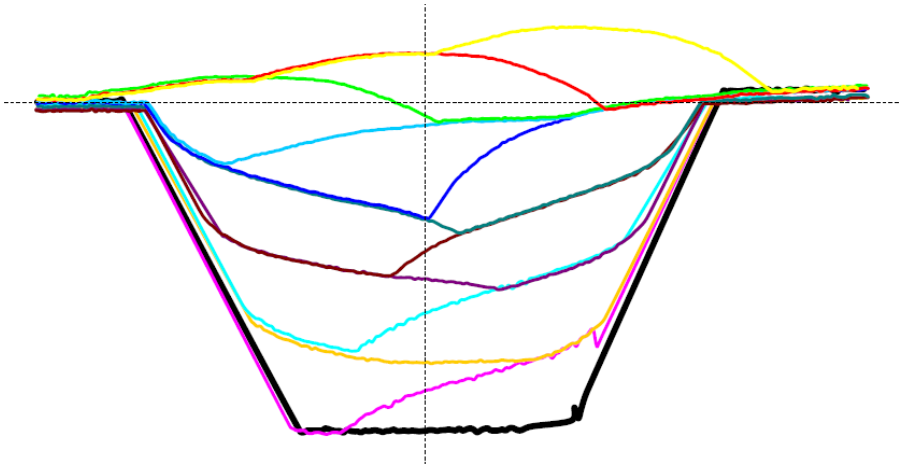

Figure 3-4 Example Laser Profilometry Data (Courtesy: EPRI)

3.2.2. Cylindrical Specimens

The fabrication materials for the cylindrical specimens included 304L stainless steel (SS), 308 SS, and plain carbon steel (CS). Five cylindrical specimens were welded, according to the geometry in Figure 3-5. One of those specimens was used for material property characterization, while the others were used for WRS measurement. The specimens were fabricated with increasing weld complexity, as shown in Figure 3-6. Table 3-4 summarizes the specimen designations: C-1, C-3, C-4, and C-5. One specimen type consisted of two 304L SS cylinders welded with Alloy 82 (cylinder C-1). The second specimen type consisted of CS and 304L SS ring for base material (cylinder C-3). The joint between the two materials included an Alloy 82 buttering weld. Finally, the most complex specimen consisted of a CS ring joined to a SS safe end with a buttering weld and an Alloy 82 dissimilar metal (DM) weld (cylinder C-5). The safe end was welded to a 304L SS ring with an E308L SS weld. Cylinder C-5 most closely

approximated actual nuclear component welds, as illustrated in Figure 1-1. A repair weld was also applied to cylinder C-5. This repair involved machining a cavity into the weld, according to Figure 3-7, and filling the cavity with Alloy 82 weld metal.

The welding method for the circumferential butt weld was automated gas tungsten arc welding. Seven weld passes were deposited for each weld. The welding parameters for the three specimen types are shown in Table 3-5. The starts and stops were confined to a 90 degree sector, so that measurement could be taken on the opposite side of the weldment.

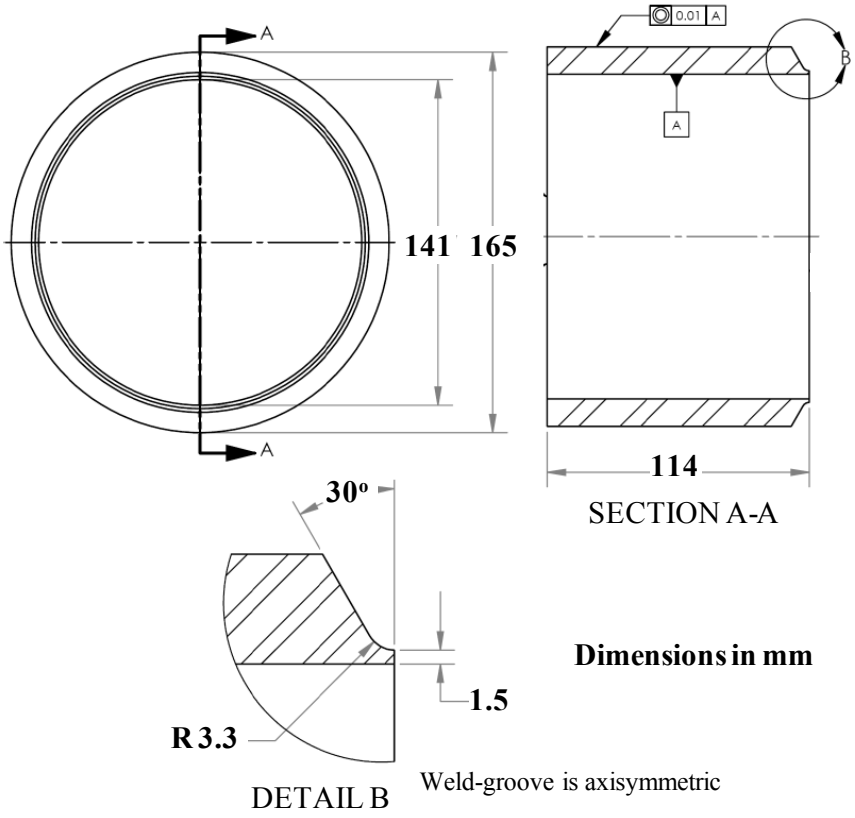

Figure 3-5 Cylindrical Specimen Geometry (Courtesy: EPRI)

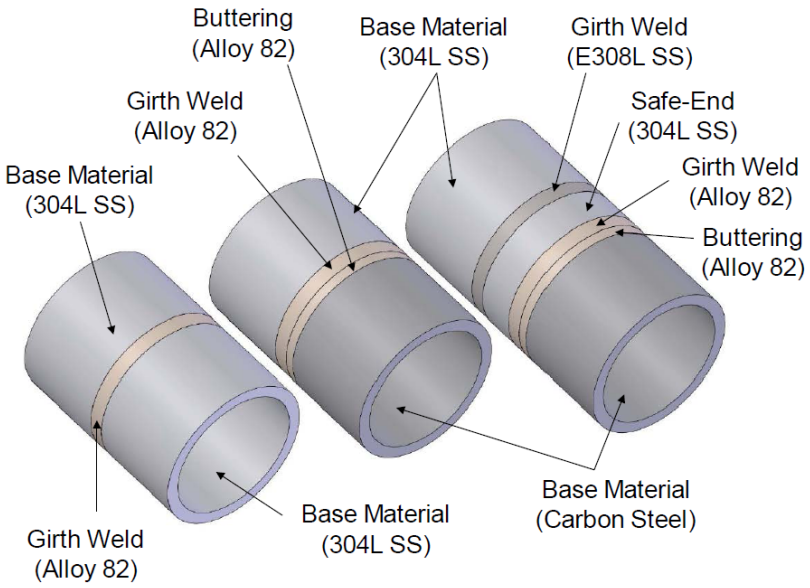

Figure 3-6 Three Specimen Types (Courtesy: EPRI)

Table 3-4 Cylinder Specimen Designations (Courtesy: EPRI)

	ID	Specimen Description	No. Passes	Butter PWHT
Phase 1B Cylinders	C-1	SS Cylinder to SS Cylinder Weld	7	-
	C-3	Buttered CS Cylinder to SS Cylinder Weld	7	Yes
	C-4	Buttered CS Cylinder (No PWHT) to SS Cylinder Weld	7	No
	C-5	Buttered CS Cylinder to SS "Safe End" → SS "Safe End" to SS Cylinder	7	Yes

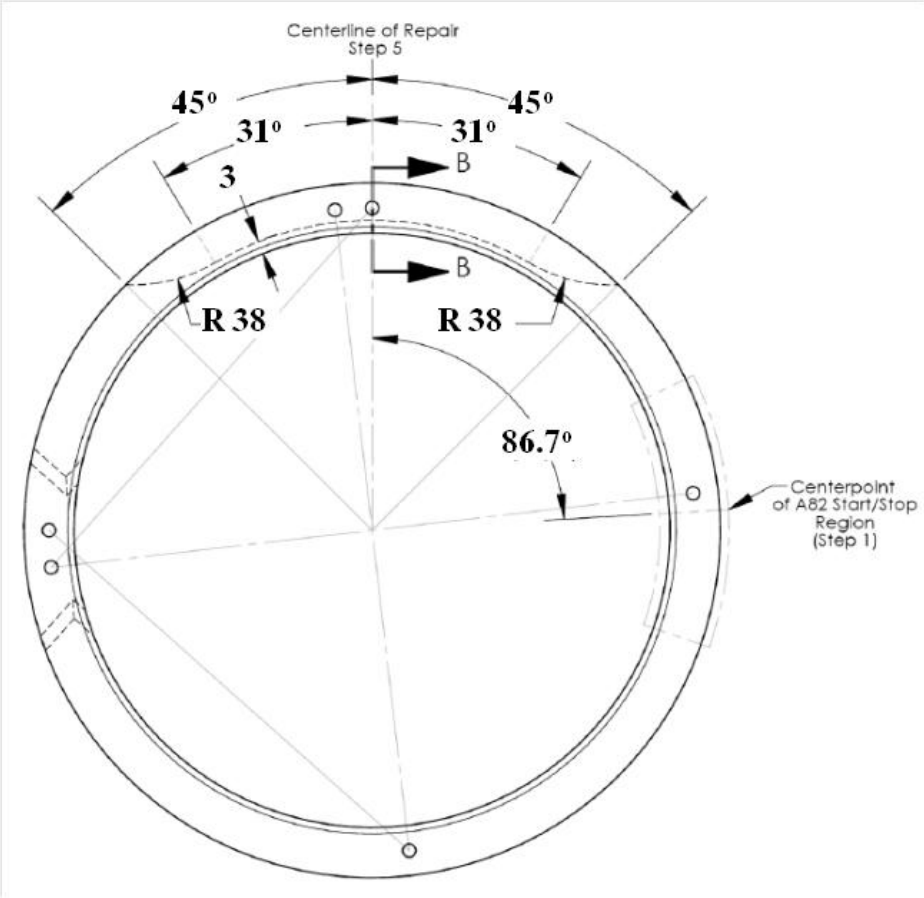

Figure 3-7 Cylinder C-5 Repair Weld Geometry (Courtesy: EPRI)

Table 3-5 Cylindrical Specimen Weld Parameters (Courtesy: EPRI)

	Weld Passes	Current (A)	Voltage Range (V)	Travel Speed Range (in/min)	Wire Feed Speed (in/min)
SS-A82-SS	1	210/160	9.0-9.8	5.7-6.2	22 ± 2
	2	210/160	9.0-9.8	5.7-6.1	52.5 ± 5
	3	250/220	9.4-9.8	5.5-5.9	100 ± 5
	4 and up	350/300	10.5-11.5	5.5-5.9	96 ± 5
ButterCS-A82-SS	1	190/150	9.4-10.0	5.7-6.2	25 ± 2
	2	210/160	9.0-9.8	5.7-6.1	57 ± 6
	3	250/220	9.4-9.8	5.5-5.9	80 ± 5
	4 and up	300/270	10.5-11.5	5.5-5.9	96 ± 5
SS-ER308L-SS	1	190/150	9.4-10.0	5.7-6.2	25 ± 2
	2	190/150	9.0-9.8	5.7-6.1	47 ± 5
	3	250/220	9.4-9.8	5.5-5.9	75 ± 5
	4 and up	300/270	10.5-11.5	5.5-5.9	96 ± 5

3.3 Results and Discussion

This section describes representative results from Phase 1 of the WRS Validation Program. Comprehensive results are found in the EPRI report MRP-316 [45].

3.3.1. Surface Stress Measurements

Figure 3-8 and Figure 3-9 show comparisons of several surface measurement techniques on the plate specimens. The results are plotted as the longitudinal and transverse components as a function of depth from the surface, where a position of 0 represents the original plate surface, a negative position represents the weld crown that extended above the plate surface, and a positive position represents distance through the thickness of the plate. In general, the surface techniques do not show good agreement. Figure 3-10 shows x-ray measurement results along a line perpendicular to the weld for a plate specimen. Since the same material exists on each side of the weld, more-or-less symmetric data is expected. This data showed rather high-magnitude values (i.e., ± 1,000 MPa) and unexpected asymmetry relative to the weld centerline.

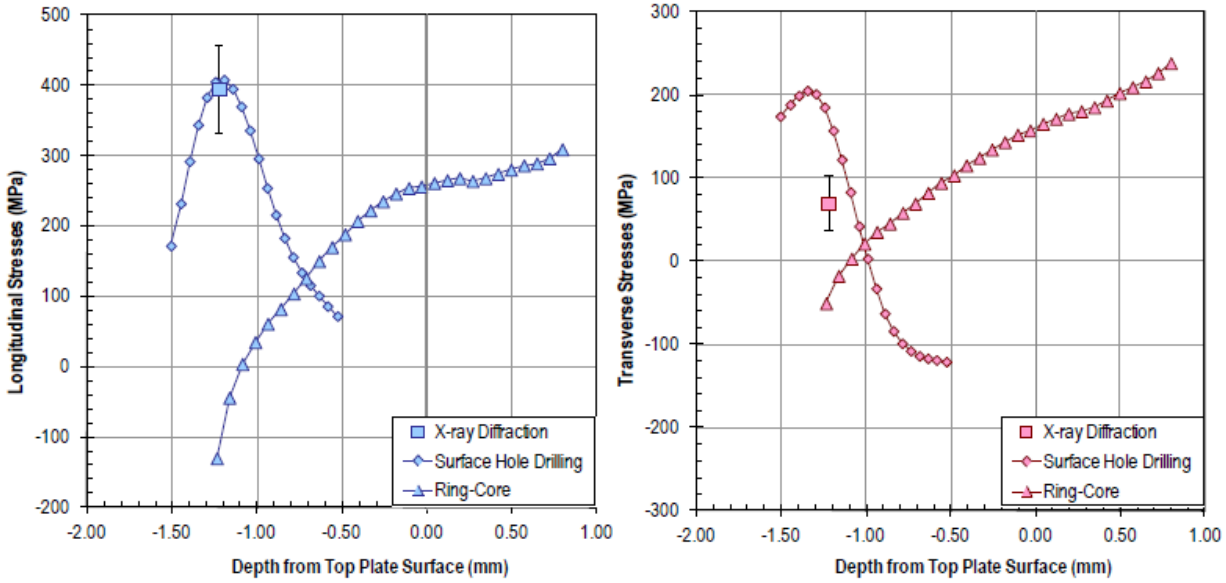

Figure 3-8 Surface Stress Measurements for Plate P-3 (Courtesy: EPRI)

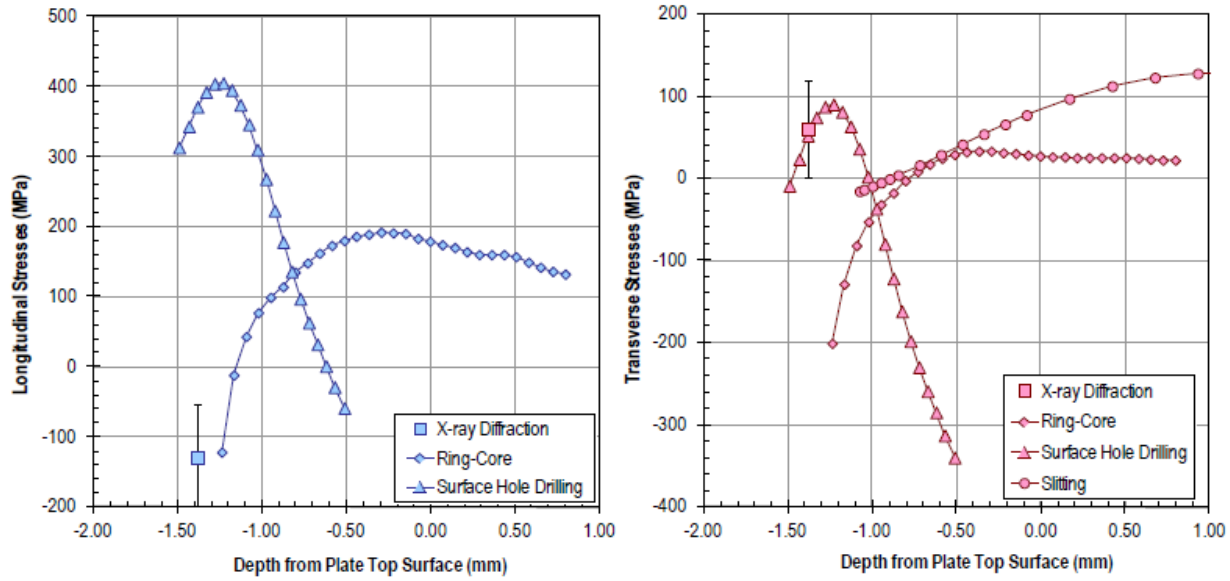

Figure 3-9 Surface Stress Measurements for Plate P-4 (Courtesy: EPRI)

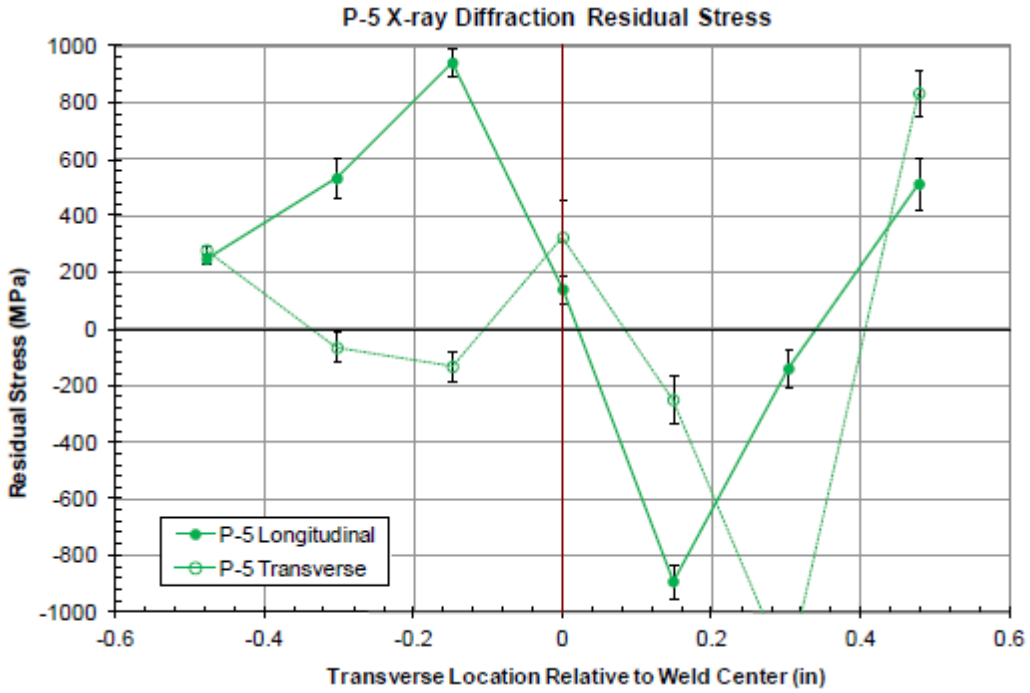

Figure 3-10 X-ray Results Across the Weld (Courtesy: EPRI)

Figure 3-11 shows deep hole drilling results through the depth of a cylindrical specimen, as measured from a hole drilled through the weld centerline. Analogous results are shown for the repair weld centerline in Figure 3-12. These results showed reasonable magnitudes and smooth trends. They also demonstrated an increase in the hoop stress in the small cylinder resulting from the repair weld.

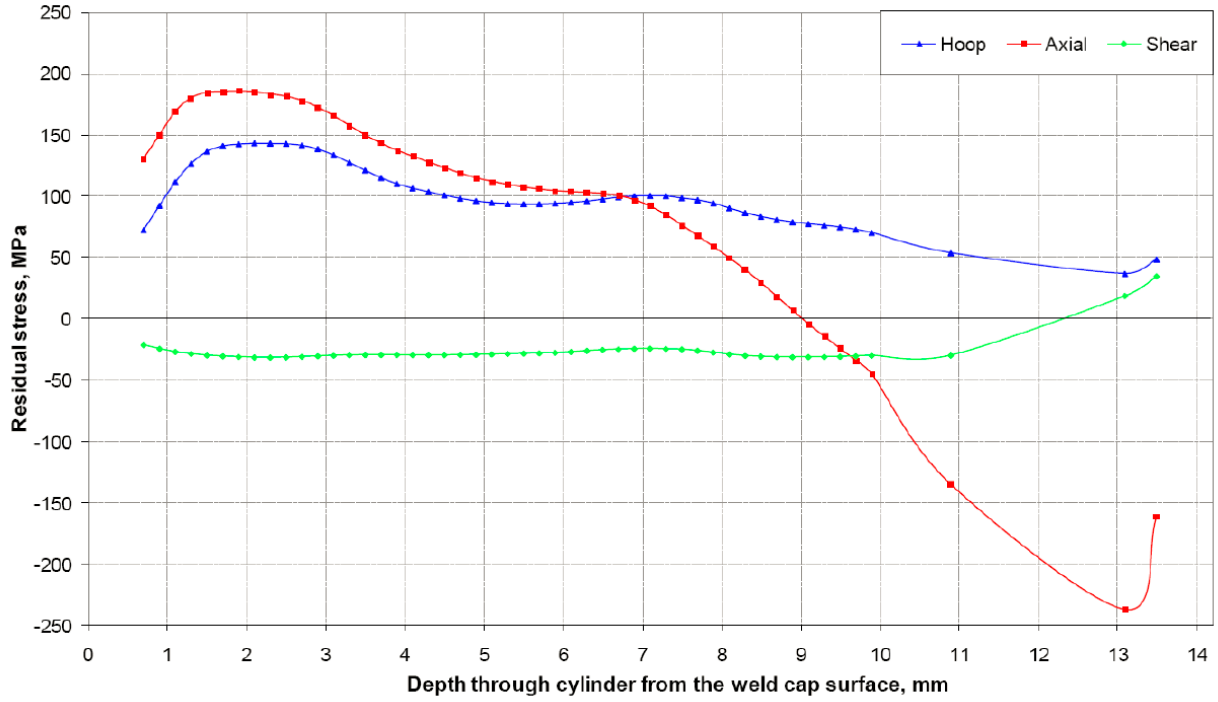

Figure 3-11 Deep Hole Drilling Results (Courtesy: EPRI)

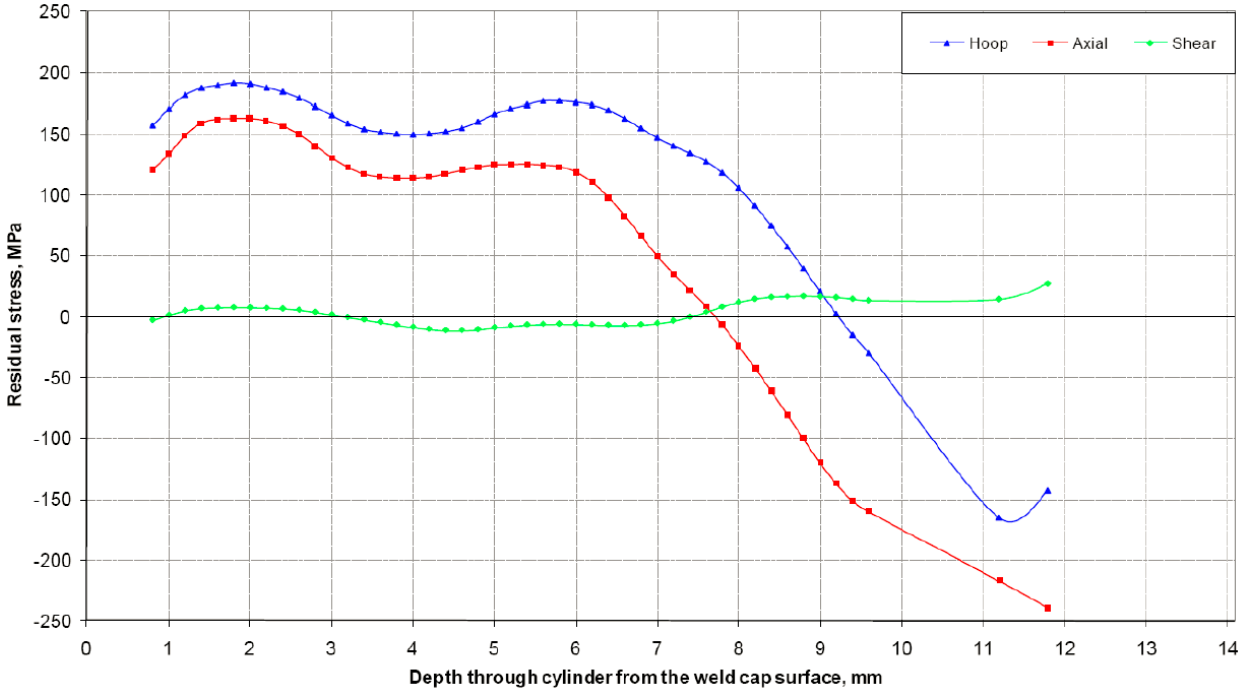

Figure 3-12 Deep Hole Drilling Results for along Repair Centerline (Courtesy: EPRI)

Example results from the contour method are shown in Figure 3-13, which demonstrates that the contour method provides stress values distributed over a cross-section. The results from the contour measurements provided reasonable magnitudes and smooth trends.

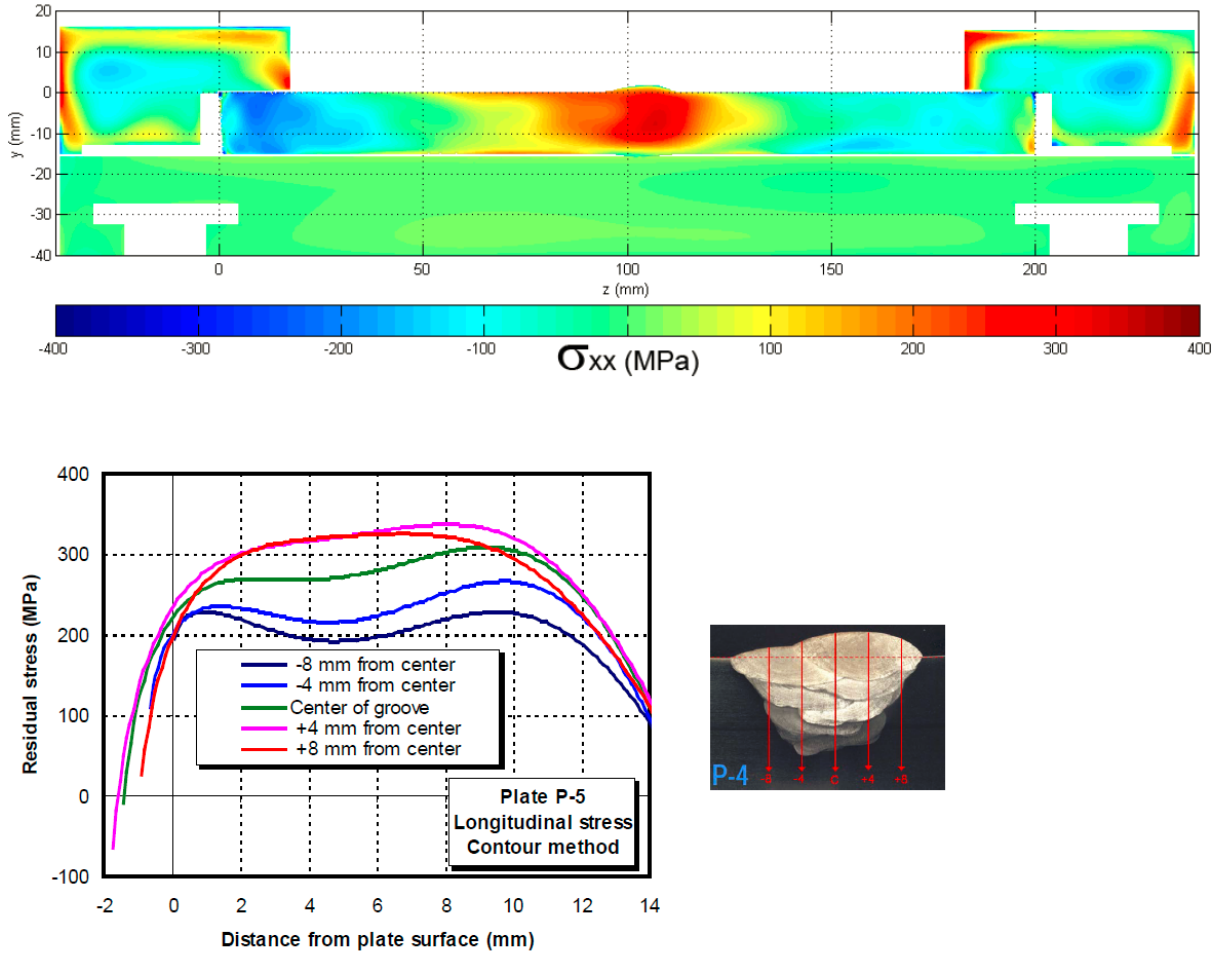

Figure 3-13 Contour Method Results (Courtesy: EPRI)

Figure 3-14 and Figure 3-15 show a comparison of through-thickness modeling and measurement results for a plate specimen. Similar results for a cylindrical specimen are shown in Figure 3-16 and Figure 3-17. Model A in these figures implemented the elastic-perfectly plastic hardening law, while Models B and C implemented the isotropic hardening law. Model D used a bilinear kinematic hardening law. The best agreement between modeling and experiments was observed for the transverse stress in the plate specimen (Figure 3-15).

In some cases, most notably in Figure 3-16 and Figure 3-17, the neutron results exhibited a large degree of scatter. Nickel alloy welds can have large grains, preferred orientation, and chemical concentration gradients when joining dissimilar base materials. These effects can combine to affect results and greatly increase experimental difficulty. The large scatter in the data reported here is likely a result of these effects.

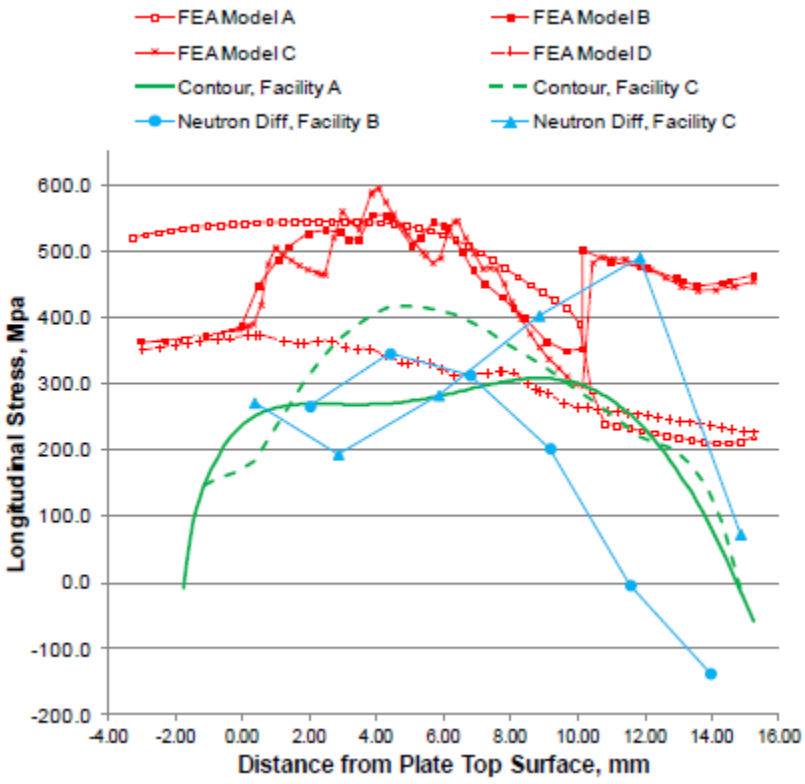

Figure 3-14 Longitudinal Stress for Plate P-4 (Courtesy: EPRI)

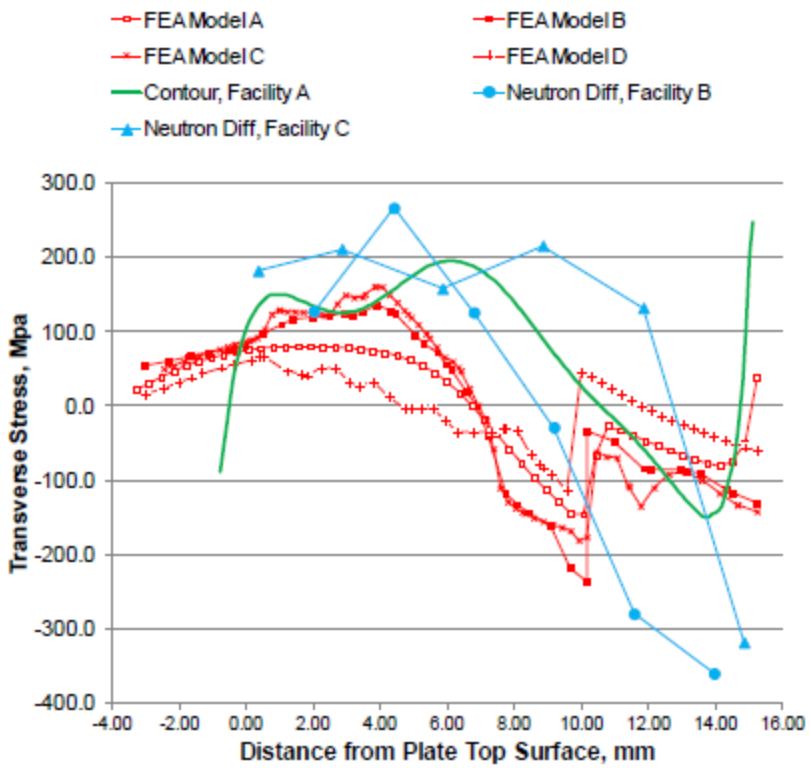

Figure 3-15 Transverse Stress for Plate P-4 (Courtesy: EPRI)

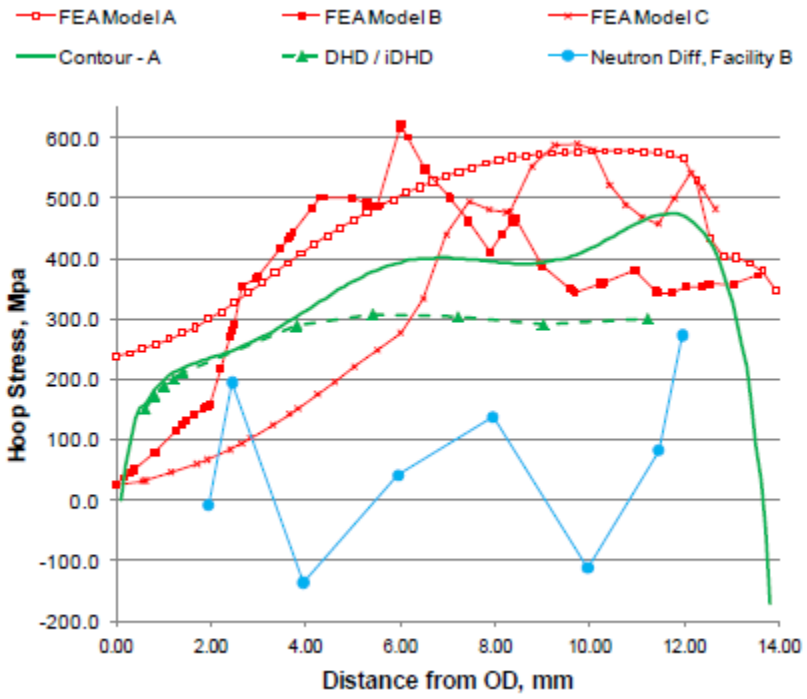

Figure 3-16 Hoop Stress for Cylinder C-3 (Courtesy: EPRI)

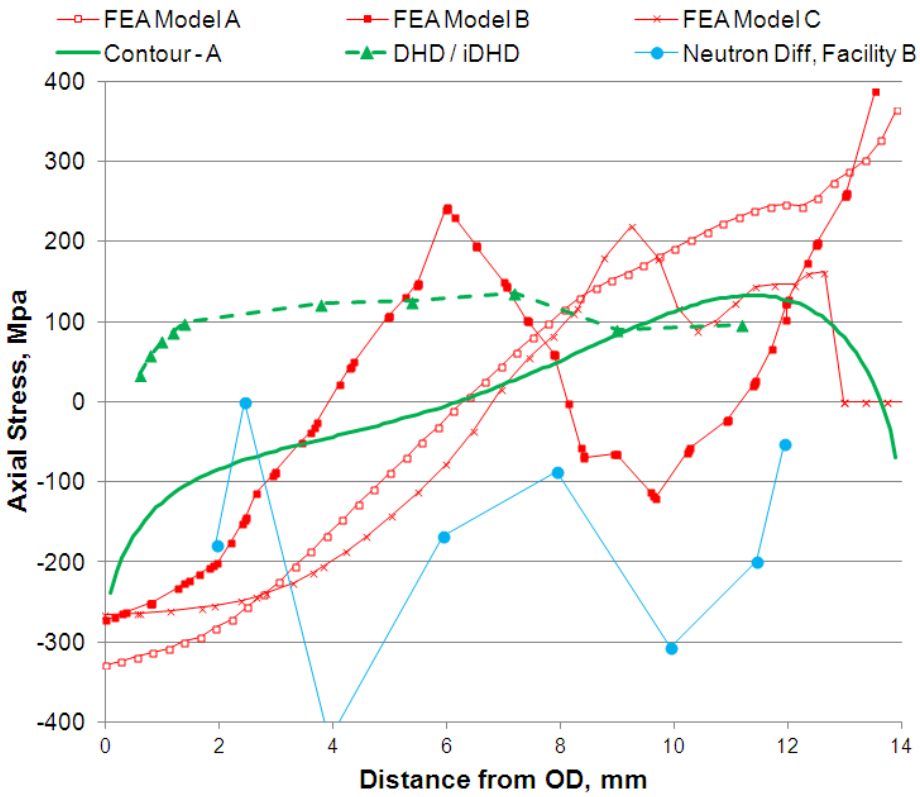

Figure 3-17 Axial Stress for Cylinder C-3 (Courtesy: EPRI)

3.3.2. Sources of Measurement Error

The diffraction-based results exhibited scatter. Chemical concentration gradients created during the welding process can affect the measured d_{hkl}. This effect requires that the specimen be cut into small coupons to relieve the stress. A spatially-dependent $d_{hkl,0}$ can then be measured. This process increases the experimental complexity and experimental error, as the scattering volume for the reference measurement may not be identical to that of the original measurement. Also, large grains and crystallographic texture, both of which may be present in weldments, can cause problems with scattering statistics. Performing the experiment at a pulsed neutron source, using techniques described by Brown et al. [48], may mitigate these problems. The stress measured at a pulsed neutron source can be based upon several diffraction peaks, rather than just a single peak. Results from a pulsed neutron source are shown in Figure 3-18 [48]. In this case, the neutron results showed reasonable trends and agreed well with modeling and an independent contour measurement. In general, however, diffraction techniques may not be optimal for the materials of interest in safety-related nuclear component welds. The data in Figure 3-18 is also shown in Figure 3-14 and Figure 3-15 as “Neutron Diff Facility C” and “Contour Facility C.”

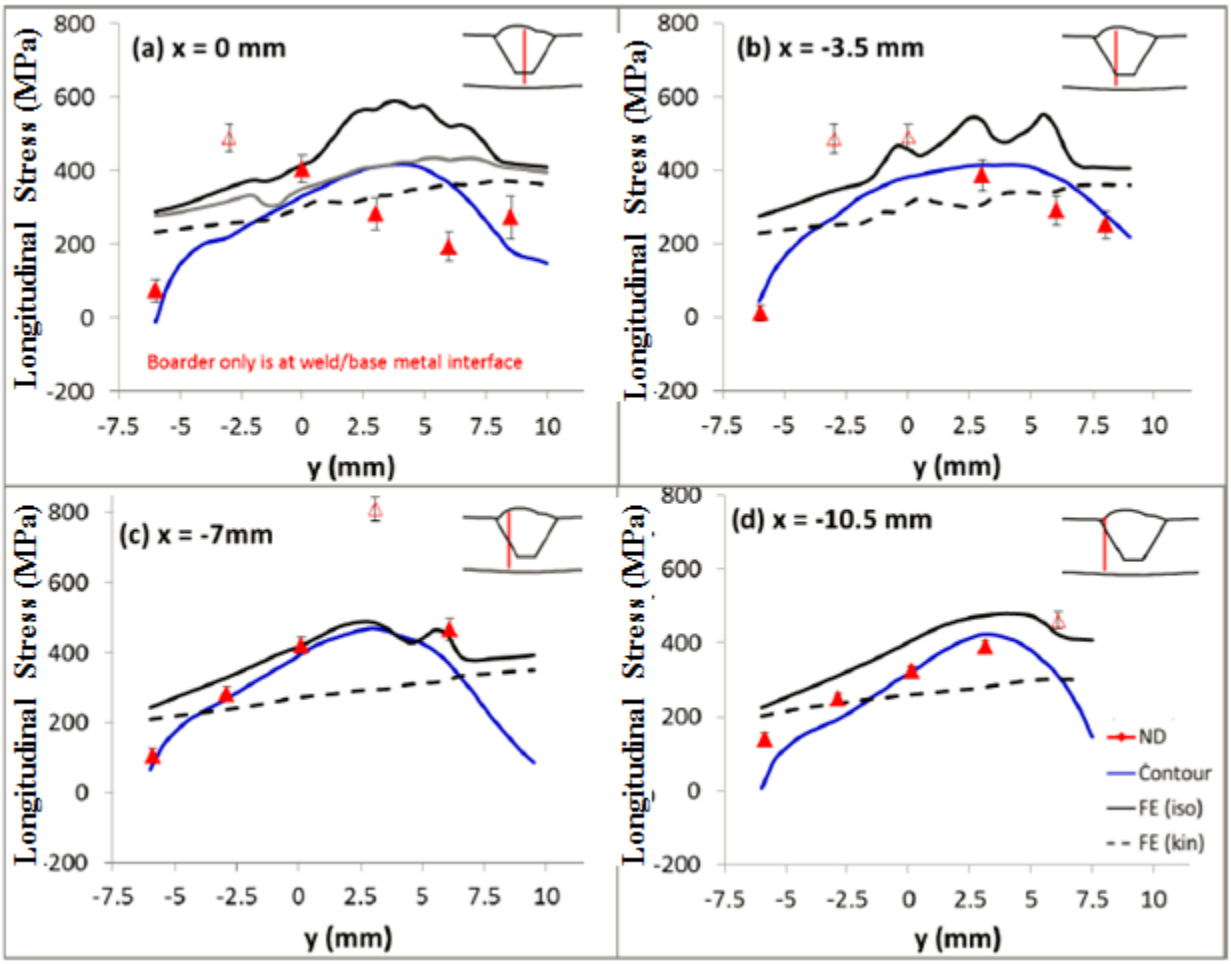

Figure 3-18 Stress Results from a Pulsed Neutron Source (open symbols: at weld/base metal interface)

3.3.3. Sources of Modeling Uncertainty

It is evident in Figure 3-14 through Figure 3-18 that the various modeling results do not agree. The choice of hardening law, in particular, can be a large source of modeling uncertainty, since it has a direct effect on the calculation of stress. A lack of common procedures for post processing may have contributed to observed modeling uncertainty. Modeling variability increased when considering the cylinder specimens. This model geometry was likely more dependent on modeler assumptions taking weld cavity shrinkage into account for weld bead size and shape in the cylinder specimens, since the cylinder welds were less constrained than the plate specimens.

3.4 Phase 1 Conclusions

Phase I of the NRC/EPRI WRS Validation Program consisted of small scientific specimens for the purpose of developing modeling and measurement capabilities. Conclusions from this work include:

- Small plate and cylinder specimens allowed development of WRS measurement and modeling techniques.
- Results from near-surface stress measurements, using a variety of techniques, did not compare well with each other. Therefore, uncertainties are larger for near-surface residual stresses than for bulk residual stresses.
- Select results from diffraction-based techniques exhibited high scatter. The likely cause is the combined effects of large grains, crystallographic texture, and chemical concentration gradients associated with the nickel alloy DM weld. While certain experimental procedures can mitigate these effects, diffraction techniques may not be optimal for the materials present in safety-related nuclear component welds.
- Through-thickness strain relief measurements provided reliable results, in these studies.
- Potential sources of modeling uncertainty in the Phase 1 work included choice of hardening law, differences in post-processing procedures, and differences in weld bead geometry for the cylindrical specimens.
- Measurements and models showed some agreement.
- The Phase 1 results served to develop measurement and modeling techniques for application to prototypic mockups in later phases of the WRS Validation Program. While the hardening law assumption at this stage was known to be a source of modeling uncertainty, no attempt was made to restrict the choice of hardening law in studies that followed. The effect of hardening law can easily be separated when comparing various modelers' results to each other and to experimental data. Through-thickness strain relief-based techniques were determined to be the primary source of WRS measurement information for the remaining phases of the WRS Program.

4 PHASE 2A: FABRICATED PROTOTYPIC NOZZLE

4.1 Introduction

The Phase 2a effort consisted of measurement and modeling on a prototypic pressurizer surge nozzle mockup. This phase of the research was intended to compare WRS model results with measurements and to assess modeling uncertainty. The modeling effort in this phase of the work included a double-blind finite element modeling round robin, where measurement data was hidden from the analysts. Discussion of the Phase 2a work can also be found in EPRI's MRP-316 report [45]. Phase 2b was an ongoing effort as of the publication of this document.

4.2 Mockup Fabrication

The geometry chosen for the WRS round robin was representative of a pressurizer surge nozzle, due to its safety significance and relevance to flaw evaluation [50]. The overall geometry is shown in Figure 4-1. The SA-105 carbon steel nozzle was attached to a hot-rolled steel plate to represent the stiffness of the nozzle in service. The stiffened nozzle was buttered with Alloy 82 (American Welding Society A5.14, ERNiCr-3, UNS N06082) weld material, post weld heat treated, and then welded to a forged F316L stainless steel safe-end. Finally, the safe end was welded to a TP316 stainless steel, 14-inch diameter Schedule 160 pipe using a TP308 weld.

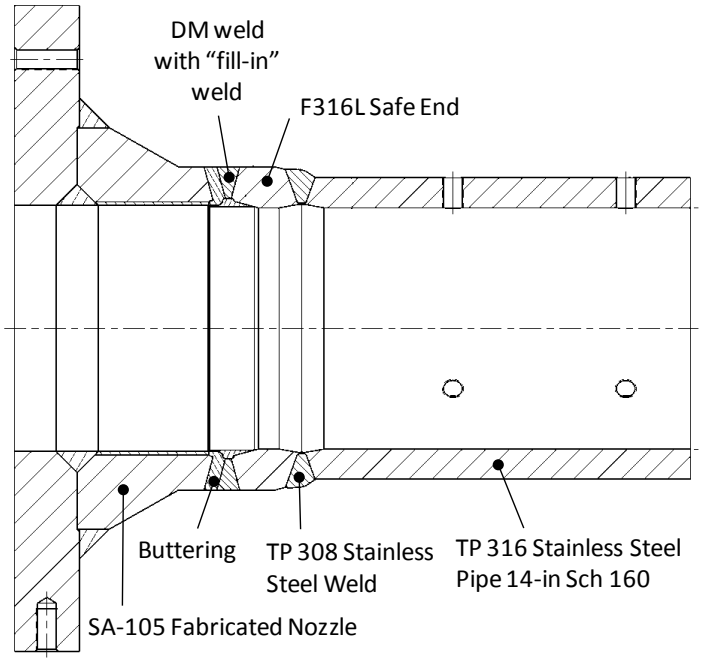

Figure 4-1 Phase 2a Mockup

Mockup fabrication occurred in the following five steps.

- 137 butter passes of Alloy 82
- Heat treat (600-650^{o}C for 3 hours) and machining of the butter
- 40 passes of Alloy 82 (constituting the DM weld) to join the carbon steel nozzle to the stainless steel safe end.
- Machining of the DM weld root (i.e., at the inner diameter location.)
- 27 passes of Alloy 82 to make up the 360 degree fill-in weld.

At this point, residual stress measurements were made on the DM weld. The residual stress measurements were followed by the TP308 stainless steel safe end to pipe weld, with a second set of residual stress measurements made investigating the effect of the safe end to pipe closure weld. For the main DM weld and fill-in weld, laser profilometry measurements mapped the contour of each weld pass.

Temperature during mock-up welding was recorded as a function of time using thermocouples placed on the inner diameter (ID) and outer diameter (OD). Six thermocouples were placed on the top dead center location during the butter welding (three thermocouples each on the ID and OD). Thermocouple measurements were also made at both 45 and 90 degrees circumferentially from the top dead center (again, three thermocouples each on the ID and OD). For the repair and fill-in weld, the same thermocouple location could not be used on the ID, so the locations of these thermocouples were shifted axially.

The materials for each component of the mock-up are shown in Table 4-1.

Table 4-1 Phase 2a Mockup Material Specifications

Component	**Material**
Nozzle	Carbon steel (SA-105)
DM Weld (including buttering, and fill-in)	Alloy 82: AWS A5.14 ERNiCr-2 (UNS N06082)
Safe End	F316L forged stainless steel
Stainless Pipe	TP 316 stainless steel, 14-inch diameter Schedule 160
Stainless Steel Weld	TP 308 stainless steel

The main DM weld was deposited using gas tungsten arc welding (GTAW) with 40 passes of 1.1 mm (0.045 in.)-diameter Alloy 82 welding wire being fed externally (see Table 3-2). The welding parameters for the main DM weld are given in Table 4-2.

Table 4-2 Typical Parameters for Main DM Weld

Parameter	Value
Current	220-285 A
Voltage	10.7-11.2 V
Travel Speed	2.54 mm/s

After the main DM weld was completed, the ID was machined to simulate the cavity for a 360 degree weld repair. The fill-in weld was deposited using automated GTAW with a total of 27 passes. The typical welding parameters used to deposit each weld pass are listed in Table 4-3.

Table 4-3 Typical Parameters for Fill-in Weld

Parameter	Value
Current	200 A
Voltage	15.5 V
Travel Speed	2.54 mm/s

The safe end to stainless steel pipe weld with material TP308 was completed in 28 passes with weld parameters given in Table 4-4.

Table 4-4 Typical Parameters for Stainless Steel Weld

Parameter	Value
Current	90 - 147 A
Voltage	9.2 - 26 V
Travel Speed	1.27 mm/s

4.3 Weld Residual Stress Measurement

Various measurement techniques were discussed in Section 2.2. For this configuration, the through-wall axial and hoop stresses were of greatest interest since, in in-plant configurations, these stresses lead to mode I opening of circumferential and axial flaws, respectively. Based upon experience in Phase 1 (see Chapter 3), strain relief-based techniques were determined to be appropriate [32]-[38].

For the Phase 2a round robin mockup, a combination of deep hole drilling (DHD)/incremental deep hole drilling (iDHD) [32] was chosen for the through-thickness measurements. One goal of the round robin study was to assess the effect of the safe end to stainless steel pipe weld on stresses in the main DM weld. Hence, the above WRS measurements were taken before and after completion of the safe end to stainless steel pipe closure weld. Figure 4-2 shows the location of the WRS measurements: the DHD/iDHD measurements were taken through the centerline of the DM weld. The iDHD measurements were taken on the ID and OD of the DM weld. A total of six hole drilling measurements were performed at different locations around the circumference of the weld. Two sets of those measurements were performed without knowledge of the finite element data (i.e., double-blind), two prior to and two following the stainless steel pipe closure weld. The other four measurements were made after the finite element modeling data was made public.

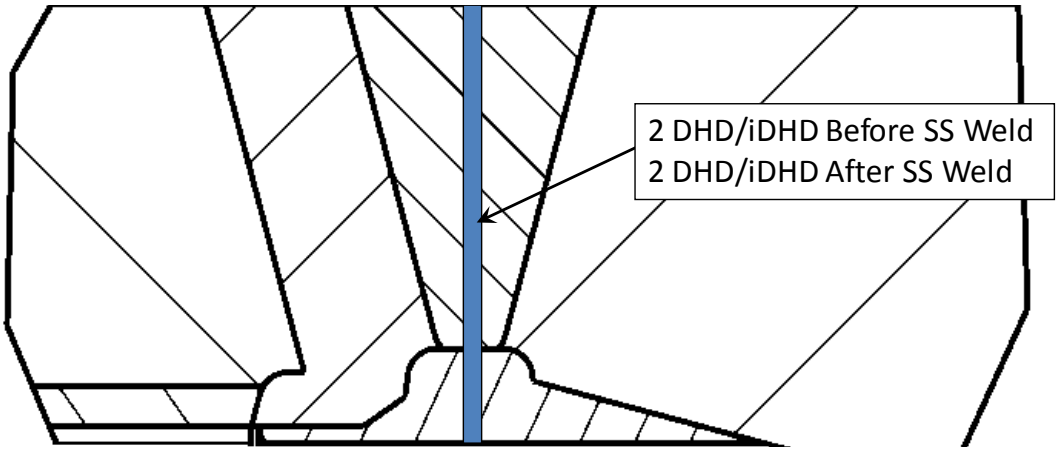

Figure 4-2 Weld Residual Stress Measurement Location

Subsequent to the double-blind finite element (FE) round robin, the U.S. Nuclear Regulatory Commission (NRC) commissioned a set of contour measurements on the Phase 2a mockup. This data does not meet the double-blind criteria, but it does provide a useful independent check of the hole drilling data.

4.4 Double-Blind Finite Element Round Robin

This program consisted of an analytical international FE round-robin for the prototypical PWR pressurizer surge nozzle geometry. The results from the round robin FE modeling were compared to physical measurements performed on the mock-up. The study was double blind, i.e., the FE analysts and measurement practitioners were not allowed to compare their results before submission, permitting the NRC staff to develop unbiased measures of uncertainties in WRS predictions.

4.4.1. Initial Approach to Assessing Modeling Uncertainty

Before initiating the round robin, heat input and material properties were considered to be the most likely sources of modeling uncertainty. Therefore, the international round robin FE analyses were completed in two stages. In Analysis 1a, the geometry modeled included the nozzle and DM weld only (with no stainless steel weld). The analysts were not provided with either material properties or thermocouple data, but they were provided with laser profilometry data. For Analysis 1b, the NRC supplied each analyst with thermocouple data obtained during the fabrication process. For Analysis 1c, the NRC provided material properties extracted from test coupons matching the materials used in the actual nozzle mockup. It was thought that modeling uncertainty would decrease as the participants were provided more information from which to refine their models. In Analysis 2, the full mockup nozzle fabrication was modeled, including the stainless steel weld. Laser profilometry and thermocouple data for the stainless steel weld were provided to the analysts. These analysis stages are summarized in Table 4-5.

Table 4-5 Analysis Stages

Designation	Stainless Steel Closure Weld	Thermocouple Data	Material Property Data
Analysis 1a	Prior	No	No
Analysis 1b	Prior	Yes	No
Analysis 1c	Prior	Yes	Yes
Analysis 2	Post	Yes	Yes

4.4.2. Round Robin Participants

Thirteen organizations representing the United States (eight), European Union (two), Japan (two), and Australia (one) submitted WRS FE results in support of the WRS FE round robin effort, summarized in Figure 4-3. Participation was not uniform for all analyses. Analysis 1a included ten independent results (and two late results), while Analysis 1c included nine independent results and Analysis 2 included eight independent results (and one late result). Three participants varied the hardening law assumed for a given analysis (typically isotropic and kinematic hardening), yielding multiple WRS profiles for a given model. Results marked as 'late' were received after the blind deadline and were not included in the data analysis, but were plotted against the dataset as a whole for comparisons.

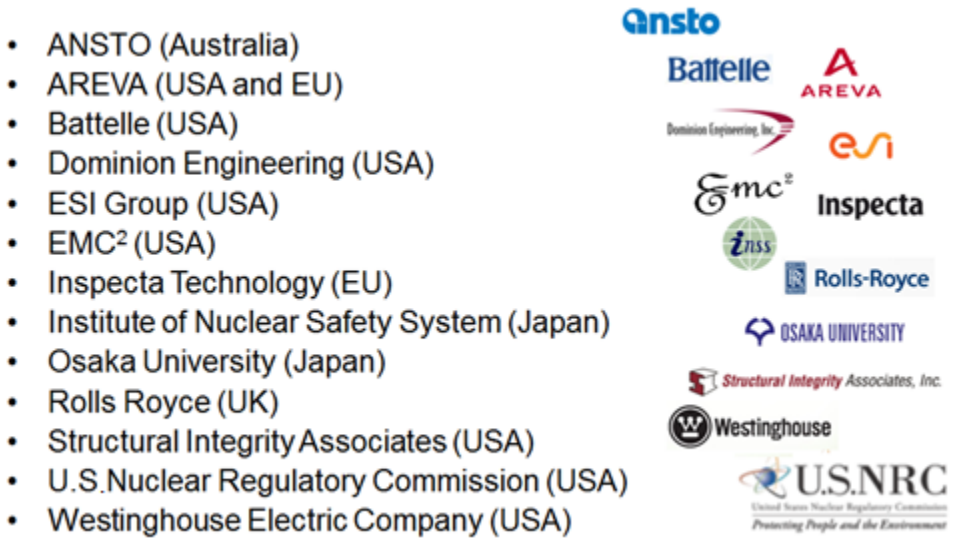

Figure 4-3 Round Robin Participants

4.4.3. Modeling Package

NRC and EPRI prepared a modeling package in order to provide a formalized problem statement to each participant. Subject to the restrictions listed in Table 4-5, the modeling package included the following information:

- fabrication drawings that specified mockup dimensions
- thermocouple measurement locations and associated transient temperature data, such as shown in Figure 3-3
- laser profilometry data on the weld beads, such as shown in Figure 3-4
- punch mark locations and associated weld cavity shrinkage measurements
- WRS measurement locations, but not the associated data
- nominal material specifications
- welding details: bead sequence, current, voltage, wire feed speed, and travel speed

4.4.4. Model Description

FE modeling of WRS, in general, was introduced in Section 2.3. This section describes one participant's model, as a demonstration of the approach one may take. The details in this section do not represent information that was provided to the participants. A 2-D schematic of the major geometric features modeled is provided in Figure 4-4 including the Alloy 82 butter, main DM and fill-in welds, and the stainless steel safe end weld. The mesh is fine around the weld locations.

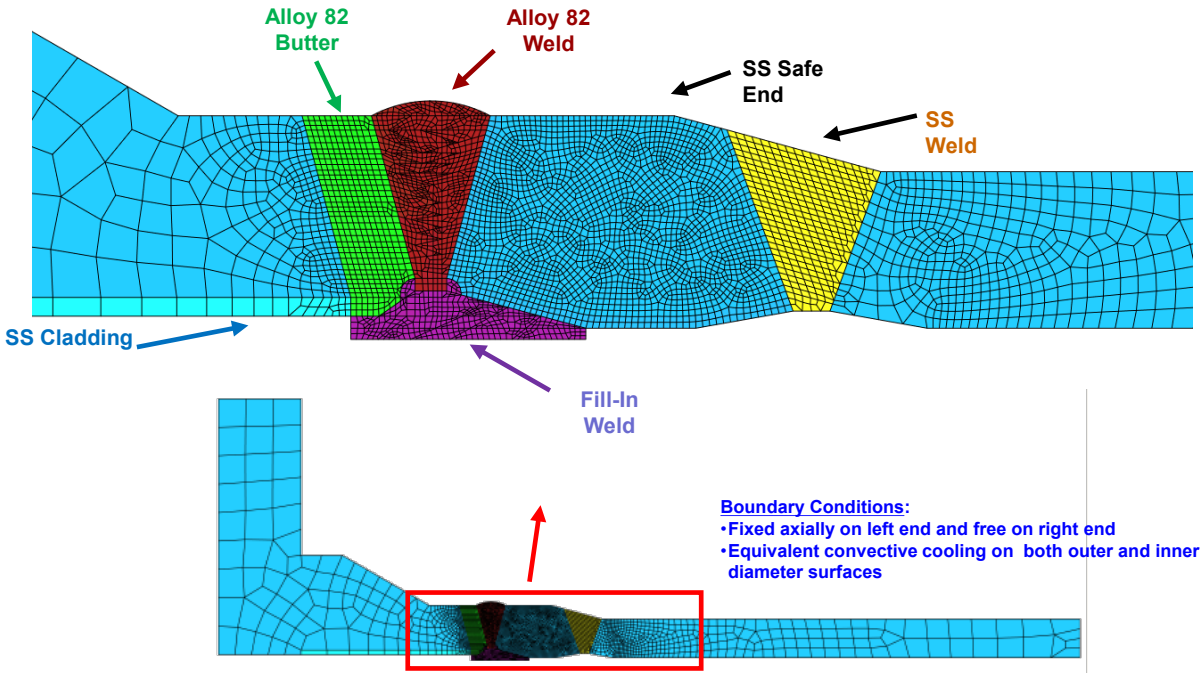

Figure 4-4 Example Model Features

Round robin participants employed a wide range of weld bead refinement in modeling the butter layer. A high degree of weld bead refinement is shown in Figure 4-5, where 137 butter weld beads were deposited, closely approximating the mock-up weld bead geometry as measured by laser profilometry. Bead lumping, where the heat input of several weld passes was combined into a single larger weld bead, was also conducted by some analysts for the butter. Bead lumping ranged from four to eight beads to an entire row. After deposition of the butter, the weld was post-weld heat treated at 866-922 K for 3 hours. The butter was machined after heat treatment to the V-groove geometry required for the main DM weld. This machining process was implemented in the FE by material removal, followed by stress redistribution (equilibrium). Surface stresses imparted by the machining process were not captured by the FE, in any case.

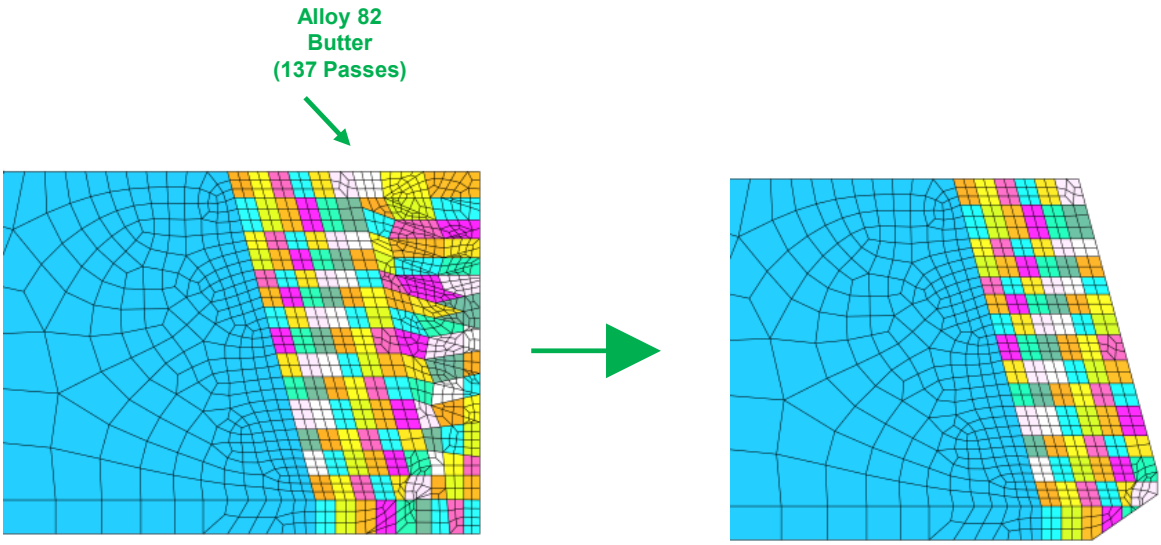

Figure 4-5 Butter Layer and Machining

Not all analysts used the laser profile data to generate bead geometry. In cases where the bead geometry was not used, individual weld beads were idealized as rectangles similar in area to the average bead size measured with the laser profilometry data. Unlike the buttering, lumping of the main DM weld beads was not conducted, and all models were based on the DM Alloy 82 weld passes deposited during mock-up fabrication. Figure 4-6 is an example of how laser data was converted to DM weld bead geometry. Note that the final V-groove geometry was used to account for the shrinkage that occurs during initial weld passes when developing the model geometry.

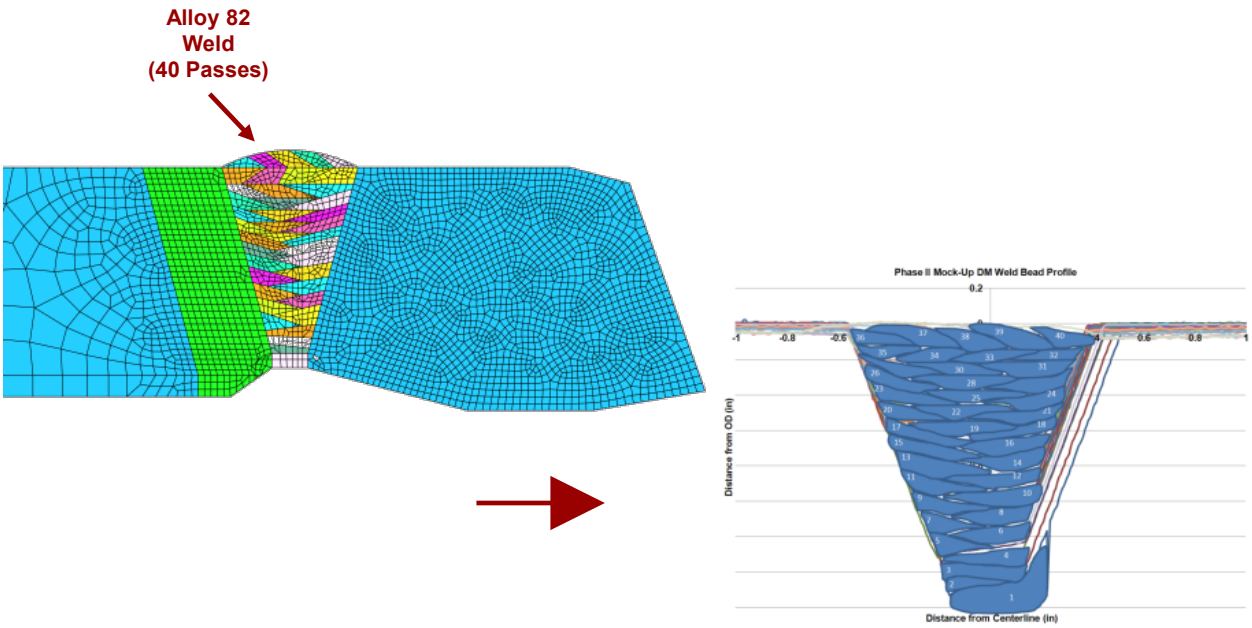

Figure 4-6 Weld Bead Geometry from Laser Data

After completion of the main DM weld, the ID surface was machined to the geometry required for the 25 percent thickness fill-in weld. In the FE models, material was removed on the ID to generate a smooth surface, and stresses were allowed to redistribute, followed by the Alloy 82 fill-in weld. This sequence is illustrated in Figure 4-7, modeling 27 weld passes and estimating the bead geometry from the laser data.

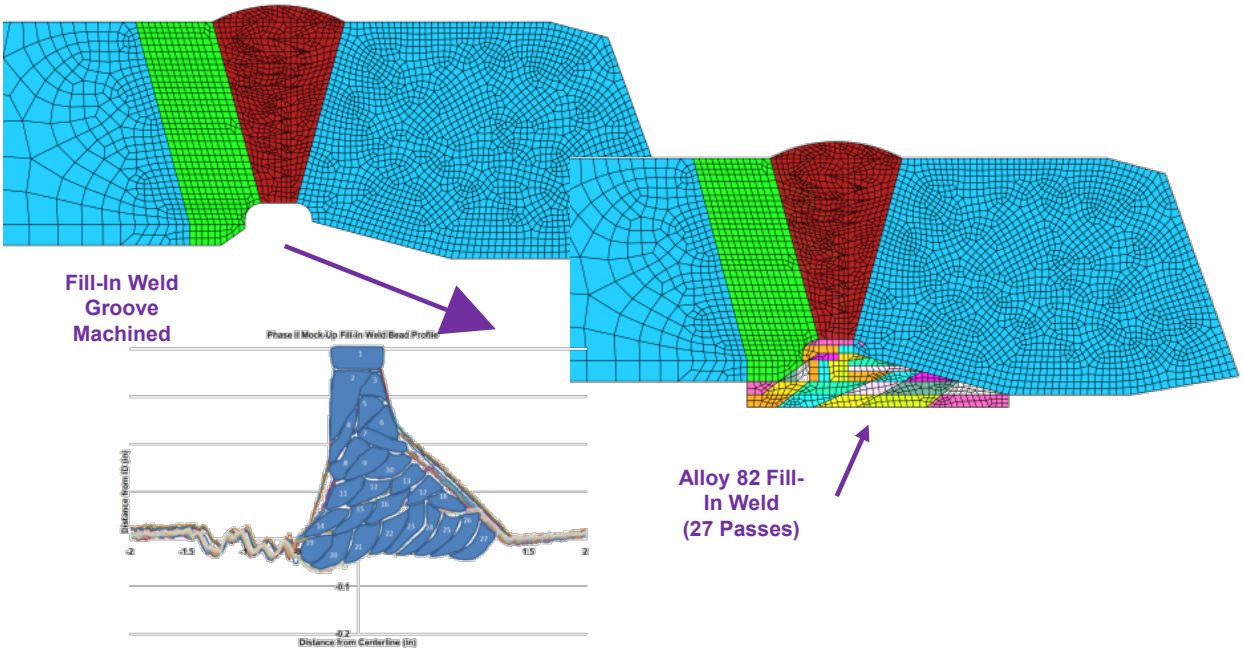

Figure 4-7 Fill-In Weld

The step pictured in Figure 4-8 removed the crown from the main DM weld and the fill-in weld, machined to the final geometry, and allowed stress redistribution (equilibrium).

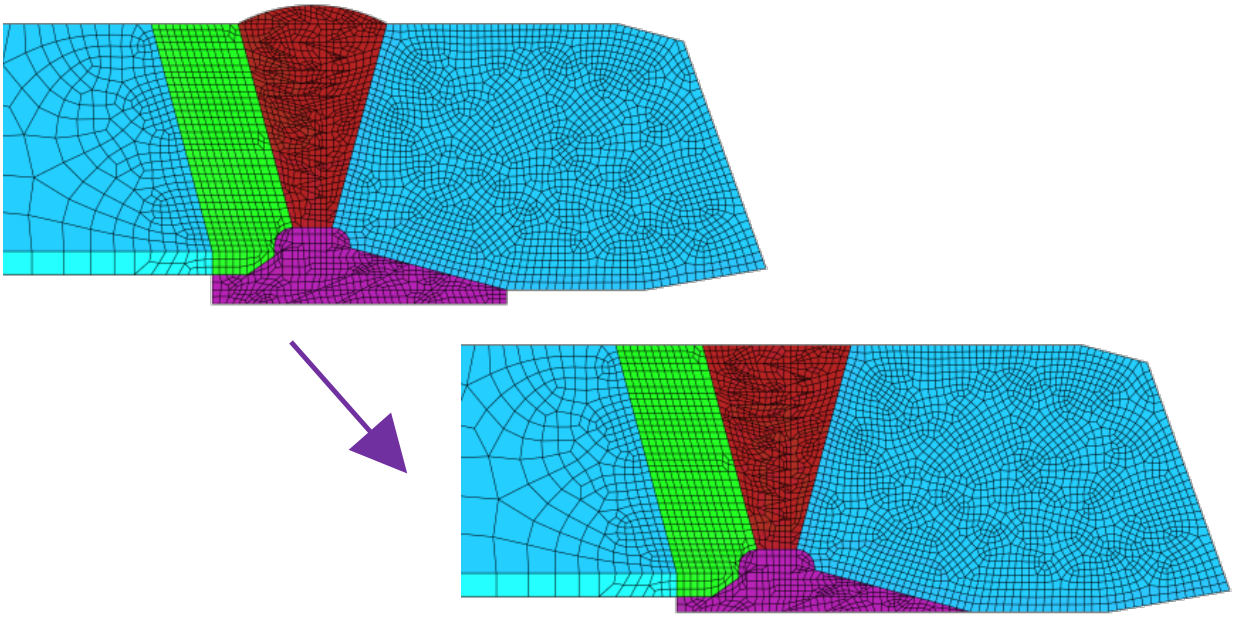

Figure 4-8 Machining Steps

The final step in the FE models was the application of the stainless steel weld. For the model illustrated in Figure 4-9, 52 idealized weld passes were assumed for the stainless steel closure weld. Laser profilometry data for the safe end weld was distributed with the modeling package; the 52 beads in Figure 4-9 represent a specific analyst's assumption, while the actual mockup had 28 beads.

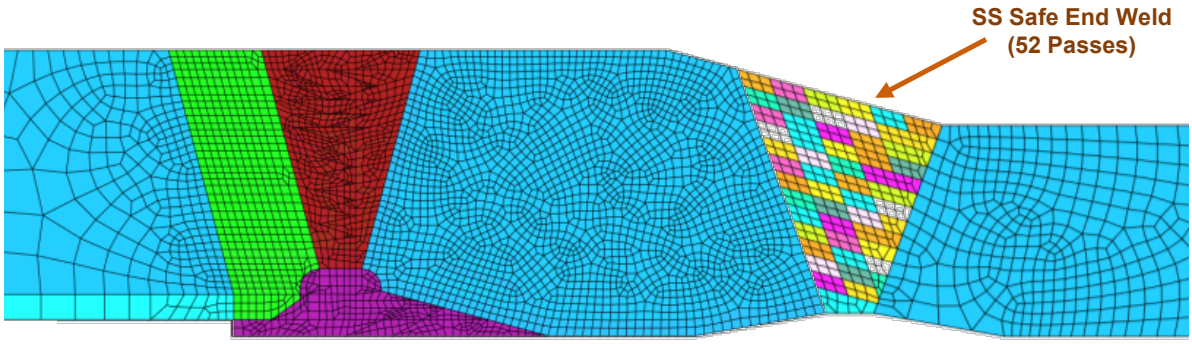

Figure 4-9 Stainless Steel Closure Weld

4.4.5. Post-Processing of Finite Element Results

Through thickness residual stress measurements were made at two locations 180 degrees apart, both before and after the application of the safe end weld. The DHD measurements provided experimental axial and hoop residual stress data. Round robin participants extracted model results along the centerline of the DM weld in order to allow direct comparison to experimental results, as illustrated in Figure 4-10. Since the DHD measurements were taken at room temperature, participant FE results were extracted at room temperature.

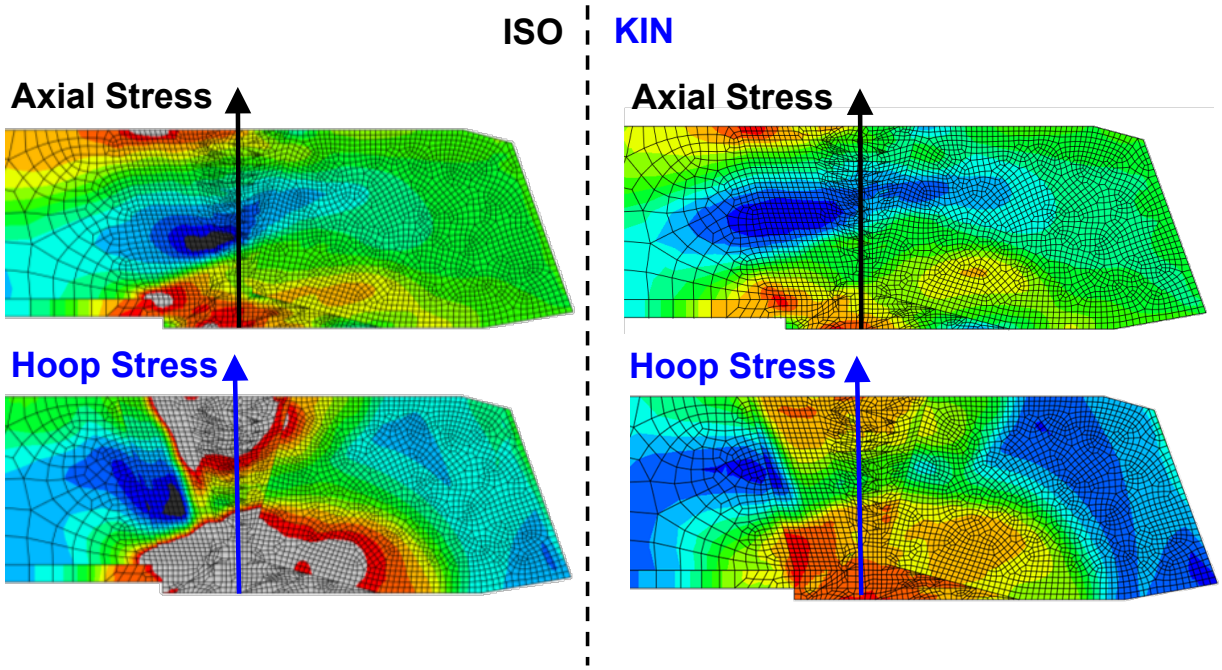

Figure 4-10 Extraction of Results

As shown in Figure 4-10, the centerline of the DM weld was not the location of maximum stress, and further the stress distribution was asymmetric about the centerline of the DM weld. The development of an asymmetric residual stress profile across the can be attributed to the asymmetric geometry of the ID fill-in weld and the different material properties on each side of the weld centerline. While the DHD measurements represented a stress averaged over the 5 mm core diameter used to make the DHD measurements, no effort was made to conduct similar averaging for the FE results.

4.4.6. Data Analysis

In the raw data, round robin participants provided stress results at different divisions through thickness (as a result of mesh geometry and extraction methodology), and the end state thickness of the component varied from model to model. To create uniform point spacing, the raw stress data was linearly interpolated to 50 uniform points through-thickness, producing an approximately 1-mm spatial resolution sufficient to capture the features present in the raw data. The variation in end state thickness of the nozzle ranged from 46.5 to 51.6 mm in Analysis 1c. To account for this variation, raw data was normalized by thickness (x/t). DHD measurements were not able to measure surface stresses, and this data was normalized by the thickness of the nozzle at the measurement location. Variation in geometry modeled can have an effect on a given residual stress distribution, and geometry variability from participant to participant is discussed in detail below.

4.5 Results and Discussion

4.5.1. Measurement Results

Figure 4-11 and Figure 4-12 show the DHD/iDHD WRS measurement results for both axial and hoop stress components before application of the stainless steel weld as a function of through-thickness distance from the ID to the OD through the centerline of the DM weld. For each stress component, two measurements were taken in the nozzle 180 degrees apart from one another. As is typical of configurations in which the final weld passes are completed on the ID, the pre-stainless steel weld axial stress component was highly tensile at the ID and followed a commonly observed profile thereafter. Equilibrium considerations require that, on average, the integrated through-wall area under the axial stress distribution curve equate to zero, provided the stress is axisymmetric. This is reasonably observed in the axial DHD/iDHD results. The pre-stainless steel weld hoop stress distribution remains highly tensile between approximately 0 and 500 MPa.

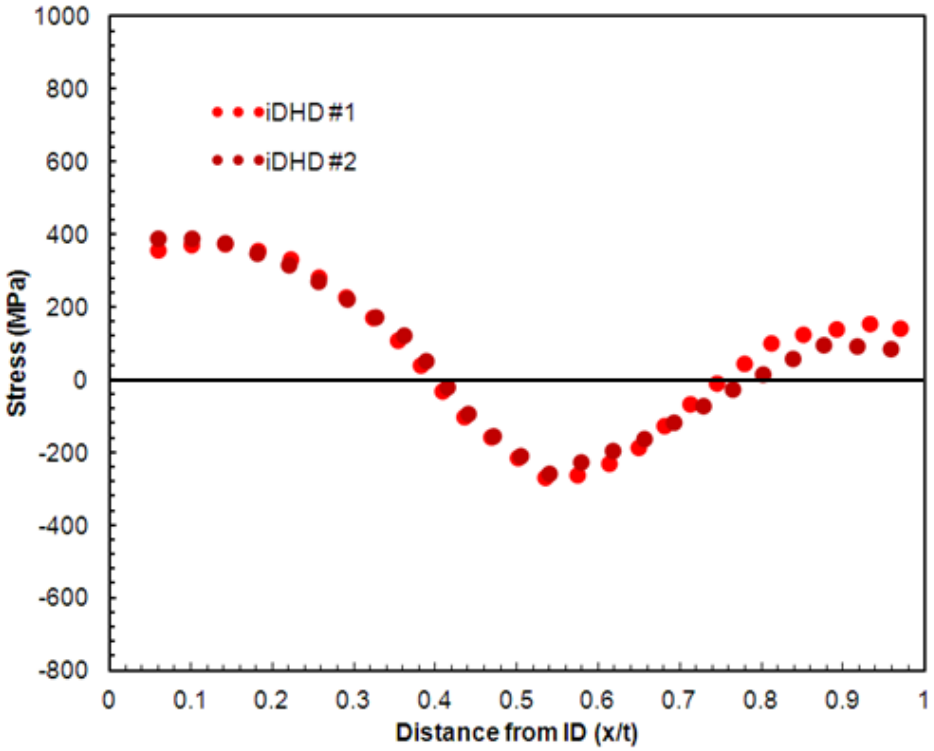

Figure 4-11 Axial Stress DHD/iDHD Measurements before Stainless Steel Weld

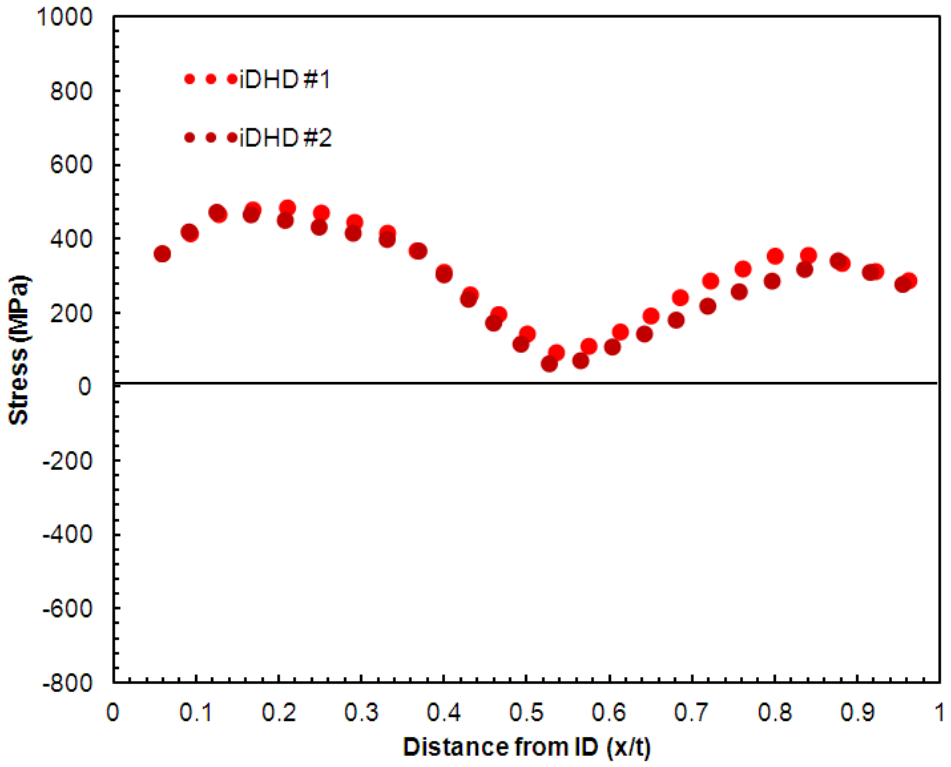

Figure 4-12 Hoop Stress DHD/iDHD Measurements before Stainless Steel Weld

DHD/iDHD WRS measurements taken after the stainless steel weld are shown in Figure 4-13 and Figure 4-14. The axial and hoop stresses at the ID location reduced significantly as a result of the stainless steel weld. This reduction in ID stress after the stainless steel weld for certain geometries is significant for stress corrosion cracking susceptibility. After application of the stainless steel weld, the stresses still appear axisymmetric.

Also shown in Figure 4-13 and Figure 4-14 are contour measurements that were obtained after the round robin study results were made public. This independent measurement confirmed the stress magnitudes and concave down trend of the hole drilling data near the ID, although the hole drilling and contour hoop stress data did not agree for $0.3 \leq x/t \leq 0.45$. The contour measurements show lower stress magnitudes near the OD than the hole drilling measurements.

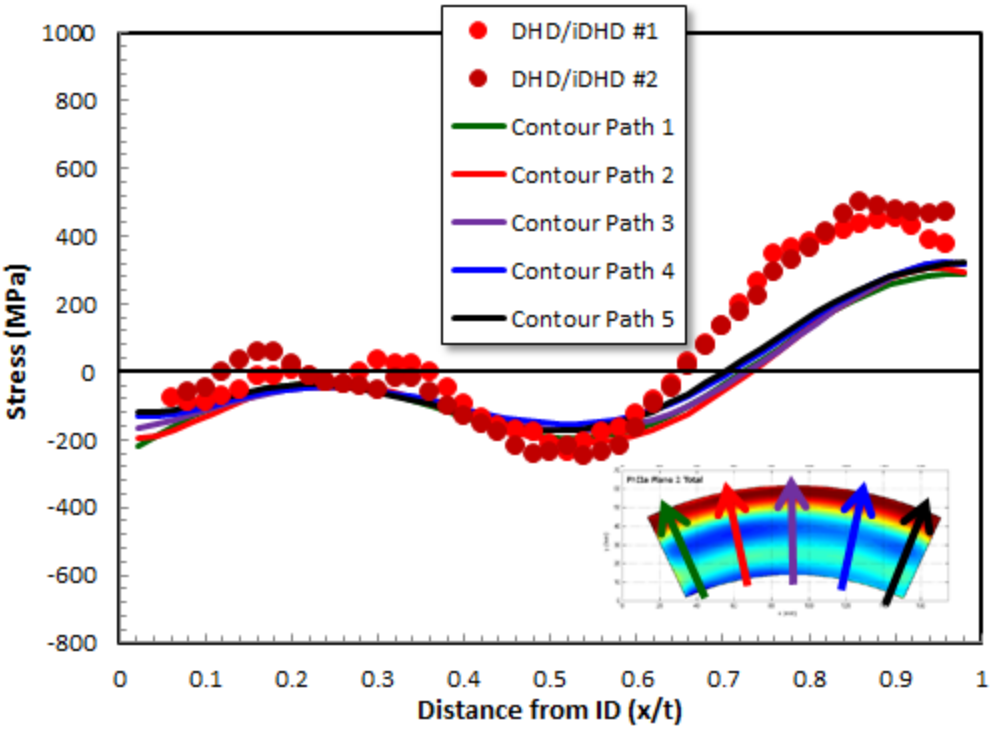

Figure 4-13 Axial Stress Measurements after Stainless Steel Weld

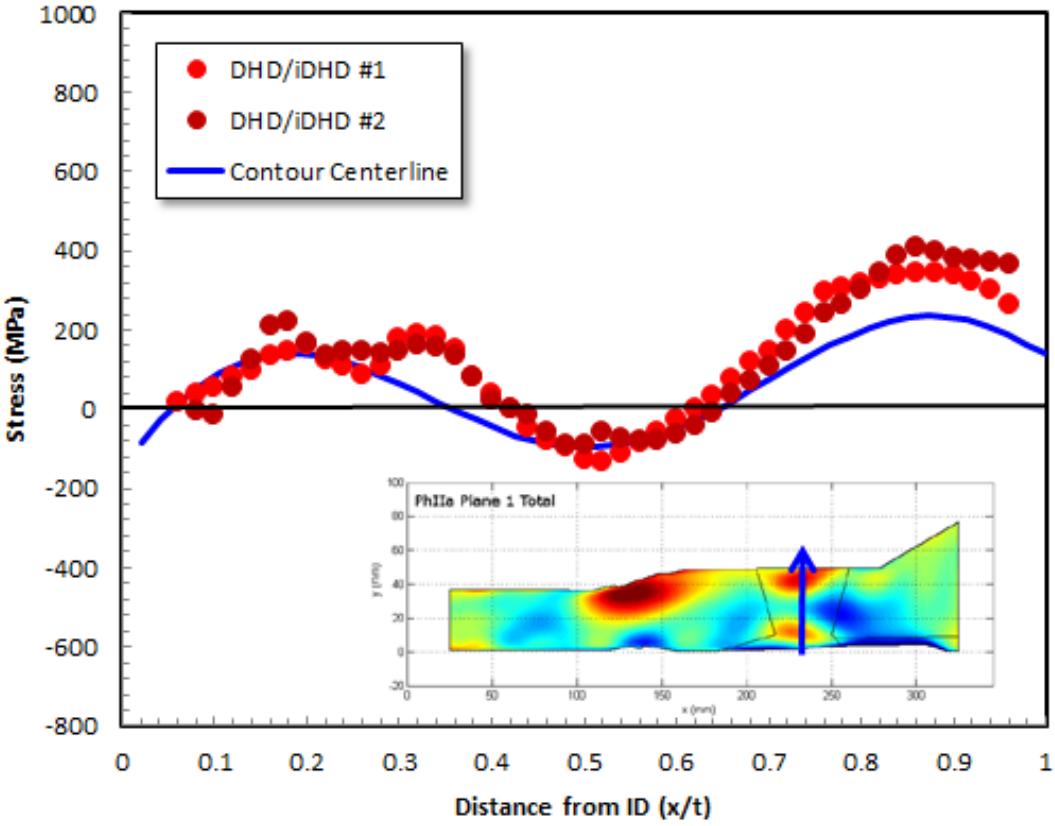

Figure 4-14 Hoop Stress Measurements after Stainless Steel Weld

4.5.2. Finite Element Modeling Results

The figures in this section represent the round robin data set using the following conventions:

- Individual FE results are shown as squares, with individual models identified as A through J.
- Measurement results are shown as red circles.
- The blue lines in the figure represent the average of the FE dataset.
- The results are segregated by Analyses 1a, 1c, and 2, as described in Table 4-5. Note: Analysis 1b results are neglected in Section 4.5.2, since they do not provide additional insight.

Figure 4-15 plots axial stress results for Analysis 1a prior to the application of the stainless steel weld, where participants were supplied neither mechanical properties nor thermocouple data. As is typical of the configuration in which the final weld passes were completed on the ID, the weld axial stress component is highly tensile at the ID. The FE results deviate from the average by a maximum of about ±200 MPa through thickness. At the OD the scatter is driven by result 'J', which shows a trend between 0.8 to 1 x/t not observed in any other results. At mid-thickness from 0.3 to 0.6 x/t, the increase in variability is attributed to differences in where the zero stress is crossed. Late results are included in Figure 4-16 and are consistent with other results submitted for Analysis 1a.

The average of the modeling results and the axial stress measurement data did not always agree in magnitude, mainly for $0.1 \leq x/t \leq 0.4$ and $x/t \geq 0.65$. The FE results tended to underpredict the measurements in these areas. Both the measurements and the modeling showed a general trend of tension at the ID, decreasing to compressive stress at approximately $x/t = 0.6$, followed by an increase in stress to the OD.

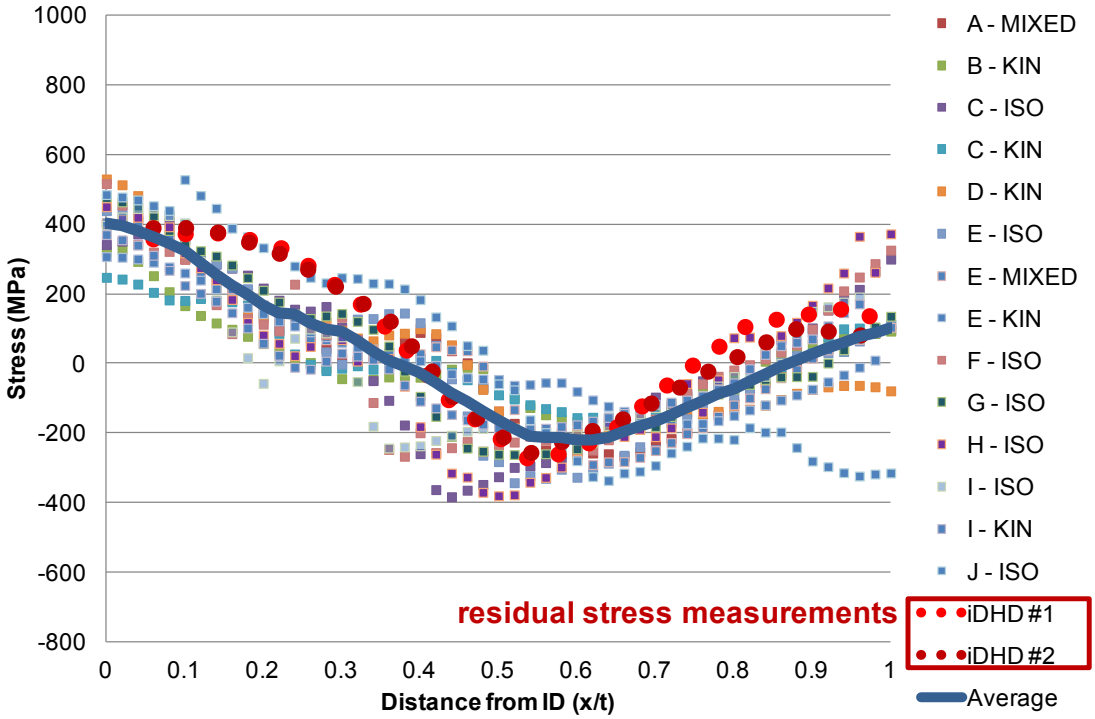

Figure 4-15 Analysis 1a Axial Stress

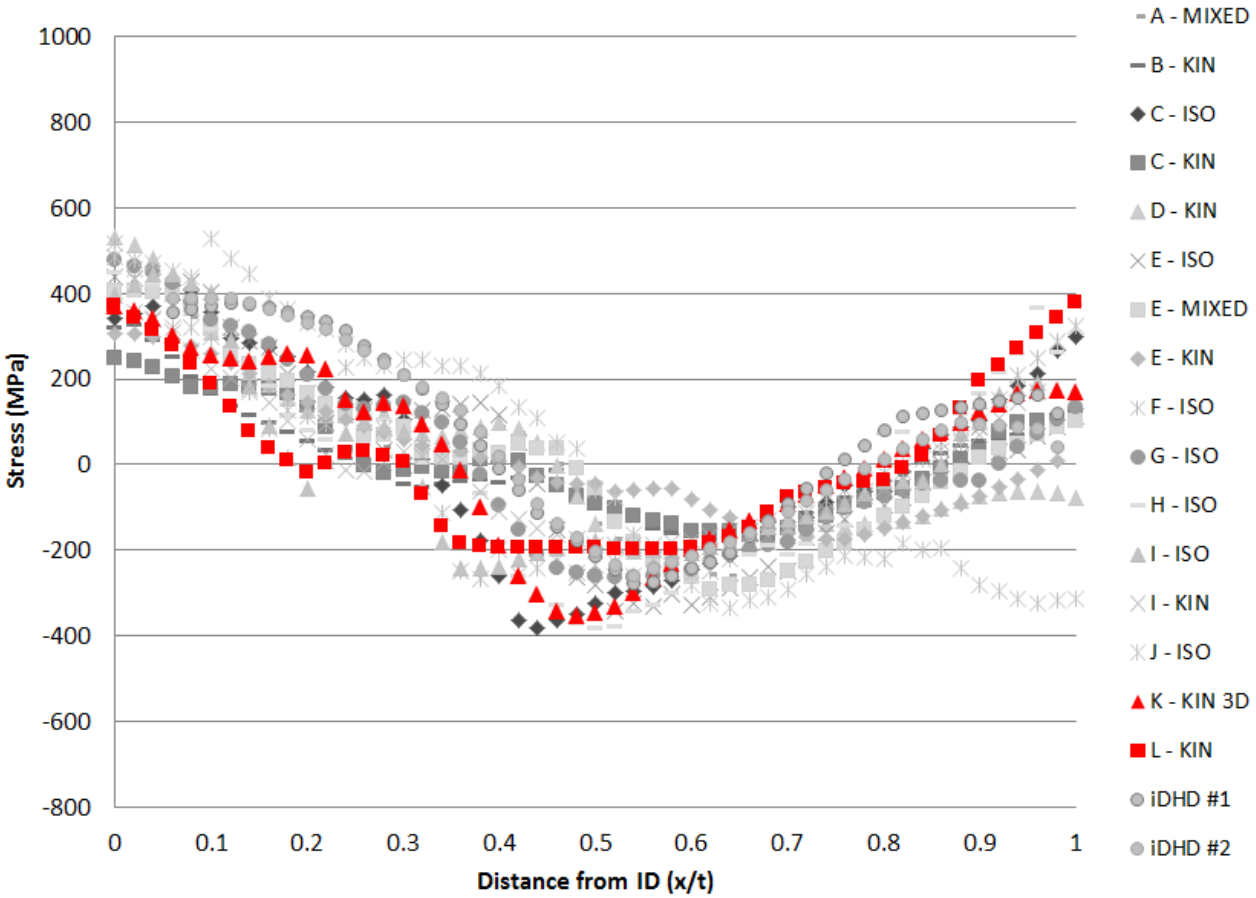

Figure 4-16 Analysis 1a Axial Stress, Late Results.

Round robin participants were provided both thermocouple data and material property data for Analysis 1c. Analysis 1c axial stress results are plotted in Figure 4-17, showing very similar trends to Analysis 1a. Results from U.S. participants in the round robin, comprising results from NRC and industry contractors, are plotted in Figure 4-18 and show a similar variability in results to the entire dataset.

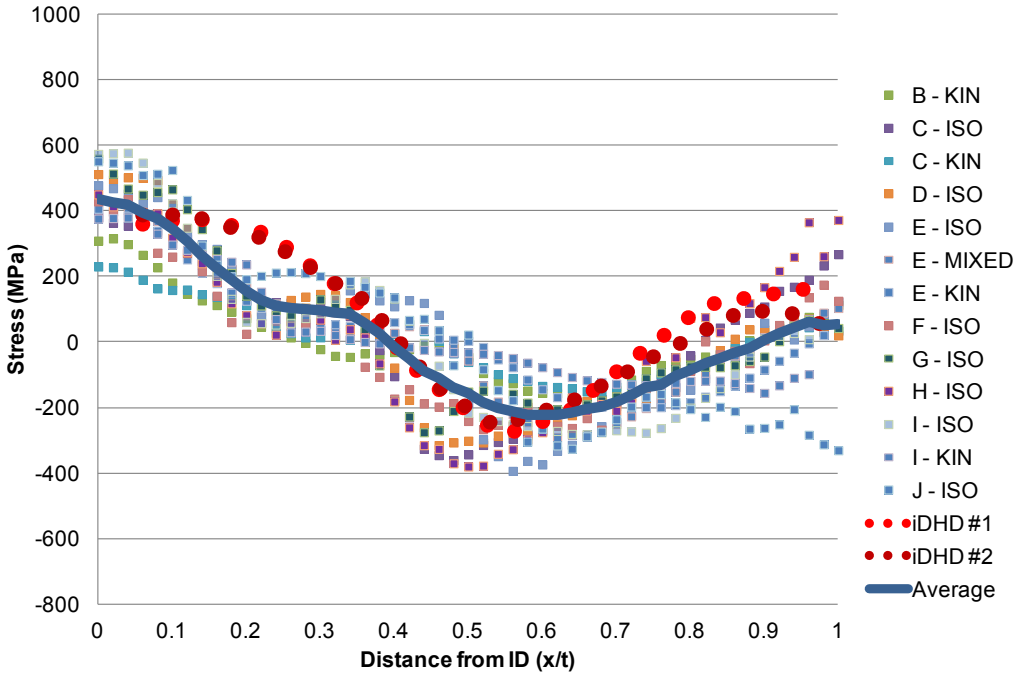

Figure 4-17 Analysis 1c Axial Stress

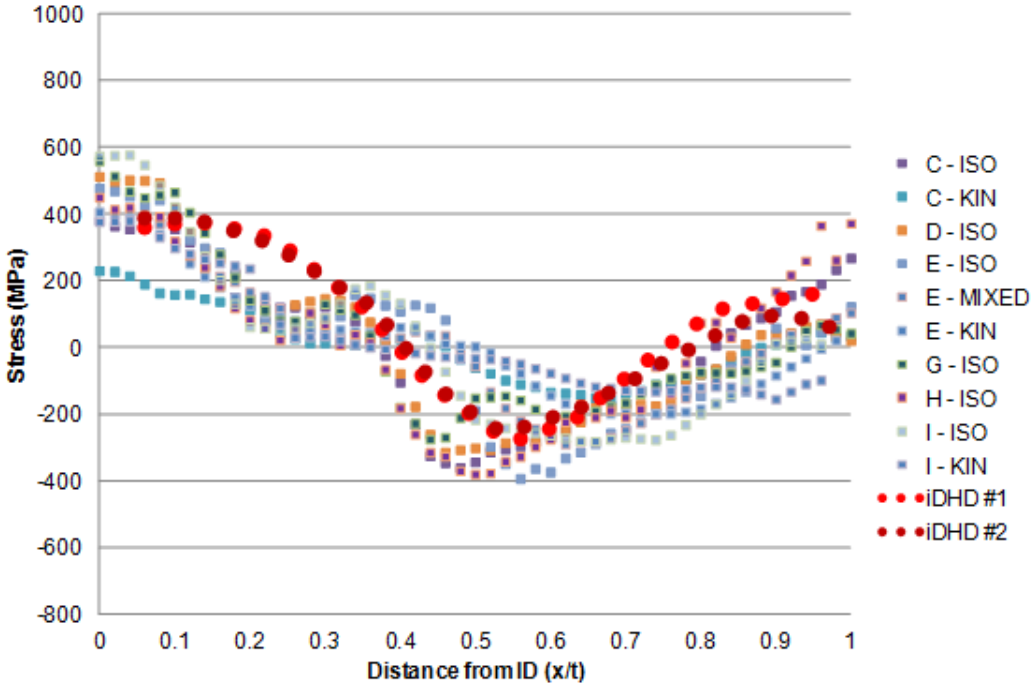

Figure 4-18 Analysis 1c Axial Stress, US Participants

Figure 4-19 plots hoop stress results for Analysis 1a prior to the application of the safe end weld, where participants supplied their own mechanical properties and were not provided thermocouple data. The pre safe end weld hoop stress distribution is highly tensile through thickness ranging between approximately 200 and 600 MPa through-thickness. The DHD results showed reasonable agreement with the average stress of the dataset. However, the scatter about the mean was as much as ±200 MPa, including the effect of hardening law. Late results not included in the calculated average are included in Figure 4-20 and are consistent with other results submitted for Analysis 1c.

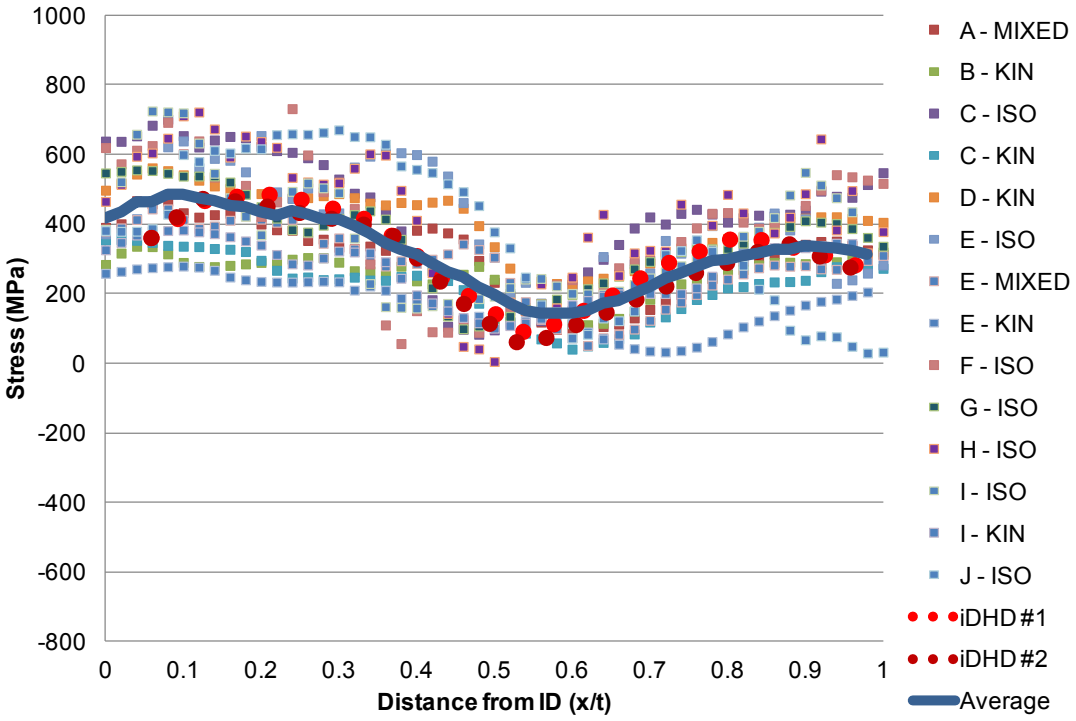

Figure 4-19 Analysis 1a Hoop Stress

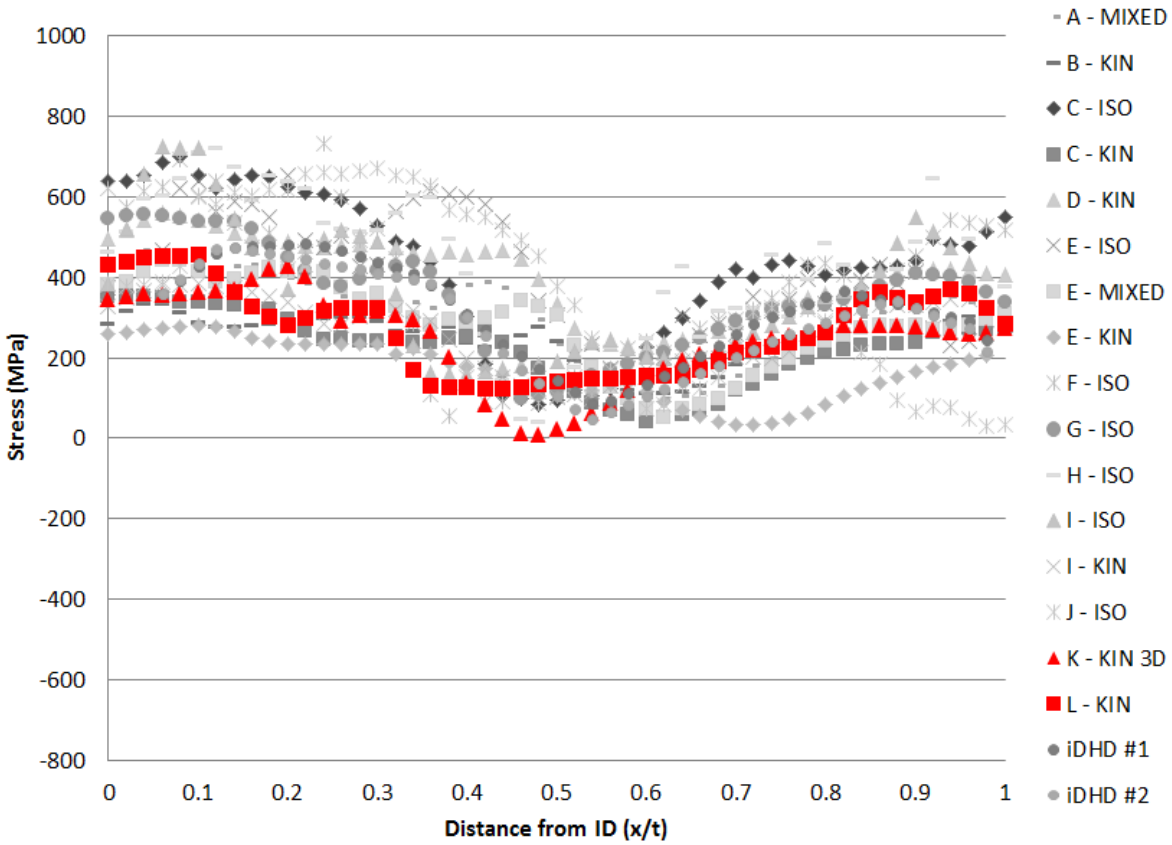

Figure 4-20 Analysis 1a Hoop Stress with Late Data

Round robin participants were provided both thermocouple data and material property data for Analysis 1c, with hoop stress results plotted in Figure 4-21. The average stress of the dataset and the DHD measurements showed a similar trend: tension at the ID, followed by a decrease in stress to approximately x/t = 0.55, and ending with an increase in stress to the OD. The magnitudes of the average stress and the measurements did not always agree. The high scatter about the average observed in the previous results is also present. Results from U.S. participants in the round robin, comprising results from NRC and industry contractors, are plotted in Figure 4-22 and show a similar variability in results to the entire dataset.

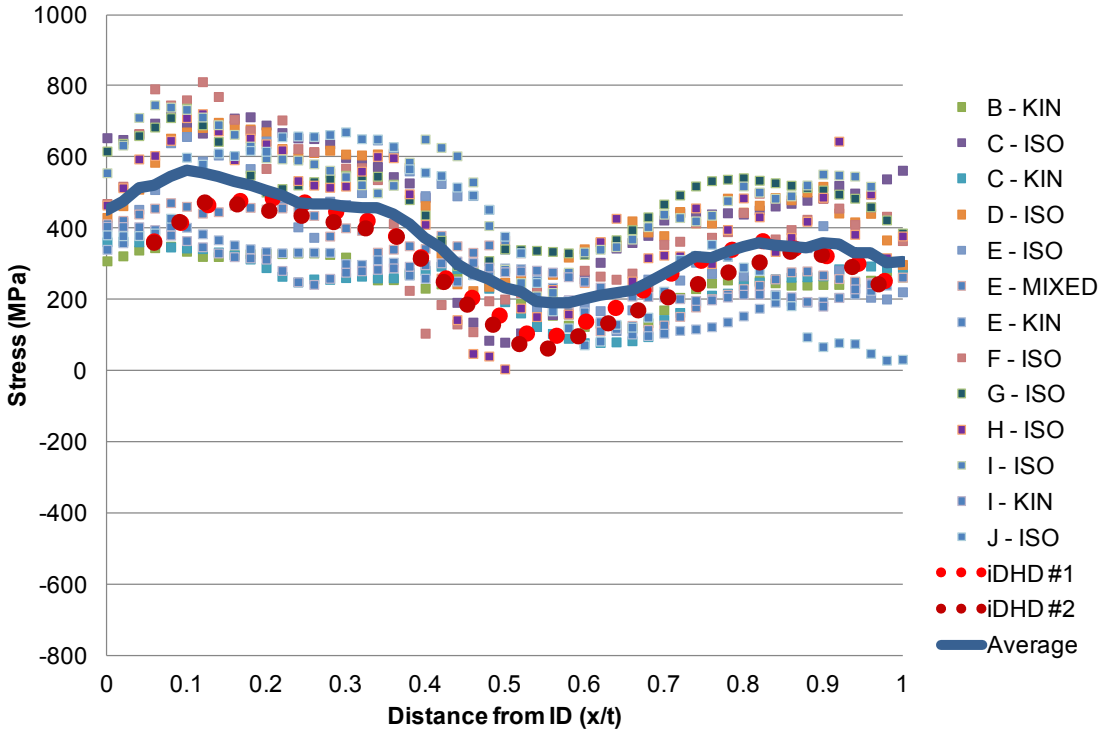

Figure 4-21 Analysis 1c Hoop Stress before Safe End Weld

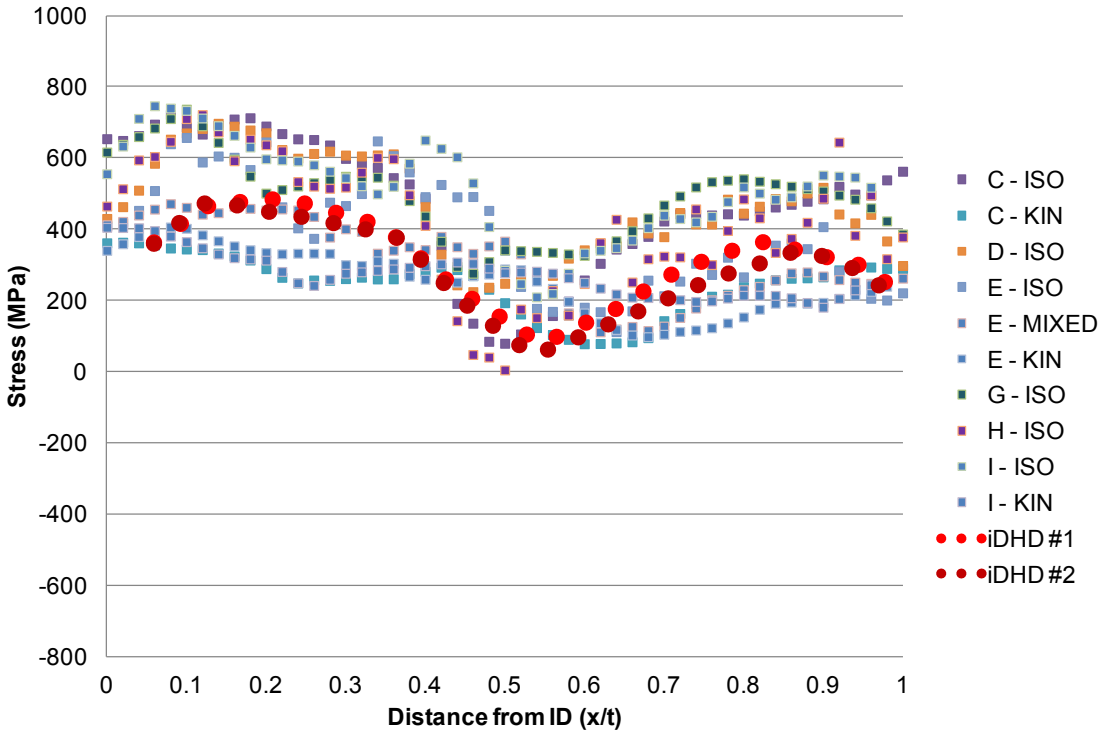

Figure 4-22 Analysis 1c Hoop Stress before Safe End Weld, US Participants

Application of the safe end weld produced a decrease on the ID axial stresses, clearly observed in the Analysis 2 axial stress dataset plotted in Figure 4-23 and Figure 4-24. The through thickness variability in predicted axial stresses observed in the data post safe end weld is very similar to that observed prior to the safe end weld. But, the agreement between the average stress of all data and the DHD measurements is somewhat less favorable than from the analyses with no safe end weld. Specifically, between 0.1 and 0.4 x/t the DHD data is consistently higher than the FE dataset average, and the FE results tended to underpredict the measurements as the OD surface is approached. There is also a difference in the concavity of the data in the ID region, with the measurements indicating concave down trends and the models indicating concave up trends. Late finite element results and measurements not included in the calculated average are included in Figure 4-25.

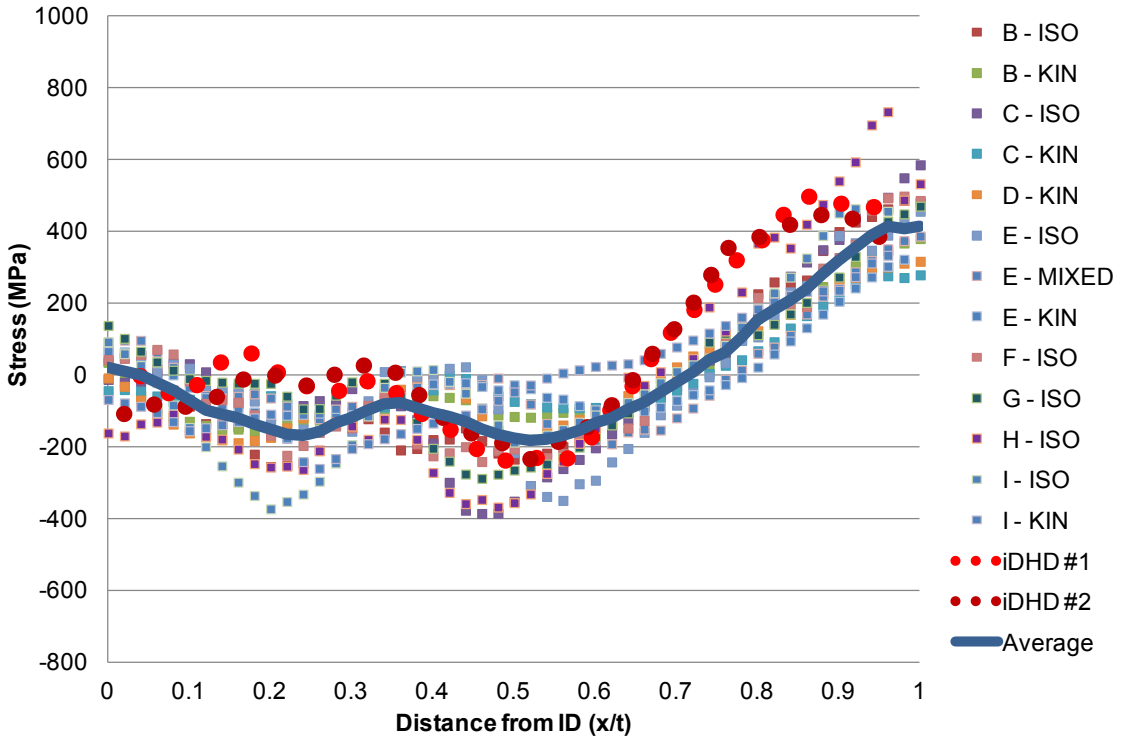

Figure 4-23 Analysis 2 Axial Stress

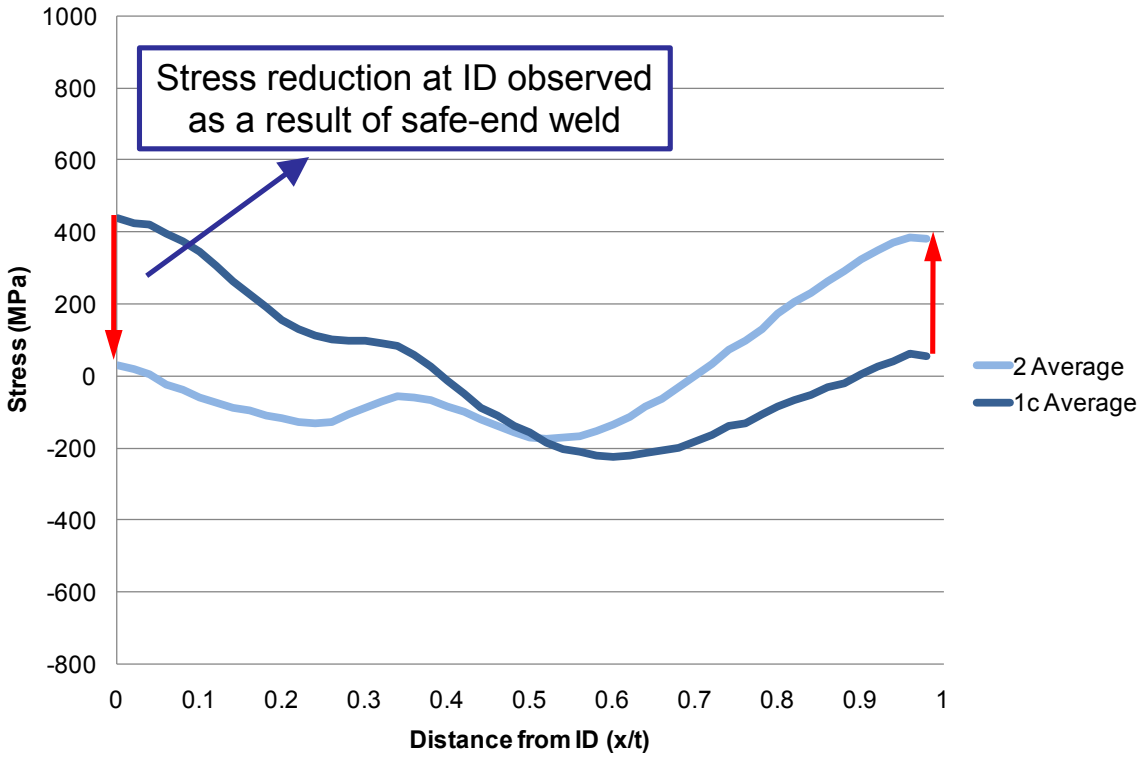

Figure 4-24 Effect of Safe End Weld on Axial Stresses

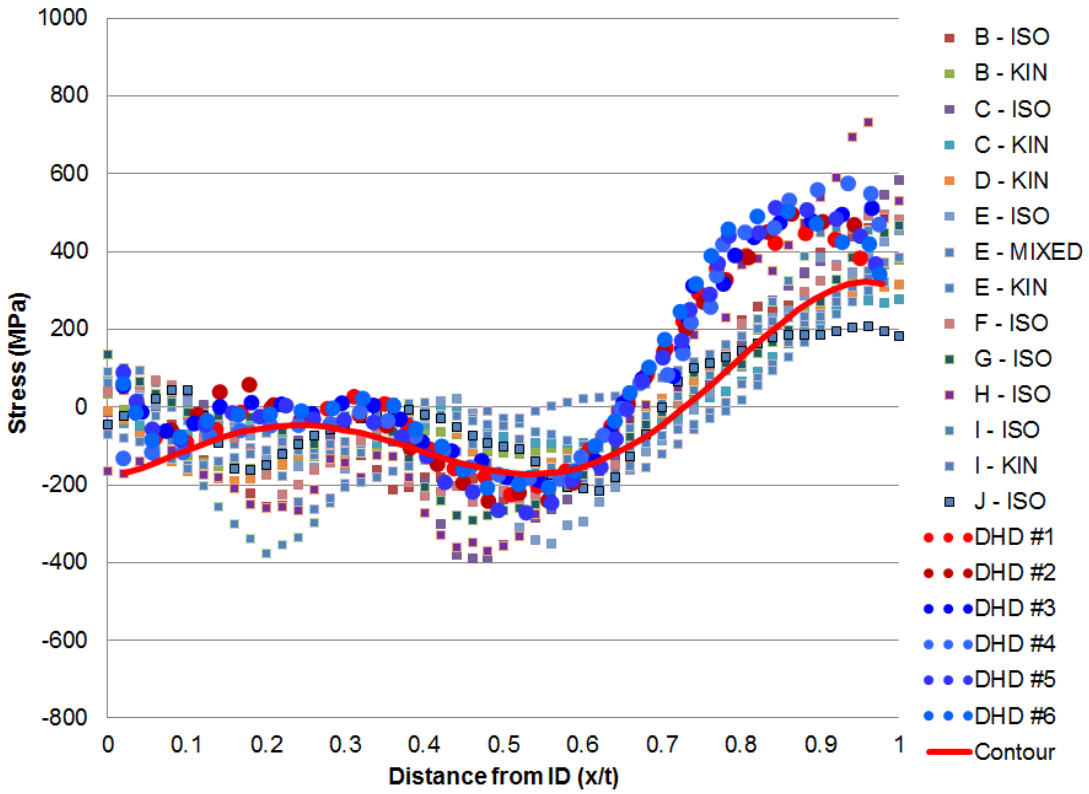

Figure 4-25 Analysis 2 Axial Stress, with Late Results and Measurements

Application of the safe end weld produced a decrease on the ID hoop stresses, clearly observed in the Analysis 2 hoop stress dataset plotted in Figure 4-26 and the Figure 4-27. The through thickness scatter in hoop stresses observed in the data post safe end weld is very similar to that observed prior to the safe end weld. But, the agreement between the average stress of all data and the DHD measurements is somewhat less favorable. The measurements exhibit lower stresses than the FE average from the ID to 0.65 x/t and showing reasonable agreement outside of this range. Late modeling and measurement results are included in Figure 4-28. Late modeling result 'J' is not consistent with FE results submitted for Analysis 2, but there is reasonable agreement between result 'J' and the DHD measurements, except at the OD. At the OD, result 'J' shows a drop in stress that is persistent in Analyses 1 and 2 for both axial and hoop stresses.

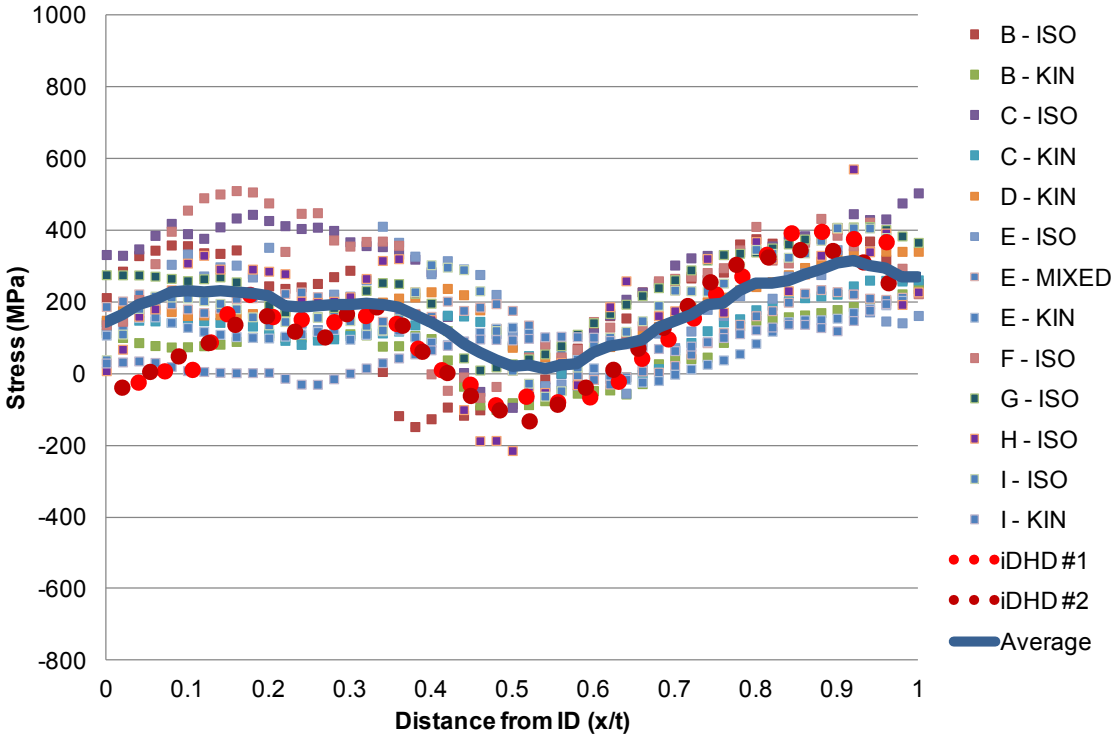

Figure 4-26 Analysis 2 Hoop Stress

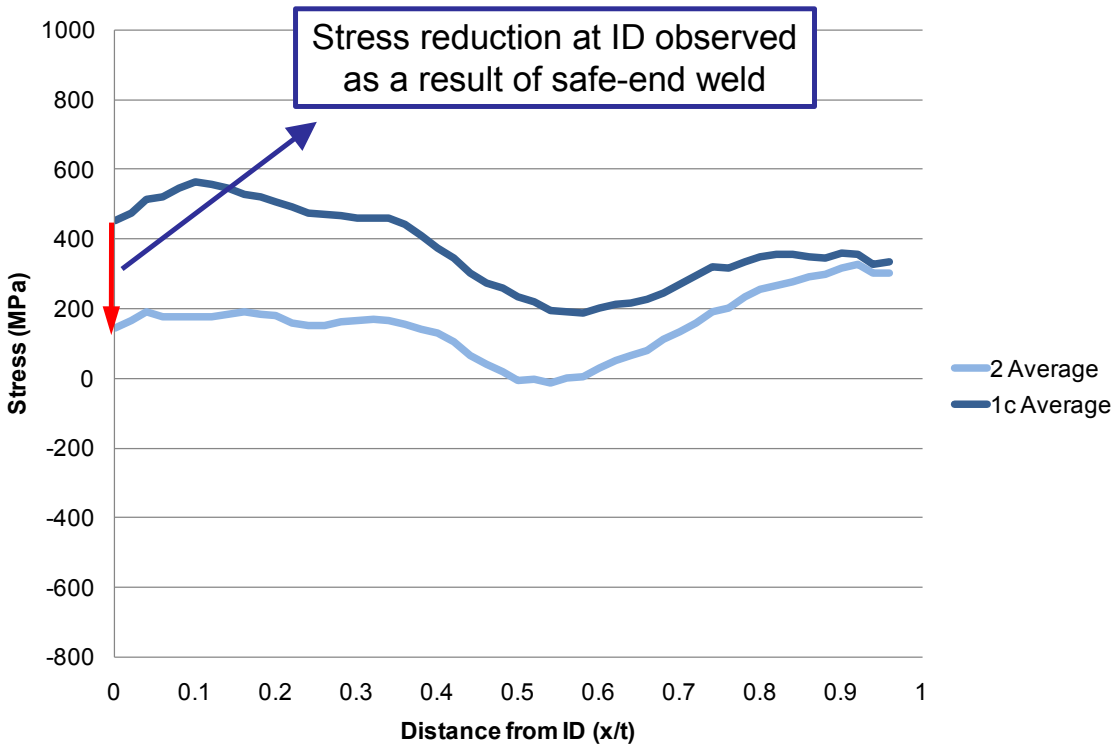

Figure 4-27 Effect of Safe End Weld on Hoop Stress

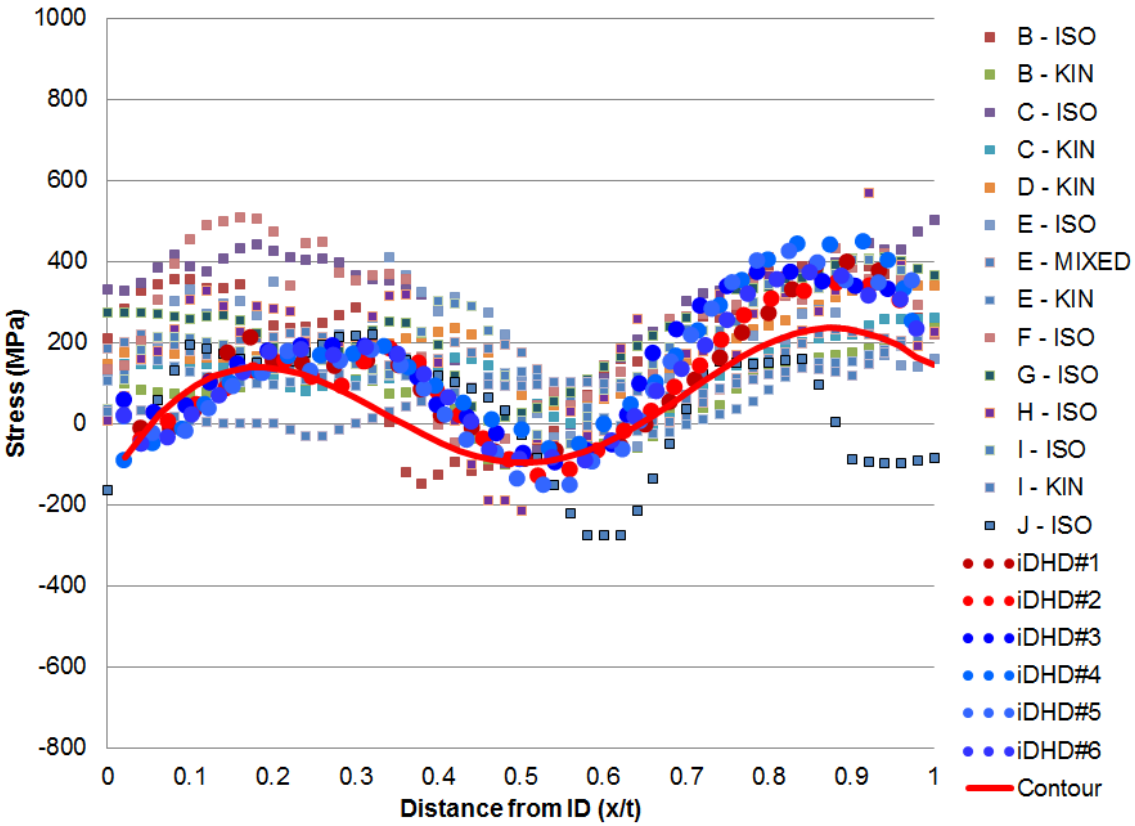

Figure 4-28 Analysis 2 Hoop Stress, with Late Result after Safe End Weld

4.5.3. Finite Element Dataset Trends

The intent of this section is to study trends in the round robin dataset and, to a more limited extent, identify why some individual results trend differently than the dataset as a whole. Global trends in the dataset are examined in the areas of material hardening law, thermocouple data, material properties, and the effect of safe end weld. The effect of material hardening law assumptions is investigated by plotting isotropic and kinematic results against the dataset as a whole. Difference plots are used to individually isolate the effect of providing thermocouple and material properties, as well as the application of safe end weld to the mock-up. For example, residual stress data from Analysis 1b are subtracted from the Analysis 1c for a given residual stress profile to isolate the effect of providing thermocouple data. This is referred to as a difference plot, showing the change in residual stress profile resulting from tuning the thermal model to thermocouple data or other single parameter change to the model. The effect of thermal model assumptions and part geometry are also assessed for select individual model results, though this is discussed in greater detail in the sensitivity studies described in Section 4.6.

As previously noted in this section, the choice of hardening law will have a large effect on the magnitudes of stresses evolved during a WRS simulation. This trend is evident in Analysis 1c when the data are grouped by hardening law. The grouping of results in Figure 4-29 represent round robin results that applied isotropic hardening; isotropic results develop greater maximum and minimum stresses when compared to the dataset as a whole. The grouping of results in Figure 4-30 is the subset of isotropic results from U.S. participants in the round robin.

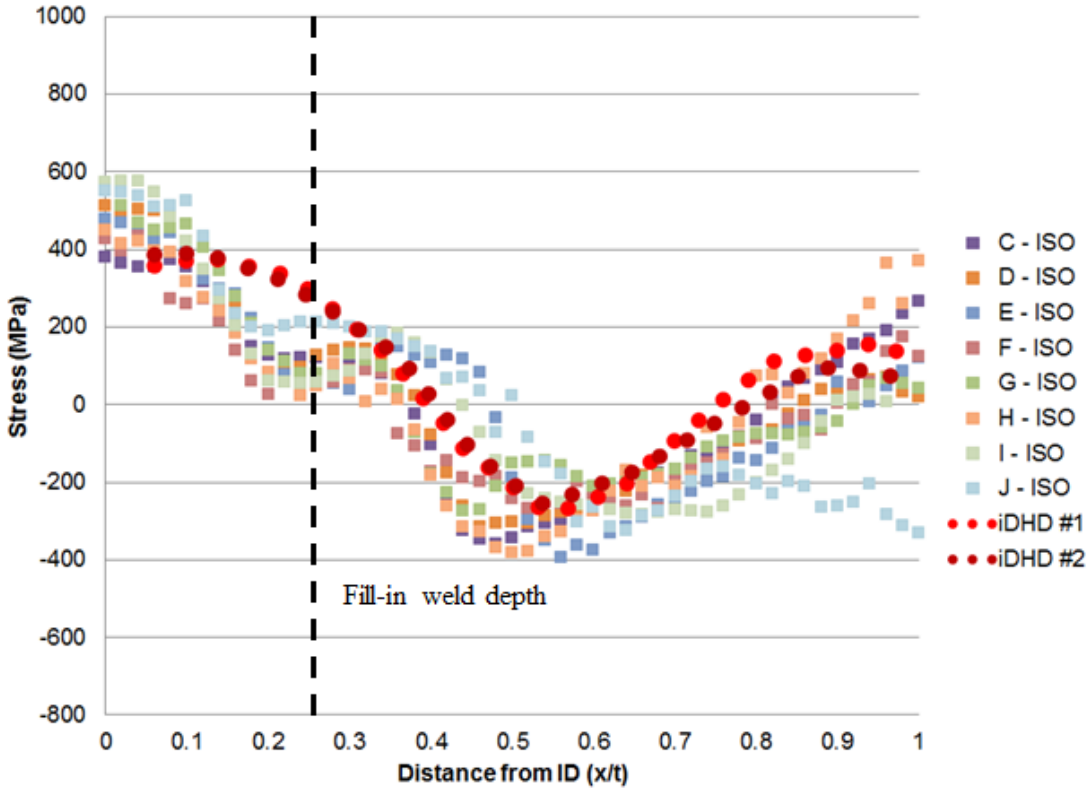

Figure 4-29 Analysis 1c Axial Stress - Isotropic Hardening

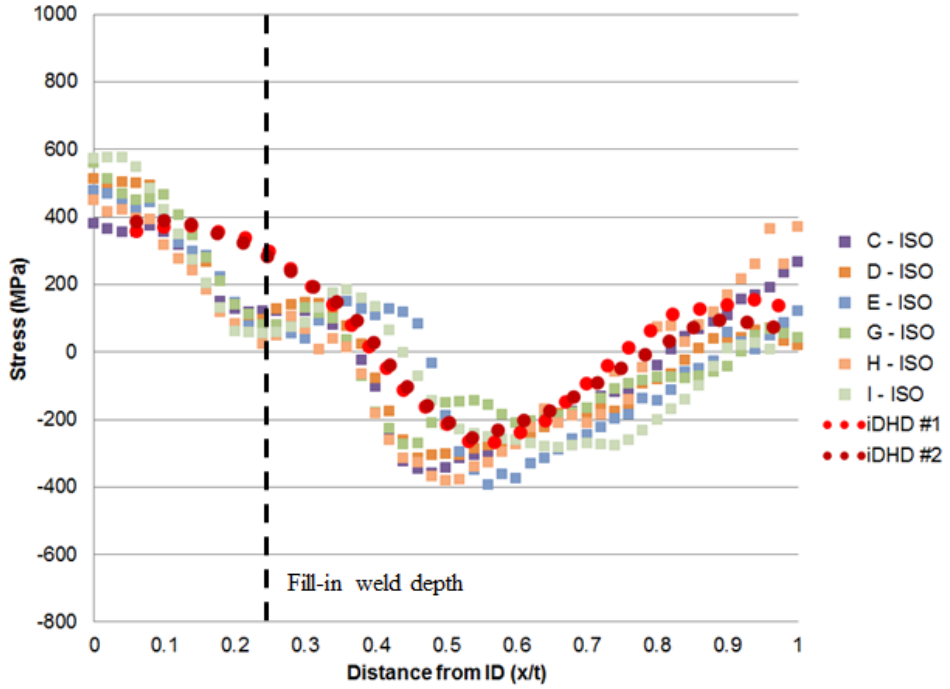

Figure 4-30 Analysis 1c Axial Stress - Isotropic Hardening, US Participants

The grouping of results in Figure 4-31 represent round robin results that applied kinematic hardening (both linear and multi-linear); the shape of these curves is flatter as lower magnitude stresses are developed when compared to the dataset as a whole.

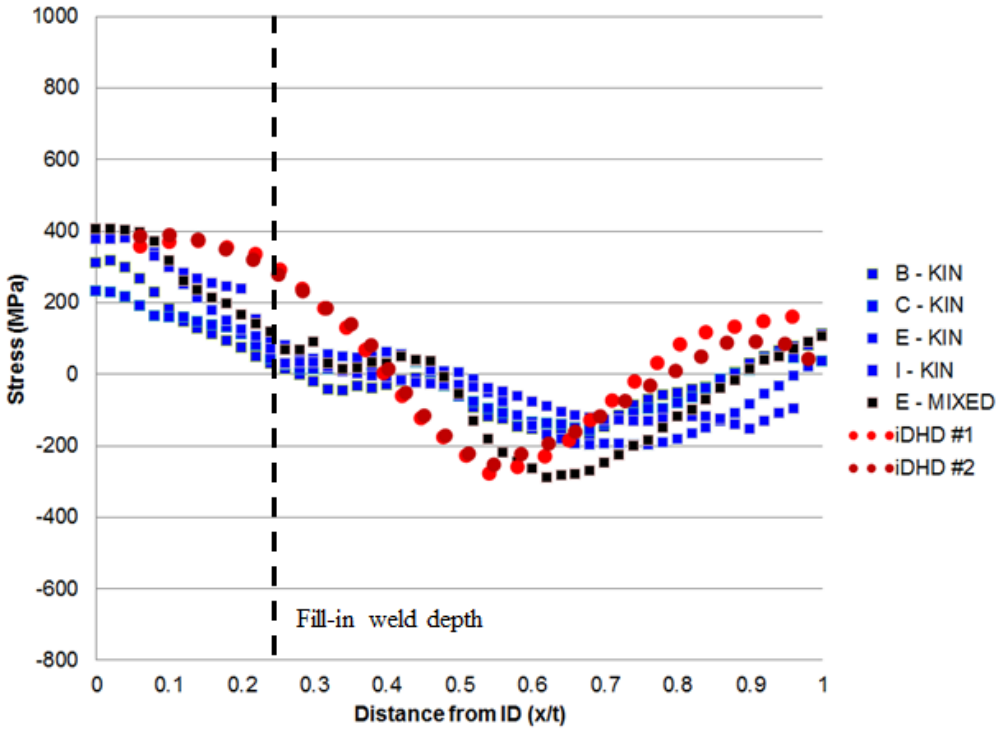

Figure 4-31 Analysis 1c Axial Stress - Kinematic and Mixed Hardening

Isotropic results tend to develop higher magnitude tensile axial stresses at the ID and OD than what is observed in the DHD data, while kinematic results tend to develop lower magnitude tensile axial stresses in this region. A similar trend is observed mid-thickness, with the isotropic results developing higher magnitude compressive stress and the kinematic lower than the DHD data. The magnitude of the stresses developed at the ID, OD, and mid thickness for the mixed hardening cases submitted show the best agreement with the stress magnitudes from the DHD measurements, though it is difficult to draw a conclusion from a single result given the scatter present in the dataset.

Highlighting isotropic and kinematic results for a given model provides additional insight to the global trends discussed above. Isotropic and kinematic results for a given model do not completely bound the dataset, as plotted in Figure 4-32 for model 'C' and in Figure 4-33 for model 'E'. In the context of flaw evaluation (since initiation and growth depend strongly on residual stress), these results suggest variation in hardening law is an appropriate sensitivity study, but may not completely characterize model-to-model variability.

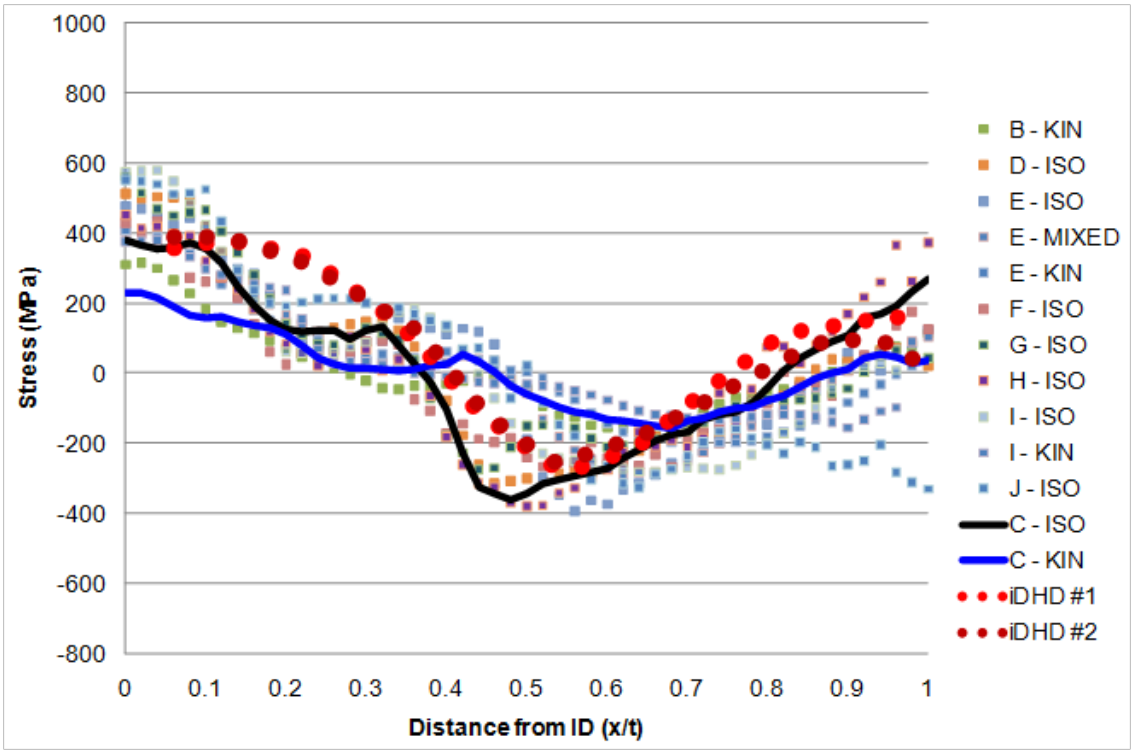

Figure 4-32 Analysis 1c Axial Stress - Isotropic and Kinematic, Model 'C'

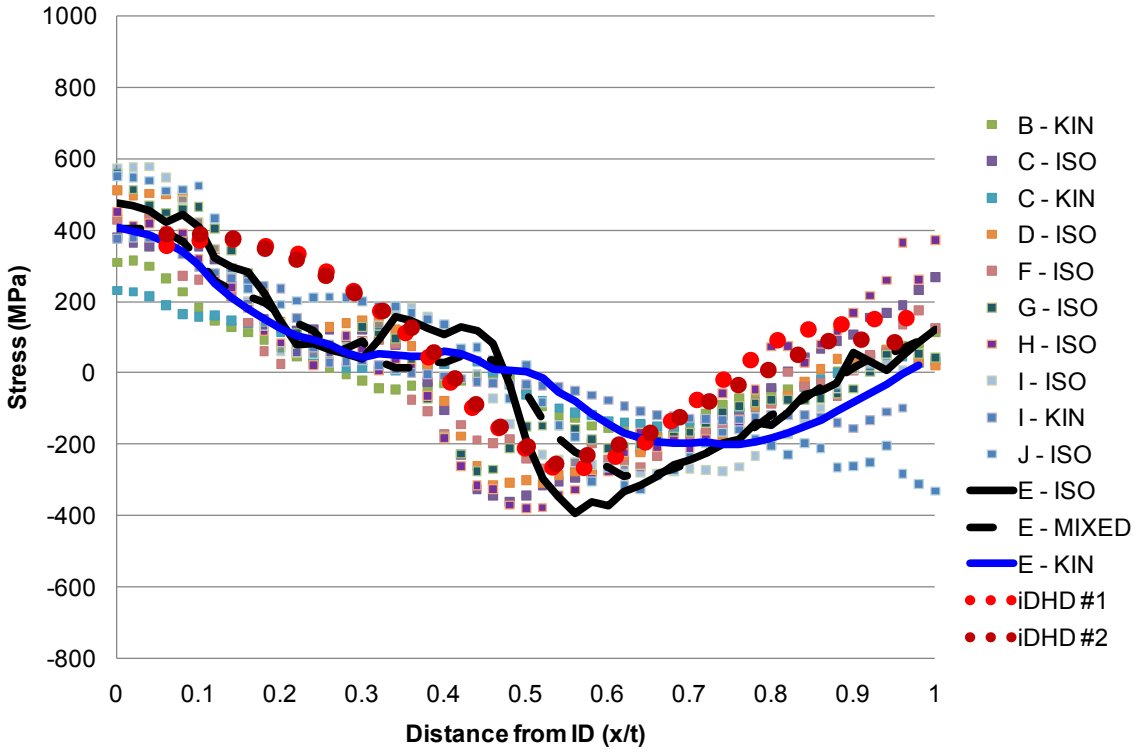

Figure 4-33 Analysis 1c Axial Stress - Isotropic, Kinematic, and Mixed, Model 'E'

In addition to the discussion of magnitude, differences in the shapes of the WRS profiles must be considered. On this point there are subtle but significant differences between the results. Figure 4-34 shows that DHD measurements cross zero stress at 0.4 and 0.75 x/t. The FE results show a broader distribution, crossing between 0.25 to 0.55 x/t, and again between 0.8 to 1 x/t. These observations are consistent with sensitivity to thermal model tuning discussed later in this section, where similar magnitude shifts in the zero-stress location for isotropic models were produced when the heat input model was adjusted to match thermocouple data.

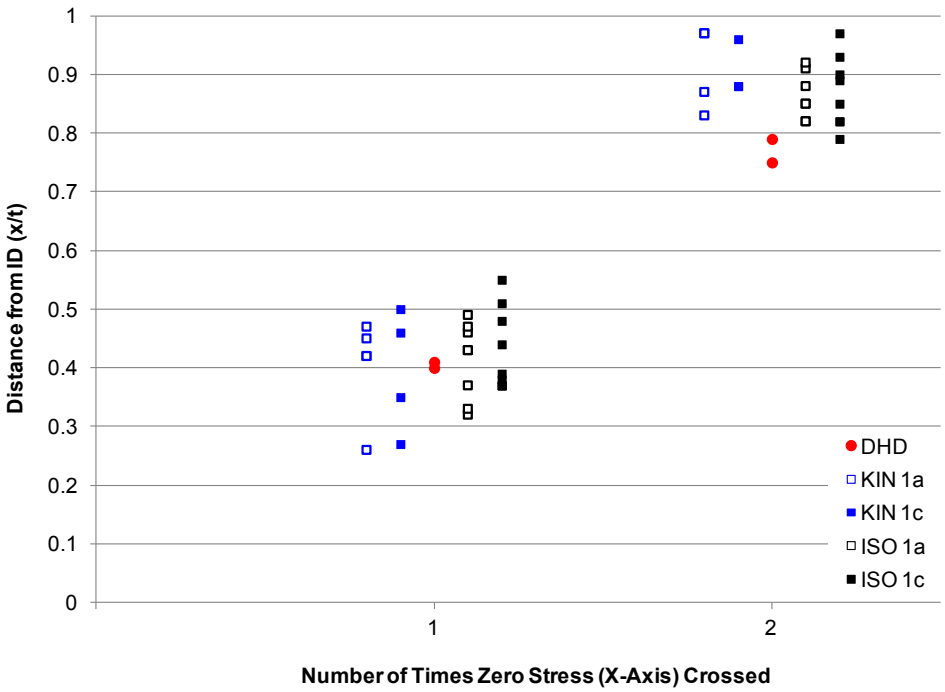

Figure 4-34 Number of Times the Zero Stress is Crossed

Grouping of hoop stress data by hardening law shows similar trends to those observed for the axial stresses. The grouping of results in Figure 4-35 represents round robin results that applied isotropic hardening; these isotropic results develop higher magnitude stresses than the dataset as a whole. The grouping of results in Figure 4-36 is the subset of isotropic results from U.S. participants in the round robin. The grouping of results in Figure 4-37 represents round robin results that applied kinematic hardening; the shape of these curves is flatter as lower magnitude stresses are developed when compared to the dataset as a whole. One set of mixed hardening results is plotted on Figure 4-37 in black. The mixed hardening results are similar to the kinematic results, but show better agreement with DHD data as higher stresses are developed from 0.1 to 0.3 x/t than are in the kinematic results. At $0.4 \leq x/t \leq 0.6$, however, the mixed hardening results overpredicted the measurements.

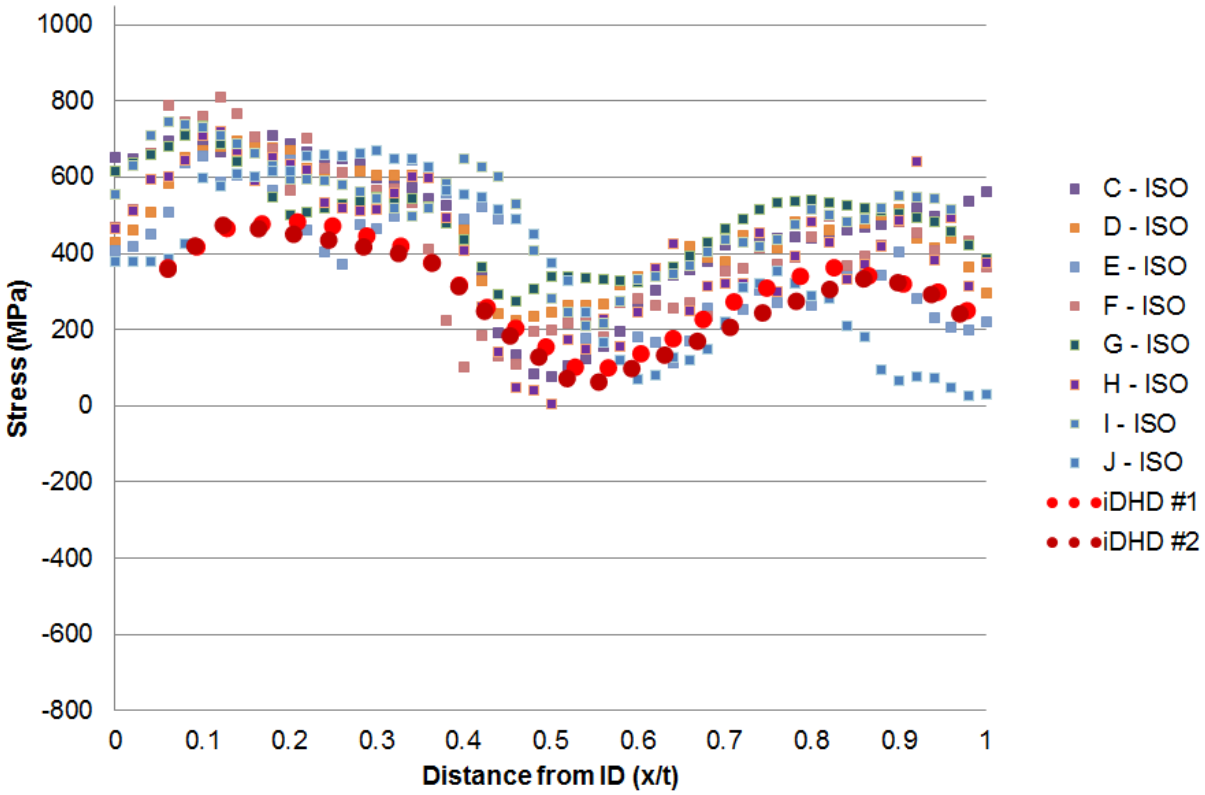

Figure 4-35 Analysis 1c Hoop Stress - Isotropic Hardening

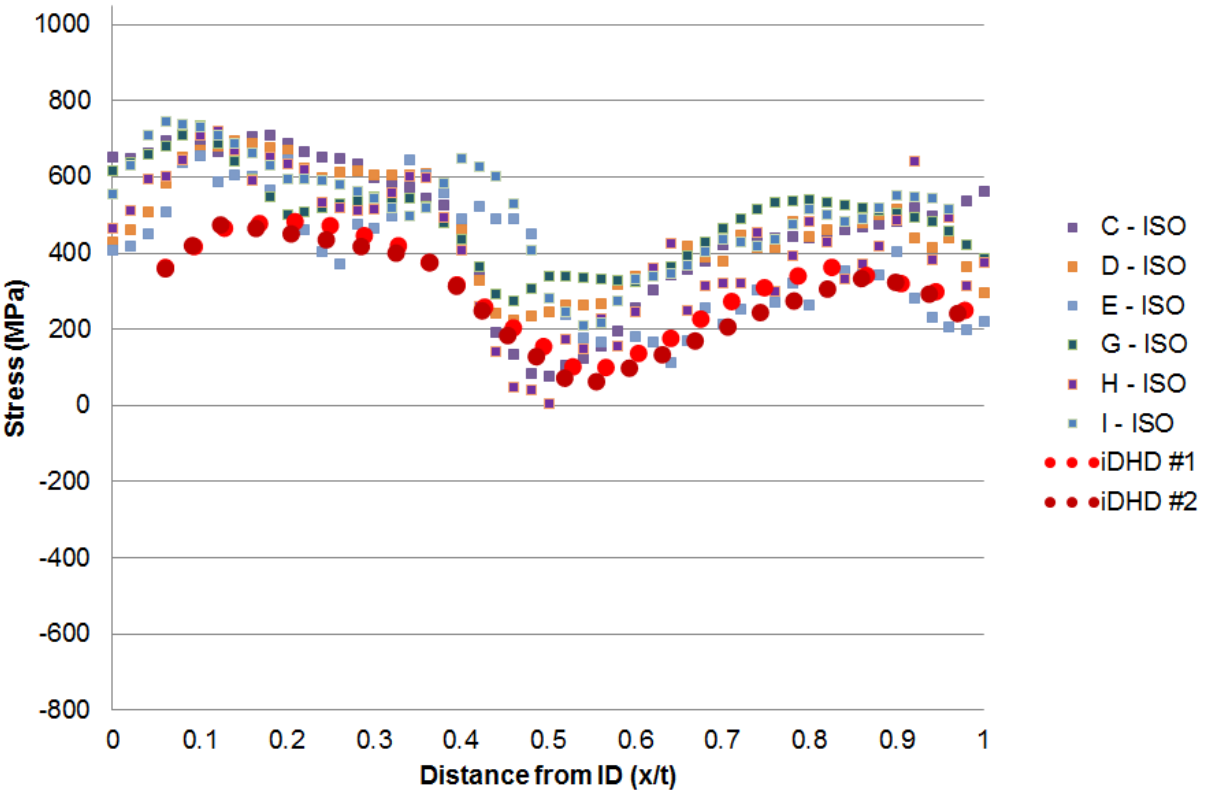

Figure 4-36 Analysis 1c Hoop Stress - Isotropic Hardening, US Participants

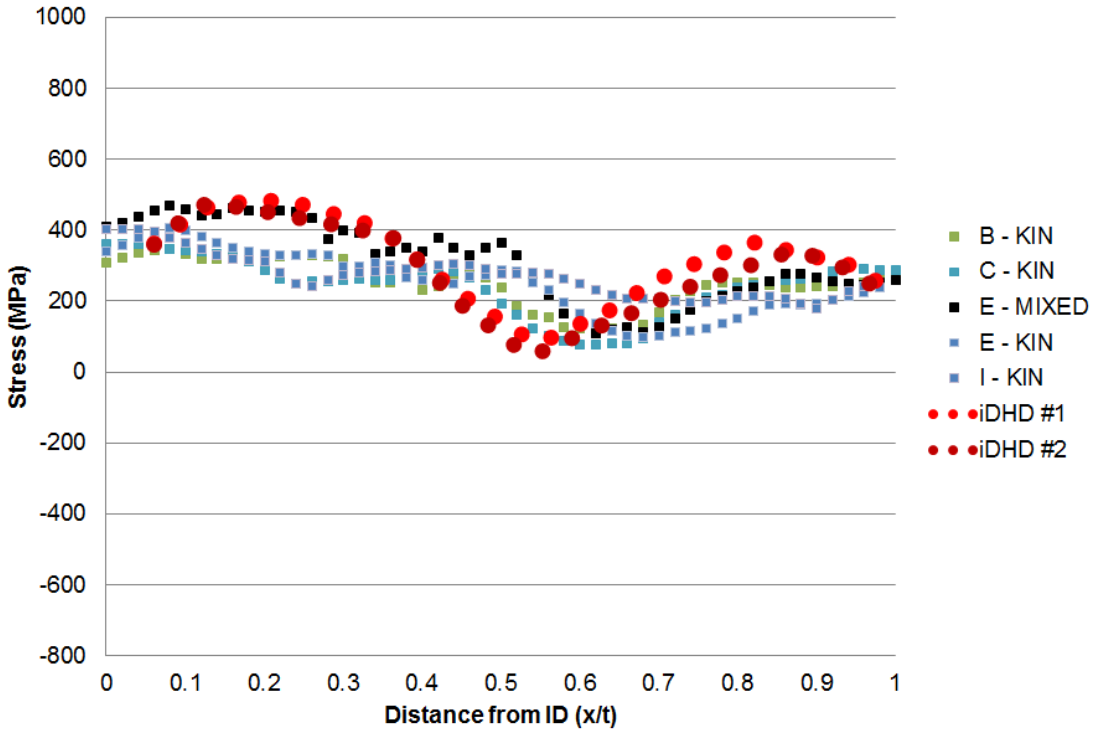

Figure 4-37 Analysis 1c Hoop Stress - Kinematic Hardening

Highlighting isotropic and kinematic results for a given model provides some additional insight to the global trends discussed above. As with the axial stresses, isotropic results for a given model do not completely bound the dataset. Results for model C plotted in Figure 4-38 bound a greater fraction of the dataset than results from model E plotted in Figure 4-39.

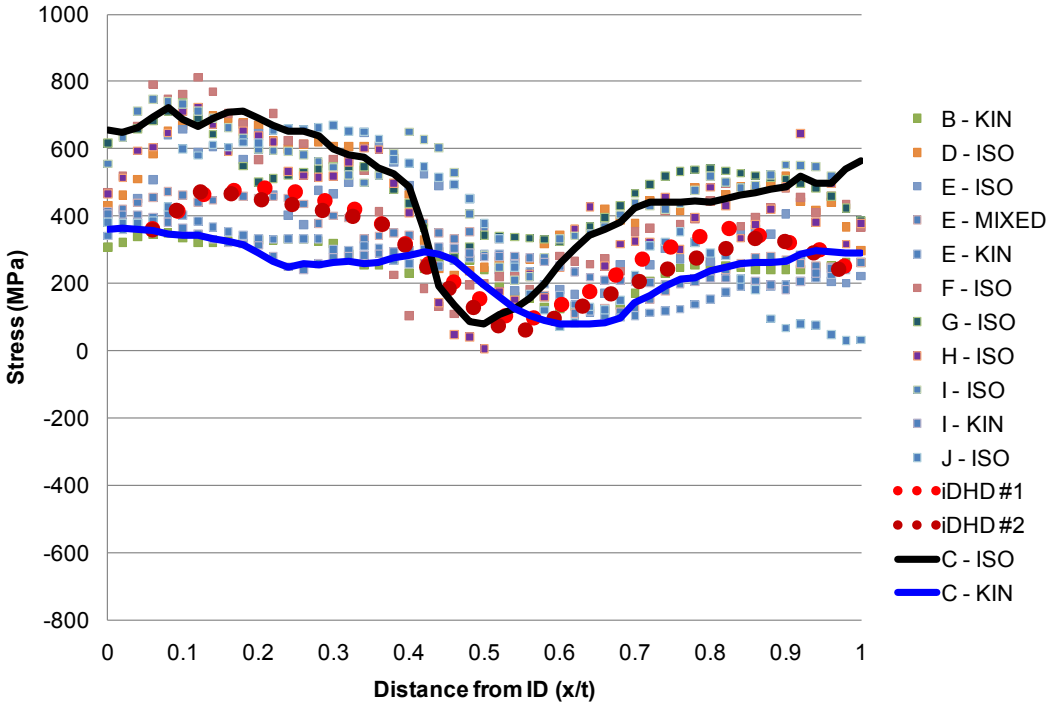

Figure 4-38 Analysis 1c Hoop Stress - Isotropic and Kinematic, Model 'C.'

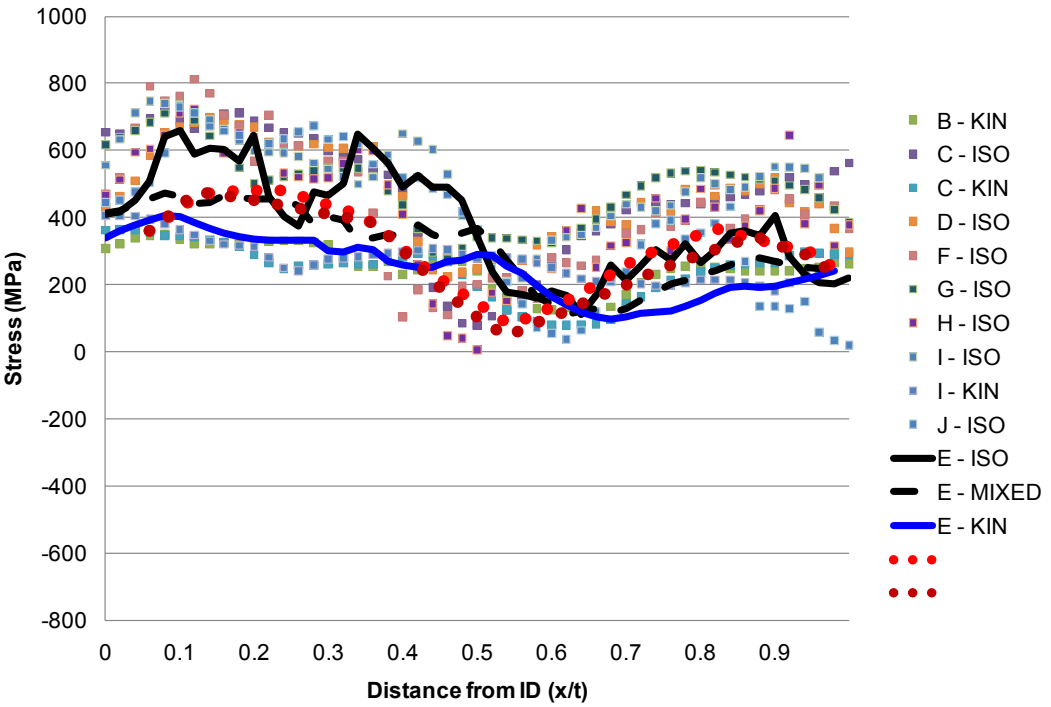

Figure 4-39 Analysis 1c Hoop Stress - Isotropic and Kinematic, Model 'E.'

As previously discussed there is general agreement in terms of the WRS profile shape and the DHD data, visualized by the comparison of the FE averages to the DHD measurements. Two averages are plotted in Figure 4-40 and Figure 4-41, the average of FE results using (1) isotropic and (2) kinematic hardening as this affects the form of the WRS profile. Neither

average captures the behavior of the measurement data. Furthermore, which average provides a better prediction of the measurements depends on the through-thickness location.

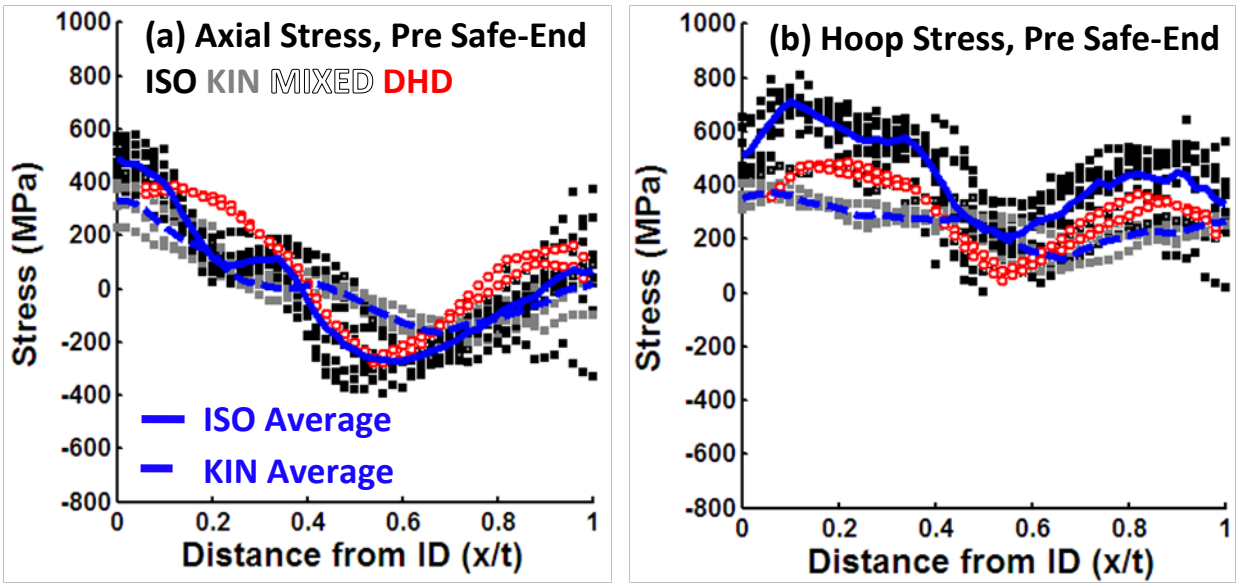

Figure 4-40 Analysis 1c Data with Averages Highlighted

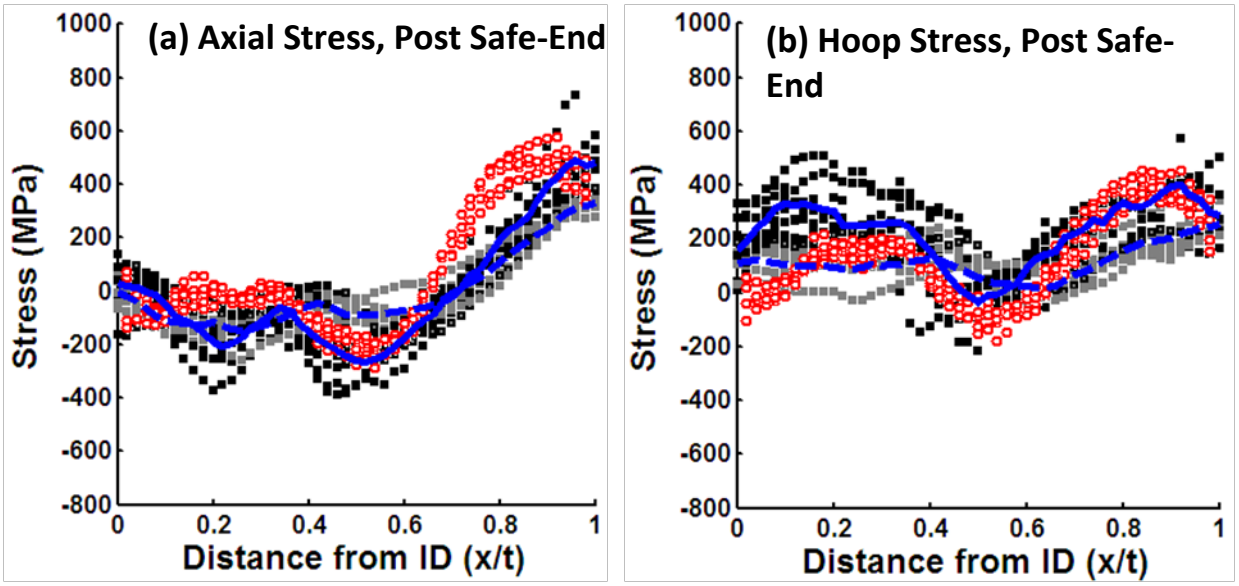

Figure 4-41 Analysis 2 with Averages Highlighted

The effect of tuned thermal models on axial centerline WRS profiles is summarized in the difference plot (1b – 1a) in Figure 4-42. Not all participants chose to update their thermal model. For example, 'B' judged the 1a thermal model based on bead geometry was in reasonable agreement with the thermocouple data and did not update the thermal model for Analysis 1b. Results from 'I' highlighted in blue in Figure 4-42 represent the greatest sensitivity of WRS profiles to the thermal model tuning conducted in Analysis 1b. Comparison of the Analysis 1a thermal model results for 'I' to thermocouple data in Figure 4-43 show the heat input was originally significantly underestimated. In fact, the predicted temperatures were far below the melting temperature of the filler metal. The Analysis 1b updated thermal model results for 'I'

plotted in Figure 4-44 are in much better agreement with the thermocouple data. For Analysis 1b, 'I' significantly increased the heat input to the weld producing changes to the ID and OD stresses, as well as to the mid-thickness stresses. Also illustrated in Figure 4-42 is that isotropic hardening shows a greater sensitivity to heat input changes than the kinematic results, a trend that is observed in all thermal model updates.

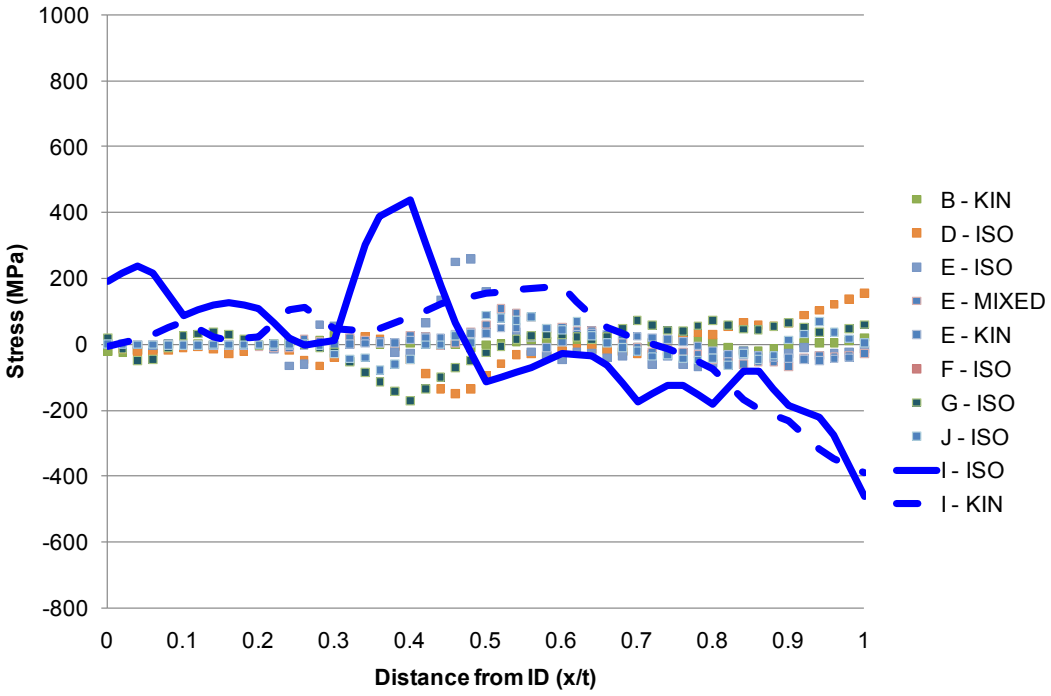

Figure 4-42 Analysis 1a Axial Stress Difference Plot

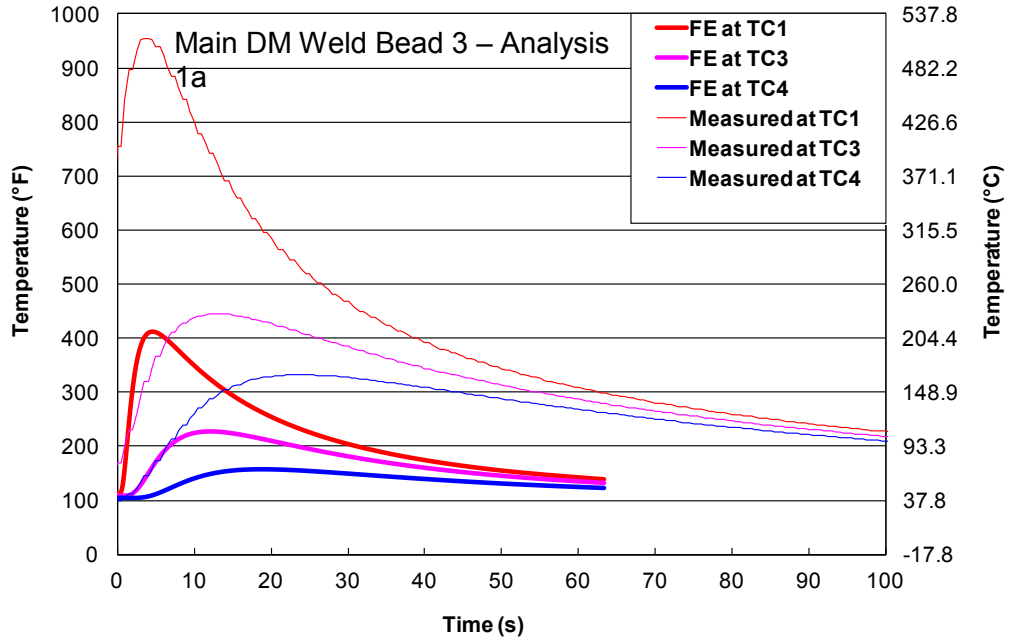

Figure 4-43 Measured and Predicted Temperature History – Analysis 1a, Model 'I'

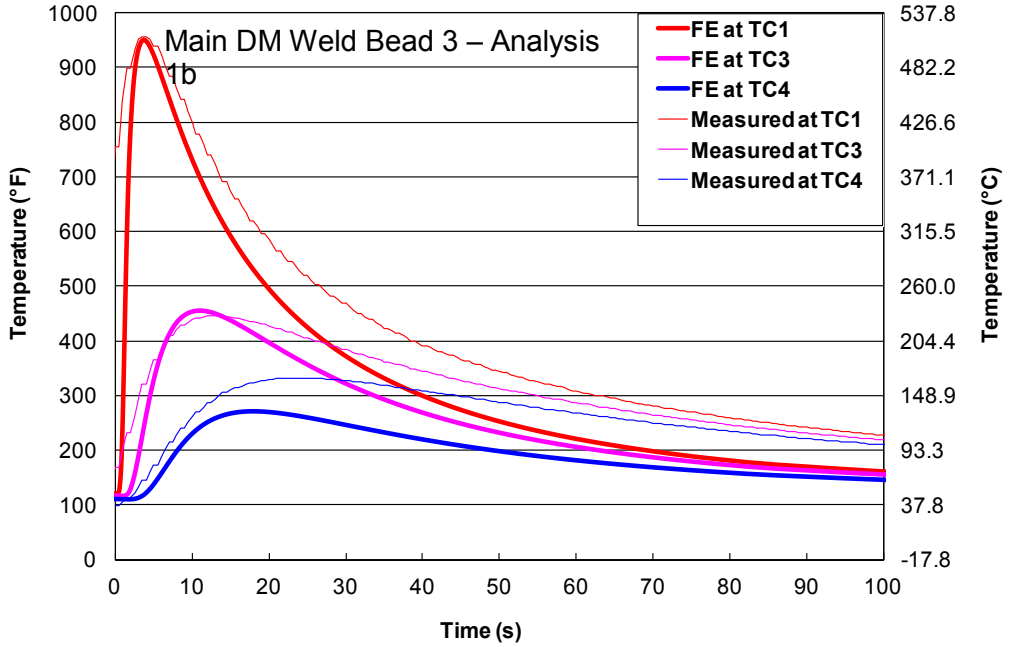

Figure 4-44 Measured and Predicted Temperature History – Analysis 1b, Model 'I'

Removing result 'I' from the dataset, as in Figure 4-45, shows that the thermal model tuning had a more modest effect on the centerline WRS profiles. Here kinematic results are largely unaffected by tuning of the thermal model in 1b. Isotropic results, however, exhibit a change in stress (increase or decrease) between 0.3 and 0.6 x/t indicating that zero stress has been crossed at a different location as a result of the thermocouple tuning. Further, the centerline WRS profile shape was largely insensitive to tuning of the thermal model, provided that the heat input was not significantly underestimated originally.

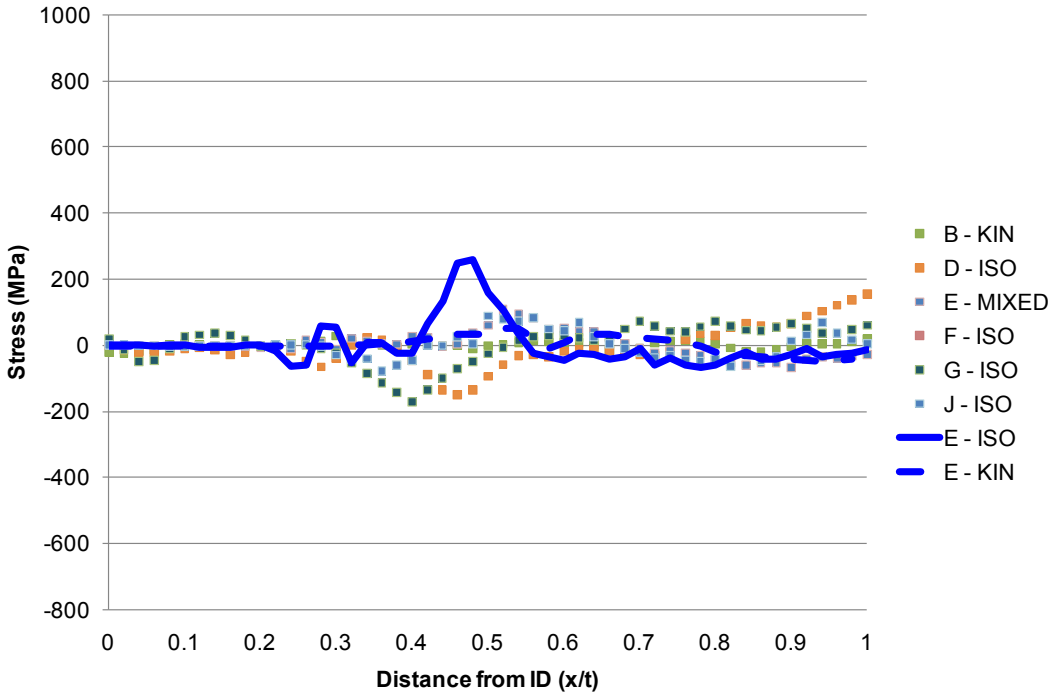

Figure 4-45 Analysis 1a Axial Stress Difference Plot – Excluding Model 'I'

Similar trends were observed for the hoop stress data, as illustrated in Figure 4-46. The above discussion suggests that the weld bead geometry and weld parameter data provided in Analysis 1a was, in most cases, sufficient to constrain the heat input for the thermal modeling. The thermocouple data provided in Analysis 1b allowed verification of the heat input assumptions made in Analysis 1a. These observations are consistent with the sensitivity of WRS profiles to heat input described in Section 4.6, which notes that if the total amount of heat input is approximately correct the end state WRS profiles are stable. However, the time over which the heat is applied may have some effect.

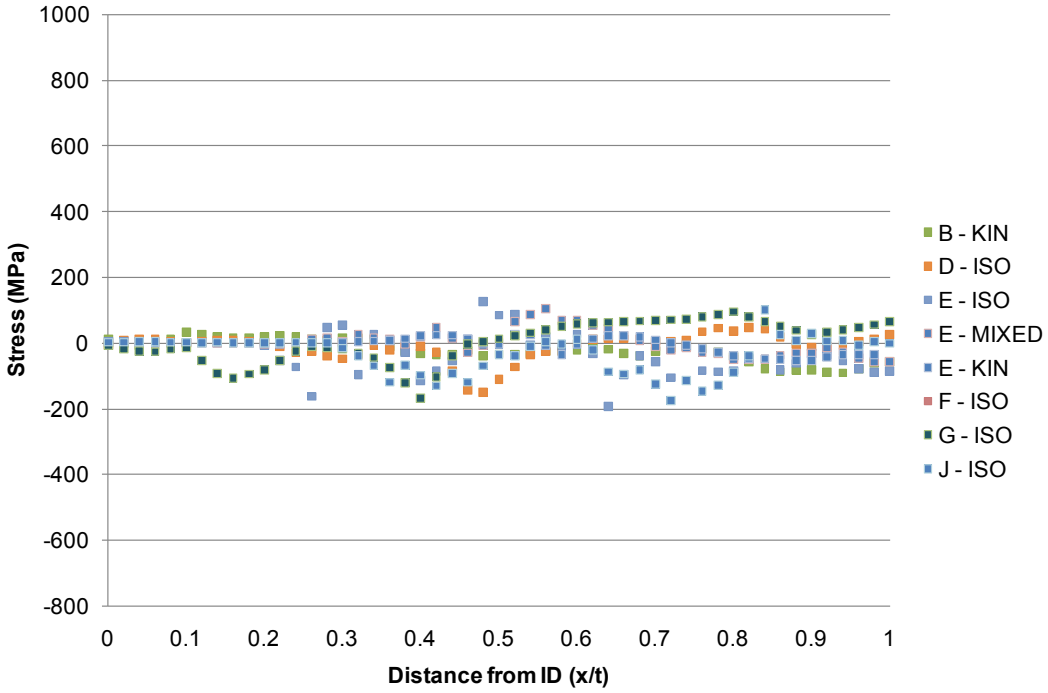

Figure 4-46 Analysis 1a Hoop Stress Difference Plot – Excluding Model 'I'

The sensitivity to material properties was not as large as anticipated at the onset of this study, where it was assumed that use of a common material property dataset would produce a reduction in scatter for the end state centerline WRS profiles. While the use of the NRC material property had an effect on the axial WRS profiles, systematic variation is not observed for the (1c – 1b) difference plot in Figure 4-47. The hoop stresses appear more sensitive to material properties than the axial stresses, as shown in the (1c – 1b) hoop stress difference plot in Figure 4-48. Unlike the axial stresses, there are some hoop stress results that show systematic variation, specifically result 'G' is higher than the other results and result 'J' is lower in stress through-thickness than the average response. Aside from the two hoop results identified that show systematic variation, axial and hoop stress values change from 100 to 200 MPa through thickness using the NRC material property dataset with no reduction in the scatter observed in the Analysis 1c results. The sensitivity of hoop stresses to material property input observed here is consistent with the findings of the FE sensitivity studies discussed in Section 4.6 of this report.

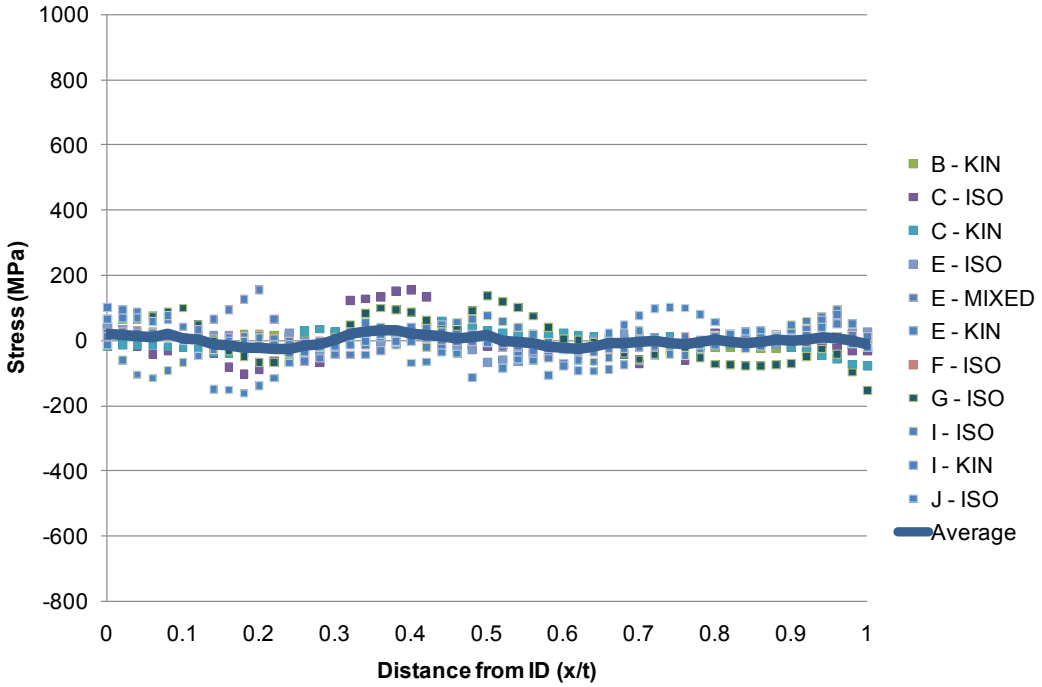

Figure 4-47 Analysis 1c – 1b Axial Stress Difference Plot

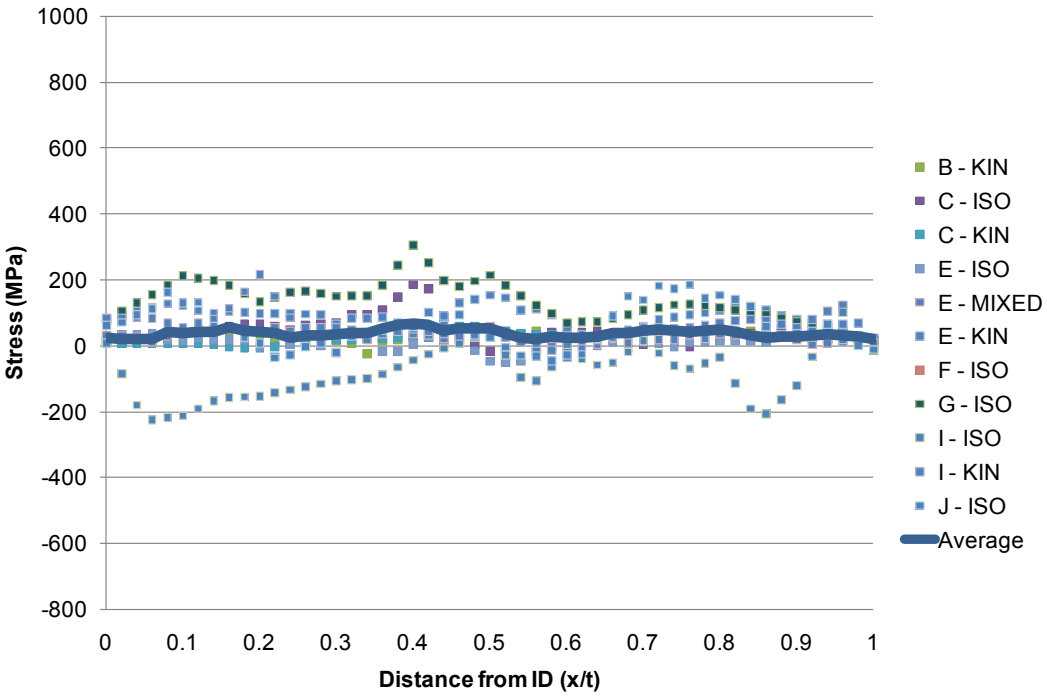

Figure 4-48 Analysis 1c – 1b Hoop Stress Difference Plot

The driver for the axial and hoop ID stress reduction is the through-wall bending that occurs as a result of the safe end weld application. This stress reduction is important since SCC is likely to initiate in susceptible material on the pipe ID, therefore an appropriately sized safe end will lower the likelihood of SCC initiation through this reduction in ID stress. Figure 4-49 is the axial stress centerline difference plot (2 – 1c) showing the effect of the through-wall bending, while

Figure 4-50 is the same for the hoop stress. The through-wall bending is predominantly elastic for both the FE and DHD results. A couple of the isotropic FE results show minor deviation from linearity, indicating that plasticity has occurred during the application of the safe end weld. DHD results show a drop off in stress as the OD approached. Scatter in the difference plot is similar in magnitude as for Analysis 1c and 2.

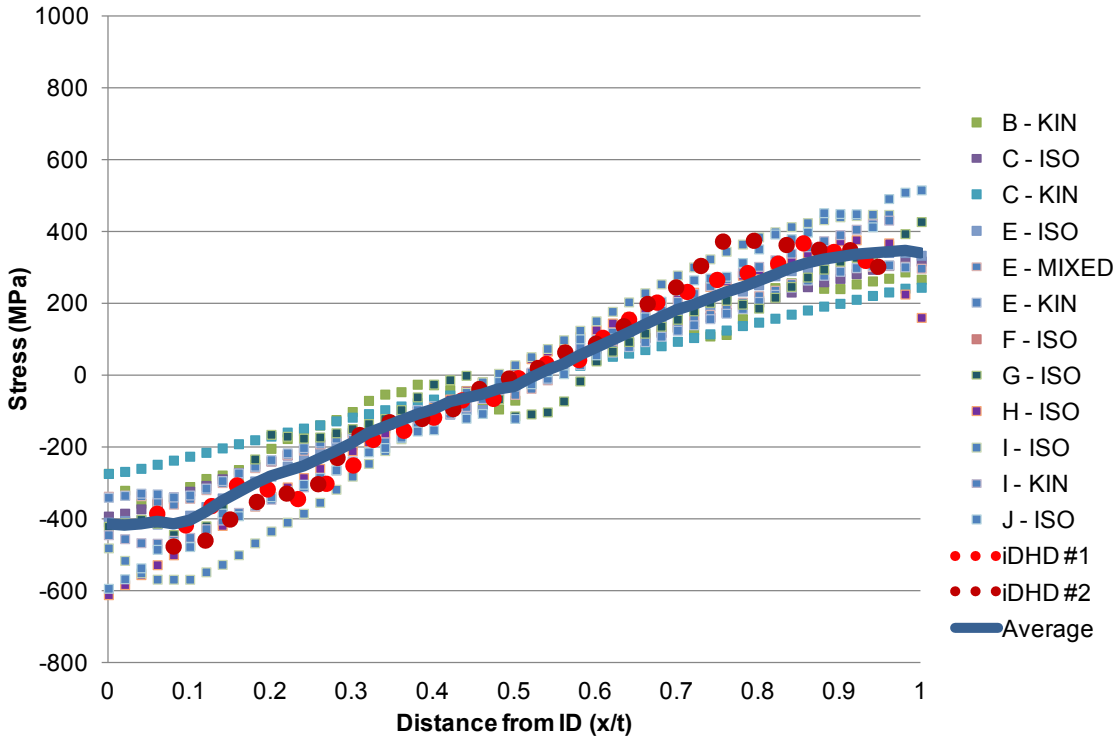

Figure 4-49 Axial Stress Through Wall Bending Caused by Safe End Weld

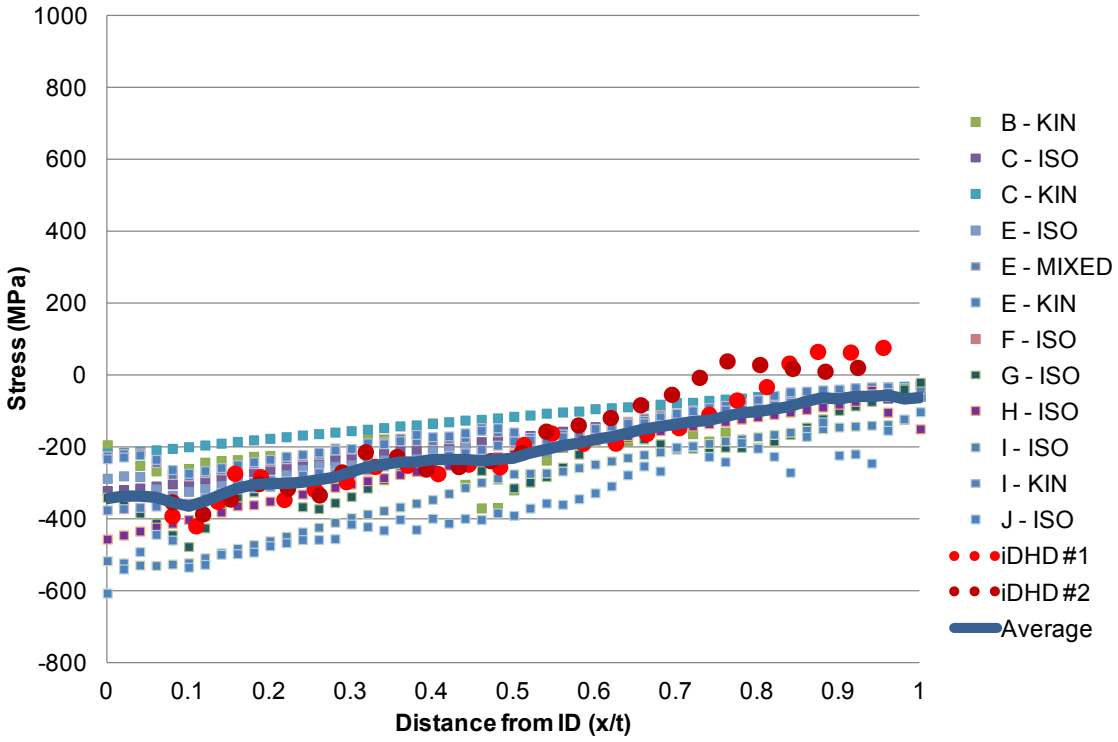

Figure 4-50 Hoop Stress Through-Wall Bending Caused by Safe End Weld

Though the round robin problem statement provided detailed geometric information, there were still variations in geometries modeled by some participants. All round robin participants informed the weld bead geometry by the laser profilometry data, whether by explicitly incorporating the laser profilometry data into the FE model or using the profilometry data to inform the idealized weld bead size.

Even with detailed geometric data provided, the thicknesses of the component modeled ranged from 46.8 to 49 mm, representing a difference in component thickness of 5 percent that was accounted for by using a normalized thickness (x/t) and contributing to the model-to-model variability observed in the dataset. Result 'E' modeled a component thickness of 51.6 mm, but on closer examination this was a result of the weld cap and fill-in weld not being machined to the final component geometry specified. This will have an effect on the WRS profile, specifically the location of where the WRS profile will cross the zero stress axis. To estimate the magnitude of this effect, profile 'E' was normalized to the correct thickness by removing the part of the WRS profile associated with the fill-in weld (first 3 mm of the WRS profile) and weld cap (last 2 mm of the WRS profile). Stress redistribution was not accounted for, but the stress redistribution expected is not significant as it should be near an equilibrium condition. The plot in Figure 4-51 shows that the location of zero stress shifts by approximately 3 percent and the start of the fill-in weld by approximately 5 percent, contributing to the model-to-model variability observed in the dataset.

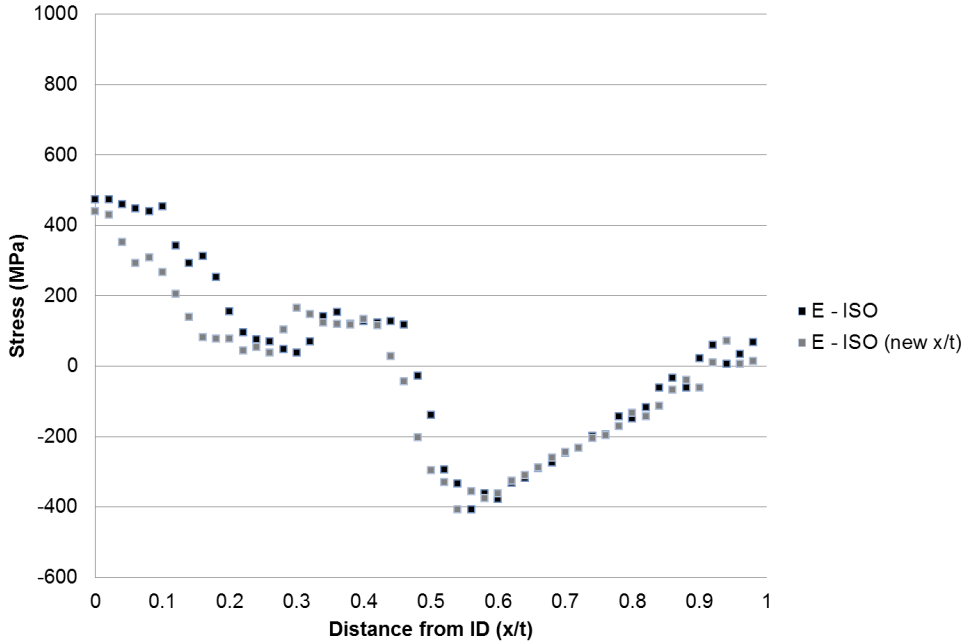

Figure 4-51 Results 'E' As-Submitted and Corrected for Geometric Variation

4.5.4. Summary of Round Robin Results

At the onset of the FE WRS round robin, it was assumed that providing thermocouple and material property data would reduce the variability associated with FE WRS models. This outcome was not observed in the dataset; rather similar variability was present in all phases of the study regardless of the amount of information provided to FE round robin participants. While there was significant scatter present in the international FE WRS round robin dataset, there were consistent trends in the dataset, which are summarized below.

- Shape of the mean WRS profiles calculated by FE and experimentally measured by DHD were similar in Analysis 1 and 2. There is favorable agreement between the average of all results and the experimental DHD measurements for Analysis 1. For Analysis 2, the DHD measurement tended to be higher in magnitude than the average of all results until mid-thickness of the component.
- FE models using isotropic hardening evolved stresses higher in magnitude than those using kinematic hardening, with the annealed material properties provided by the NRC for Analysis 1c.
- In most cases the weld bead geometry and weld parameters provided were sufficient to constrain the FE thermal models; refining thermal models based on thermocouple data shifted the zero stress location.
- FE models using isotropic hardening showed a greater sensitivity to heat input, specifically the location of zero stress was sensitive to heat input. FE models using kinematic hardening showed less sensitivity to heat input. This observation can be attributed to annealing procedures in certain finite element packages. The yield surface expansion is reset when the temperature reaches the prescribed annealing temperature, leading to heat input sensitivity of the isotropic hardening models.
- The stainless steel safe end weld led to a pronounced reduction in stresses at the ID for both hoop and axial stresses, as a result of through-wall bending.

- Geometric variations (different component thicknesses, fill-in weld depths, and weld shrinkage) in models produced observable differences in WRS profiles, but these differences do not account for the entire model-to-model variation observed in the round robin dataset.

4.6 Sensitivity Studies

Given the presentation and analysis of the previous section, it is apparent that significant variation exists in the round robin FE data sets. In practice, this scatter inherently reduces confidence that FE calculation results are robust approximations to the true, physical state of stress of a structure. WRS FE simulations are complex in that there are many input variables and methods for approximating model details. Further, WRS fields are known to have a significant effect on flaw evaluation and probabilistic fracture mechanics calculation results. Therefore, it is important to gain an understanding of the significant sources of variability in WRS FE calculations. As a corollary, it is also useful to understand which FE input parameters have negligible effects on results, to avoid unnecessarily expending resources on model aspects that have little to no bearing on final results.

The standard procedure for assessing the impact of individual FE model inputs and features is to systematically vary individual parameters, run the analysis, and determine the effect on the results. This study employed the following procedure:

(1) Develop an FE model that produces reasonable results compared to other FE models and measurements.
(2) Identify the full set of possible model inputs and features that are likely to have a significant impact on final results.
(3) Systematically vary the remaining model input parameters and features; observe and quantify the results.

4.6.1. Baseline Model

The baseline model geometry followed the specifications included in the original design package. Special mesh considerations were made to accurately model the mockup fabrication evolution, including ID back-chip and re-weld, and weld crown and ID machining. The main DM weld, ID re-weld, and stainless steel weld bead geometries followed laser profilometry data included in the modeling package. There was a high mesh density in the DM weld region and medium mesh density in the regions away from the welds (i.e., nozzle and pipe). The resulting mesh, as shown in Figure 4-52, had 7140 nodes and 6962 4-node linear axisymmetric quadrilateral elements. Figure 4-53 shows a close-up of the mesh in the vicinity of the DM and stainless steel welds.

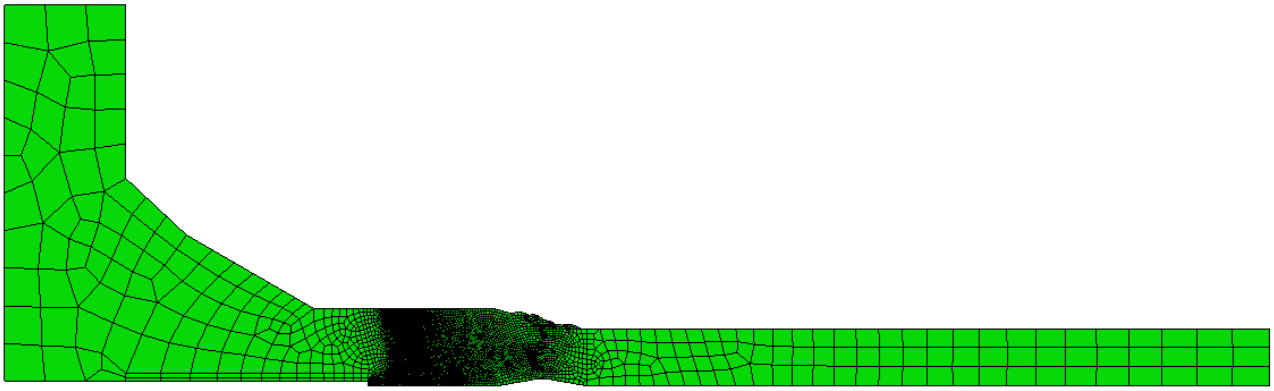

Figure 4-52 Baseline Model Finite Element Mesh

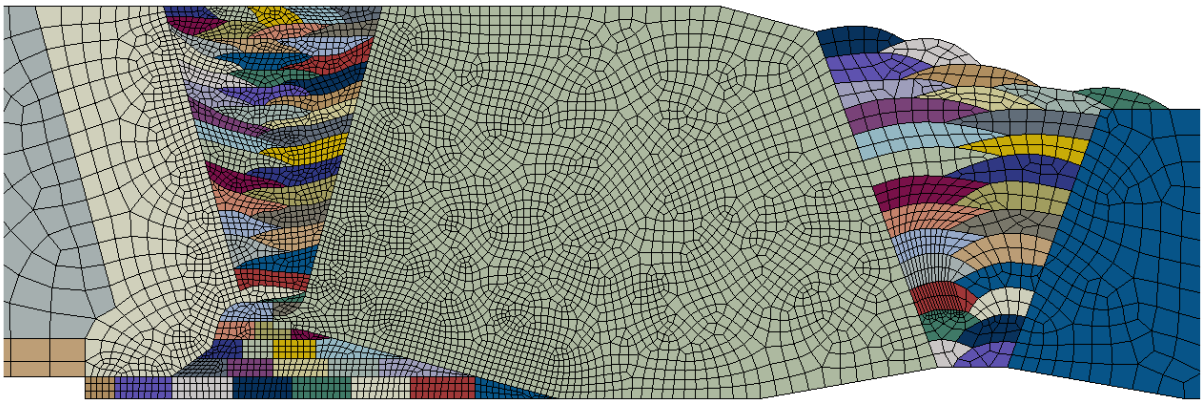

Figure 4-53 DM and Stainless Steel Weld Meshes

Figure 4-54 shows a plot of the peak temperature in Kelvin achieved in the main DM weld and re-weld region. All weld beads were observed to have reached the annealing temperature of approximately 1500 K. In addition, the fusion zone surrounding the weld was a reasonable approximation to commonly observed sectioned and etched pipe welds. The baseline analysis assumed isotropic hardening. The material properties were identical to those used by other analysts in Analyses 1c and 2 in the round robin study.

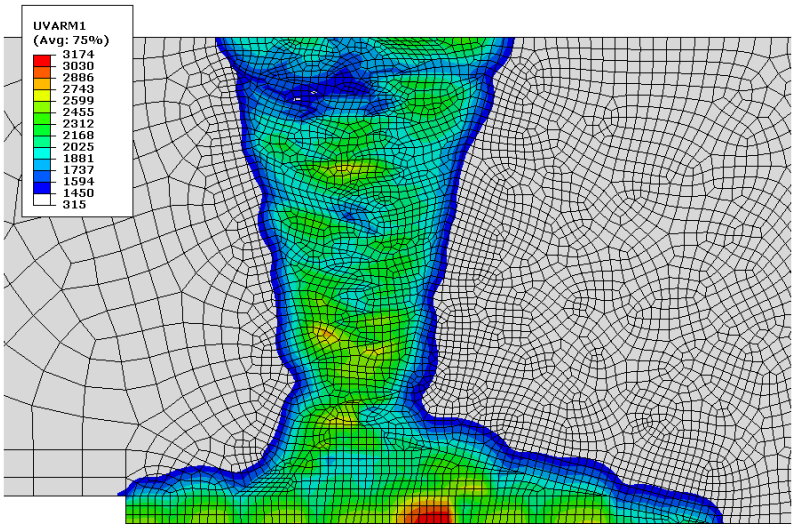

Figure 4-54 Peak temperature [K] Achieved in the Baseline Thermal Analysis

Figure 4-55 through Figure 4-58 show the axial and hoop stresses from ID to OD along the centerline of the DM weld model before and after application of the stainless steel weld. As seen in Figure 4-55, the pre-stainless steel weld axial stress was highly tensile at the pipe ID, consistent with the fact that the final weld passes were in this region. Figure 4-57 shows a significant reduction in the ID axial stress due to the bending moment applied by the stainless steel weld. Figure 4-56 and Figure 4-58 show that the through thickness pre-stainless steel weld hoop stress was highly tensile and reduced in magnitude by the stainless steel weld. The baseline model results agreed well with the average of the round robin participants. This model should, therefore, provide a reasonable reference for the sensitivity studies in Sections 4.6.2 through 4.6.8.

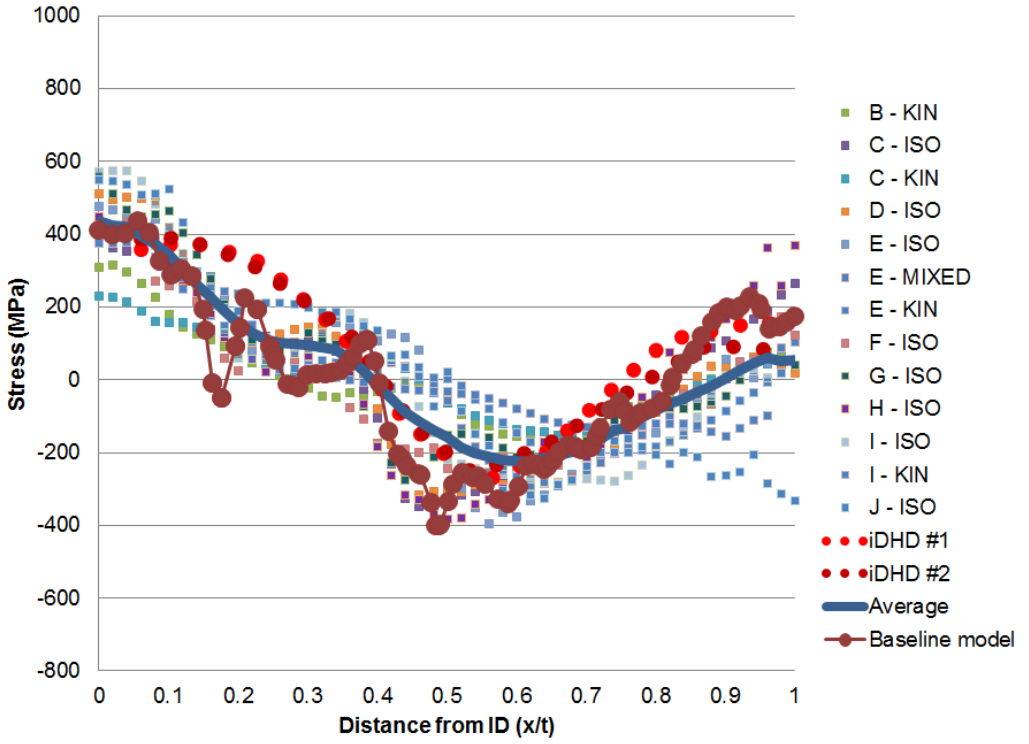

Figure 4-55 Axial Stress from Baseline Model before Stainless Steel Weld

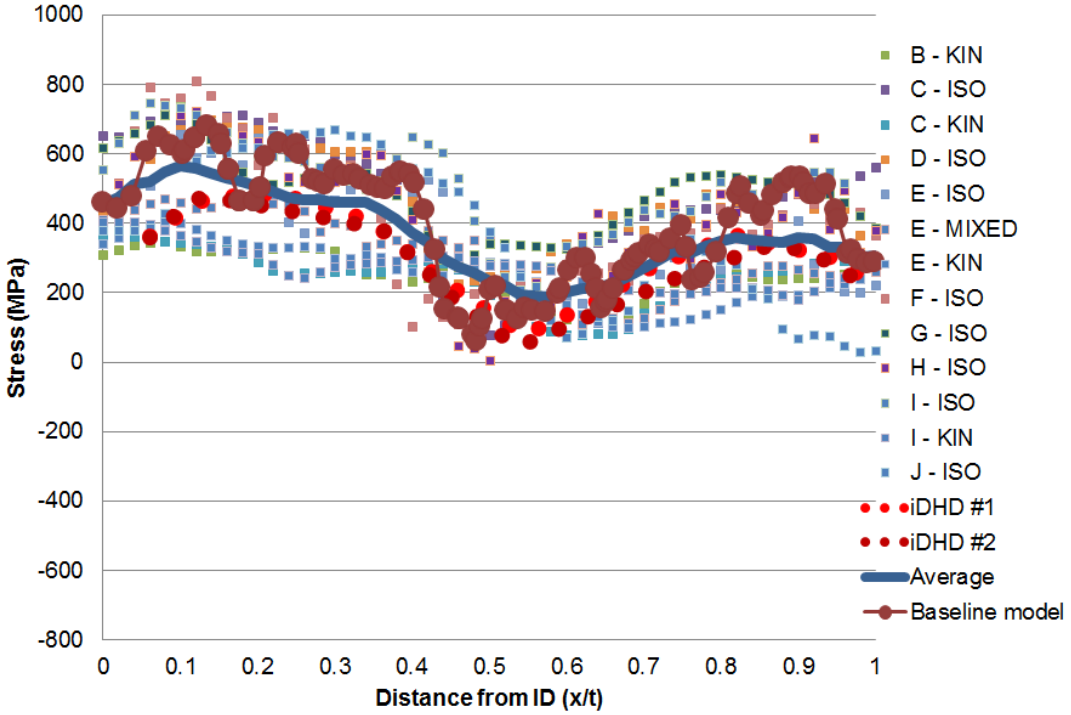

Figure 4-56 Hoop Stress from Baseline Model before Stainless Steel Weld

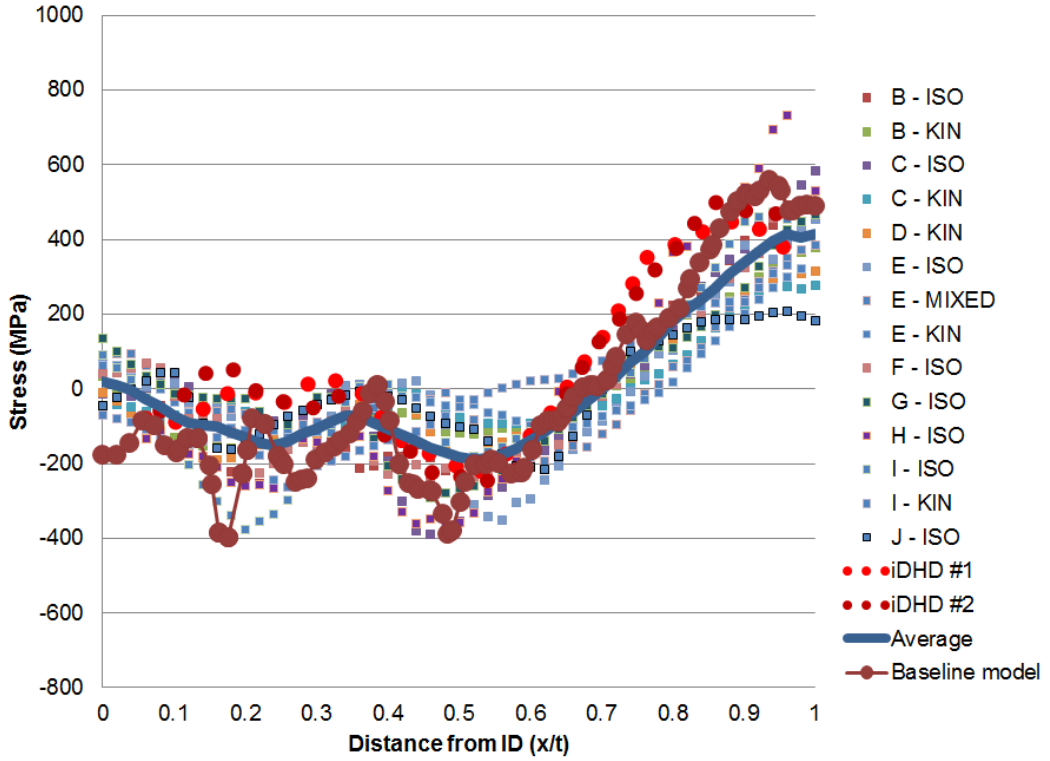

Figure 4-57 Axial Stress from Baseline Model after Stainless Steel Weld

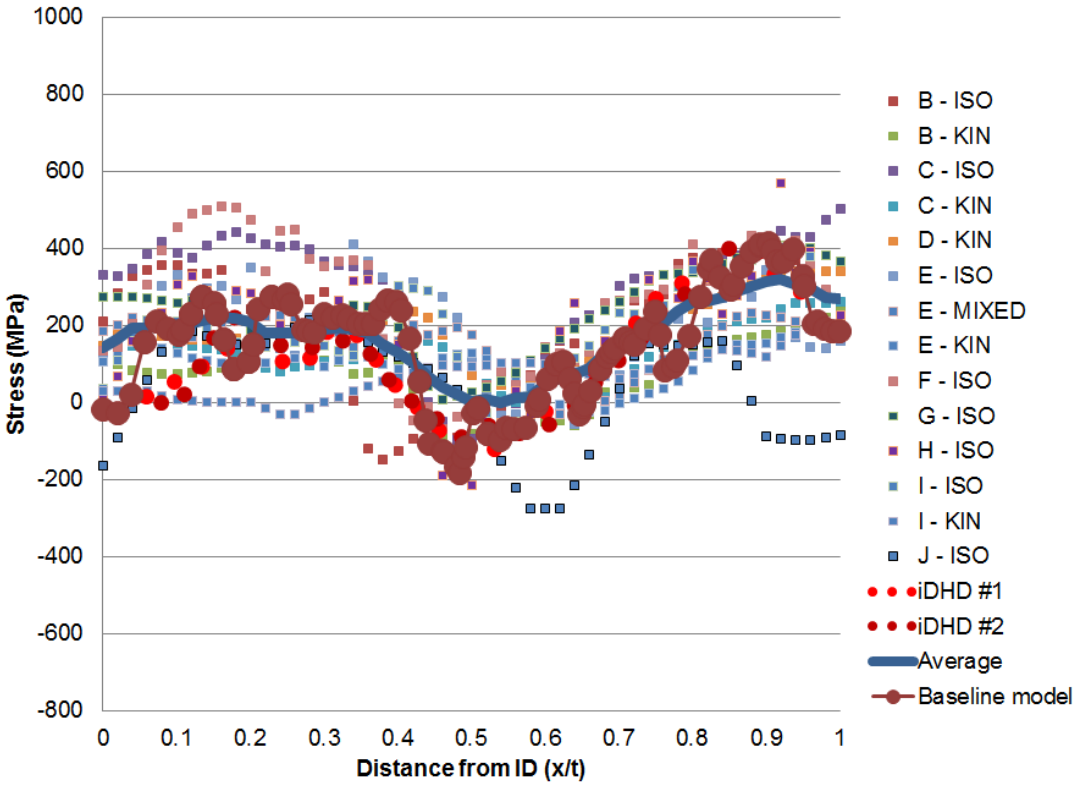

Figure 4-58 Hoop Stress from Baseline Model after Stainless Steel Weld

4.6.2. Sensitivity Parameter Selection

The input categories considered in WRS FE analyses can be consolidated into the following groupings:

Thermal

- energy magnitude and duration (dictated by weld voltage, current, arc efficiency and deposition speed)
- density
- latent heat
- conductivity
- specific heat
- convective heat transfer coefficient

Mechanical

- coefficient of thermal expansion
- elastic properties (modulus and Poisson ratio)
- plastic properties (true stress vs. plastic strain)
- hardening law
- anneal temperature

Other

- weld bead shape
- weld pass order of deposition

The parameters chosen for this sensitivity study included energy magnitude and duration, coefficient of thermal expansion, plastic properties (true stress vs. plastic strain), hardening law (isotropic and kinematic), anneal temperature, and weld pass order of deposition. The following sections describe systematic variation of these model parameters and aspects, and their impact on centerline through-wall DM weld axial and hoop stresses. It was found that some of these model parameters had a significant effect on weld residual stresses, and some had a negligible effect.

In these studies, three representative sets of material properties are referred to:

- one employed a British Energy (BE)-led WRS validation effort [24], referred to as “BE properties,”
- one distributed to round robin participants referred to as “Phase 2 properties,” and
- the property set used in the baseline model, referred to as “Baseline properties.”

4.6.3. Coefficient of Thermal Expansion Sensitivity Study

Figure 4-59 shows the coefficient of thermal expansion as a function of temperature for the three sets of properties. The coefficient of thermal expansion values contained in the baseline model were replaced by those from the BE and Phase 2 properties, and the analysis was re-run to determine the sensitivity to these parameters.

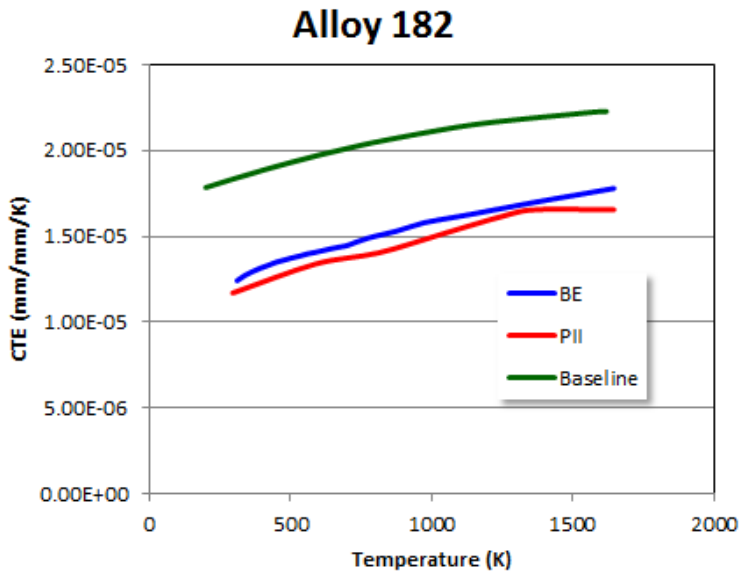
Alloy 182
2.50E-05
2.00E-05
1.50E-05
1.00E-05
5.00E-06
0.00E+00
CTE (mm/mm/K)
0
500
1000
1500
2000
Temperature (K)
BE
PII
Baseline

(a)

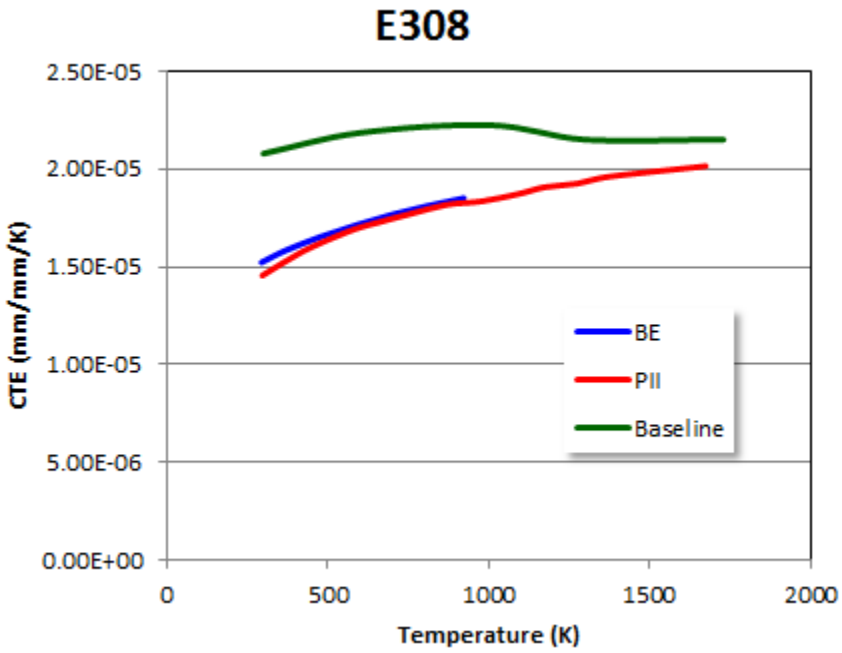
E308
2.50E-05
2.00E-05
1.50E-05
1.00E-05
5.00E-06
0.00E+00
CTE (mm/mm/K)
0
500
1000
1500
2000
Temperature (K)
BE
PII
Baseline

(b)

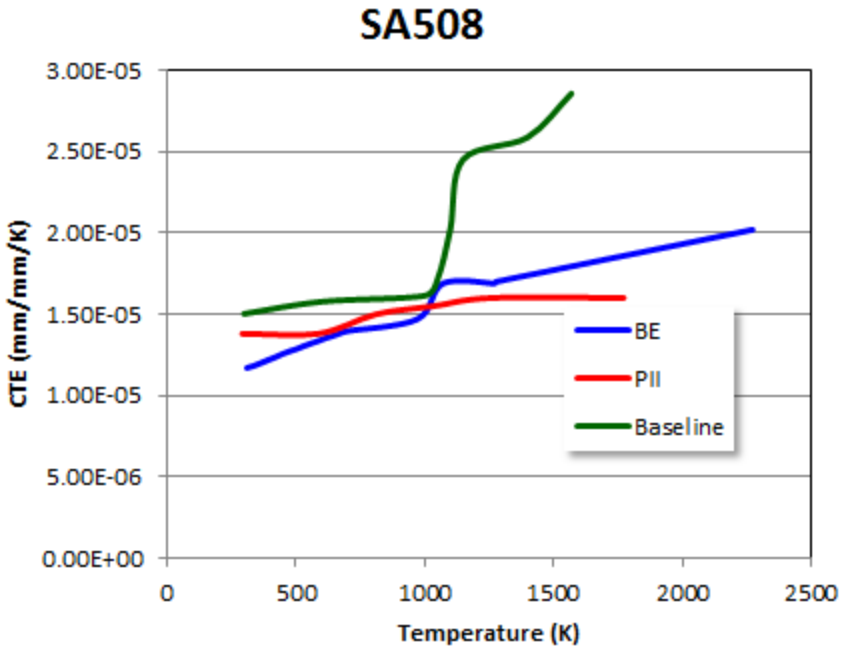

(c)

Figure 4-59 Coefficient of Thermal Expansion vs. Temperature for Three Materials

Figure 4-60 and Figure 4-61 show the through-wall axial and hoop stress distributions along the centerline of the DM weld, before and after application of the stainless steel weld. Relatively small variation is seen in the results, indicating that variations in coefficient of thermal expansion, within the range of typical material property sets used by experienced modelers, has a negligible effect.

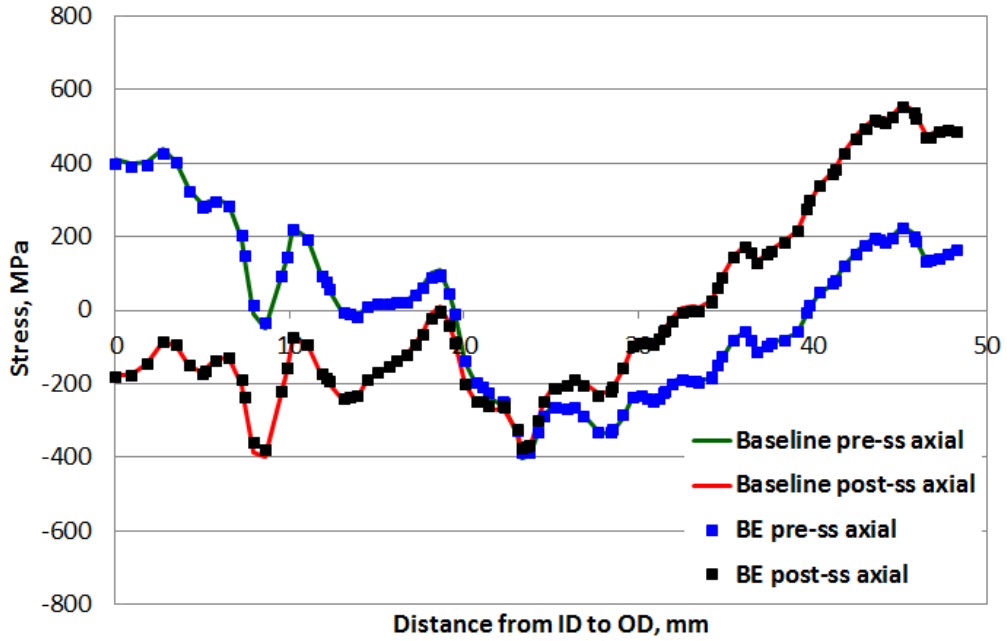

Figure 4-60 Axial Stress for Coefficient of Thermal Expansion Sensitivity Study

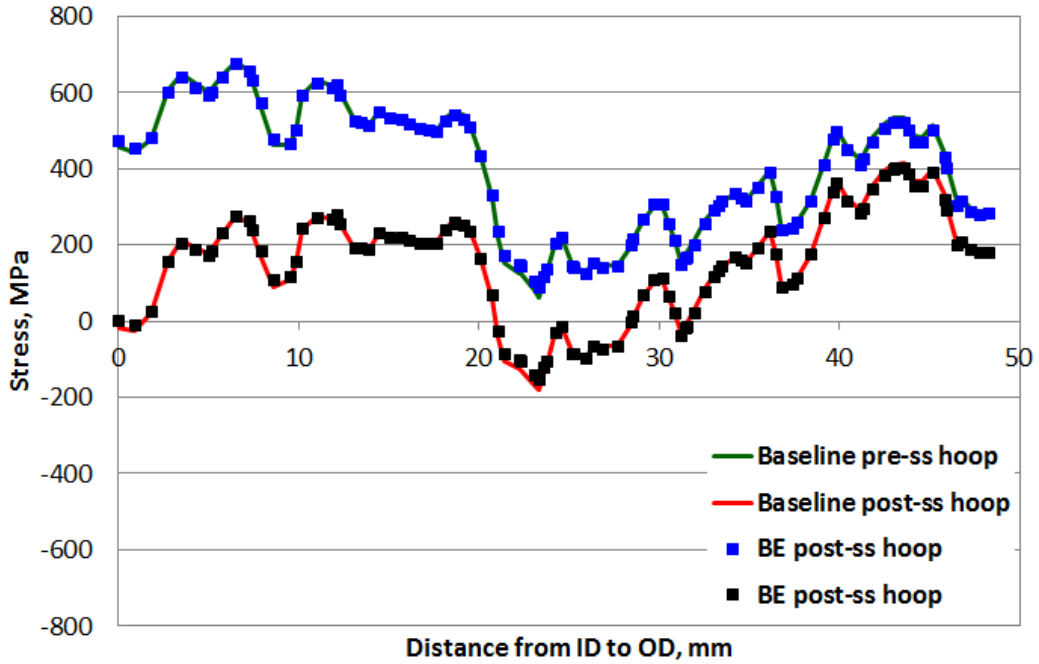

Figure 4-61 Hoop Stress for Coefficient of Thermal Expansion Sensitivity Study

4.6.4. Heat Input Sensitivity Study

Intuitively, the magnitude and duration of heat flux input during the welding simulation would have an effect on final through-wall stress distributions. To quantify these effects, independent sensitivity studies were performed in which the magnitude and duration of weld heat flux were varied relative to the baseline analysis. The thermal model described in Equation 2-3 provided a convenient means of independently varying weld heat flux magnitude and duration; by varying

input parameters in this model, a range of heat flux magnitudes and durations can be achieved. The magnitude of heat flux varies linearly with arc efficiency. In this study, the baseline arc efficiency values were scaled by factors of 0.25, 0.5 and 1.5 to provide a wide range of heat flux values. Note that only the arc efficiencies of the DM weld were scaled, whereas the arc efficiencies of the stainless steel weld remained unchanged. This range of heat inputs would significantly affect the peak temperatures calculated in the model. Figure 4-62 shows the resulting heat flux magnitudes as a function of time, including the baseline case. Figure 4-63 and Figure 4-64 show the final through-wall centerline DM weld axial and hoop stress distributions, after application of the stainless steel weld, for the various heat flux magnitude inputs. Clearly, for the magnitude of heat flux variation chosen, significant differences in final through-wall stresses were observed for these large changes in heat input. As the analysis in Figure 4-42 through Figure 4-45 indicates, however, these models are relatively insensitive to heat input given the modeling choices of most experienced analysts.

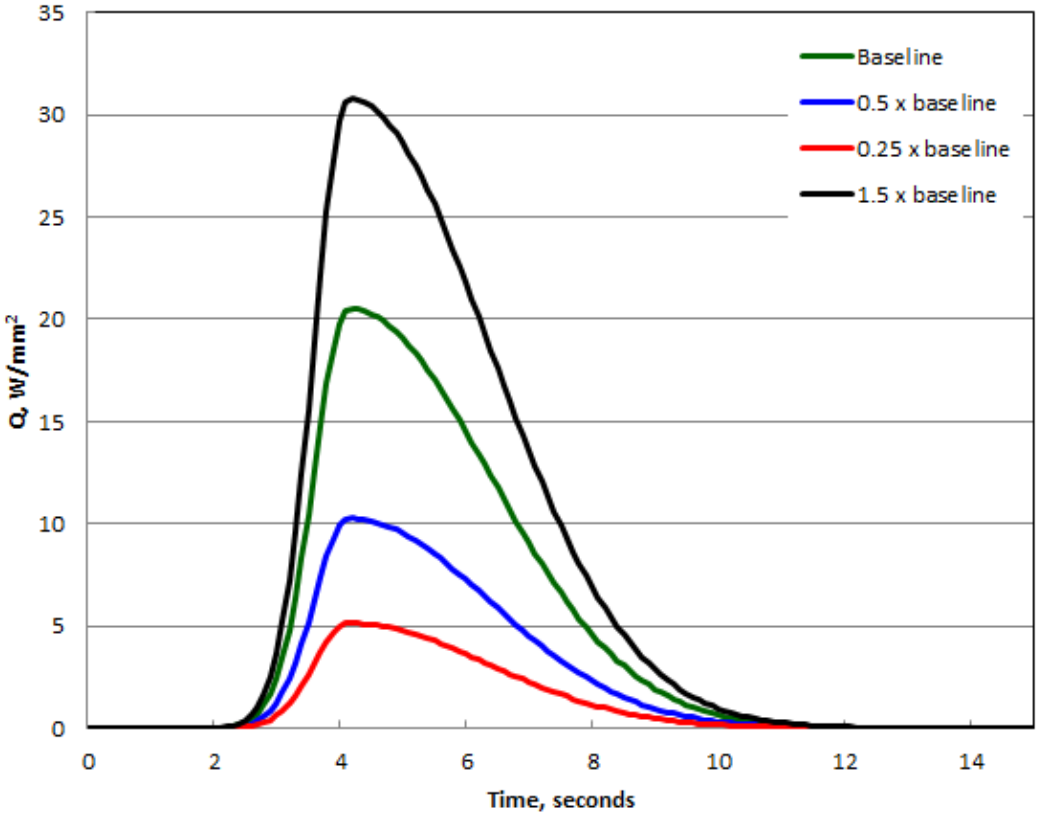

Figure 4-62 Heat flux vs. Time for Magnitude Sensitivity Study

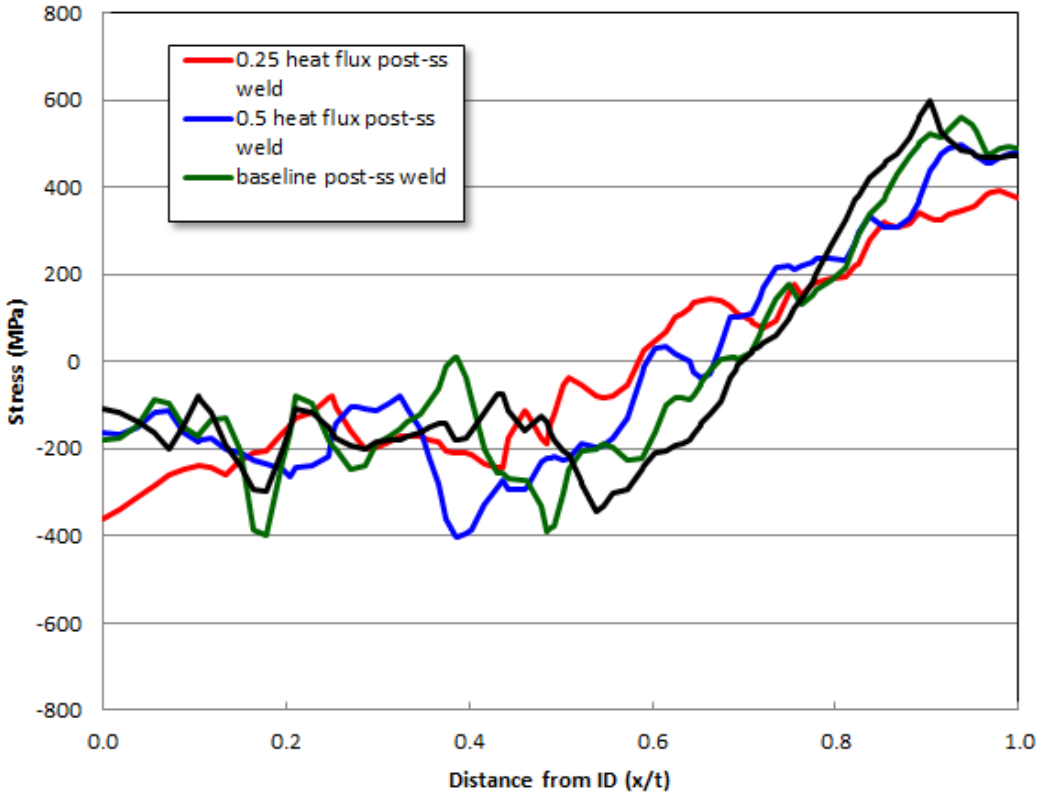

Figure 4-63 Axial Stress for Heat Flux Magnitude Sensitivity Study

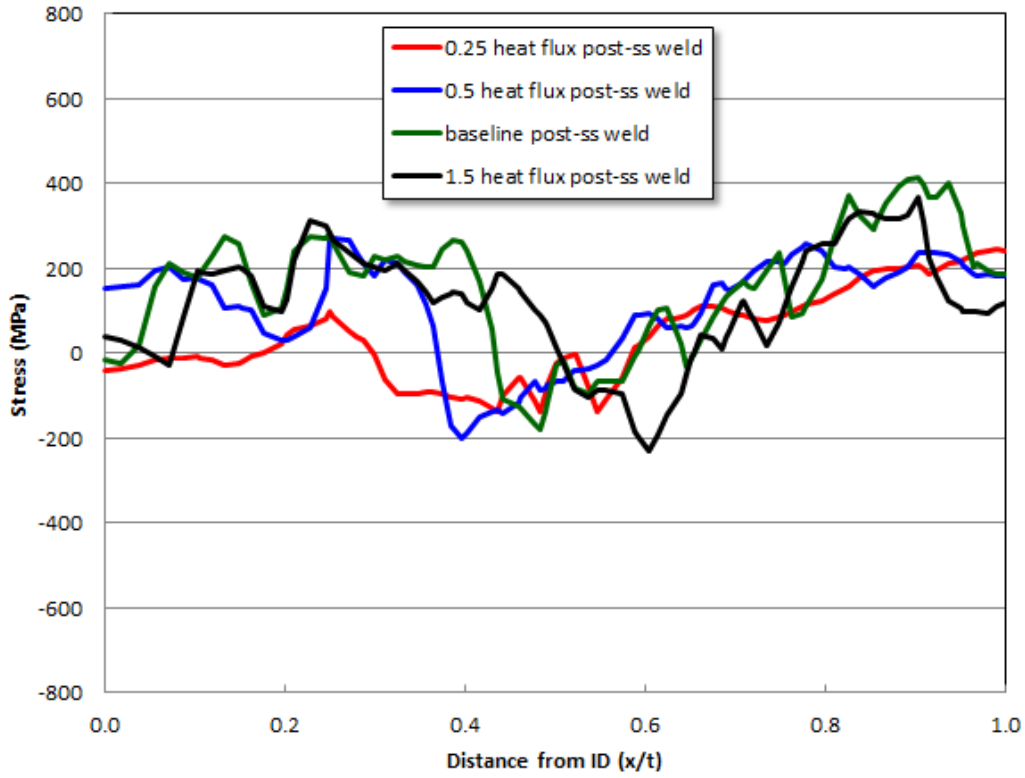

Figure 4-64 Hoop Stress for Heat Flux Magnitude Sensitivity Study

In the thermal heat flux model of Equation 2-3, $S(p)$ is the weld speed for a given pass. By varying the weld speed, the duration of time over which the heat flux is applied changes. However, the total energy applied, calculated as the integral of the heat flux with respect to time, remains the same. In the baseline analysis, the travel speed was approximately 2.54 mm/s, with minor variations for specific passes. To provide a wide range of heat flux durations in the sensitivity studies, the travel speeds of 0.75, 1.75, and 5.0 mm/sec were analyzed. Figure 4-65 shows the resulting heat flux magnitudes as a function of time, including the baseline case. Figure 4-66 and Figure 4-67 show the final through-wall centerline DM weld axial and hoop stress distributions, after application of the stainless steel weld, for the various heat flux duration inputs. Relatively minor variations in the stress predictions based upon varying travel speeds are observed in these results.

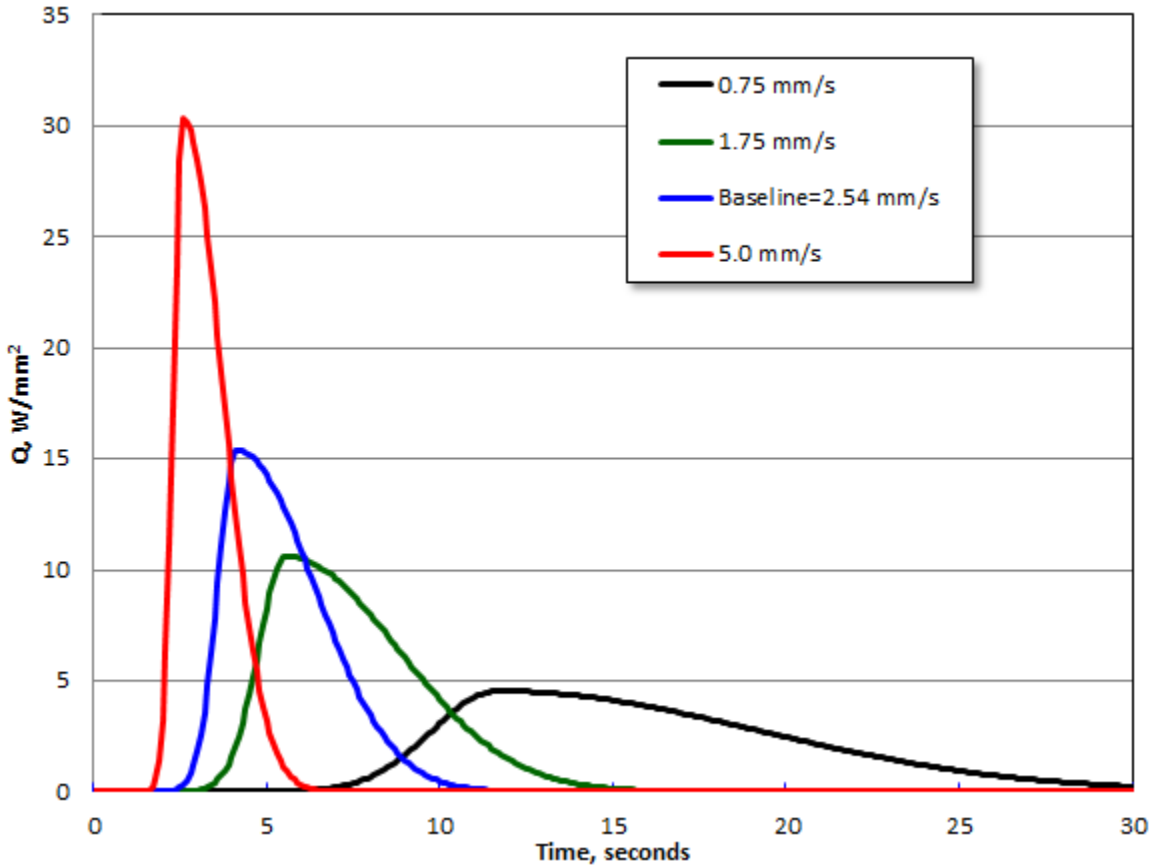

Figure 4-65 Heat Flux vs. Time for Duration Sensitivity Study

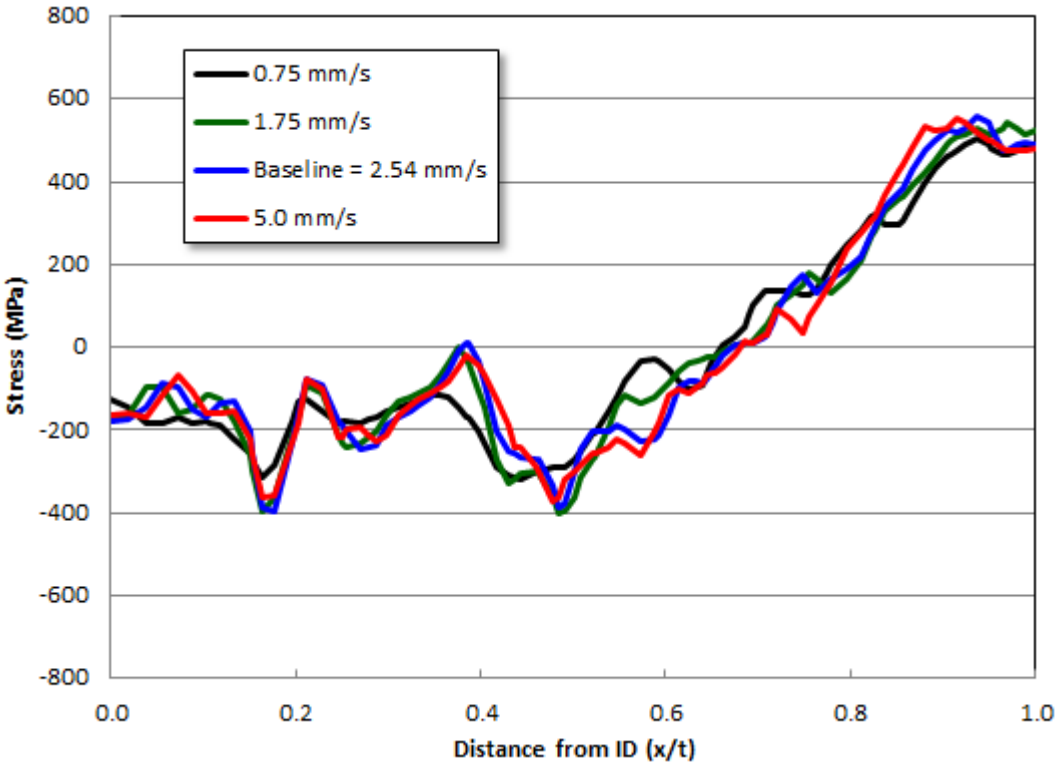

Figure 4-66 Axial Stress for Heat Flux Duration Sensitivity Study

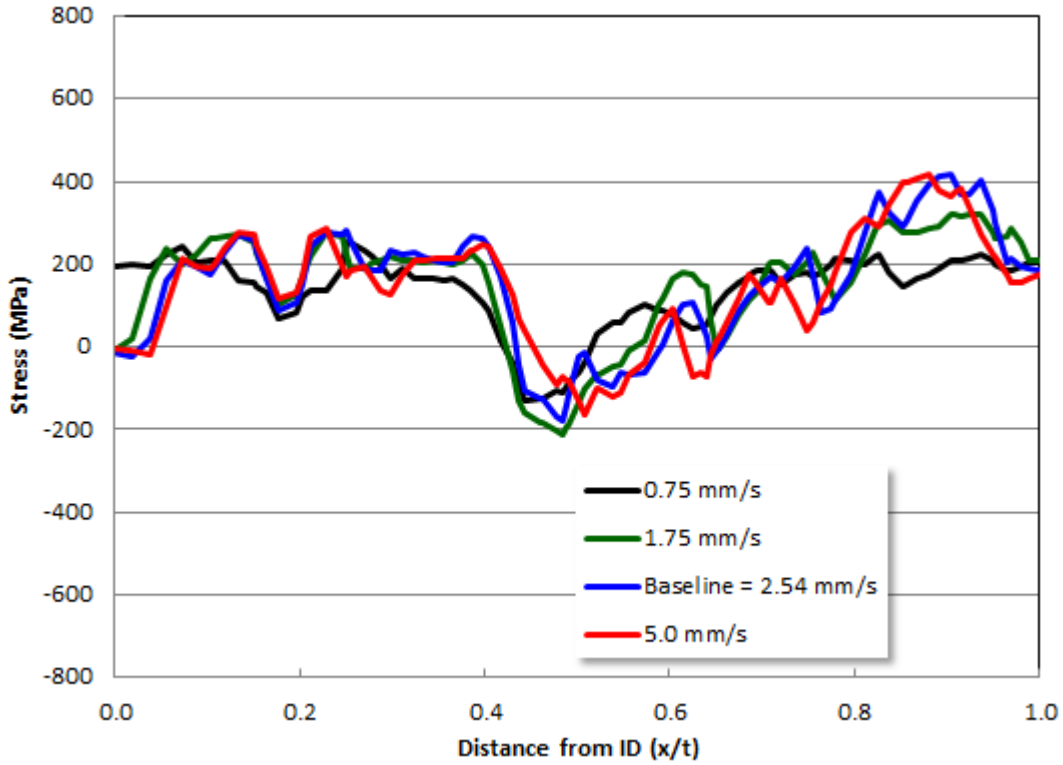

Figure 4-67 Hoop Stress for Heat Flux Duration Sensitivity Study

4.6.5. Plastic Stress-Strain Response Sensitivity Study

A sensitivity study was performed in which the plastic stress-strain response for the BE, Phase 2, and baseline properties were employed. Note that each of these material property sets correspond to the annealed condition. Figure 4-68 and Figure 4-69 provide the axial and hoop stress results for these material properties. The models showed significant differences at the normalized through-wall distance of approximately 0.15. Other than the difference at x/t = 0.15, the remainder of the stress distributions are fairly consistent, with a moderate variation.

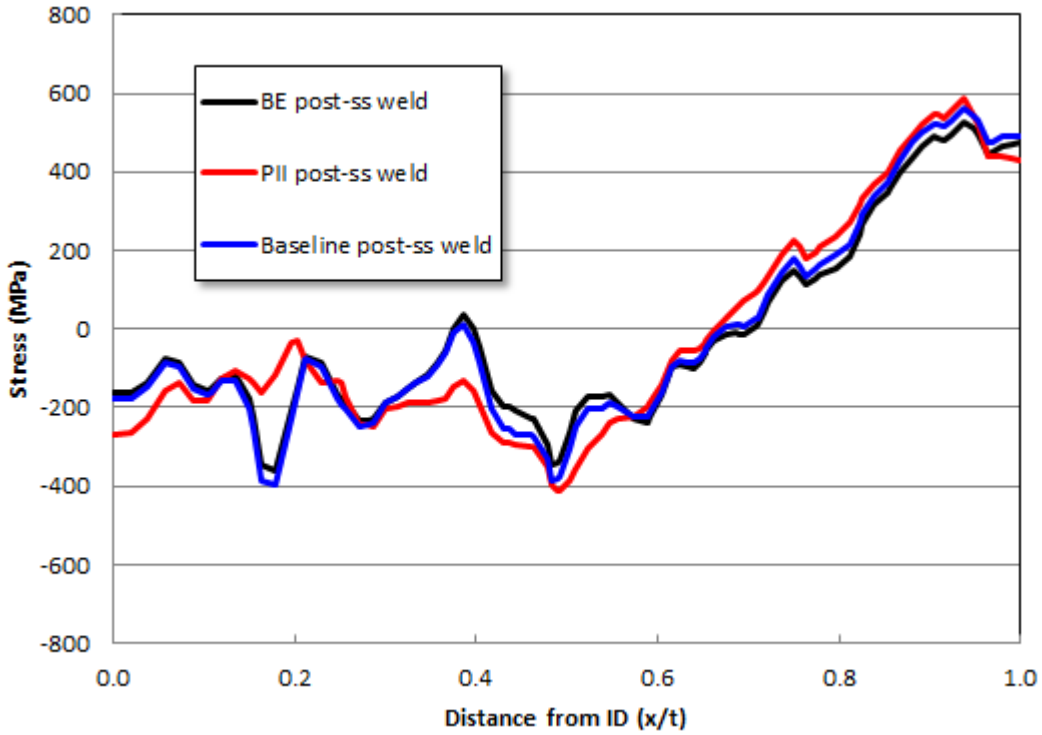

Figure 4-68 Axial Stress for Plastic Stress-Strain Response Sensitivity Study

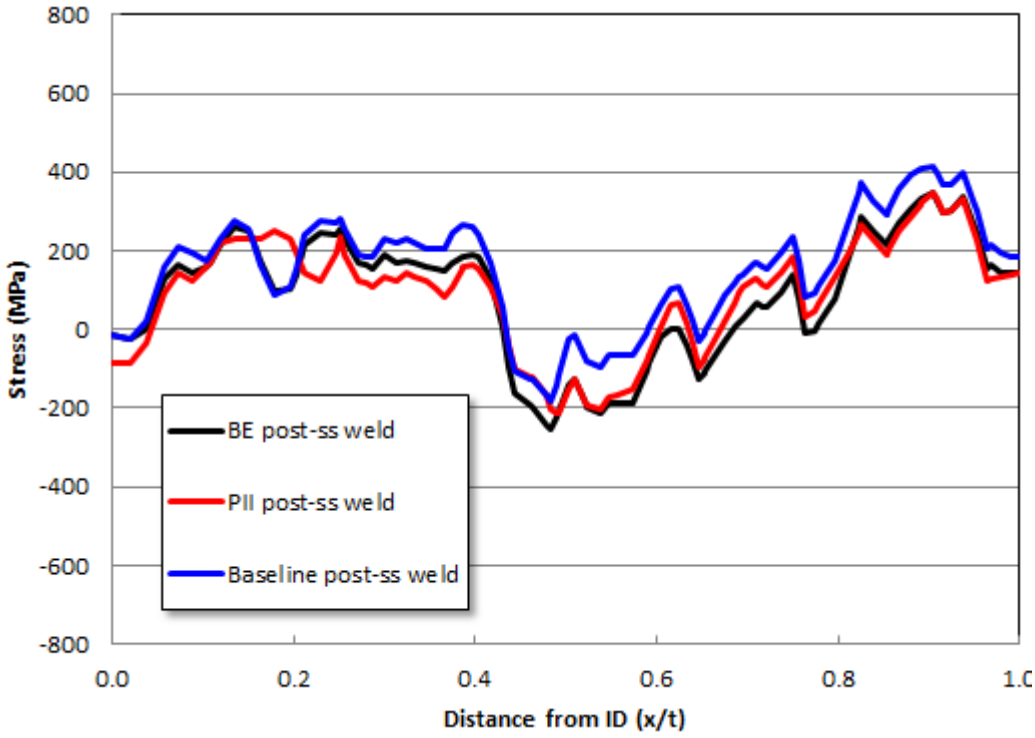

Figure 4-69 Hoop Stress for Plastic Stress-Strain Response Sensitivity Study

4.6.6. Strain Hardening Law

A sensitivity study was performed in which the baseline material properties were used with linear kinematic and isotropic hardening laws. Note that only linear kinematic was studied; multi-linear kinematic and mixed isotropic/kinematic were not considered here. Figure 4-70 and Figure 4-71 respectively provide the axial and hoop stress results for the hardening law sensitivity studies. Clearly, changing the hardening assumption from isotropic to linear kinematic resulted in a large variation in stress distribution.

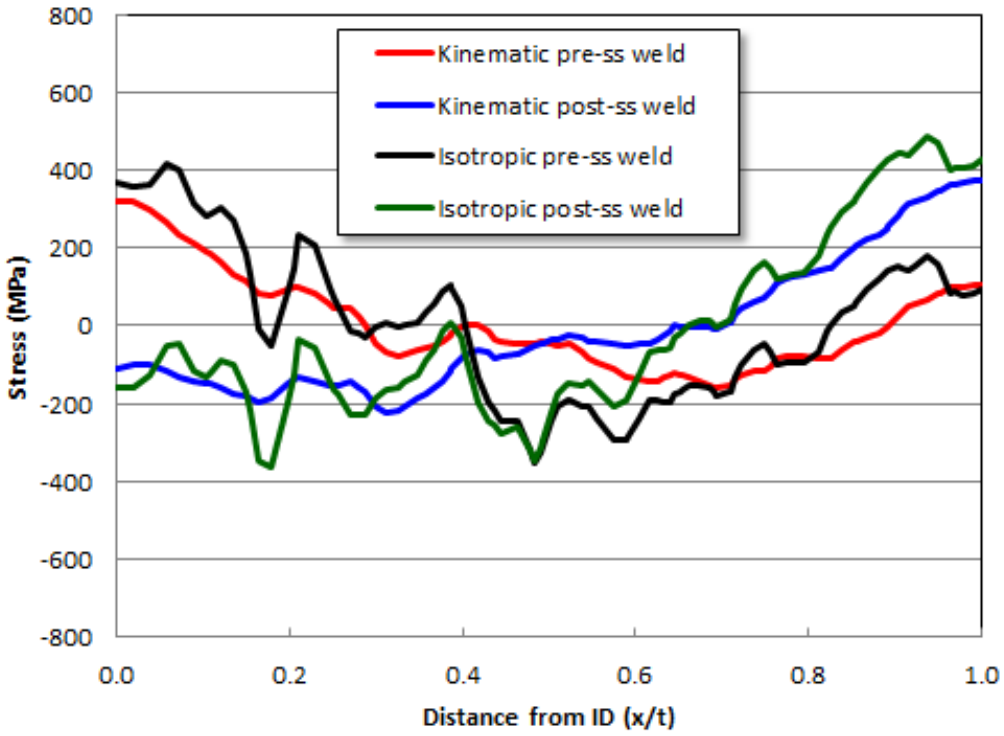

Figure 4-70 Axial Stress for Hardening Law Sensitivity Study

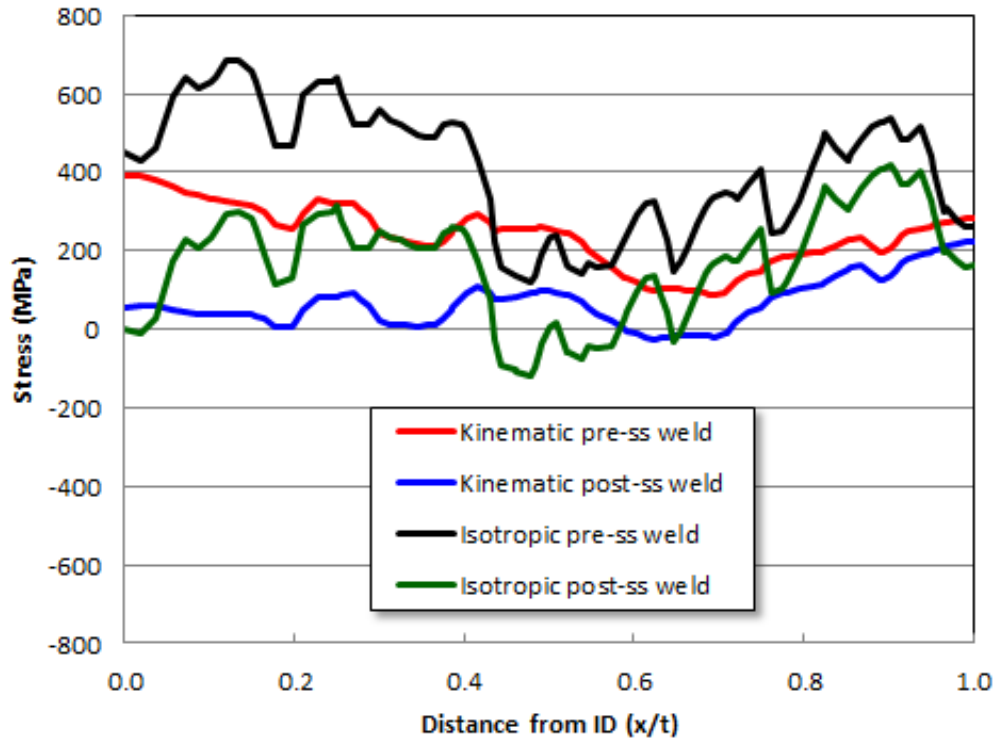

Figure 4-71 Hoop Stress for Hardening Law Sensitivity Study

4.6.7. Anneal Temperature

A sensitivity study was performed in which the anneal temperature for the Alloy 82/182 main DM weld was varied. For the baseline case, the anneal temperature was 1574 K, and for the sensitivity study, this temperature was varied to 1625 K and 1675 K. Figure 4-72 and Figure 4-73 provide the results for this sensitivity study. Little difference resulted from varying the anneal temperature.

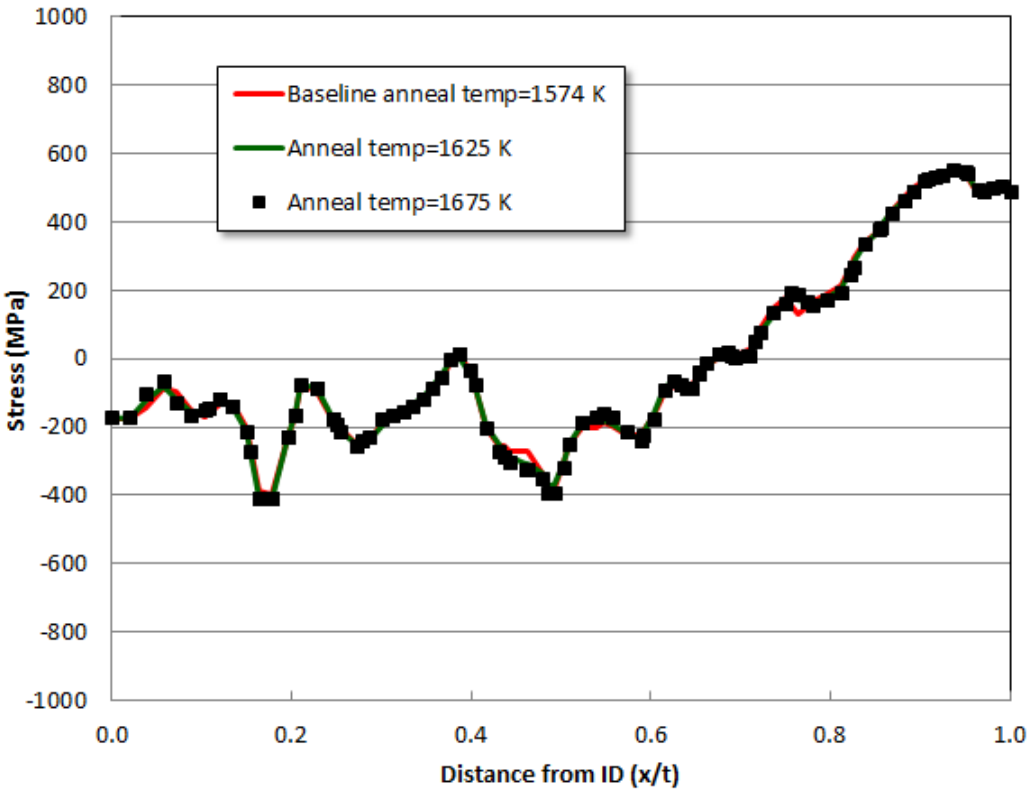

Figure 4-72 Axial Stress for Annealing Temperature Sensitivity Study

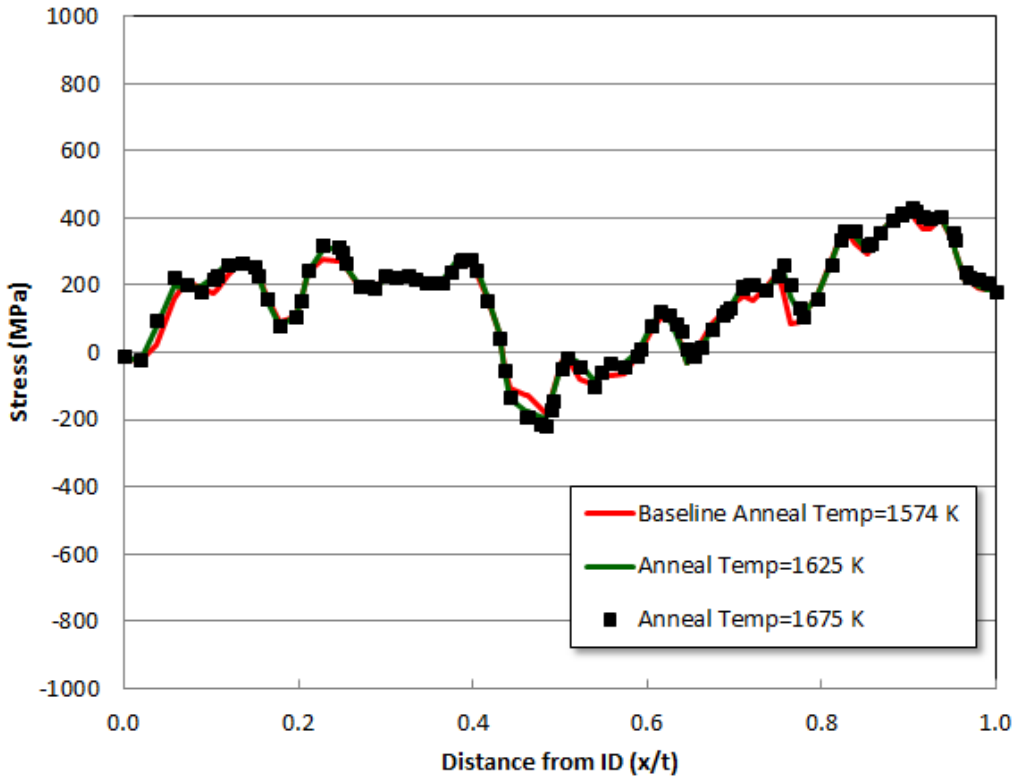

Figure 4-73 Hoop Stress results for Annealing Temperature Sensitivity Study

4.6.8. Weld Pass Sequence

A sensitivity study was performed in which the order of deposition for the top two layers of the baseline model was reversed. Figure 4-74 and Figure 4-75 show the axial and hoop stress results, respectively, for this sensitivity study. The stress distributions were almost identical, except near the top of the main DM weld where the order of deposition was reversed, implying that order of deposition can play a significant role in stress distributions.

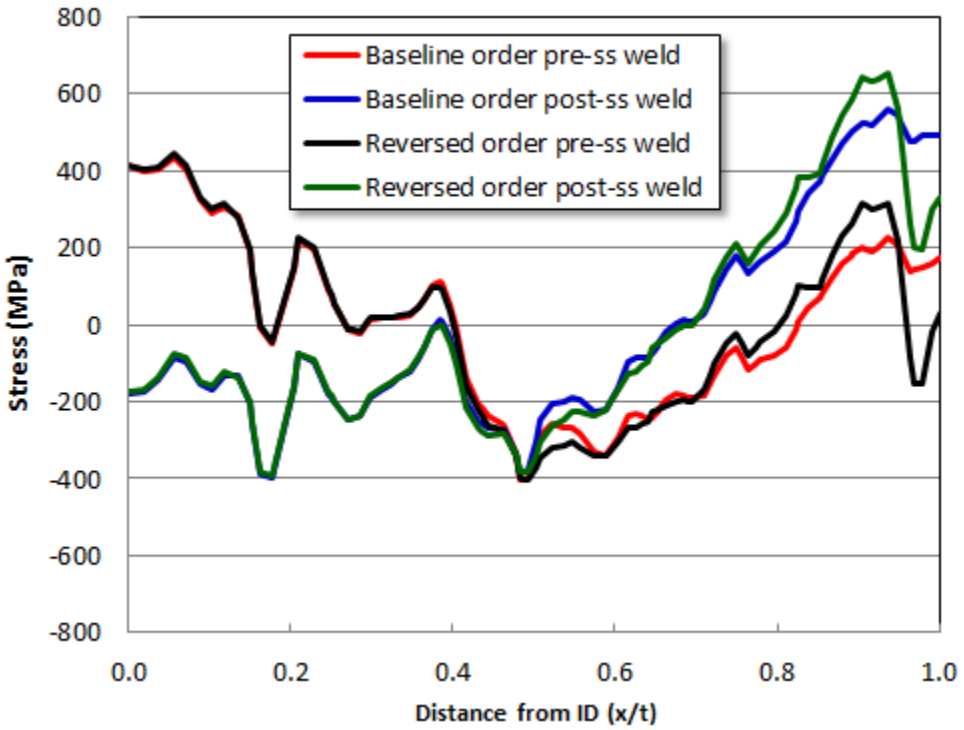

Figure 4-74 Axial Stress for Weld Pass Order Sensitivity Study

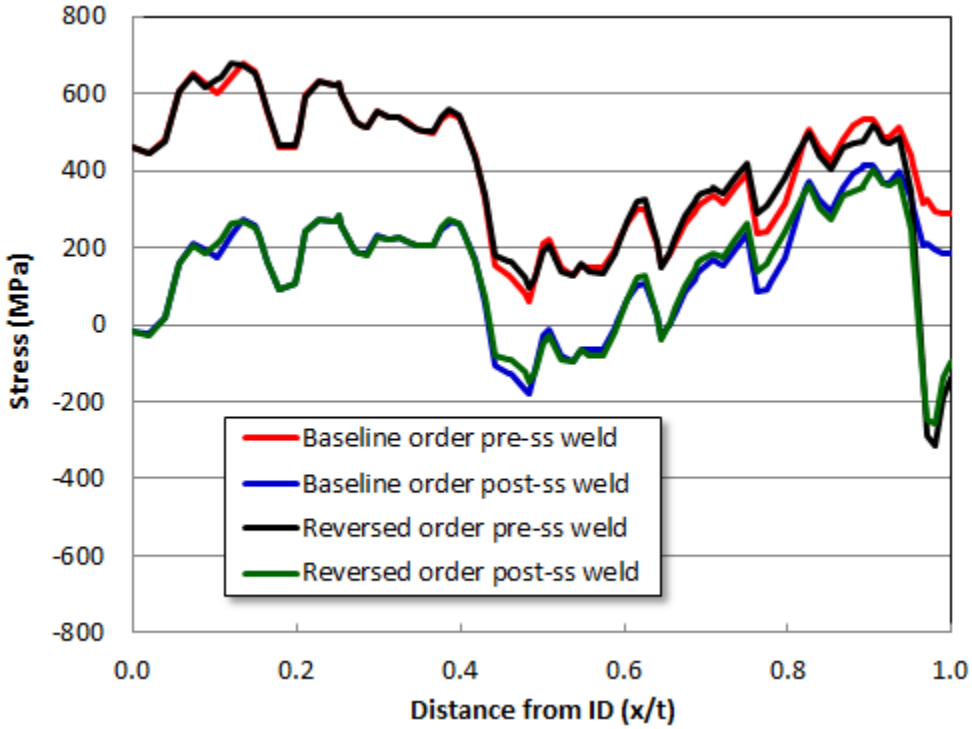

Figure 4-75 Hoop Stress for Weld Pass Order Sensitivity Study

4.7 Phase 2a Conclusions

Phase 2a of the NRC/EPRI WRS Validation Program consisted of measurements on a prototypic pressurizer surge nozzle mockup. A double-blind finite element round robin study was also completed, where measurement practitioners and modelers did not have access to each other's results. Conclusions from this work are as follows:

- Deep hole drilling and incremental deep hole drilling measurements of the prototype mockup provided the following insights.
  - Measurements at two locations along the circumference, but not at weld start/stop positions, showed similar magnitudes prior to the safe end to stainless steel pipe closure weld. After the stainless steel closure weld, axis symmetry was maintained.
  - The measurements showed that, for the particular geometry studied here, the safe end to stainless steel pipe weld had a beneficial effect on the stresses at the dissimilar metal weld location.
  - Contour measurements, obtained after the Phase 2a results had been made public, confirmed certain trends noted in the hole drilling data. The contour results showed lower stress magnitudes near the OD than the hole drilling results.
- The double-blind finite element round robin study, which was conducted to gain an unbiased view of WRS modeling uncertainty, showed that:
  - In some cases, the average of all modeling results compared well with the experimental results, both in magnitude and in trend. There were instances, however, where the measurements and models did not agree.
  - The FE models captured the beneficial effect of the safe end to stainless steel pipe weld, which was also observed in the experimental work.
  - Significant model-to-model variability exists.
  - Providing information on thermocouple measurements and material property data did not reduce the model-to-model variability.
- Model uncertainty was assessed in this study, as described below.
  - The aggregate modeling results deviated from the average by as much as ±200 MPa.
  - The position at which the individual stress profiles passed through 0 varied from model to model, contributing to the model uncertainty.
  - The choice of hardening law, while easily separable, contributed to the uncertainty observed in this study. Isotropic hardening tended to overpredict the measurements at the ID and OD, while underpredicting the measurements at the mid-thickness location. The kinematic hardening models showed the exact opposite trends.
- Sensitivity studies performed by a single analyst provided the following insights:
  - Coefficient of thermal expansion and annealing temperature were found not to have a significant impact on modeling results.
  - Total heat input and the duration over which heat is applied were found to affect final modeling results. However, the changes in these model inputs studied here were quite large compared to what may be expected to occur among experienced analysts. The observations from the round robin study and the sensitivity studies indicate that the model results are only weakly sensitive to heat input.

- Plastic stress-strain properties were found to affect modeling results at specific through-wall locations.
- The choice of hardening law was shown to affect WRS modeling results.
- Weld bead application sequence was found to affect calculated stress profiles, especially near the OD when the bead sequencing changed in the final layer at the OD.

5 PHASE 3: PRESSURIZER NOZZLES FROM A CANCELLED PLANT

5.1 Introduction

The Phase 3 effort consisted of measurement and modeling on safety/relief pressurizer nozzles from a cancelled plant. This phase of the research was intended to compare weld residual stress (WRS) models with experiments and to assess modeling uncertainty. The modeling effort in this phase of the work included double-blind finite element (FE) modeling, where measurement data was hidden from the analysts. The modeling effort for Phase 3 was not as extensive as Phase 2a. Discussion of the Phase 3 work can also be found in the Electric Power Research Institute's (EPRI's) Materials Reliability Program (MRP)-316 report [45].

5.2 Pressurizer Safety/Relief Nozzle Mockups

The Phase 3 mock-up components consisted of two safety/relief nozzles from the pressurizer of a canceled plant. Residual stress measurements were taken before and after the application of the stainless steel pipe weld. Two different nozzles were needed to accomplish this because of the destructive nature of the contour method (see Section 2.2.2). Figure 5-1 shows a schematic of the nozzle after the stainless steel (SS) weld was performed to join the nozzle to SS pipe. The dissimilar metal (DM) weld is indicated at the location of the Alloy 82 Butter and Weld material.

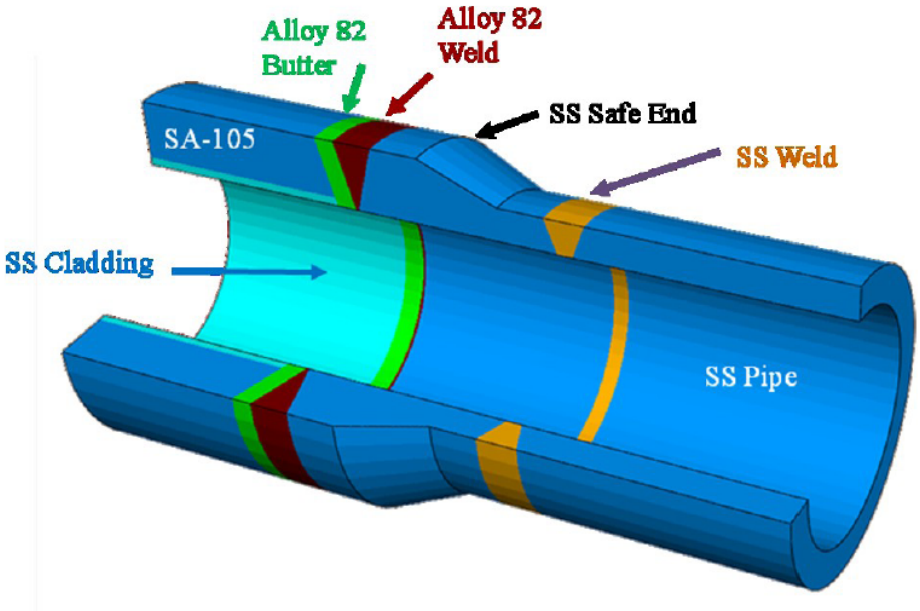

Figure 5-1 Schematic of the Safety and Relief Nozzle

Figure 5-2 shows one of the actual nozzles and finite element representations of it in the state both before and after the SS pipe weld. The nozzle without the SS pipe will be called Nozzle #2, and the nozzle with the SS pipe weld will be called Nozzle #3 throughout this Chapter. The two nozzles used for measurements were slightly different leading to variation in the measurements between the two nozzles. Each nozzle had its DM weld completed and was

prepared for the subsequent SS weld to pipe section before it was removed from the canceled plant.

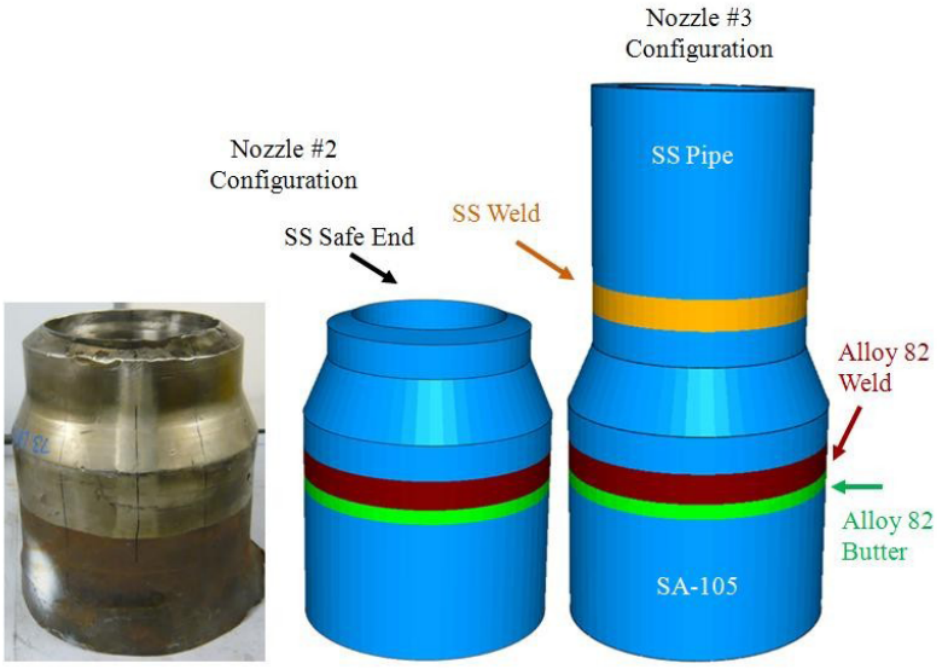

Figure 5-2 Actual Nozzle and FE Model before and after Pipe Weld

Nozzle #2 was 375 mm long with a 203 mm outer diameter (OD) and a 133-mm inner diameter (ID) at the DM weld location. Nozzle #3 was 711 mm long with a 201 mm OD and an ID of 113 mm at the SS pipe location.

5.3 Weld Residual Stress Measurements

Various WRS measurement techniques were discussed in Section 2.2. Two techniques were used by two independent providers in Phase 3. Deep hole drilling (DHD) and its variant, incremental deep hole drilling (iDHD), were performed on the nozzle mock-ups. The contour method was also used on the nozzle mock-ups. Both methods were used to find stresses in several locations in the mock-ups, but the measurements discussed here will be restricted to those measurements made along the through-thickness centerline of the DM weld areas of the mock-ups with no repair welds. Nozzle #2 was used in the pre-SS pipe weld state, and Nozzle #3 was used only in the post-SS pipe weld state. Obviously, variations in the welding of the two different DM welds were introduced by this necessity and must be considered. The DHD/iDHD measurements were taken before the nozzles were sectioned for the contour method.

The DHD/iDHD measurements to be shown here were taken from drilled holes in the centerline of the DM weld producing both axial and hoop stress measurements for each hole drilled. The contour method produced an entire plane to measure with each cut. The nozzles were cut axially into arcs, producing two surfaces on which to measure hoop stresses through the DM weld thickness. Once these measurements were complete, the removed arc was then cut again on the transverse plane revealing an axial stress surface to measure. This surface passed through the center of the DM weld. The contour measurement report thus provided two hoop stress measurements for each nozzle, and a plane of axial stresses which was used to produce four separate through-thickness axial measurements at different circumferential positions on the

plane (see Figure 4-13 as an example). The multiple hoop and axial stress contour measurements were each averaged to simplify the presentation here.

5.4 Finite Element Models

Details of FE modeling of weld residual stress were discussed in Section 2.3. Four different analysts created FE models using geometry measurements reported and by scaling dimensions from micrographs taken at the planes where the contour method cuts were made. Each model was slightly different due to the differences in the nozzles themselves and the differences in the scaled dimensions used. Results are reported as through-thickness stresses with the distance through the thickness normalized to take out the variation in wall thickness in the models and the actual nozzles.

Other variations in the models were typical of those that would occur in industry when various modelers make FE predictions of the same geometry. The meshes were different. The butter and DM weld beads were visible in the micrographs provided and each modeler made assumptions as to the welding bead shape to use in their FE model. Two different software packages were used (ANSYS and ABAQUS). The nozzle component materials were known, but modelers used their own library of material properties representing behavior over the range of the welding process temperatures. Also, different hardening laws were used for the materials making a total of nine through-thickness stress predictions using isotropic hardening, kinematic hardening, or mixed hardening material behavior. In all cases, thermal models were calibrated against the provided weld micrographs, but the number and specific geometry of the weld passes modeled varied from analyst to analyst.

5.5 Results and Discussion

Figure 5-3 and Figure 5-4 show the results of the nine FE predictions for axial and hoop stress, respectively, through the thickness of the centerline of the DM weld. These results will later be compared to the measurements at the same location. The results were for the case after the SS pipe weld was performed (Nozzle #3 configuration). Each of the modelers found that, for this geometry, there was almost no difference at the DM weld mid-thickness stress before and after the SS weld was performed. However, stresses were different at other axial locations due to the application of the SS weld. This fact was attributed to the reduction in diameter and wall thickness at the SS pipe and the distance of the SS weld from the DM weld (126 mm). The SS weld provided some reduction in the DM weld stresses in more uniform geometries as shown in Chapter 4 and other studies [58]-[61].

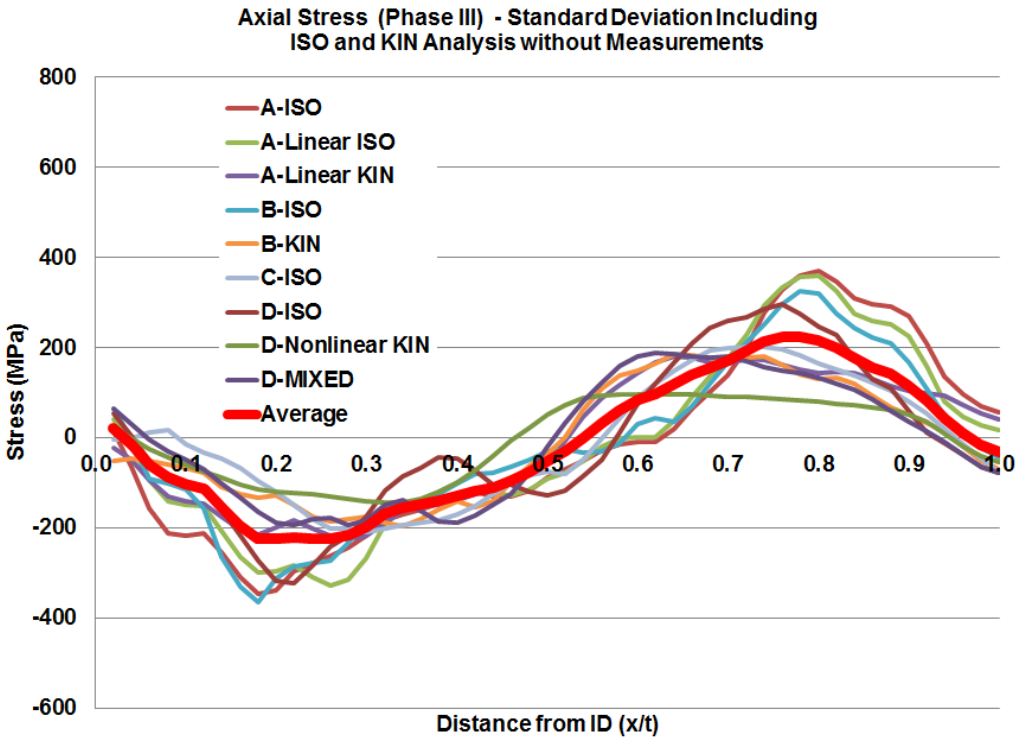

Figure 5-3 Axial Stress FE Predictions

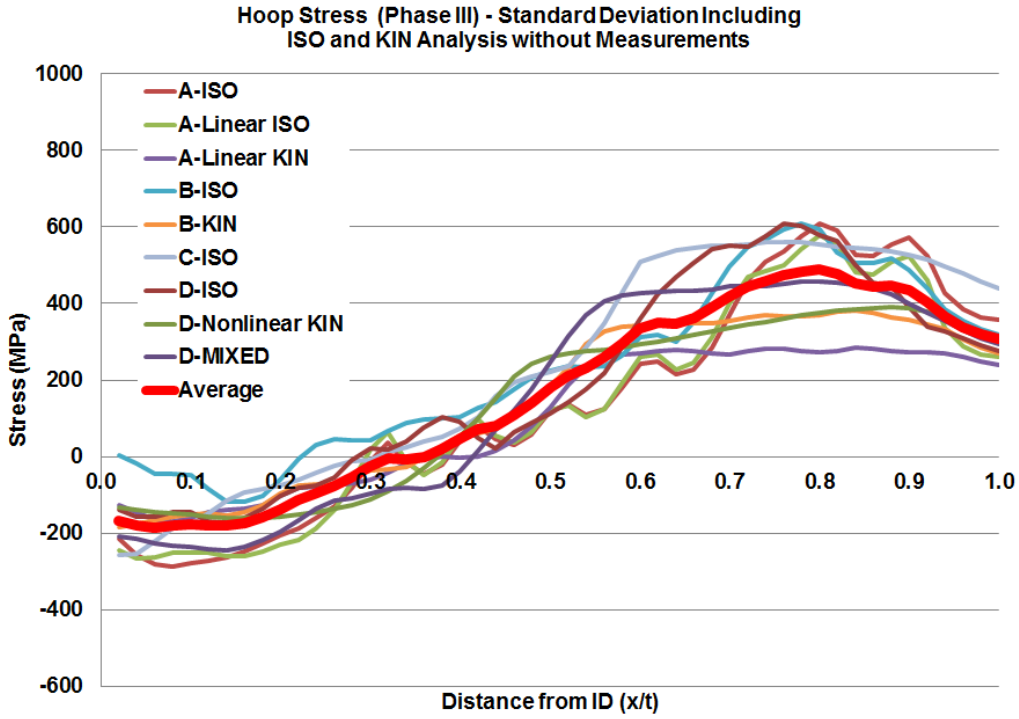

Figure 5-4 Hoop Stress FE Predictions

Each modeler and each measurement technique reported a different number of data points through the thickness of the nozzle. The data provided from all models and measurements were linearly interpolated between provided data points to create 50 even steps through the thickness so that tabulated results could be compared directly. Averages were calculated at each step through the thickness.

Several observations can be made from these prediction comparisons. All of the results show similar trends. The average curve shows the ID axial stress is near neutral and then dips into the compressive region until it becomes tensile at 50 percent through the thickness and finally becomes neutral again at the OD. The hoop stress average curve shows the stresses to be compressive at the ID and tensile at the OD with the curves crossing into tension somewhat before 50 percent through the thickness from the ID.

The hardening law used for each prediction is indicated in the legend text as ISO, KIN, and Mixed. The annealed mid-range yield strength for the Alloy 82 DM weld was 265 MPa (38.4 ksi). The differences come about because of the strain cycles created in the welding process. The models following the isotropic hardening law allowed the material to strain harden to progressively higher yield strength upon cyclic loading and this produced higher stresses than did the kinematic hardening law. The results produced with kinematic hardening did not exceed the stress equivalent to the annealed yield strength of the material by nearly as much as the results from the models using the isotropic hardening law. The effect was most noticeable in the axial stress graph where the isotropic models produced high compression stresses at 20 percent through the thickness and high tension stresses at 80 percent through the thickness, while the kinematic models produced more damped stress swings.

Figure 5-5 and Figure 5-6, respectively, show the axial and hoop stress comparisons between the FE predictions and the measurements produced by the two different methods. The FE predictions were all performed on the same models representing both the Nozzle #2 and Nozzle #3 configuration, and as mentioned previously, the through-thickness stresses in the DM weld were found to be almost identical for the cases before and after application of the stainless steel pipe weld. Only the Nozzle #3 configuration FE predictions are shown here because there is little or no difference from the Nozzle #2 results. The FE predictions are plotted as thin lines as in the previous figures. Both Nozzle #2 and #3 measurement results are included in the comparisons to allow an examination of the measured differences found in the cases before and after the SS pipe weld was completed. The contour method measurements are indicated by thick orange and green lines while the DHD/iDHD measurements are indicated by orange and green dots. The green colored measurements are for the Nozzle #2 (pre SS-Weld) configuration and the orange colored measurements are for the Nozzle #3 (post SS-Weld) configuration.

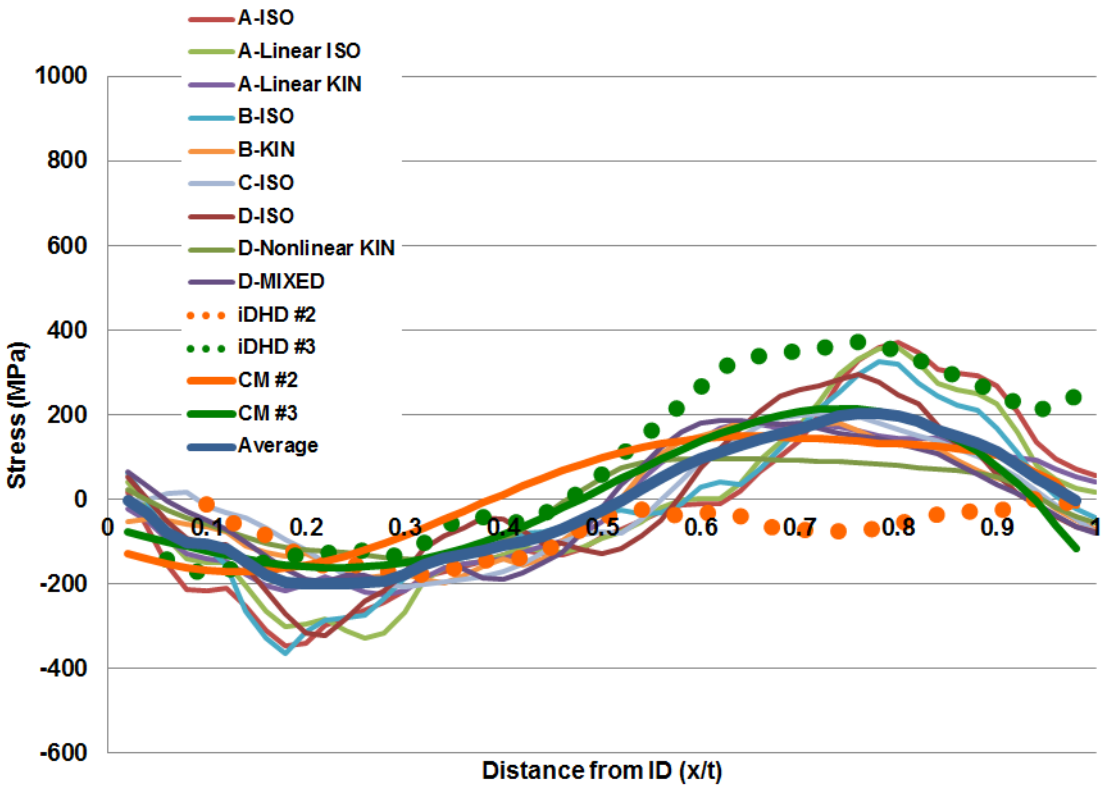

Figure 5-5 Axial Stress FE Predictions and Measurements

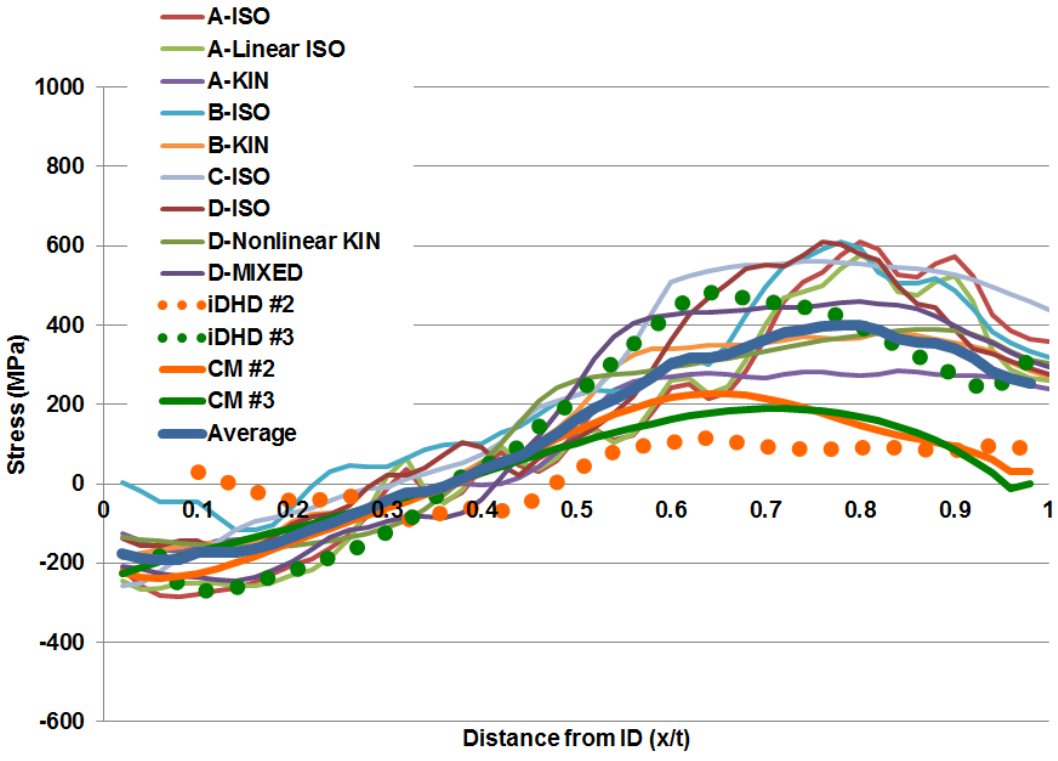

Figure 5-6 Hoop Stress FE Predictions and Measurement

Overall the FE predictions, contour method measurements, and Nozzle #3 DHD/iDHD measurements show similar trends. The DHD/iDHD measurements show a large difference in measured stress magnitude between the Nozzle #2 and #3 results that is not present in either the FE predictions or the contour method measurements. The hole drilling measurements may be showing some effect from the SS weld, as the trend is consistent with what may be expected (i.e., an increase at the OD and decrease at the ID after SS weld application). However, some of the variation in stress may be attributed to geometry differences in Nozzle #1 and Nozzle #2. The models and contour measurements did not register an effect of the SS weld.

As with the FE predictions, the measurements showed that the average ID axial stress was near neutral and dipping into the compressive region until it became tensile at or before 50 percent through the thickness. It became neutral again at the OD after rising to a peak at about 75 percent of the way through the thickness. The hoop stress graph shows the average of the stresses were compressive at the ID and neutral to tensile at the OD, with the curves crossing into tension before 50 percent through the thickness.

The four FE prediction curves from the models using isotropic hardening were distinguishable from those using kinematic hardening. The effect was most noticeable in the axial stress graph (Figure 5-5), where the isotropic models produced high axial compression stresses at 20 percent through the thickness, and high axial tension stresses at 80 percent through the thickness. The increase in tension stress toward the OD seems to match what was indicated by the DHD/iDHD measurements for Nozzle #3. The iDHD technique was applied in this area of residual stress at or above the material's yield strength in order to minimize potential plasticity-induced measurement artifacts. FE predictions with kinematic hardening fell almost exactly on both contour measurement curves along the entire data range, for axial stresses. It should be noted that both DHD/iDHD and contour techniques were potentially susceptible to plasticity measurement artifacts at or near yield, making further comment on the accuracy of the measured residual stress profiles difficult.

5.6 Phase 3 Conclusions

Phase 3 of the WRS Validation Program consisted of measurement and modeling of WRS in components intended for nuclear power service. These components were of differing geometry than the mockup studied in the Phase 2a work (see Chapter 4), so differences in stress trends were expected. The following conclusions can be supported by this work.

- The modeling results in this work provided the following insights.
  - Modeled stress trends were generally different in Phase 3, when compared to Phase 2a. The stresses started near-neutral at the ID and became tensile at the OD. Phase 2a results indicated tensile stress at the ID with stress fluctuating from tensile to compressive and back to tensile at the OD. These dissimilarities were due to the significant differences in weld and component geometry. For instance, a large ID weld deposit was present in the Phase 2a mockup, whereas the Phase 3 nozzles were single-V groove welds more commonly found in plants.
  - Unlike the observations of Phase 2a, application of the safe end to stainless steel pipe weld did not have an appreciable effect on modeling results. This observation can be attributed to different safe end geometries in the two mockups.
  - Significant analyst-to-analyst scatter was observed in Phase 3.
  - The choice of hardening law had a significant effect on the modeling results. Specifically, isotropic hardening models tended to predict higher stress magnitudes, with larger stress fluctuations, than kinematic hardening cases.

- The measurement results in this work provided the following insights.
  - Hole drilling and contour measurements both confirmed the trend noted in the modeling: neutral stress at the ID and tensile stress at the OD. The two measurement techniques differed in the magnitude of the tensile stress at the OD, however.
  - While the contour method showed no difference in measured stress before and after the safe end to stainless steel pipe weld, the hole drilling measurements indicated some differences between the two cases. At the very least, the effect of the stainless steel weld was not as dramatic in the Phase 3 studies as was observed in the Phase 2a studies, as expected considering the differences in safe end geometry.

6 PHASE 4: OPTIMIZED WELD OVERLAY ON A COLD LEG NOZZLE

6.1 Introduction

The Phase 4 effort consisted of measurement and modeling on a cold leg nozzle from a cancelled plant. This phase of the weld residual stress (WRS) Validation Program investigated the effectiveness of the Optimized Weld Overlay (OWOL), which is one method proposed by the U.S. nuclear industry for primary water stress corrosion cracking (PWSCC) mitigation. A significant portion of the work presented in this chapter consists of one analyst's studies on the effectiveness of OWOL. Several additional analysts participated in a double-blind FE modeling study, where measurement data was hidden from them. The double-blind modeling effort for Phase 4 was not as extensive as Phase 2a.

6.2 Optimized Weld Overlay and Cold Leg Nozzle Mockup

6.2.1. Optimized Weld Overlay

With the occurrence of PWSCC in U.S. pressurized water reactors (PWRs) (see Chapter 1), the commercial nuclear power industry has proposed a number of mitigation strategies for dealing with the problem. One of those strategies is the application of weld overlays that were successfully used in the past in mitigating intergranular stress corrosion cracking (IGSCC) in the BWR fleet. Since WRS provides the significant driving force for crack growth, weld overlays mitigate PWSCC by reducing the tensile residual stresses on the inside wetted surface of the dissimilar metal nozzle/pipe weld. A previous study investigated analytically the effectiveness of weld overlays, both full structural weld overlays (FSWOL) and OWOLs, as a mitigation strategy for PWSCC [51].

The minimum acceptable FSWOL thickness is equal to one-third the original pipe wall thickness as specified in Materials Reliability Program (MRP)-169 [53] and ASME Code Case N-504-4 [54]. The minimum length of the overlay is $0.75\sqrt{(Rt)}$ on either side of the dissimilar metal (DM) weld to be treated, where R is the outer radius and t is the nominal thickness of the component. The total minimum length of the FSWOL is therefore $1.50\sqrt{(Rt)}$ plus the length of the DM weld to be treated.

The OWOL has been proposed for larger geometries (hot and cold leg nozzles) where FSWOL application becomes too time consuming for a typical nuclear plant refueling outage. The OWOL thickness is less than that of an FSWOL, leading to decreased application time. The required minimum axial length of the OWOL is defined in ASME Code Case N-754 [55] and is the same as that required for an FSWOL. The code case also says that the thickness must be sufficient to provide compressive residual stresses to preclude stress corrosion cracking growth. Industry has proposed that an OWOL design is sufficient if it reduces tensile stresses in the dissimilar metal weld area to less than 69 MPa (10 ksi) with operating temperature and loads applied. Each OWOL must be designed for a specific geometry and application and must be evaluated on a case-by-case basis to demonstrate that the overlay is sufficient to mitigate the possibility of PWSCC.

6.2.2. Cold Leg Nozzle Mockup

Figure 6-1 shows a revolved version of the axisymmetric cold leg nozzle FE model with and without OWOL. Figure 6-2 shows a photograph of the Phase 4 mockup after application of the OWOL. Figure 6-3 shows the details of the cold leg nozzle geometry and materials. The nozzle was A508 class 2 carbon steel. The cladding, pipe, and safe end were stainless steel. The butter and dissimilar metal weld were made from alloy 82/182, and the secondary stainless steel (SS) weld was made from Type 309 stainless steel filler metal. This model included a 25 percent of the wall thickness deep inner diameter (ID), circumferential weld repair in the DM weld. The results without the ID repair are included with the sensitivity study results and in measurements taken in the area outside the 30 degree partial arc repair region.

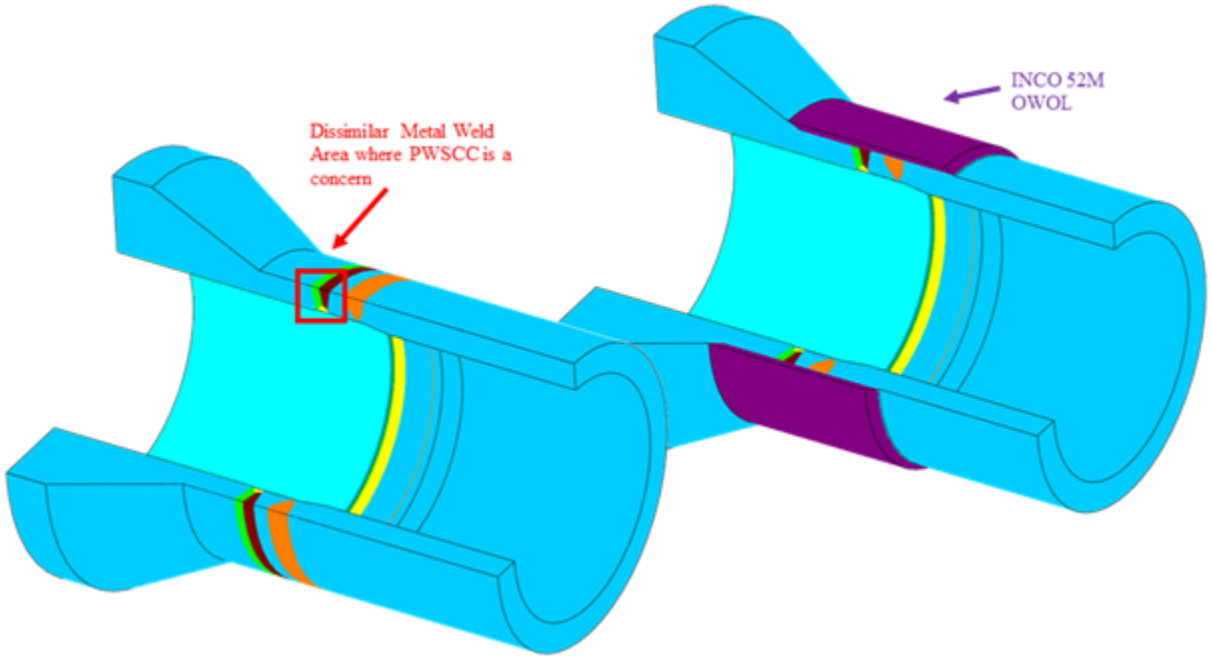

Figure 6-1 Phase 4 Model Geometry

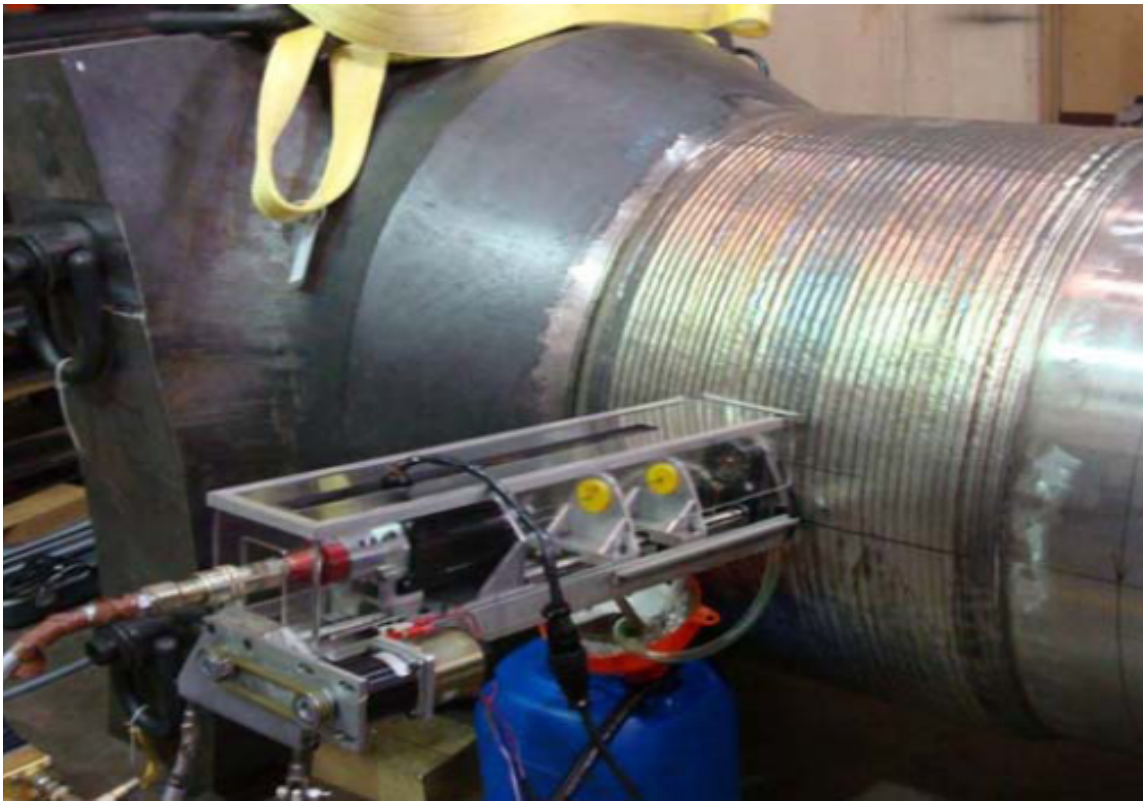

Figure 6-2 Cold Leg Nozzle Mock-Up after OWOL

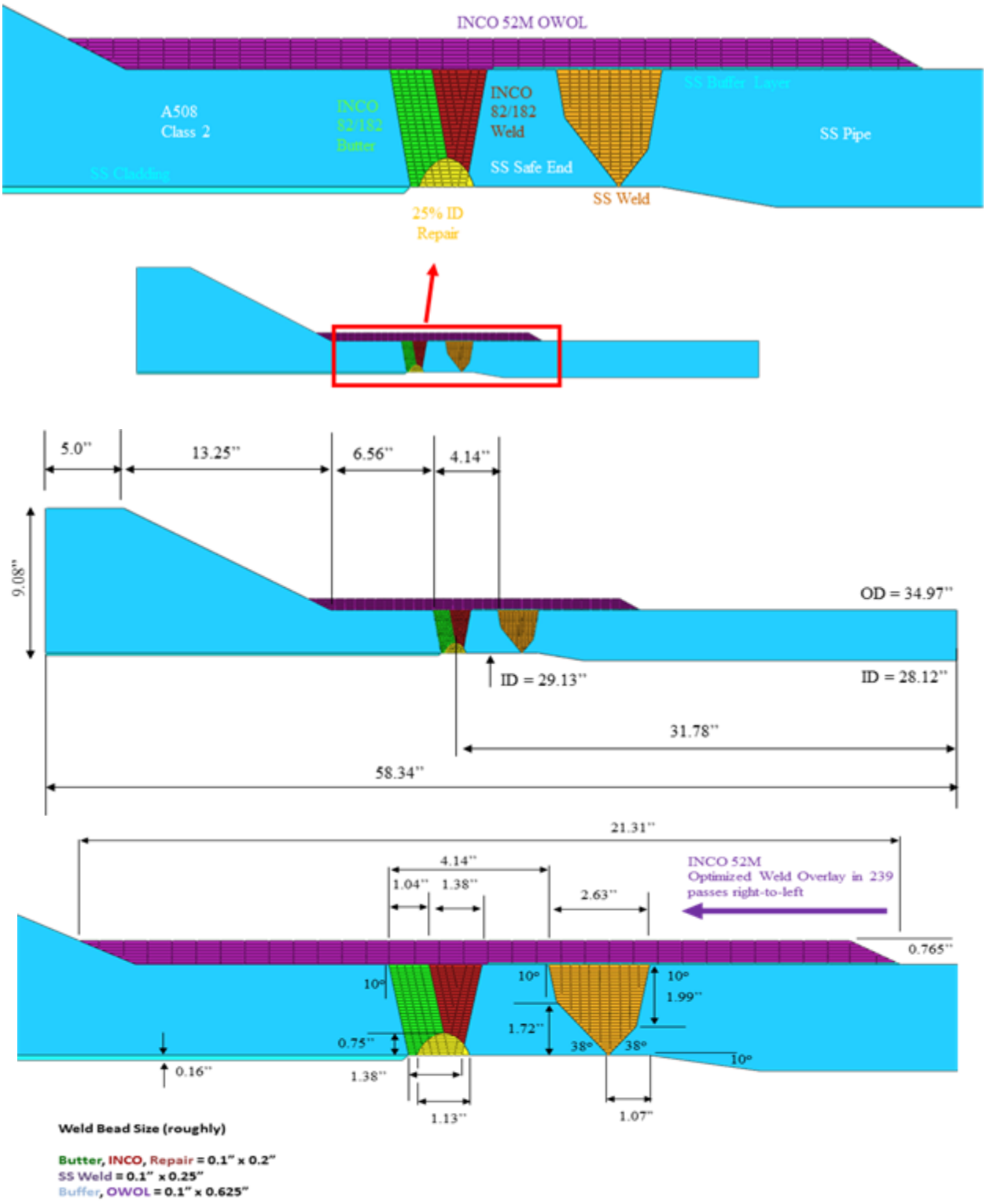

Figure 6-3 Cold Leg Nozzle Geometry and Material Details

Figure 6-3 also shows the dimensions of the cold leg nozzle model and mock-up. The pipe outer diameter (OD) was 889 mm (35 in.), and the pipe thickness was 87 mm (3.43 in.). The figure also shows the weld pass size that was used in the OWOL effectiveness studies. The butter, DM weld, and weld repair passes were roughly 2.5 mm by 5.0 mm (0.1 in. by 0.2 in.). The SS weld passes were roughly 2.5 mm by 6.3 mm (0.1 in. by 0.25 in.), and the buffer layer and OWOL weld passes were 2.5 mm by 16 mm (0.1 in. by 0.625 in.).

The minimum thickness of the FSWOL for the mock-up shown in Figure 6-3 was one-third the DM weld thickness of 74.2 mm (2.92 in.), or 24.6 mm (0.97 in.). The OWOL thickness used was 19.4 mm (0.765 in.), or approximately 25 percent of the DM weld thickness. The OWOL thickness was therefore approximately 75 percent of the minimum FSWOL thickness in this case. The total minimum length of the OWOL used for the cold leg nozzle geometry in this study was $1.50\sqrt{(Rt)}$ plus the length of the DM weld to be treated or $1.5\sqrt{(444 \text{ mm} \times 74.2 \text{ mm})} + 61.5 \text{ mm} = 356 \text{ mm}$ (14 in.), and the actual length used on the mock-up was 541.3 mm (21.31 in.) including the tapered ends. The length of the OWOL for the mockup is therefore 162% of the minimum FSWOL length.

The cold leg nozzle was similar to the Phase 2a surge nozzle (see Chapter 4) in materials and geometry. Both have a secondary SS weld in close proximity to the DM weld. The distance between centerlines of the DM weld and the SS closure weld was 95 mm (3.73 inches). A significant effect on the DM weld residual stresses would be expected from application of this weld.

6.3 Weld Residual Stress Measurements

Various WRS measurement techniques were discussed in Chapter 2. Two techniques were used by a single provider in the Phase 4 work: deep hole drilling (DHD) and its variant, incremental deep hole drilling (iDHD). To assess the effectiveness of the OWOL, the measurements were performed on the nozzle before and after application of the overlay.

6.4 Finite Element Models

Details of FE modeling of weld residual stress were discussed in Section 2.3. The modeling results presented in this study can be divided into two categories: (1) detailed analyses by one analyst on OWOL effectiveness and associated sensitivity studies and (2) double-blind analyses from different analysts (similar to, but not as extensive as, the round robin study presented in Chapter 4).

For the double-blind FE study, four different analysts created finite element models using geometric measurements reported for the mock-up features. Each model was slightly different because of the assumptions made about the weld pass layout and missing dimensions in the sketches provided. Results are reported as through-thickness stresses from the ID to the OD.

Other variations in the models were typical of those that would occur in industry when various modelers make FE predictions of the same geometry. The meshes were different. Each modeler made assumptions as to the welding bead shape to use in their FE model. Two different software packages were used (ANSYS and ABAQUS). The nozzle component materials were known, but modelers used their own library of material properties representing behavior over the range of the welding process temperatures. Also, different hardening laws

were used for the materials making a total of six through-thickness stress predictions using either isotropic hardening, kinematic hardening, or mixed hardening.

6.5 Optimized Weld Overlay Effectiveness

6.5.1. Axial Stresses, Room Temperature, Without Operating Loads

Figure 6-4 shows an example axial stress contour plot before the SS safe end weld but after all DM welding was complete, including the 25 percent ID repair (top figure), after the SS closure weld was finished (middle figure), and after the OWOL had been completed (bottom figure). The arrows through the thickness indicate the path along which the data in Figure 6-5 were extracted.

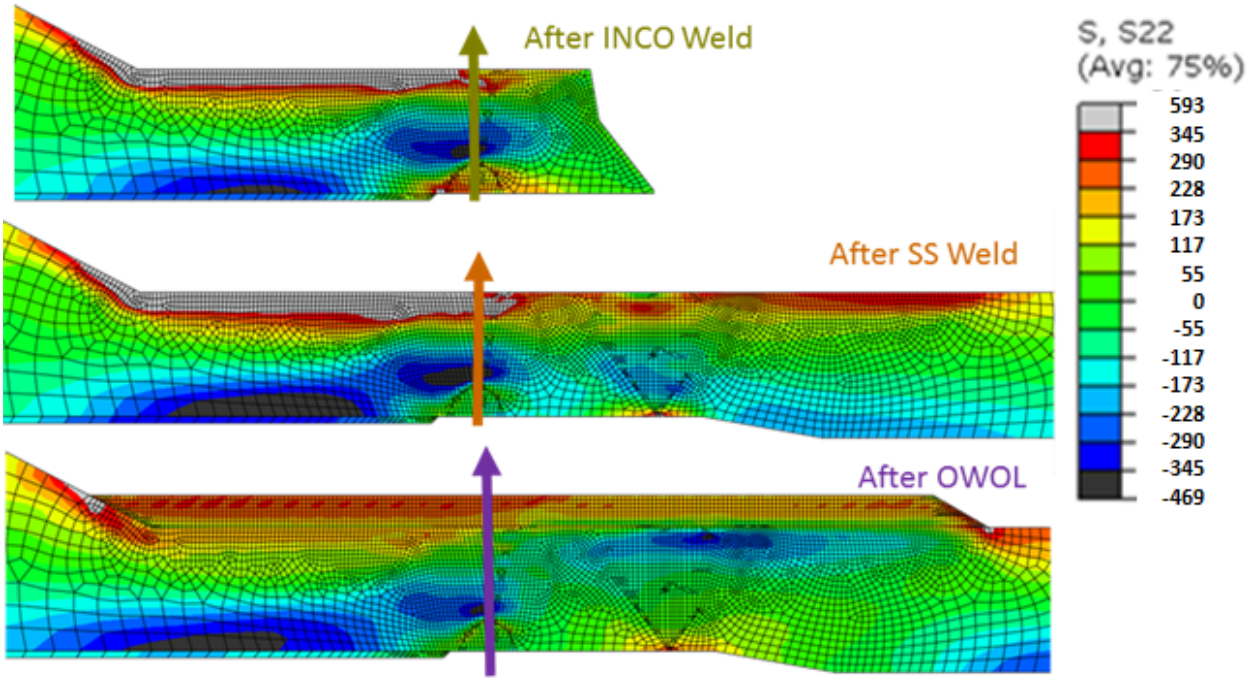

Figure 6-4 Cold Leg Nozzle Axial Stresses [MPa]

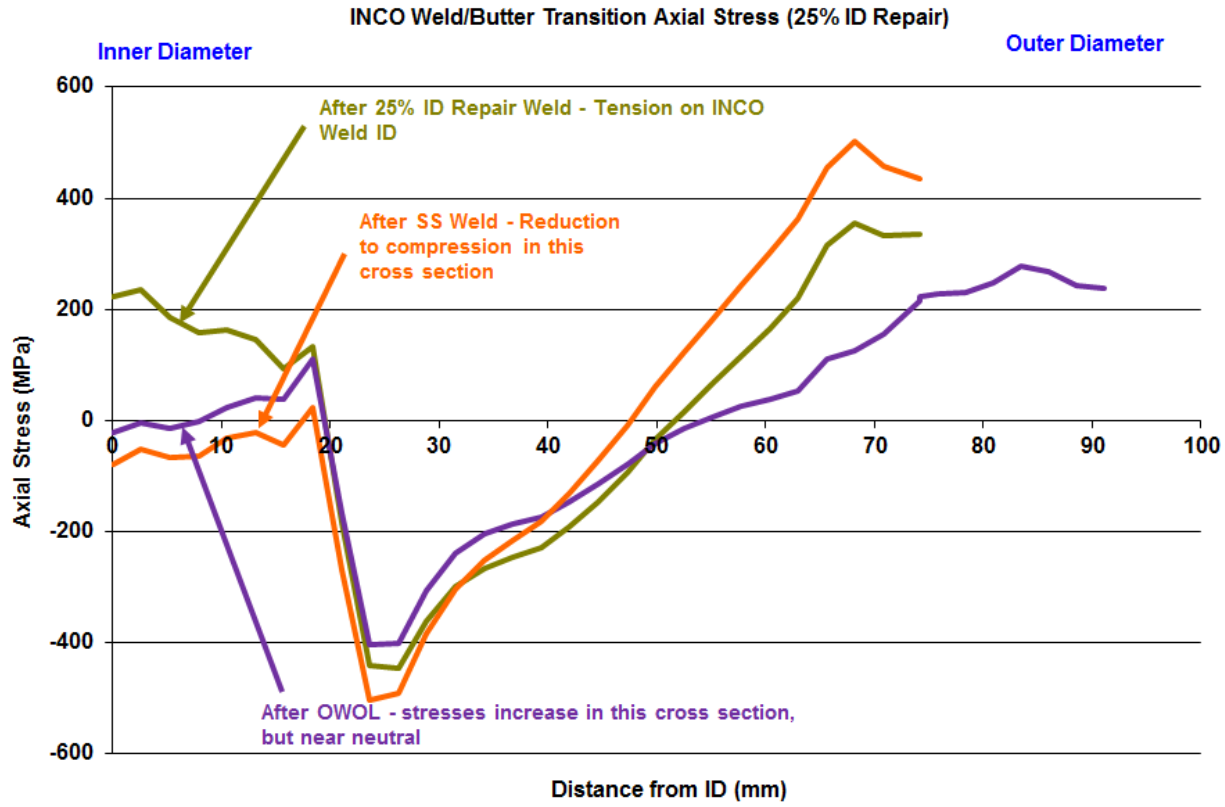

Figure 6-5 Cold Leg Nozzle Through-Thickness Axial Stresses

Figure 6-4 and Figure 6-5 show that the DM weld was in tension at the ID, compression in the center, and tension at the OD after it was completed. The application of the SS weld had the effect of lessening the tension stress on the ID of the DM weld, and in fact, making it compressive. In this cross-section, the axial stress was slightly increased after applying the OWOL, with the final ID stress near zero.

The stresses along the specified path drop to compressive values at 25 percent of the original pipe thickness, which corresponds to the depth of the weld repair. This is typical of results found with ID weld repairs. The tensile stresses caused by the weld repair pushed a zone of compressive stress just beyond the depth of the repair.

Figure 6-6 and Figure 6-7 show the ID path and axial stress along that path. Figure 6-7 indicates the position of both the DM weld and the secondary SS weld with color coded vertical bars on the graph.

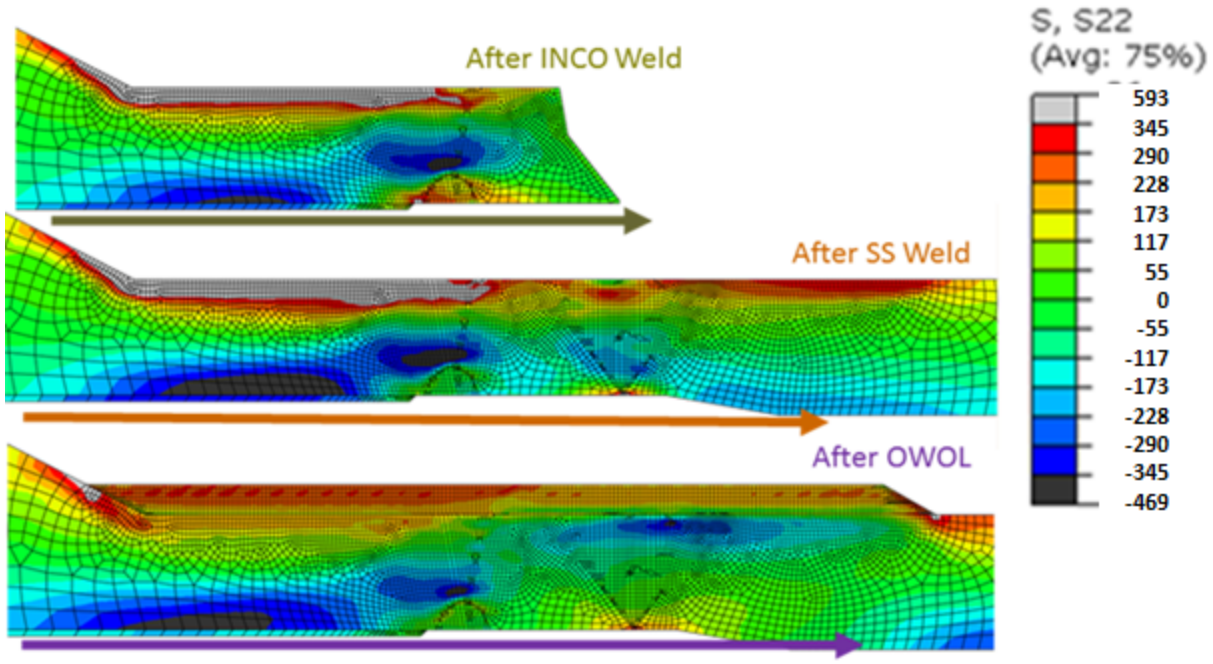

Figure 6-6 Cold Leg Nozzle Inner Diameter Axial Stresses [MPa]

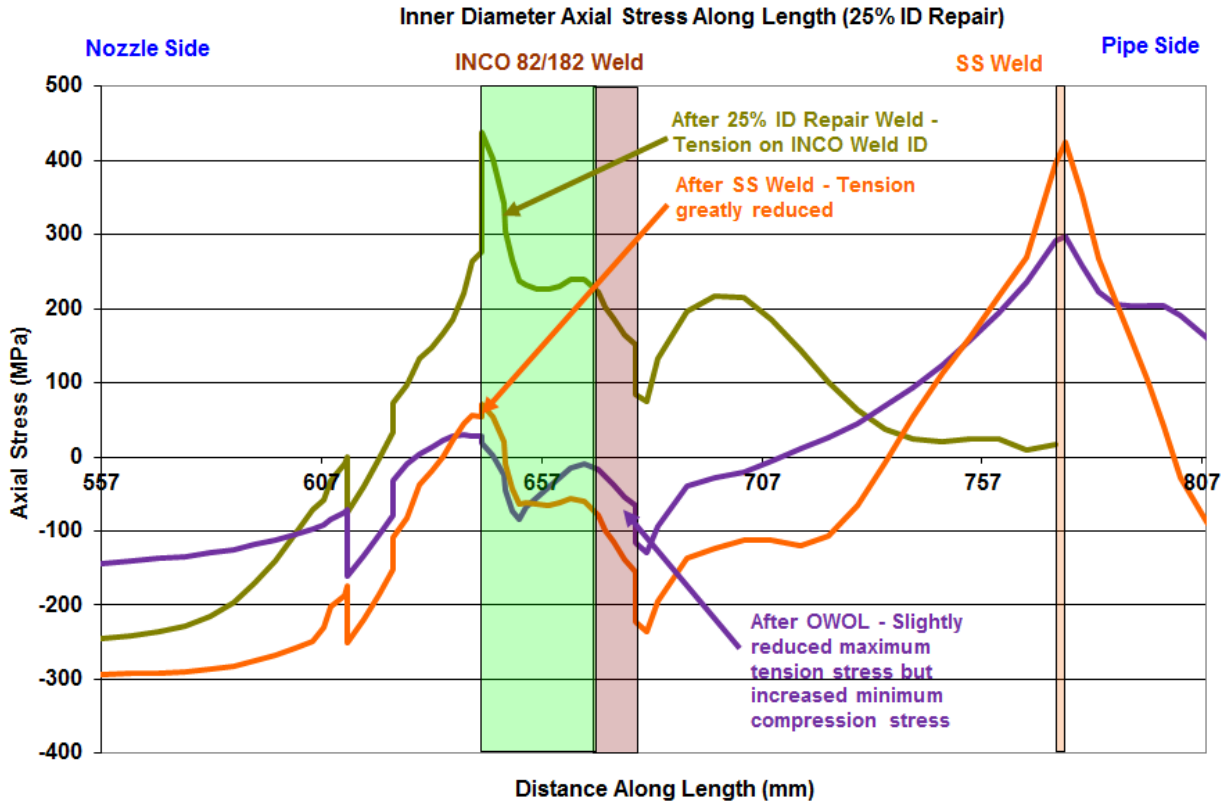

Figure 6-7 ID Axial Stresses along Length of the Pipe

The stress was very high in tension in the butter and dissimilar metal weld before the SS weld was made. Once the SS weld was completed, the stresses along the ID were primarily compressive except in the area of the transition between the carbon steel nozzle and the butter. In this area the stresses remained tensile in the range of 69 MPa (10 ksi). After the OWOL was completed the maximum tension stress was slightly reduced to 35 MPa (5 ksi), but the area that was already compressive after the SS weld was complete had its compressive stresses reduced by the application of the OWOL. These results indicated little improvement for the application of the OWOL at room temperature and with no operating loads applied.

6.5.2. Hoop Stresses, Room Temperature, Without Operating Loads

Figure 6-8 and Figure 6-9 show the through-thickness hoop stresses before and after the application of the OWOL. The stress contour plot and the graph show that the secondary SS weld had the effect of reducing the hoop stress in the DM weld, but not to the extent that it did for the axial stresses. The ID stress remained in tension in this cross-section. The OWOL reduced the through-thickness hoop stresses into compression for approximately the inner 50 percent of the original wall thickness with the exception of one small spike into the tensile region at a quarter of the way through the original thickness at the peak of the 25 percent through-thickness ID weld repair.

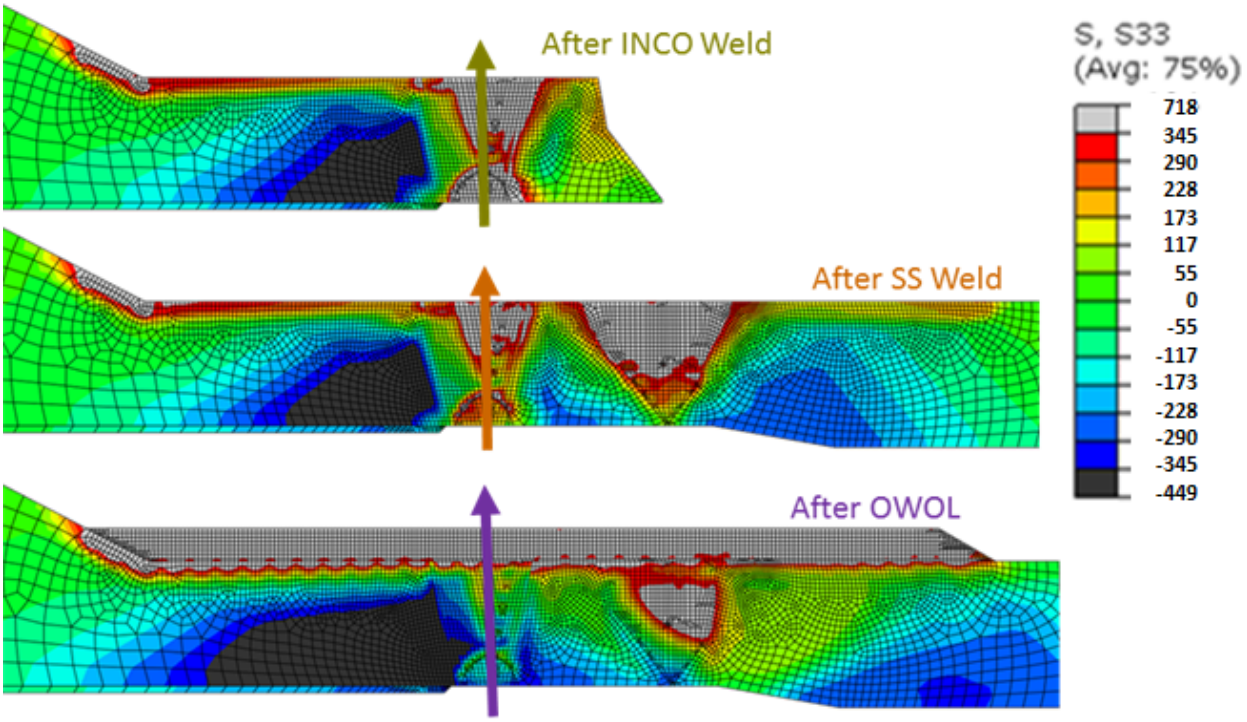

Figure 6-8 Cold Leg Nozzle Hoop Stresses [MPa]

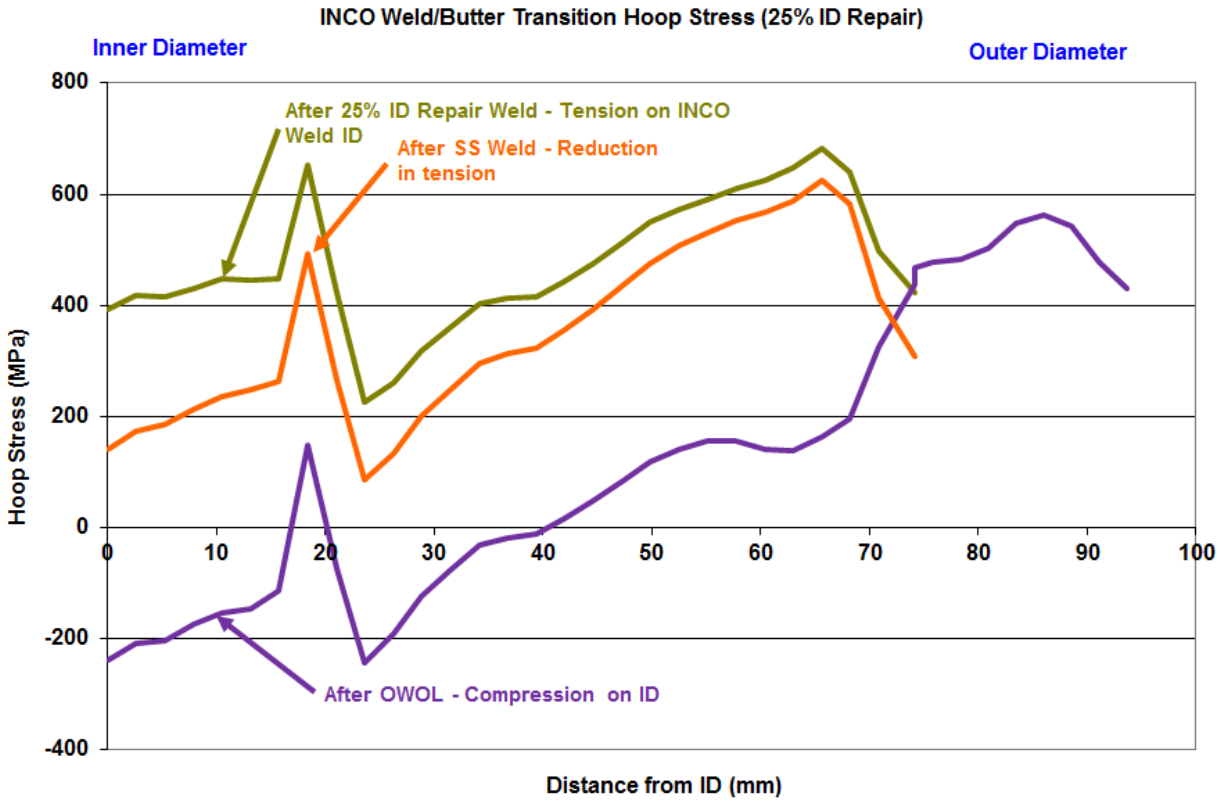

Figure 6-9 Cold Leg Nozzle Through-Thickness Hoop Stresses

Figure 6-10 and Figure 6-11 show the ID hoop stress along the length of the DM weld area of the cold leg nozzle. The graph shows that hoop stresses were very high on the ID of the DM weld before the SS closure weld was made, and were reduced but remained tensile after the SS weld was completed. The stresses were uniformly high at 414 MPa (60 ksi) in the DM weld area before the SS weld and reduced to a uniform 138 MPa (20 ksi) after it was made. The OWOL reduced the hoop stresses in the area of concern to be compressive over the entire length of the DM weld area.

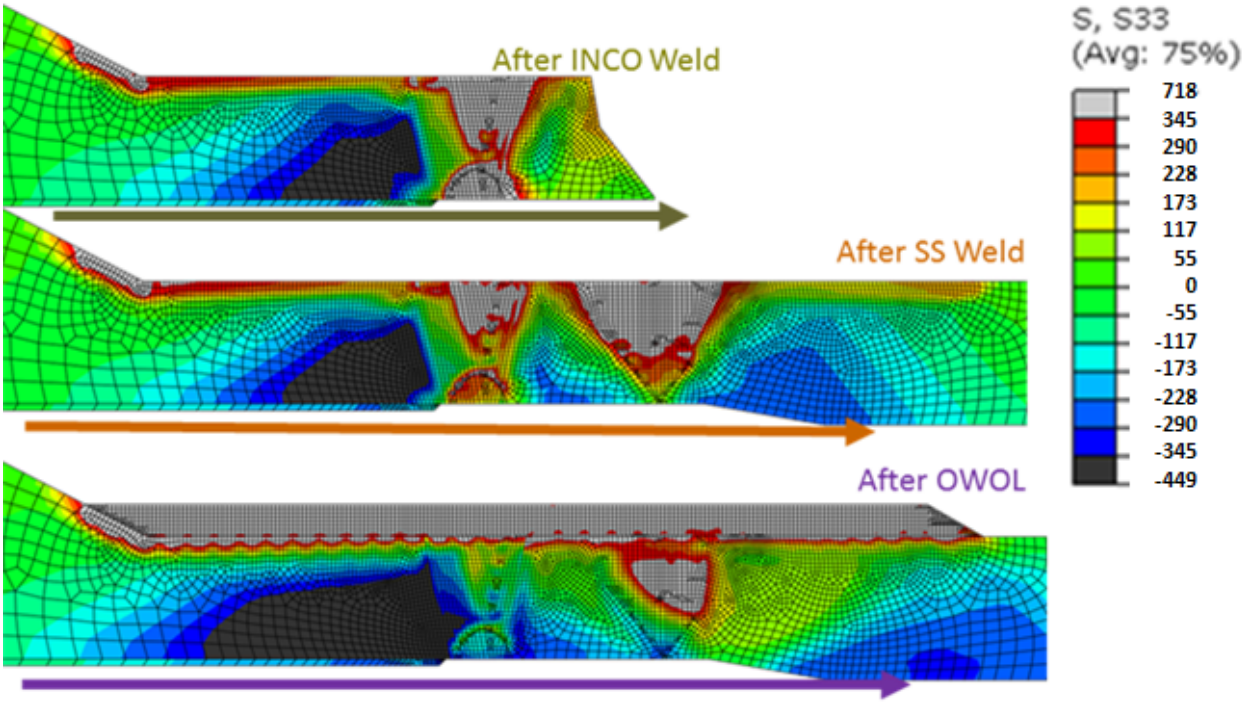

Figure 6-10 Cold Leg Nozzle Inner Diameter Hoop Stresses [MPa]

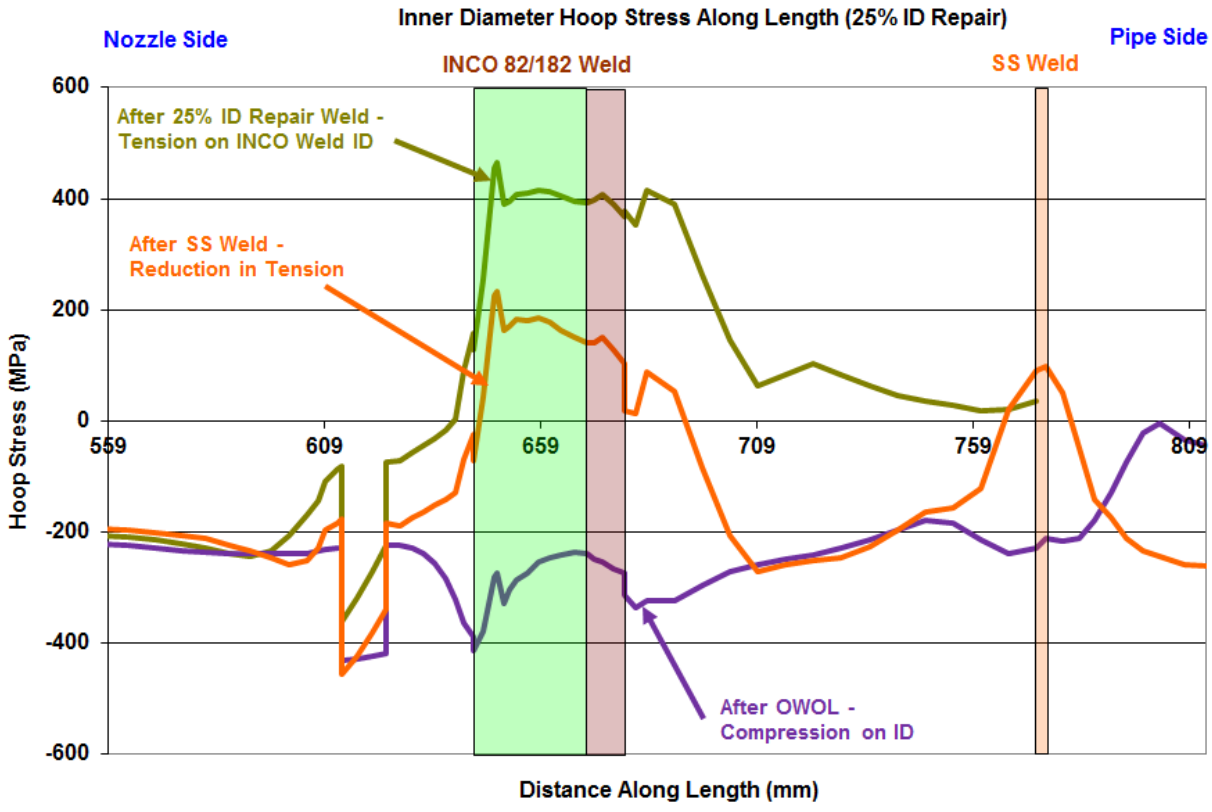

Figure 6-11 Cold Leg Nozzle Inner Diameter Hoop Stresses

6.5.3. Operating Condition Sensitivity Study

The previous cold leg nozzle stress plots were all made for analyses at room temperature and pressure. The following graphs show the effect of operating pressure and temperature on the cold leg nozzle axial and hoop stresses. An operating pressure of 15.5 MPa (2,250 psi) and an operating temperature of 300°C (572°F) were used for the cold leg nozzle analyses.

Figure 6-12 shows the ID axial stress in the cold leg nozzle DM weld area after OWOL at room temperature and then at operating temperature and pressure. The application of operating conditions had a marked beneficial effect after the OWOL. It reduced the maximum stress magnitude to -69 MPa (-10 ksi) and maintained the remainder of the stresses in the DM weld region compressive below the values achieved in the room temperature analyses.

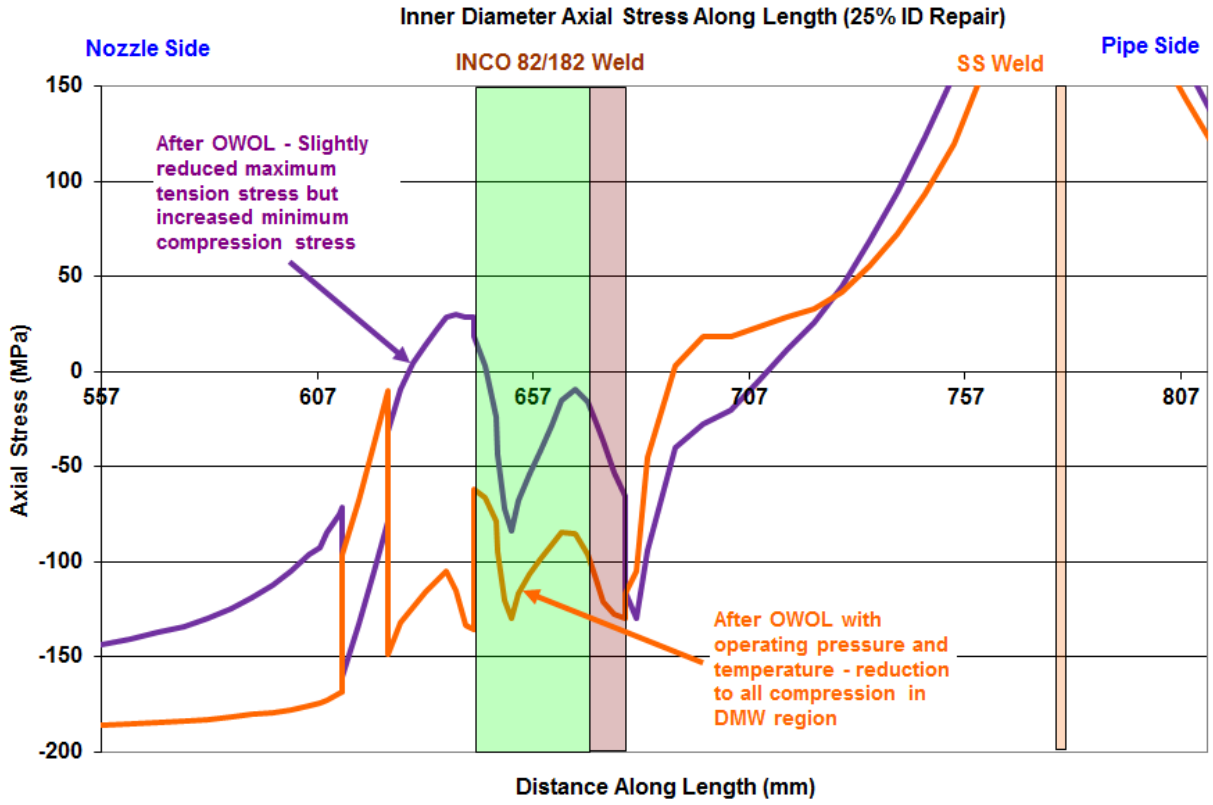

Figure 6-12 ID Axial Stresses at Operating Pressure and Temperature

Similarly, Figure 6-13 shows the ID hoop stress in the cold leg nozzle DM weld area after OWOL at room temperature and then at operating temperature and pressure. Operating conditions raised the hoop stresses in the DM weld area, but they remained in compression for the whole area of concern after the OWOL.

Figure 6-13 ID Hoop Stresses at Operating Pressure and Temperature

6.5.4. Weld Overlay Thickness Sensitivity Study

A sensitivity study was conducted to examine the effect of weld overlay thickness on the residual stresses in the DM weld. The OWOL thickness was studied by observing the stresses as each overlay layer was applied. The stresses through the thickness and along the ID were examined as was done previously. The temperature of the nozzle was allowed to cool to 21°C (70°F) after the last weld bead in each layer of the overlay.

Figure 6-14 shows the axial stress results through the thickness at the interface between the butter and the DM weld for the layers, as defined in Figure 6-3. The graph shows an oscillating behavior of the stress profile. The application of one, two, and three layers made the ID stress progressively higher than the original stress with no weld overlay. The fourth layer brought the stress back down, but not down to the level that they were with no weld overlay. The remaining layers did not change the stress much in this cross-section. The axial stresses crossed from tensile to compressive at the ID in this cross-section, so no large change would be expected.

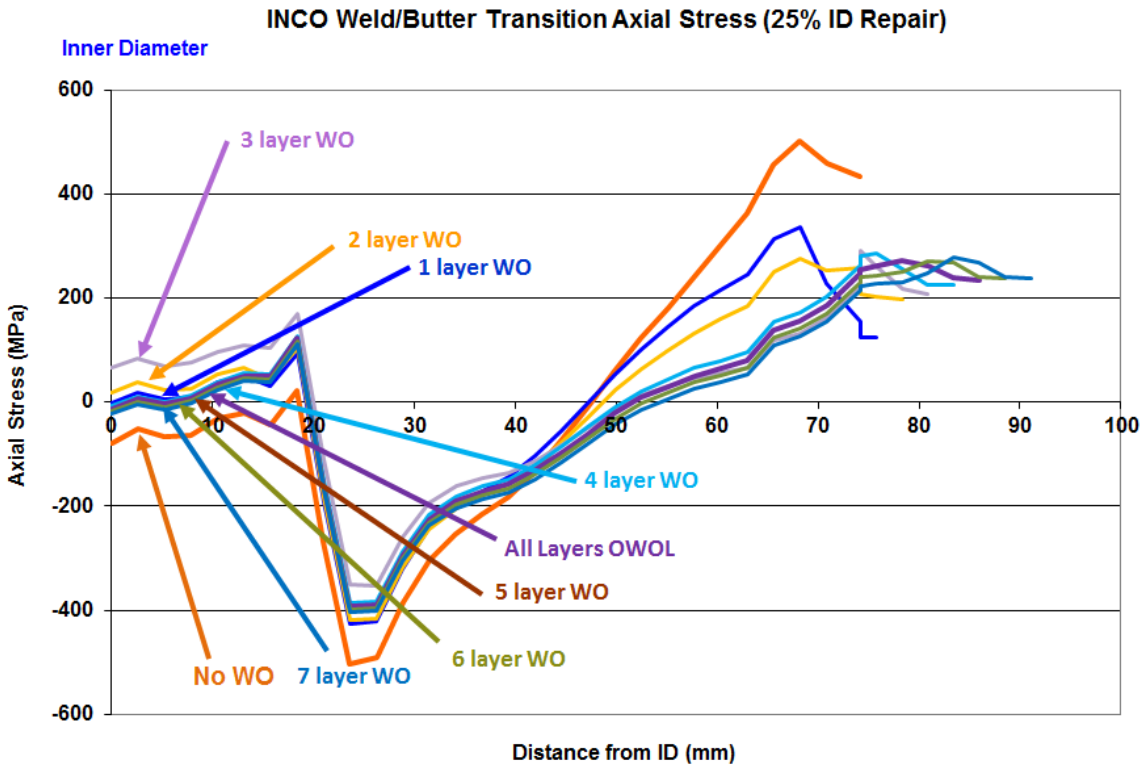

Figure 6-14 Axial Stresses through Weld Overlay Process

It is important to look at the stresses on the ID along the whole length of the PWSCC susceptible area to examine the effect on the most highly stressed region and the maximum effect of the OWOL. Figure 6-15 shows the axial stress along the ID of the cold leg nozzle. For this case, a smaller length of the nozzle is shown that includes only the butter and DM weld areas. The vertical bars in the graph indicate the location of the butter layer, as well as the DM weld, with the same color coding as used in the previous graphs. The maximum axial tension stress on the ID was found at the transition between the butter layer and the ferritic pressure vessel steel, as shown previously. The graph shows the same oscillation behavior as was displayed in the previous graph. The maximum stress with no weld overlay was 69 MPa (10 ksi). The stress in this area increased to 186 MPa (27 ksi) after two layers were applied, and stresses remained higher than the original value until four layers were applied. The maximum stresses then remained lower than the original value with no weld overlay, with subsequent layers changing the stress little. The stress improvement for layers four through the completed OWOL at the maximum stress area became a detriment about halfway along the butter width. At this point, the weld overlay increased the stress from the value with no weld overlay at all. Of course, it was shown earlier that the application of operating pressure and temperature reduced these stresses to values below what would be obtained with no weld overlay.

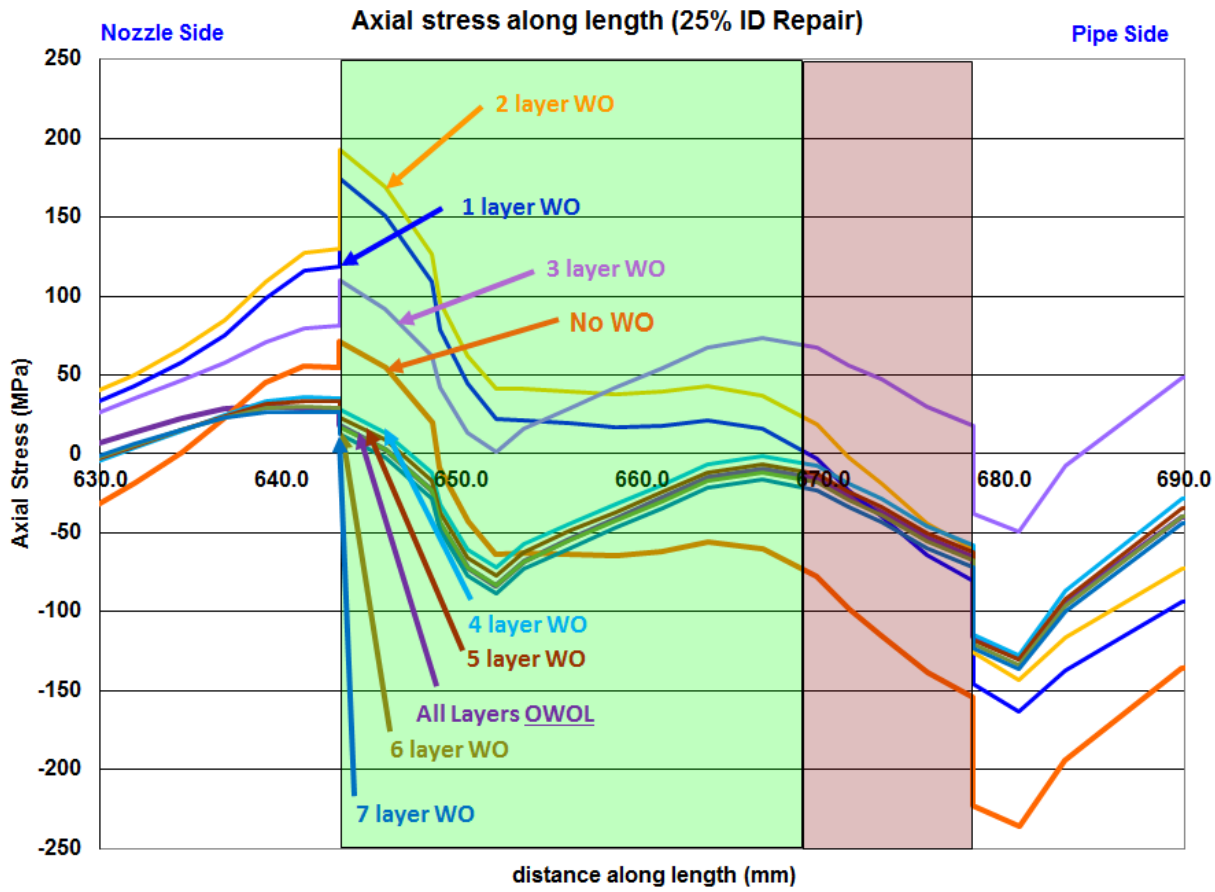

Figure 6-15 ID Axial Stresses for each OWOL Layer

Figure 6-16 shows the ID hoop stress. The graph shows that there was a progressive improvement in hoop stress with more layers of the weld overlay, but that this effect was not proportional to weld overlay thickness. The maximum value with no weld overlay was inboard of the transition between the butter and the pressure vessel steel. Application of layers one and two decreased the tension stress. The application of layer three made a large change in the hoop stress and reduced the maximum value, and the whole area encompassing the DM weld went into compression. Subsequent layers progressively improved on this by adding more compression with decreasing impact for each subsequent layer. This graph clearly shows that additional layer thickness did not improve the hoop stress substantially, and that the weld overlay could be considered “optimized” in terms of additional compressive stress being created.

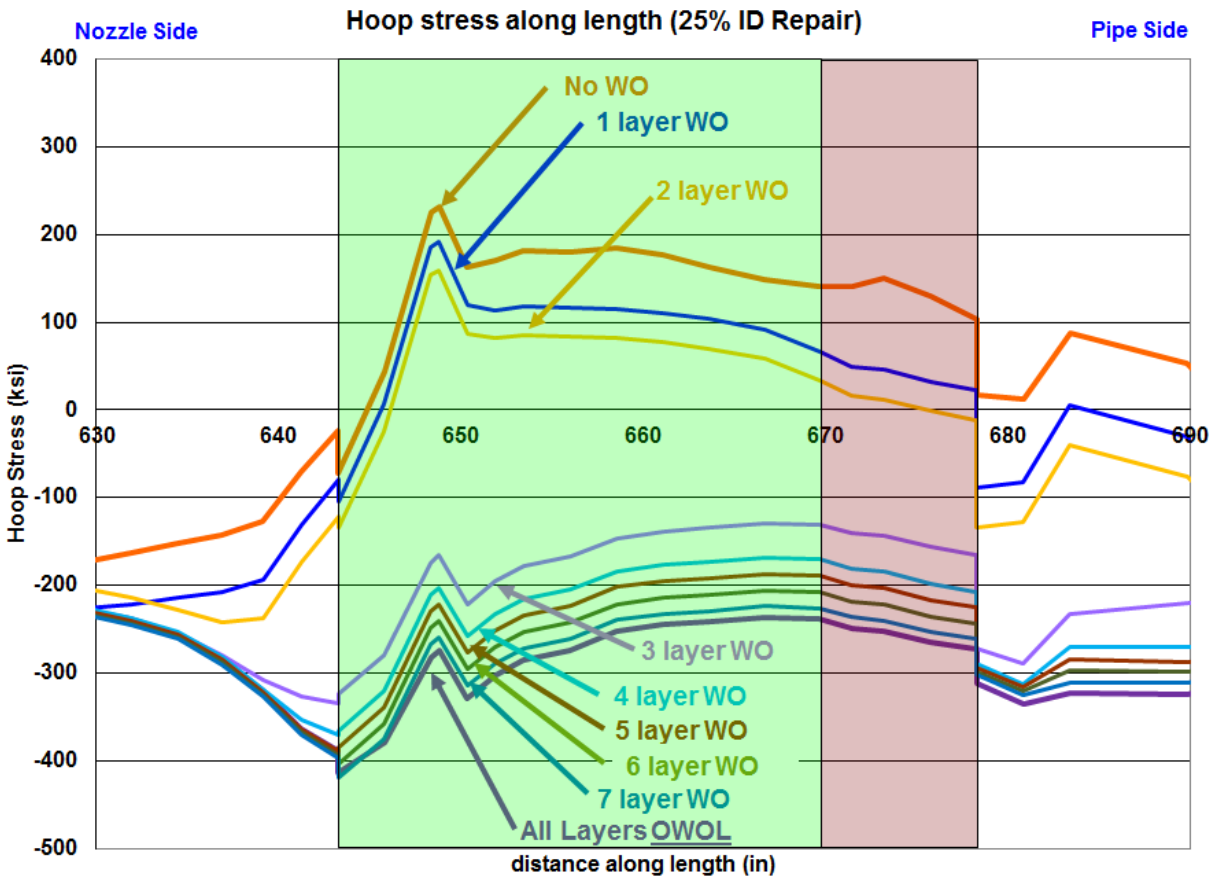

Figure 6-16 ID Hoop Stresses for Each OWOL Layer

6.5.5. Repair Weld Sensitivity Study

A sensitivity study was performed examining the effect of ID repair depth on stresses before and after weld overlay. For the cold leg nozzle 0 and 25 percent ID repair depths were examined. Figure 6-17 shows the weld area of the cold leg nozzle model with the various materials and welds color-coded. The weld repair is shown in the lower figure and is colored yellow. Its peak was located at the interface between the butter layer and the DM weld. It was 25 percent through the original thickness of the weld area, and because the model was 2-D axisymmetric, the weld repair spanned the entire circumference of the ID. The comparison of the results with no weld repair and with the weld repair will show the differences in the stresses that would be found in a nozzle with a partial arc weld repair that only spanned 30 percent of the circumference. To a first approximation, the stresses in the model with the repair represent the stresses in the partial arc repair, and the stresses in the model with no weld repair represent the stresses everywhere else.

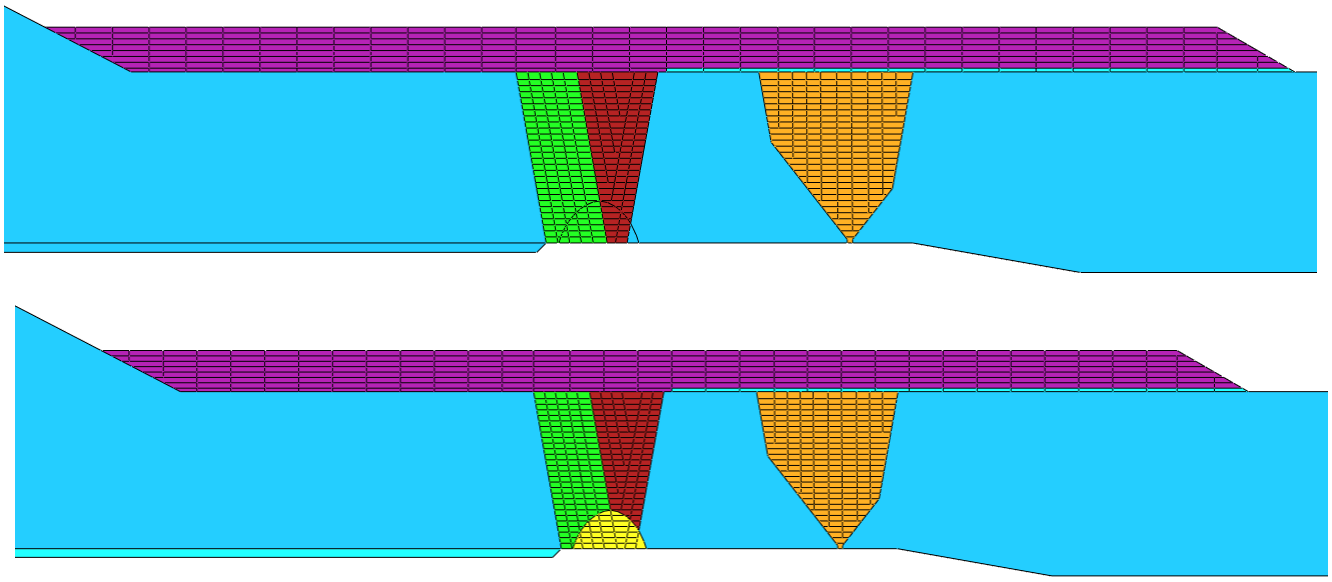

Figure 6-17 Cold Leg Nozzle with and without 25 Percent ID Repair

Figure 6-18 shows the axial stresses after welding was complete, but before any weld overlay was applied. The case with no repair is shown on the top, and the case with the 25 percent deep ID repair is shown at the bottom. There was a noticeable difference in the stress results in the area of the repair. In the case without the repair, the compressive stresses began closer to the ID, and there was a spike of tension stresses where the root pass grind out and re-weld took place. In the subsequent graphs the results for the case with no ID repair will be shown in a solid orange curve, while the 25 percent deep ID repair results will be indicated by a dashed orange curve.

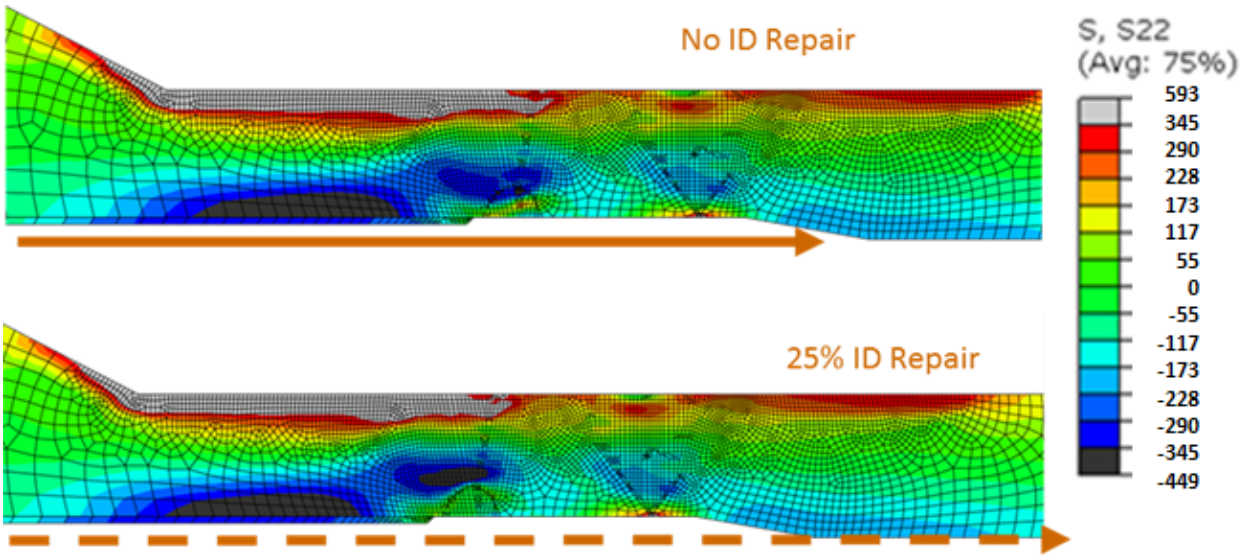

Figure 6-18 Cold Leg Axial Stresses before OWOL with and without ID Repair [MPa]

Figure 6-19 shows the axial stresses along the ID of the nozzle with the location of the butter, DM weld, and SS safe end weld indicated by vertical color-coded bars. The graph shows that

the highest tensile stress in the DM weld area was for the case without the 25 percent deep ID weld repair. The highest stress in the case with no ID repair was 138 MPa (20 ksi). The ID repair reduced this maximum to 69 MPa (10 ksi). The peak was also shifted toward the butter/steel interface at the left edge of the repair.

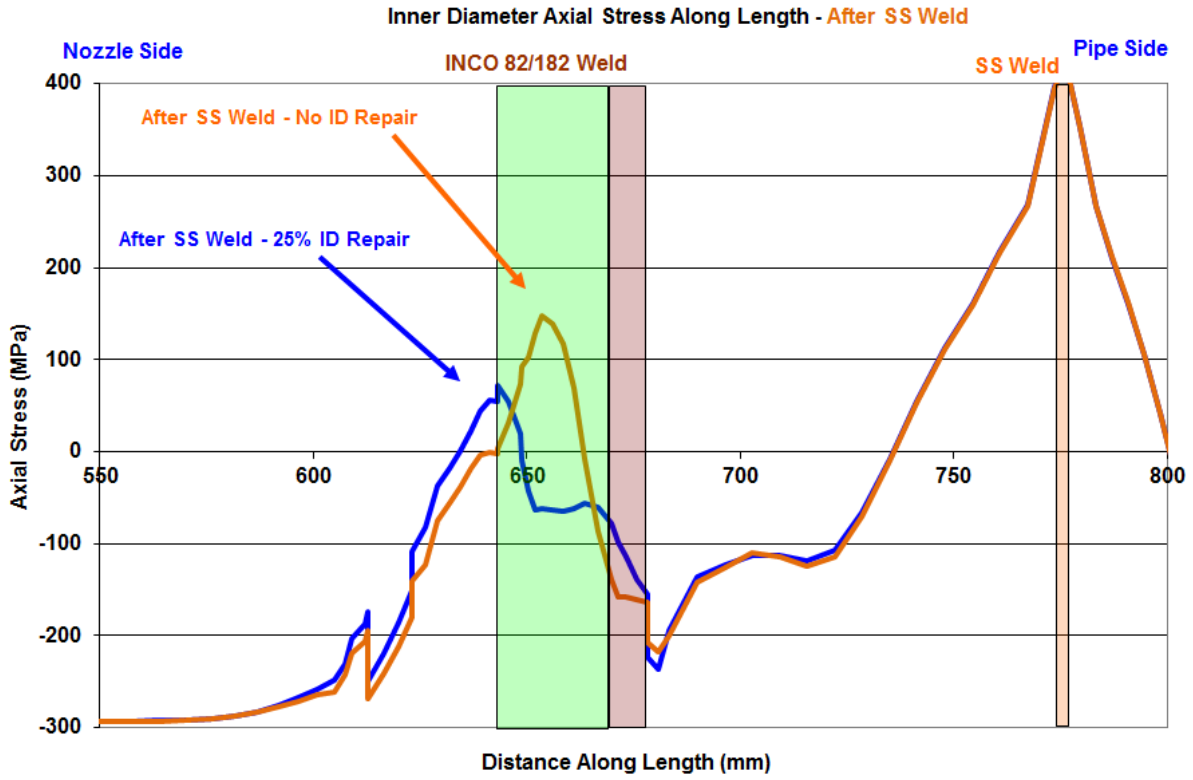

Figure 6-19 ID Axial Stresses before OWOL with and without ID Repair

Figure 6-20 shows the through-thickness axial stress at the butter/DM weld interface for this same case before any weld overlay was applied. The graph shows that, for this cross-section, the ID stresses were negative for both the case with no weld repair and for the 25 percent weld repair. Both stress distributions started out negative and proceeded slightly upward toward the tensile region before plunging back into compression, and then finally ended tensile toward the OD. The only marked difference between the two curves is that the plunge into compressive stresses took place at 25 percent through the thickness for the weld repair case, and the drop into the compressive regime for the case of no repair occurred at around 10 percent of the thickness where the ID root pass grind out and re-weld ends.

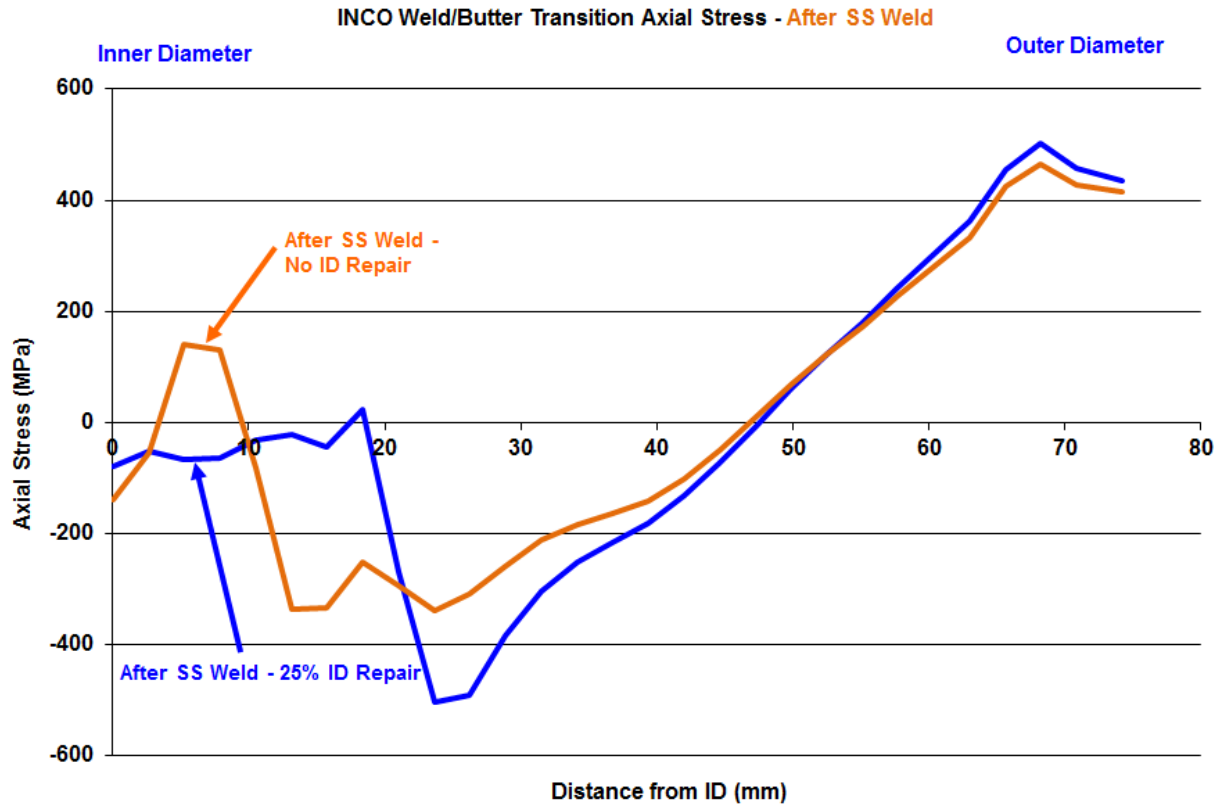

Figure 6-20 Axial Stresses before OWOL with and without ID Repair

Figure 6-21 shows the axial stress contour plot for the same two cases but after the OWOL was applied. The stress contours were similar, but with the same exception that was pointed out in the previous stress contour plot. The 25 percent ID repair pushed the area of compressive stress slightly beyond the depth of the repair.

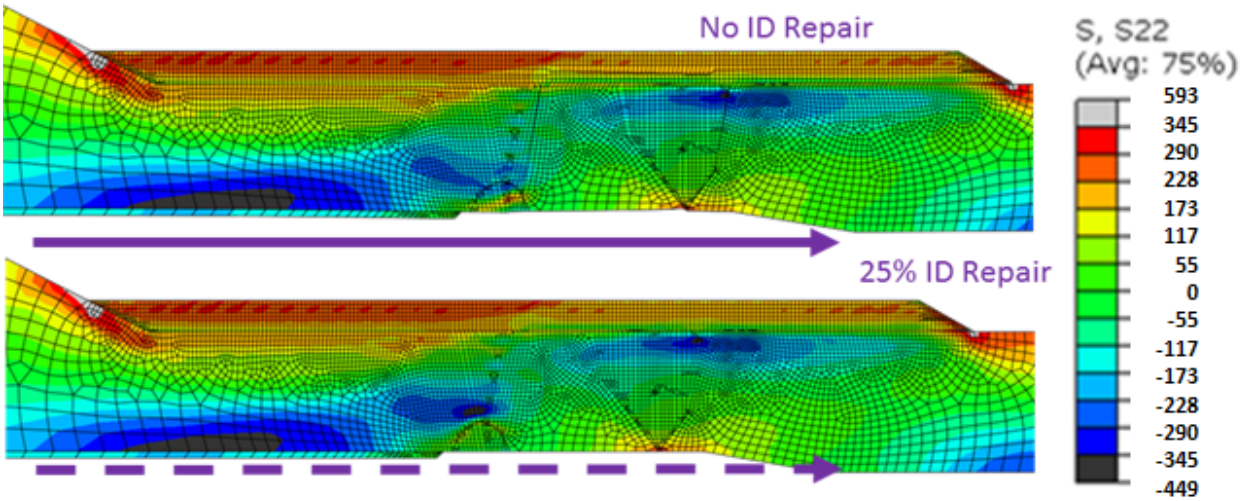

Figure 6-21 Axial Stresses after OWOL with and without 25 percent ID Repair [MPa]

Figure 6-22 shows the ID axial stresses for the two cases. The graph looks similar to that which was shown for the case before the OWOL was applied except that the axial tensile stresses have been somewhat diminished. The compressive stresses were also somewhat diminished. The peak tensile value in the DM weld area was reduced from 138 MPa (20 ksi) to 117 MPa (17 ksi) for the case with no ID repair, and from 69 MPa (10 ksi) to 34 MPa (5 ksi) for the case with the ID weld repair. These results were at room temperature, and did not take into account the benefit in stress reduction caused by operating pressure and temperature.

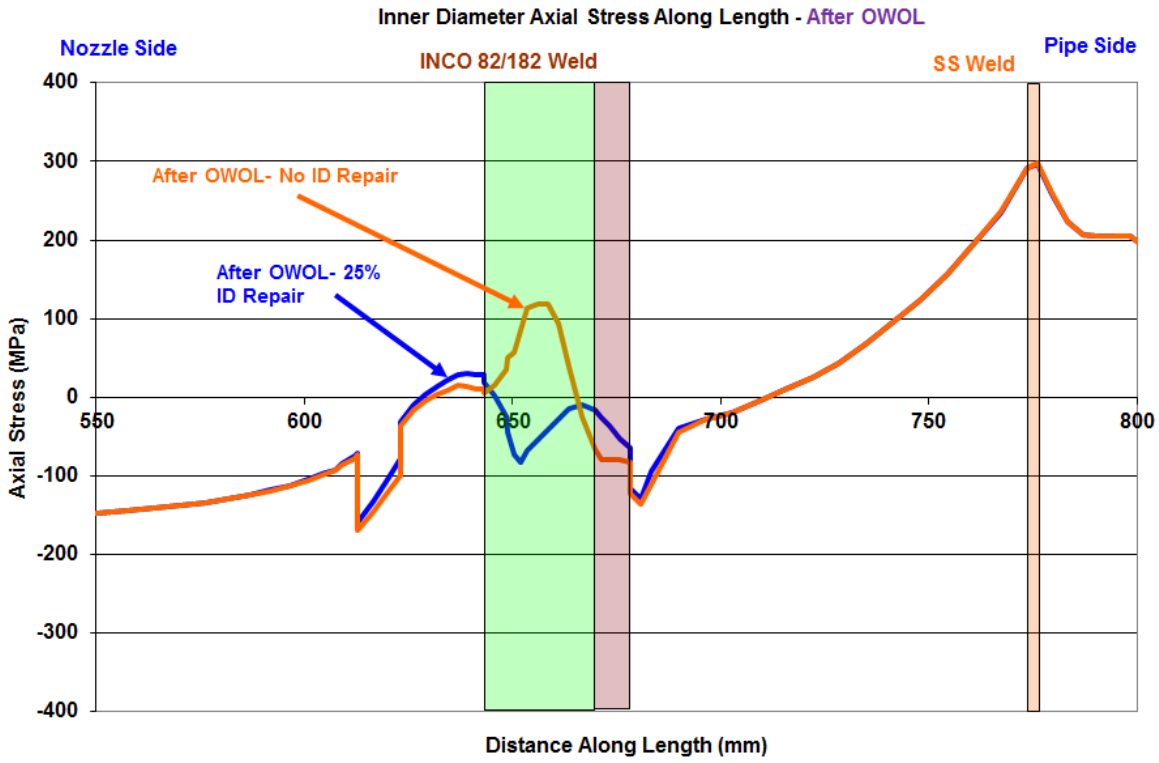

Figure 6-22 ID Axial Stresses after OWOL with and without ID Repair

Figure 6-23 shows the through-thickness axial stress plot for the interface of the butter layer and DM weld. The graph has a similar profile as the one before the OWOL was applied for this cross-section. The curves started out slightly compressive and proceeded into the tensile region before plunging into the compressive area. Equivalent tensile values followed toward the OD. For this cross-section, the stresses were increased by the OWOL, but the location at which the curve representing the 25 percent ID repair turned compressive was 25 percent of the way through the original wall thickness.

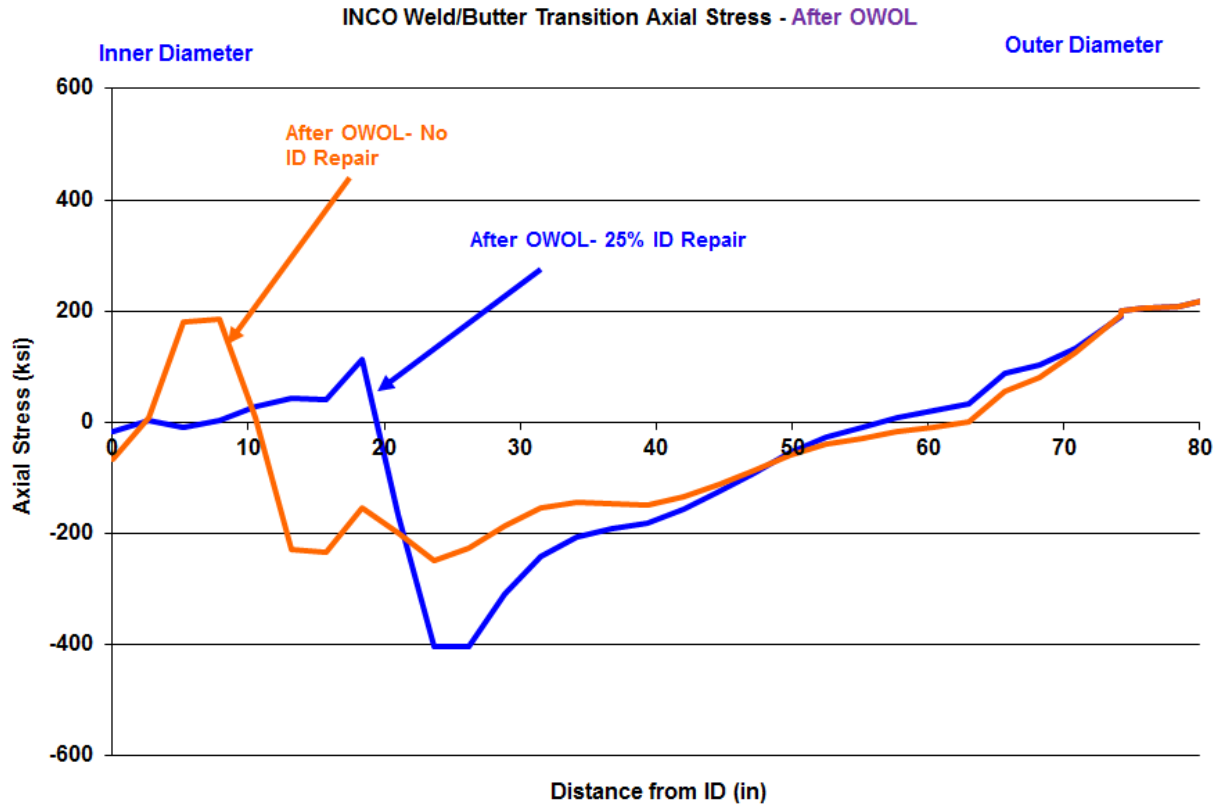

Figure 6-23 Axial Stresses after OWOL with and without ID Repair

6.6 Double-Blind Finite Element Study

6.6.1. Finite Element Predictions

Figure 6-24 and Figure 6-25 show the results of the six FE predictions of the axial and hoop stresses, respectively, through the thickness of the centerline of the DM weld before the SS safe end weld was completed. The results were from models with the 25 percent through-thickness weld repair. Not all modelers provided results for the area outside the weld repair region. The FE predictions and measurements in the area of the weld repair will be discussed first, as all of the modelers provided results for these cases.

Each modeler and each measurement technique reported a different number of data points through the thickness of the nozzle. These differences were due to the differences in models, meshes, and measurement techniques. The data provided from all models and measurements was linearly interpolated between provided data points to create 50 even steps through the thickness so that tabulated results could be compared directly. Averages were calculated at each step through the thickness. The graphs show the running average of the data presented as a thick blue line through the center of the data plots. The actual data is shown as thin color-coded lines in these graphs.

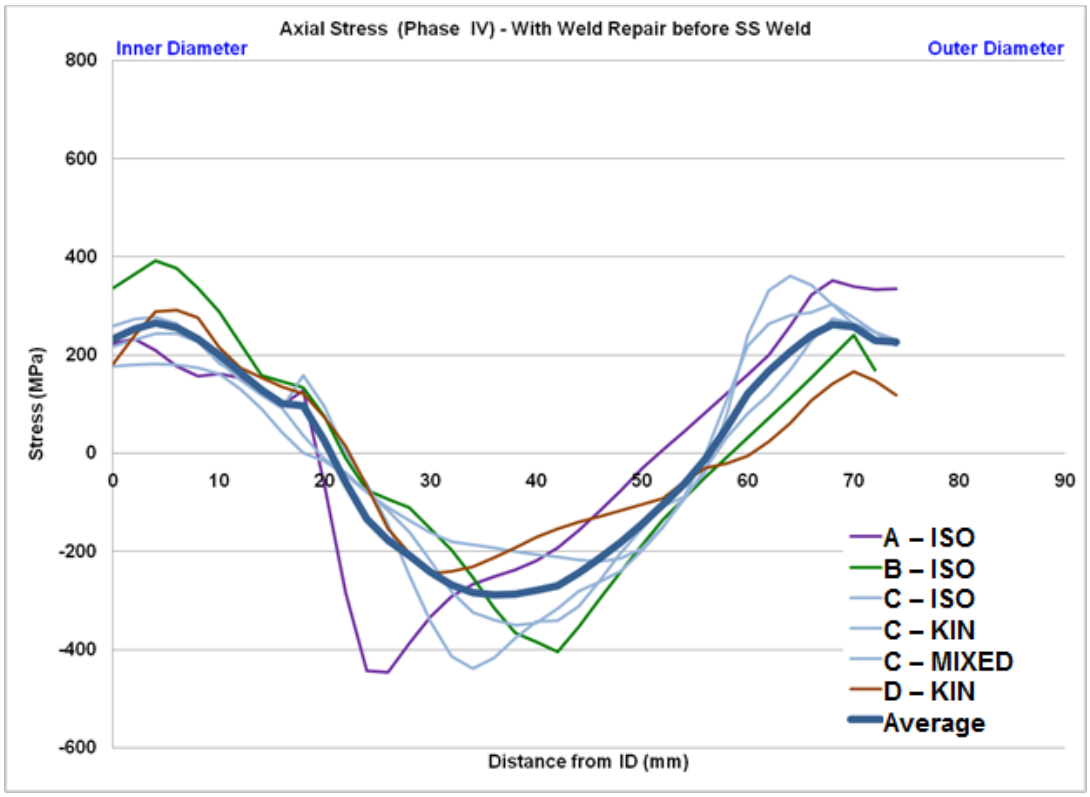

Figure 6-24 Axial Stress with Weld Repair before the SS Weld

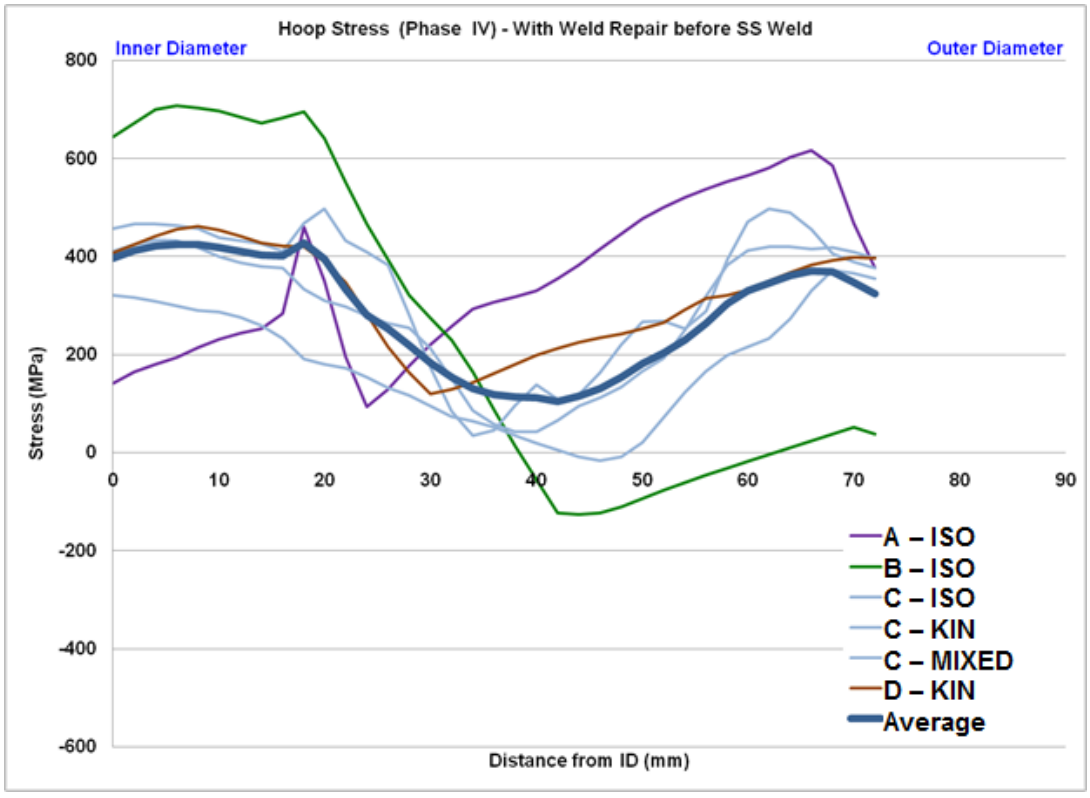

Figure 6-25 Hoop Stress with Weld Repair before the SS Weld

Several observations can be made from these comparisons of predictions. The average axial stress curve shows the ID axial stress was in tension at about 200 MPa (29 ksi) with a compressive minimum about 50 percent of the way through the thickness of the DM weld. The axial stresses then rose toward 200 MPa. The hoop stress average curve shows the stresses were tensile at the ID, while they remained tensile through the thickness of the DM weld. Two of the individual predictions dipped into the compressive region at about 60 percent of the way through the thickness. The average, and all but one individual prediction, shows that the OD hoop stress was in tension and of a similar value as the ID tension stress.

Two predictions, in particular, showed unusual results for hoop stress as compared to the rest of the dataset. For the A results, the spike at the 20 mm location was not observed in the other results. This is likely attributed to the root pass grind out assumed by the modeler. The ID stress for this model was low compared to the dataset. The B results showed much larger stress fluctuations, from +600 MPa to -100 MPa, than the other models.

The hardening law used for each prediction is indicated in the legend text as ISO, KIN, or Mixed. The annealed yield strength for the Alloy 82 DM weld was 265 MPa (38.4 ksi). The differences in predicted values caused by the material hardening law came about because of the strain cycles created in the welding process. The models following the isotropic hardening law allowed the material to strain harden to progressively higher yield strength upon cyclic loading, and this produced higher stresses than did the kinematic hardening law. The results produced with kinematic hardening did not exceed the annealed yield strength of the material by nearly as much as the results from the models using the isotropic hardening law.

6.6.2. Predictions and Measurements Compared

A series of graphs will be used to show a comparison of the FE analysis predictions with the WRS measurements. Axial and hoop stress graphs will be examined for the state before the application of the OWOL and after the application of the OWOL. In both cases the stresses were measured in the center of the ID weld repair. As in Figure 6-24 and Figure 6-25, the FE predictions are displayed as thin lines. The heavy blue line indicates the average of all predictions and measurements. The measurements are shown as red (DHD) and maroon (iDHD) dotted lines. The iDHD measurements were not taken for the whole depth of the measurements and are only shown where data was presented for this measurement technique.

Figure 6-26 and Figure 6-27 show the axial and hoop stress comparisons between the FE predictions and the measurements before the application of the OWOL. Overall the FE predictions and DHD/iDHD measurements showed very similar trends, although the A and B predictions exhibited some unusual features. The axial stress predictions were relatively close to each other, and the DHD/iDHD measurements were within the scatter of the FE predictions and very near the average value. The axial stresses started out neutral at the ID, and then dipped to compressive at the depth of the 25 percent of the wall thickness ID weld repair. Two of the predictions using the isotropic material hardening laws dipped lower than the others in this area. The stresses then increased almost linearly from their low point to an OD tension value approximately equal to the weld material's annealed yield strength.

The hoop stress predictions had a larger degree of scatter than the axial stress predictions. The predictions were relatively close to each other for the first half of the path, but diverged on the outer half. The measurements followed the predictions very well. Aside from the B prediction, all of the measurements and predictions showed the hoop stress to be in tension at the ID, to

dip to neutral or negative in the center of the thickness, and then to return to tension at or above the level found at the ID. The A hoop stress prediction significantly overpredicted the stress for *x* greater than 25 mm.

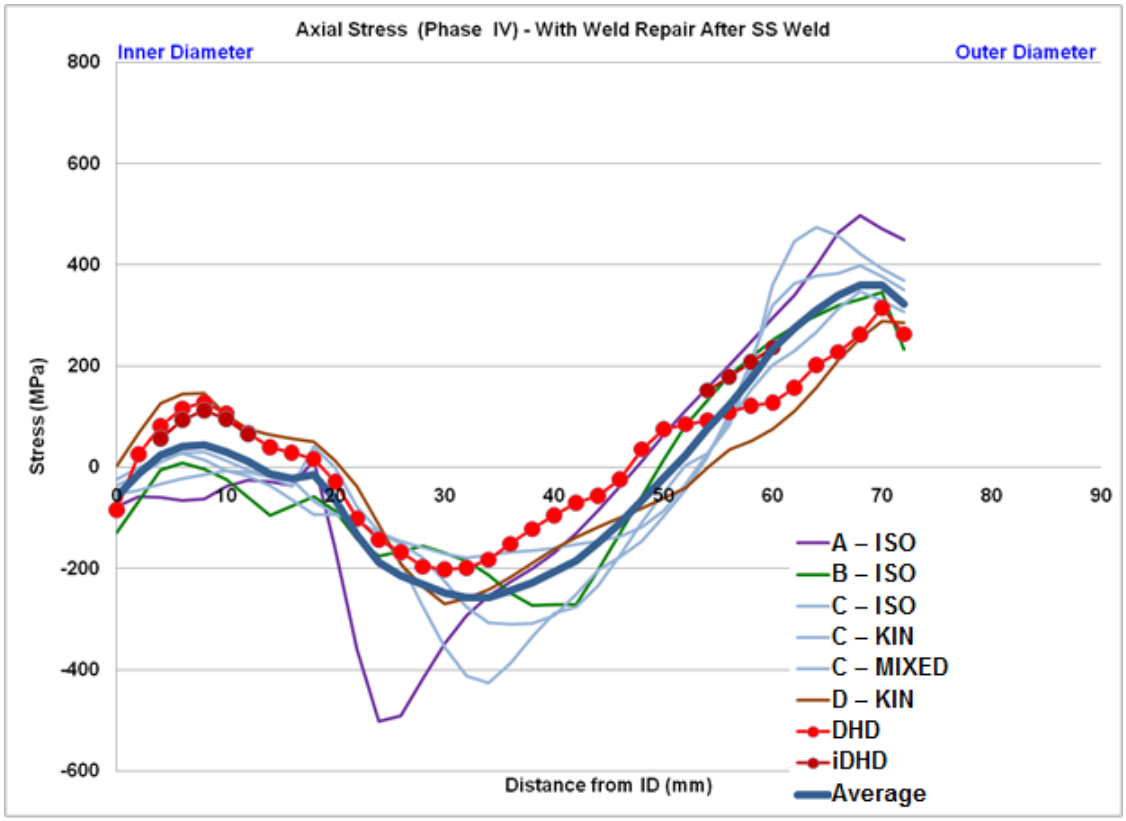

Figure 6-26 Axial Stress in Repair Region before OWOL

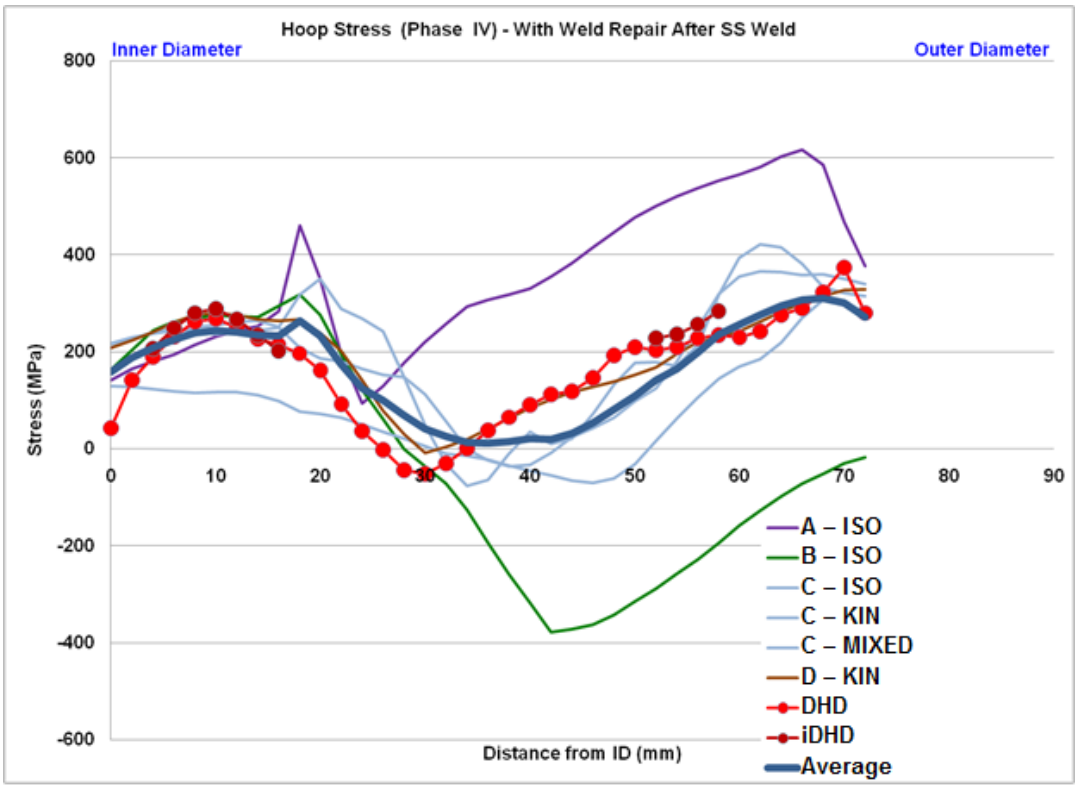

Figure 6-27 Hoop Stress in Repair Region before OWOL

After the Phase 4 results had been made public, participant B made changes to the originally-submitted model. The isotropic hardening law was modified to limit the maximum stress to be the flow stress, defined in this case as one-half the yield stress plus the ultimate tensile stress. Participant B also modified the bead sequence for the OWOL to match more closely what was done for the mockup. Figure 6-28 shows the new results compared against the original submission and participant D's results for the case prior to the OWOL. This figure demonstrates that the new procedure eliminated the large compressive stresses that were not observed in the dataset as a whole. Other example revised results are found in [27]. Remaining results from this modified procedure are not shown in the ensuing discussion, since they were not double-blind.

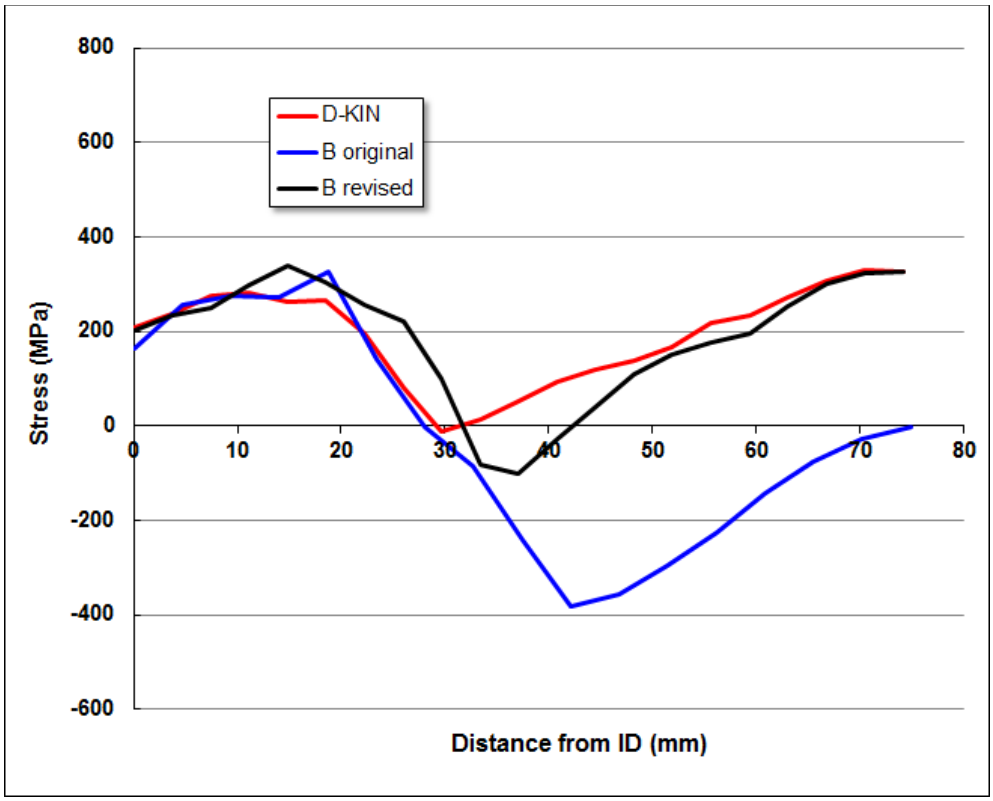

Figure 6-28 Participant B Hoop Stress from Modified Analysis

Figure 6-29 and Figure 6-30 show the axial and hoop stress comparisons between the FE predictions and the measurements after the application of the OWOL. In a general sense, there was reasonable agreement between the model results and the measurements. As before, the A and B results exhibited some features that were not present in the rest of the dataset. Most notable is the large compressive hoop stress at the ID in the B results. The axial stress at the ID was hardly changed from the values found before the OWOL, but the curve through the thickness was flattened out by the application of the OWOL. The hoop stresses were reduced at the ID by the application of the OWOL but were relatively unchanged at the OD.

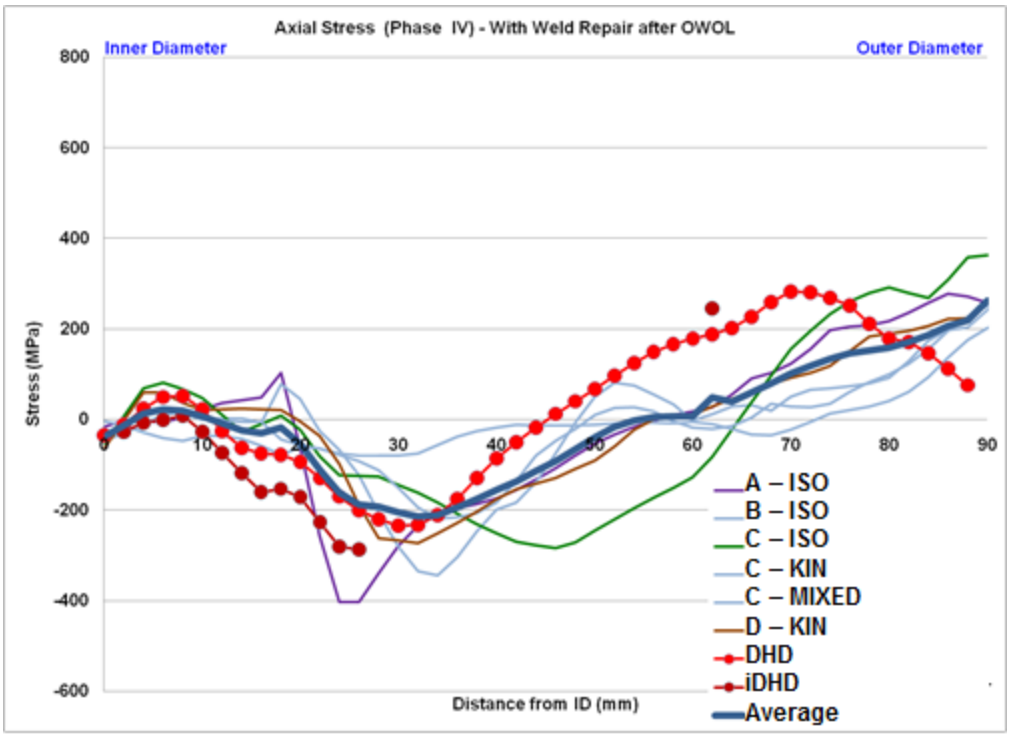

Figure 6-29 Axial Stress in Repair Region after OWOL

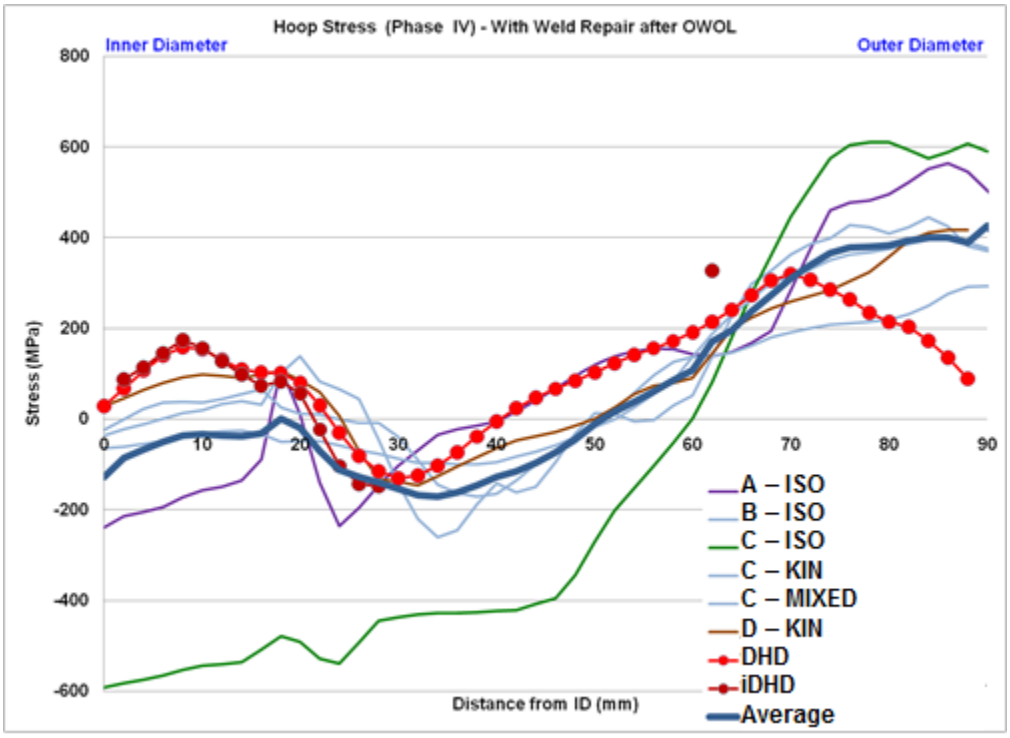

Figure 6-30 Hoop Stress in Repair Region after OWOL

A more convenient way to view the changes in stress state throughout the process is to look at the averages of all of the data in each of the states (after the DM weld but before the SS safe-end weld, after the safe-end weld but before the OWOL, and finally after the OWOL). Figure 6-31 and Figure 6-32 show the averages for the axial stress and hoop stresses, respectively, in the area of the weld repair. The axial stress plot shows a large reduction in stress due to the application of the stainless steel safe-end weld at the ID and very little change due to the application of the OWOL. The hoop stress plot shows that there was a reduction in ID stress due to the application of the stainless steel safe-end weld, and a further reduction in stress due to the application of the OWOL.

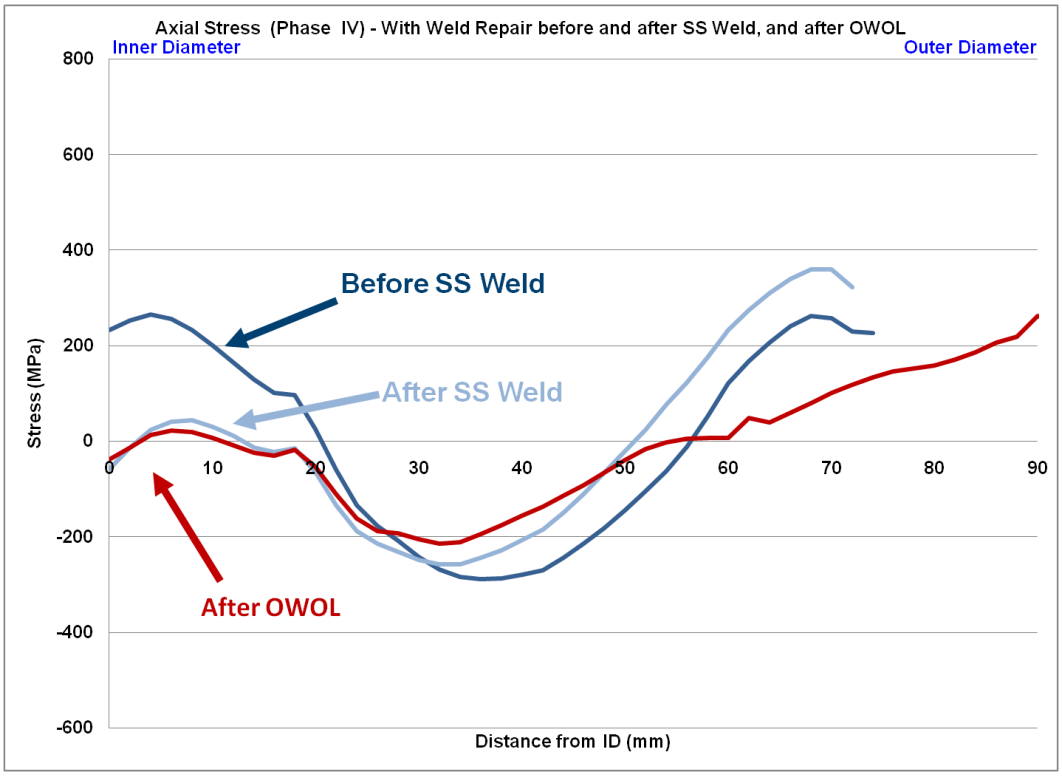

Figure 6-31 Axial Stress Averages

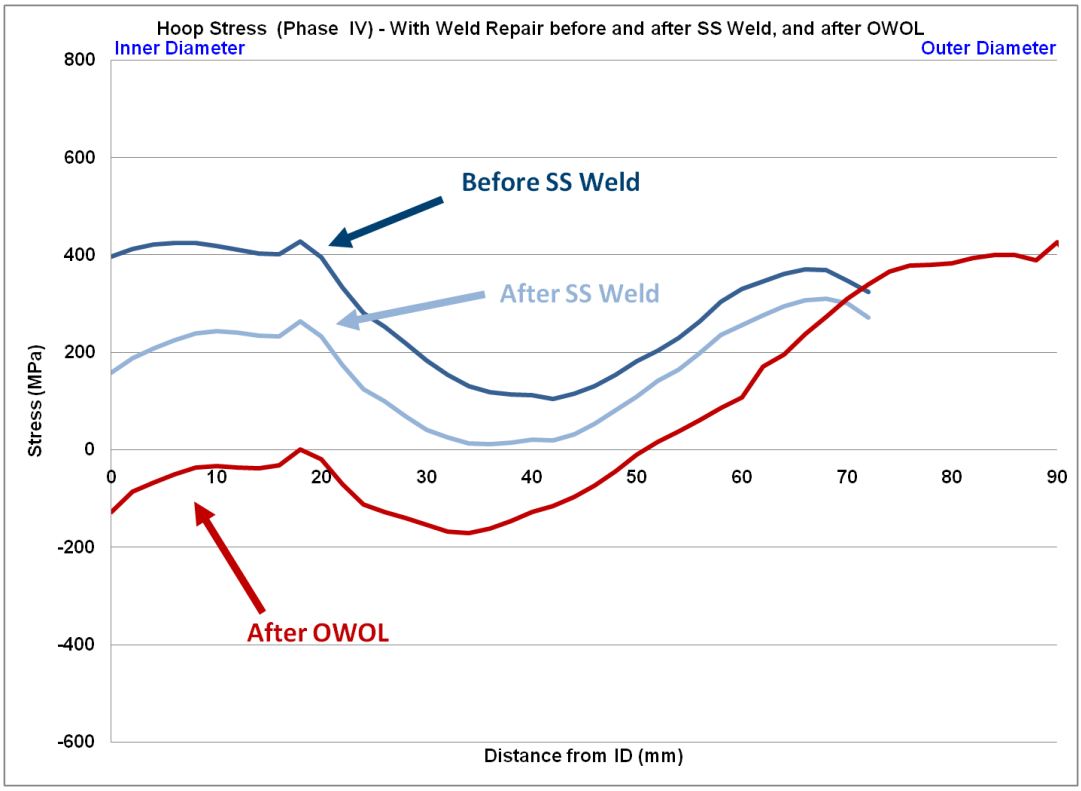

Figure 6-32 Hoop Stress Averages

6.6.3. Sensitivity Study in the Area without the Weld Repair

Only two of the providers of FE WRS predictions included results for the area without the weld repair, but measurements were taken in both the state before and after the application of the OWOL in this area of the mock-up. Figure 6-33 and Figure 6-34 show the FE predictions and DHD/iDHD measurements through the DM weld in the area 180 degrees circumferentially away from the partial arc weld repair. The FE predictions were done with two different software packages and two different material hardening laws. The A results were done in ABAQUS, and the D results were done using ANSYS. The A results used isotropic material hardening laws, and the D results used kinematic hardening. Also, the A results included an assumed root pass grind out and re-weld that was often done in larger nuclear piping welds as a last step in the DM weld process to remove inclusions in the first DM weld pass. This process was not performed on the mock-up or in the D analysis, and differences in the measurements and the A predictions indicate this fact.

The axial stress plot shows that the DHD and iDHD results were very close to each other, since plasticity effects were not present at these low stresses. Both the A predictions and measurements showed compressive stresses of nearly the same value at the ID, while the D predictions showed slight tension at the ID. The A results showed the evidence of the root pass grind out and re-weld simulation indicated by a peak tensile stress and then dip to compressive stresses at about 10 percent through the thickness, which was the depth of the re-weld. Overall, the kinematic hardening predictions from D matched the measurement trend the best.

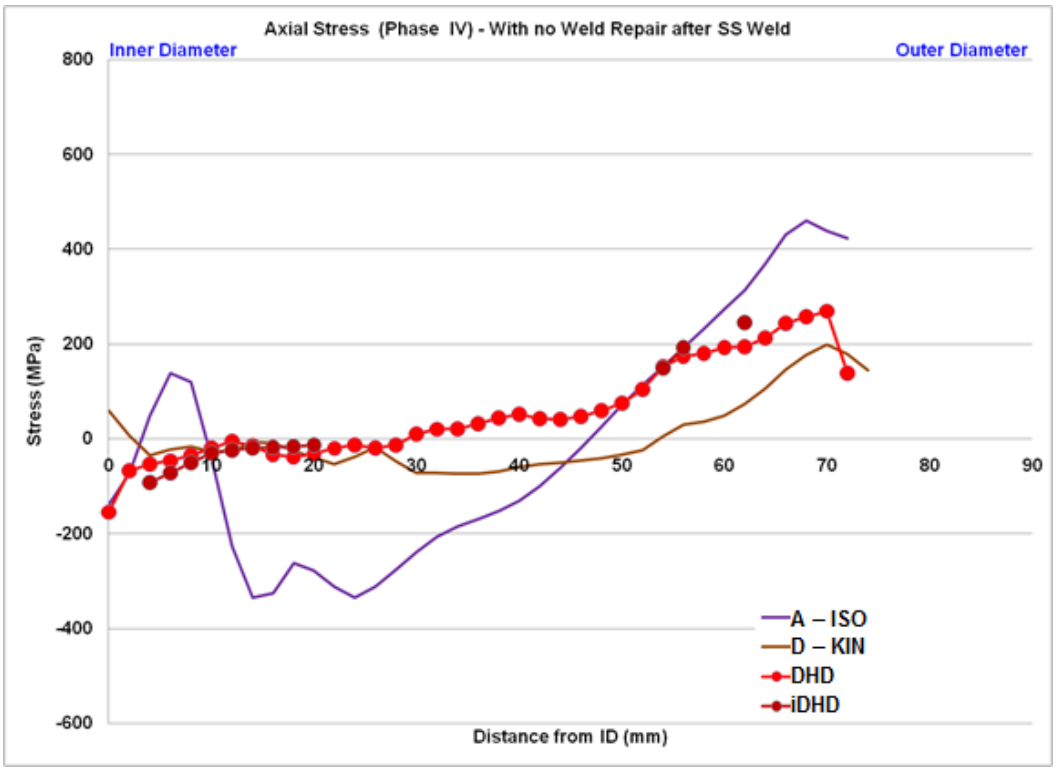

Figure 6-33 Axial Stress Outside the Repair before OWOL

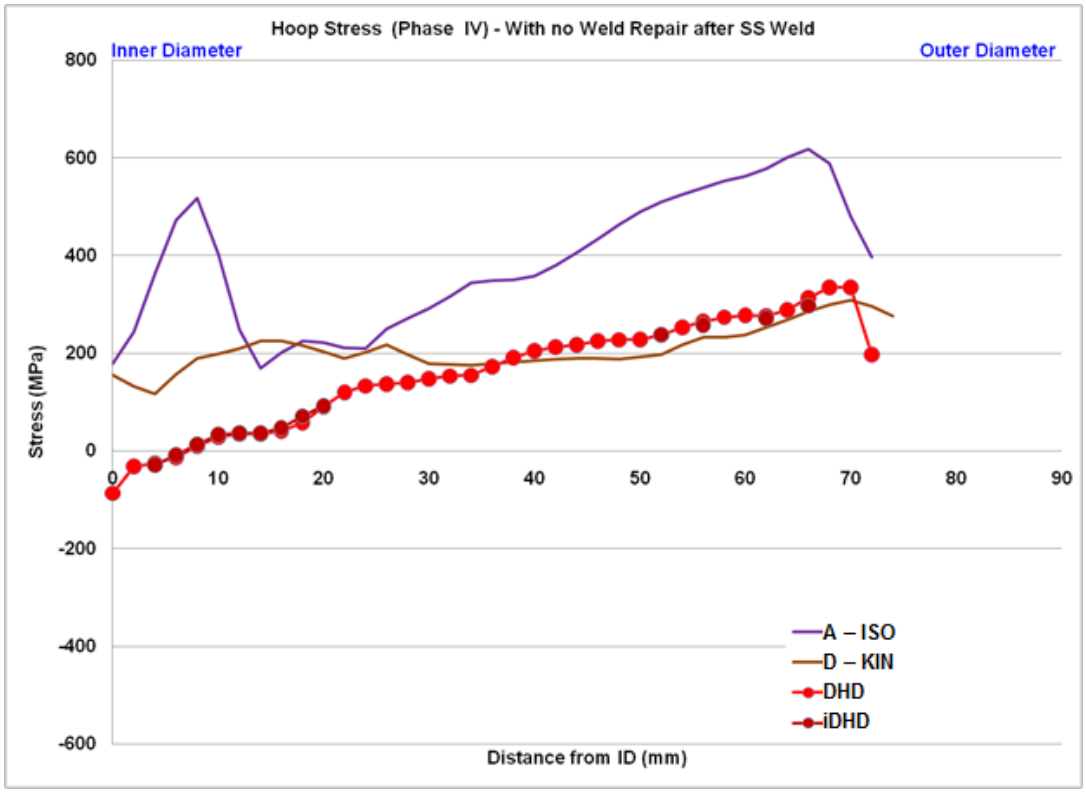

Figure 6-34 Hoop Stress Outside the Repair before OWOL

The hoop stresses plotted in Figure 6-34 showed a very close match between the DHD and iDHD results, which were lower than both of the FE predictions at the ID. The A isotropic hardening predictions and the D kinematic hardening results showed a very close match at the ID of nearly 200 MPa (29 ksi) while the measurements exhibit slightly compressive stresses. While the D kinematic hardening predictions showed a nearly flat stress profile through the thickness with tension stresses hovering around 200 MPa (29 ksi), the A results showed the stress peak caused by the root pass re-weld and then stresses climbing to a tensile peak near the OD. The measurements and D kinematic hardening predictions showed a similar slope of stress increase from the ID to the OD.

Figure 6-35 and Figure 6-36 show the post-OWOL results. Again, the DHD and iDHD measurements matched each other well. The predictions in both cases showed stresses at the ID higher than the measurements unlike in the post-OWOL plots for the weld repair region where the measurements matched the predictions well at the ID, see Figure 6-29 and Figure 6-30.

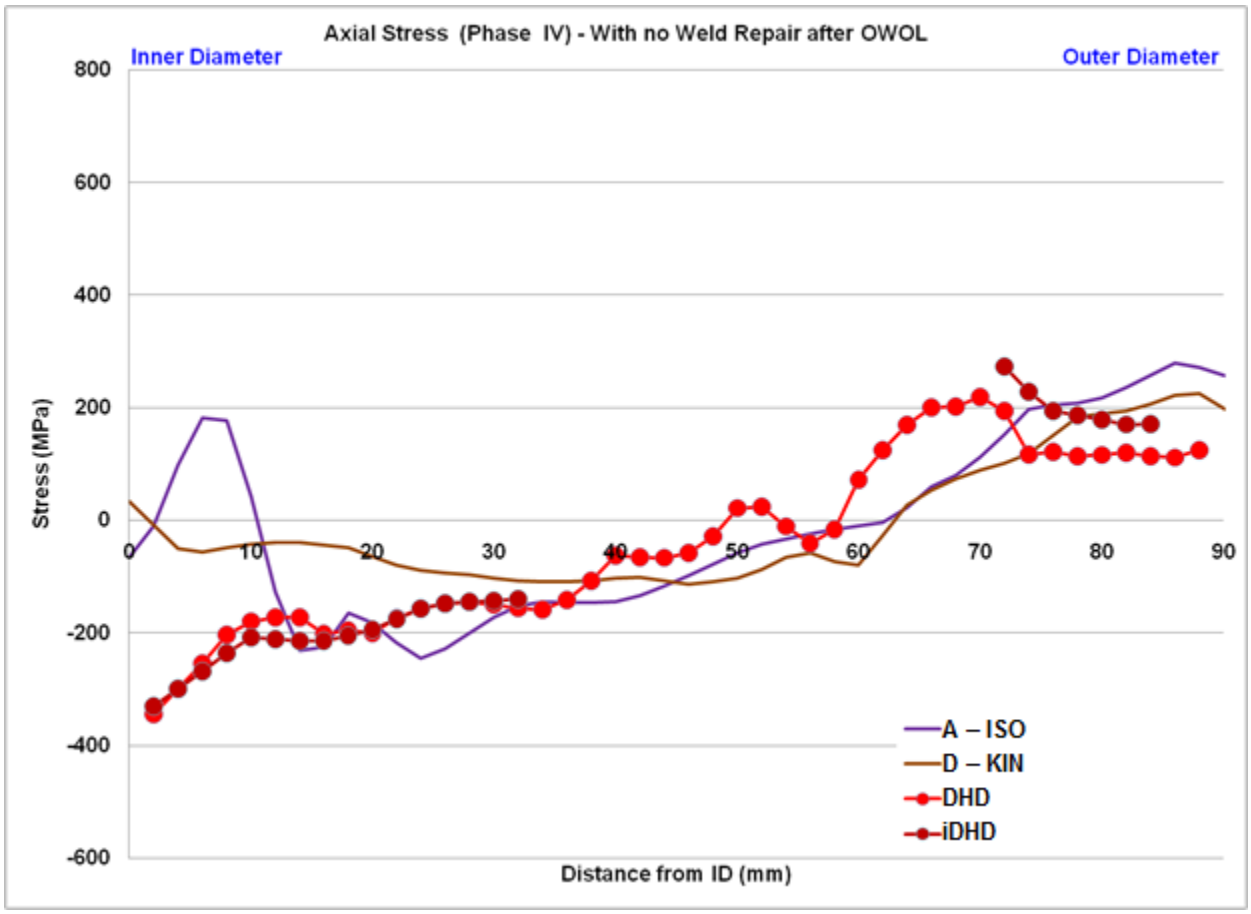

Figure 6-35 Axial Stress Outside the Repair before OWOL

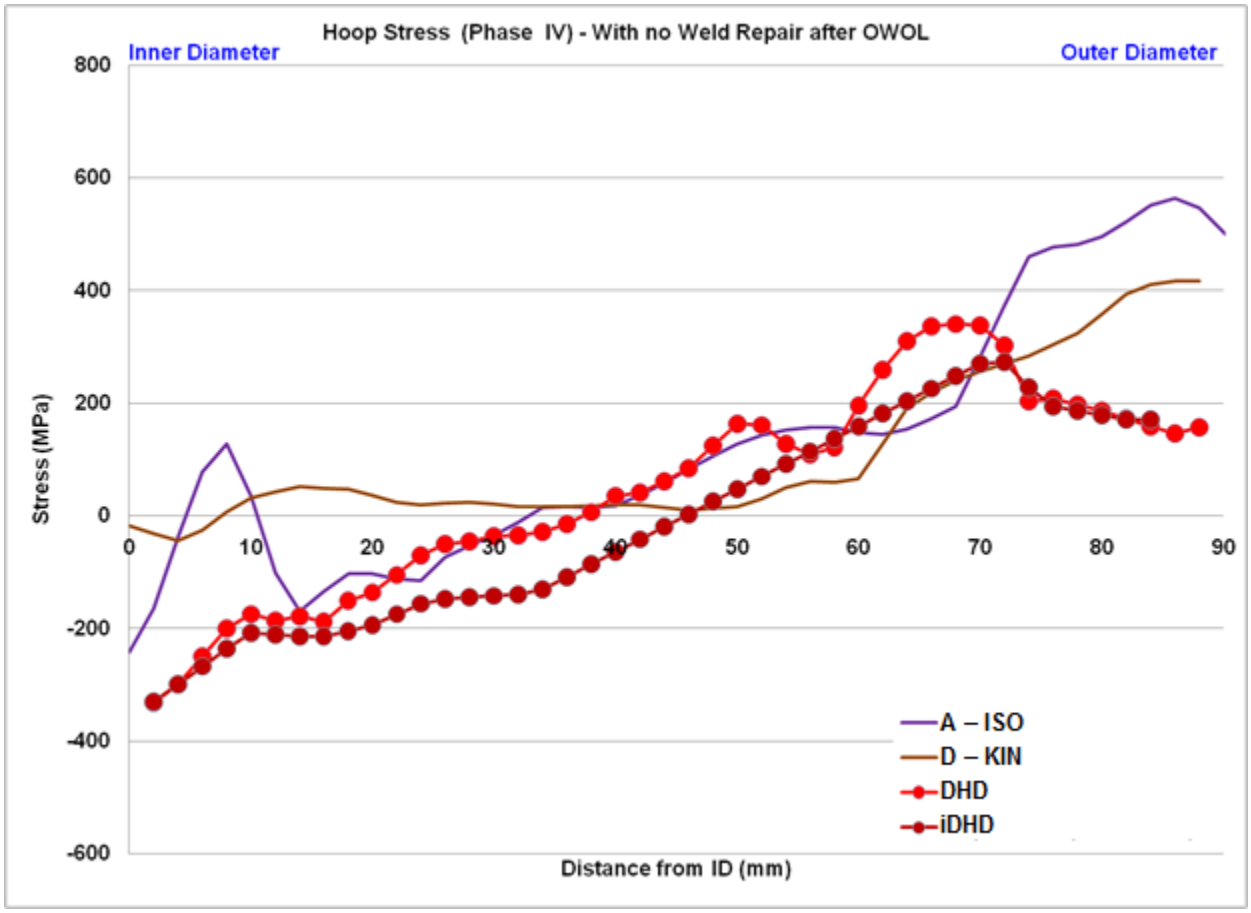

Figure 6-36 Hoop Stress Outside the Repair after OWOL

The FE axial stress predictions showed neutral values at the ID, while the measurements showed strongly compressive stresses greater than the weld material's annealed yield strength. The A prediction again showed the evidence of the root pass re-weld in the inner 10 percent of the wall thickness, but aside from this difference, the two FE predictions matched well. They both showed neutral stresses at the ID and slightly compressive stresses through the thickness, until the stresses turned tensile in the OD area that corresponds with the OWOL thickness. The measurements matched the predictions well past the first 10 percent of the thickness in showing an almost linear increase in stress from the ID to the OD.

The hoop stresses plotted in Figure 6-36 showed agreement through the thickness, but variability was observed at the ID and OD. All of the results showed a neutral to compressive stress at the ID and tensile stress at the OD, and all showed a reduction in inner diameter stress produced by the OWOL.

Figure 6-37 and Figure 6-38 show the averages for the axial and hoop stresses, respectively, outside the weld repair. The curves show the same trends that were presented previously in Figure 6-31 and Figure 6-32 in the weld repair area. The axial stress plot shows very little change due to the application of the OWOL. The hoop stress plot shows that there is a reduction in ID stress due to the application of the OWOL.

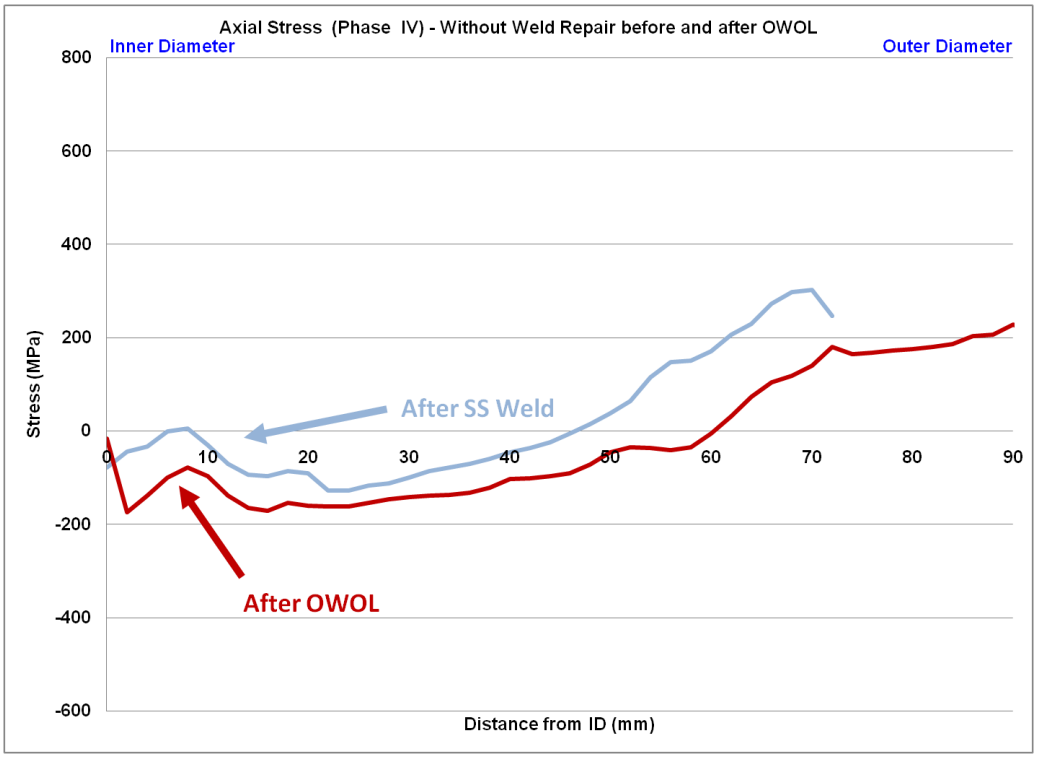

Figure 6-37 Axial Stress Averages before and after OWOL

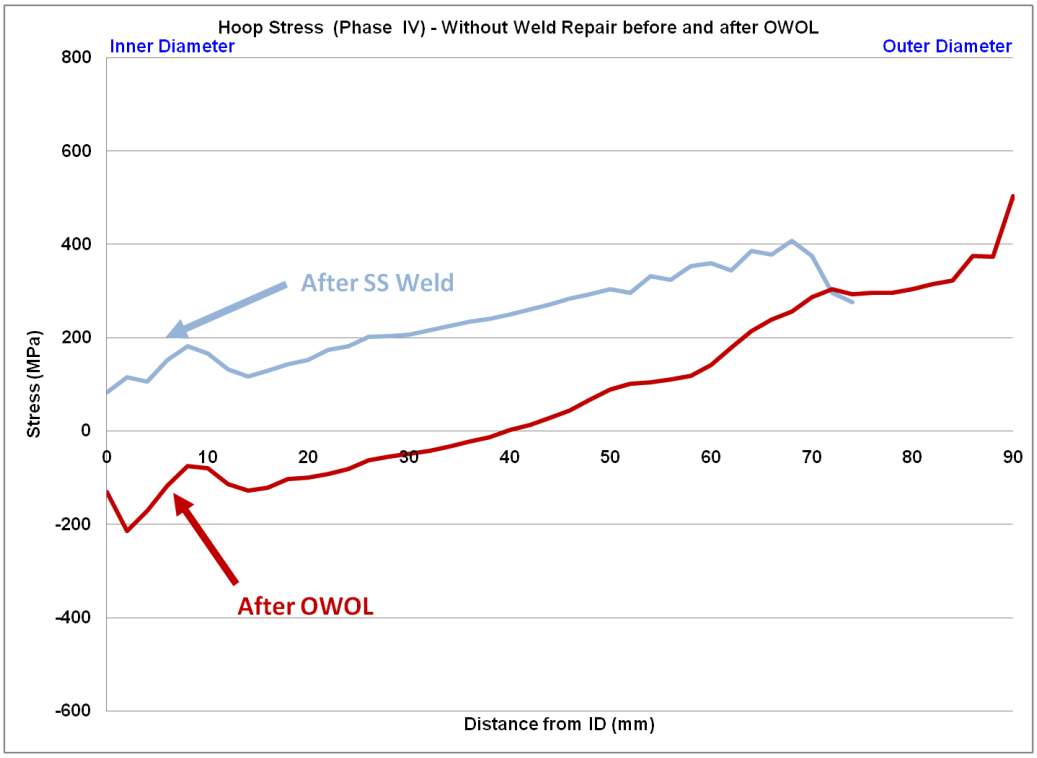

Figure 6-38 Hoop Stress Averages before and after OWOL

6.7 Phase 4 Conclusions

Phase 4 of the WRS Validation Program consisted of measurement and modeling of WRS in a cold leg nozzle intended for nuclear power service, with an OWOL applied to the OD. The purpose of the study was to assess the effectiveness of the OWOL process. This section describes the conclusions from the Phase 4 work.

- The detailed FE studies on OWOL effectiveness provided the following insights.
  - Absent operating temperature and pressure, the safe end to SS pipe closure weld was shown to have the largest beneficial effect on stress for the geometry studied here. Application of the OWOL showed a slight increase in axial stress and a slight decrease in hoop stress, relative to the SS closure weld state.
  - Upon accounting for operating temperature and pressure in the FE model, the OWOL demonstrated a marked improvement in the stresses.
  - Observing the calculated axial stresses after each OWOL layer showed that stresses tended to increase with the first two layers, decrease with the 3rd and 4th layers, and stabilized beginning with the 5th layer. The calculated hoop stresses showed continuous improvement with each layer, although the benefit of the first 3 layers was larger than that of the remaining layers.
  - Modeling results with and without a repair, along with the OWOL, showed some differences. However, the differences were within 50 MPa.
- The modeling round robin, with measurements, supported the following conclusions.
  - Two models in the dataset exhibited trends that were not observed in a majority of the models: specifically, a stress spike and large fluctuations in stress magnitude. Participant B modified the original modeling approach, after the double-blind results were made public, thereby correcting the unusual trends.
  - This work confirmed observations from the OWOL effectiveness study, namely:
    - At room temperature, the beneficial effect of the safe end to SS pipe weld outweighed the effect of the OWOL.
    - The presence of a weld repair does not significantly impact the benefit of the OWOL.

7 WRS UNCERTAINTY SCOPING STUDY

7.1 Background

As discussed in Chapter 1, a nuclear plant licensee may seek temporary relief from required repair/replacement activities or seek to extend established inspection intervals. A fracture mechanics-based flaw growth calculation (e.g., Figure 1-4) is often reviewed by the U.S. Nuclear Regulatory Commission (NRC) before such a request is approved or disapproved. In these flaw evaluations, the Mode I stress intensity factor, K_I, is calculated based upon various operating loads and the assumed through-wall weld residual stress (WRS) distribution. This Chapter uses analytical data from Phases 2a and 4 (Chapters 4 and 6, respectively) as inputs to stress intensity factor and flaw growth calculations to perform a scoping analysis on the effects of uncertainty in WRS prediction.

7.2 Stress Intensity Factor Methods

Current methods for calculating K_I for cracked pipes can be found in [14]-[17], which include the Universal Weight Function Method for surface cracks in cylinders. The American Petroleum Institute (API)-579/ASME Fitness-For-Service-1 standard [17] contains solutions developed under the principle of elastic superposition for a polynomial stress distribution [14]. This method requires fitting the actual stress profile with a 4th order polynomial, as in Equation 7-1.

$$\sigma(x) = \sigma_0 + \sigma_1\left(\frac{x}{t}\right) + \sigma_2\left(\frac{x}{t}\right)^2 + \sigma_3\left(\frac{x}{t}\right)^3 + \sigma_4\left(\frac{x}{t}\right)^4 \qquad \text{Equation 7-1}$$

where, σ_i are fitting coefficients and x is radial position along the pipe wall thickness. The stress intensity factor is then given by

$$K_I = \left[\sigma_0 G_0 + \sigma_1 G_1\left(\frac{a}{t}\right) + \sigma_2 G_2\left(\frac{a}{t}\right)^2 + \sigma_3 G_3\left(\frac{a}{t}\right)^3 + \sigma_4 G_4\left(\frac{a}{t}\right)^4\right]\sqrt{\frac{\pi a}{Q}} \qquad \text{Equation 7-2}$$

where G_i are functions of pipe and flaw dimensions, a is the crack depth, and Q is the flaw shape parameter (Equation 7-3).

$$Q = 1 + 1.464\left(\frac{a}{c}\right)^{1.65} \quad \text{for } a/c \le 1.0$$

$$Q = 1 + 1.464\left(\frac{c}{a}\right)^{1.65} \quad \text{for } a/c > 1.0 \qquad \text{Equation 7-3}$$

where c is half the crack length.

As discussed in [15], the Universal Weight Function Method does not require a polynomial fit to the stress profile. Multiple inflections in WRS profiles can cause difficulties in curve fitting. Figure 7-1 shows curve fits for an example WRS profile.

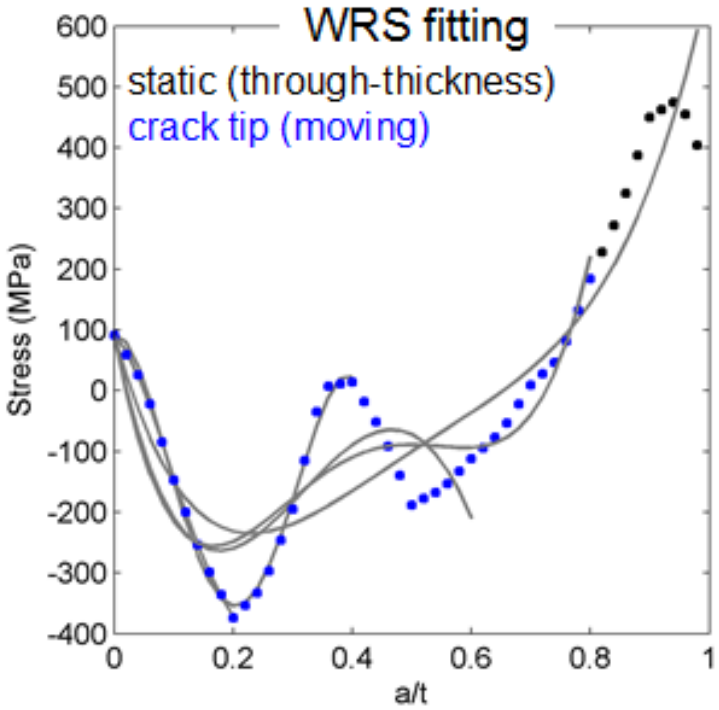

Figure 7-1 Example Curve Fits

The fits in Figure 7-1 show partial curve fits, representing fits up to the crack tip (i.e., "moving fit"), and a complete curve fit (i.e., "static fit"). Researchers [62],[63] have investigated the effect of different curve fitting strategies, as well as the use of polynomial-based equations versus the Universal Weight Function Method. The standard of comparison for these studies was the finite element K_I solution. This previous work has demonstrated that there are cases where the difficulties in polynomial fitting can affect the accuracy of the stress intensity factor calculation.

Figure 7-2 shows the flaw geometry considered in this study. The crack opened to the inside surface of the pipe wall thickness. The stress intensity factor was calculated for two locations along the crack front: the surface point, $K0$, and the deepest point, $K90$.

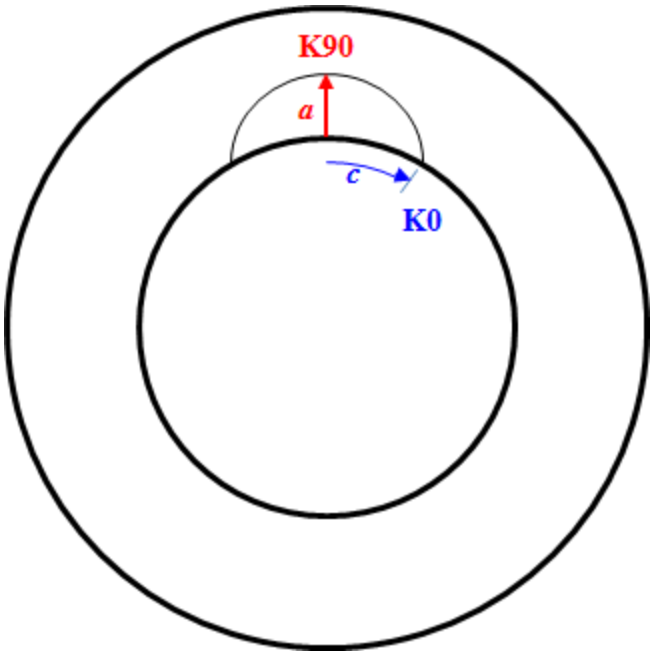

Figure 7-2 Flaw Geometry

The stress intensity factor was calculated assuming R/t = 3, c/a = 5, and a circumferential inner surface-breaking flaw. This work applies the API-579 method to calculate $K0$ and $K90$ given the WRS profiles in Chapters 4 and 6.

7.3 Results and Discussion

7.3.1. Phase 2a Stress Intensity Factor Scoping Analysis

Figure 7-3 shows $K90$ and $K0$ for the Phase 2a axial WRS distributions (see Chapter 4) for different values of a/t before completion of the safe end-to-pipe closure weld. The data points are characterized by whether the WRS input originated with an FE model and a specified hardening law or with measurement data. For $K90$, most of the data points fall below the K_I's for the measured profiles. The spread in the data is approximately 65 MPa√m for $K90$ and 45 MPa√m for $K0$.

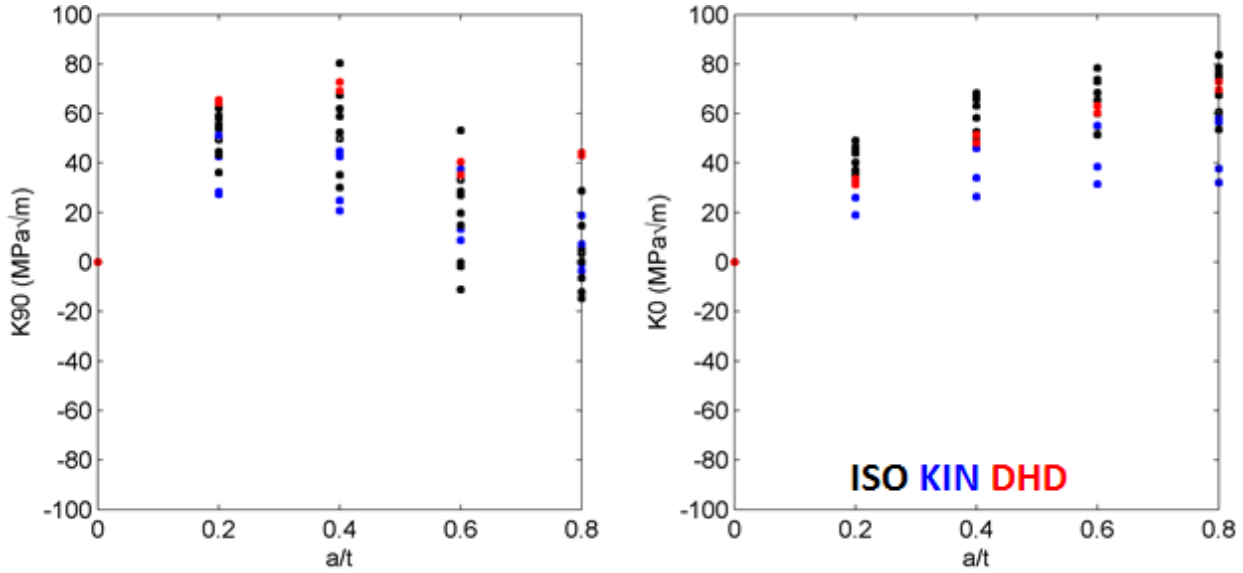

Figure 7-3 Stress Intensity Factor for Axial WRS Profiles, Pre Safe End Weld

Figure 7-4 shows the same results for Phase 2a data after completion of the safe end-to-pipe closure weld. Again, $K90$ based upon the WRS measurements was greater than that based upon WRS predictions. The spread in the stress intensity factor values was as high as 70 MPa√m for $K90$ and 50 MPa√m for $K0$.

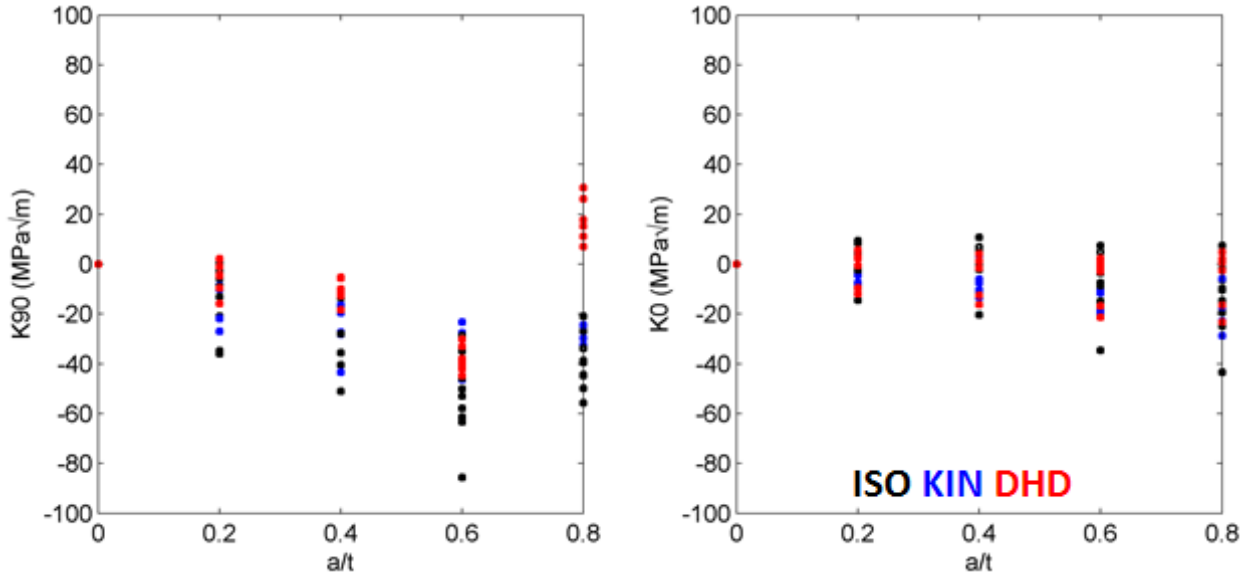

Figure 7-4 Stress Intensity Factor for Axial WRS Profiles, Post Safe End Weld

7.3.2. Phase 4 Stress Intensity Factor Scoping Analysis

Figure 7-5 shows example curve fits for the axial WRS profiles from the Phase 4 results (see Chapter 6). The polynomial fits do not capture every feature of the finite element (FE) profiles.

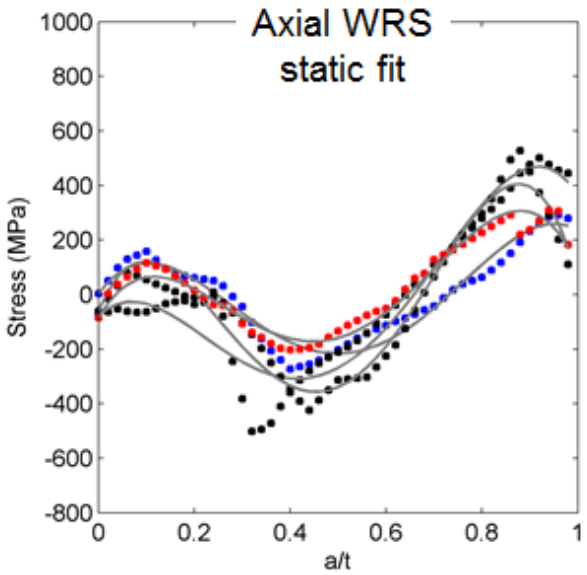

Figure 7-5 Example Fits of Phase 4 Data

Figure 7-6 shows $K90$ for FE WRS profiles prior to completion of the SS closure weld. There were no measurement data on the Phase 4 mockup in this state. The spread in this data is approximately 40 MPa√m.

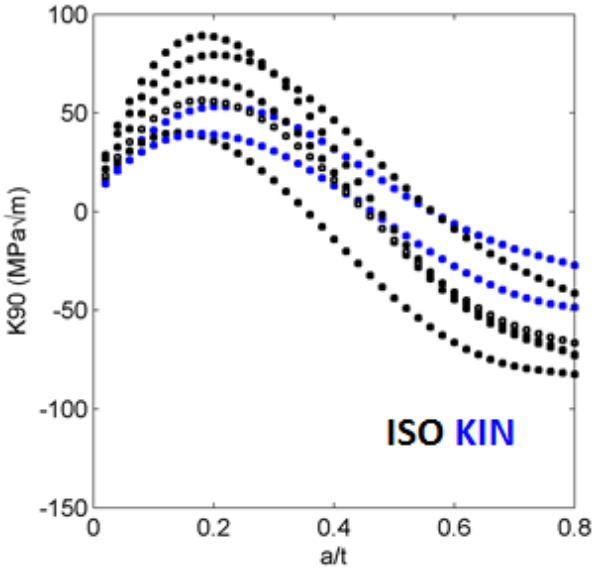

Figure 7-6 Stress Intensity Factor, Before Closure Weld

Figure 7-7 shows $K90$ calculated with a static fit and a moving fit of the WRS profile. The stress magnitudes were similar for the two cases, but the profile shapes were different. The red curve in Figure 7-7 was calculated from the measured profile, and it was generally higher than the other cases. The maximum spread in this data was approximately 85 MPa√m.

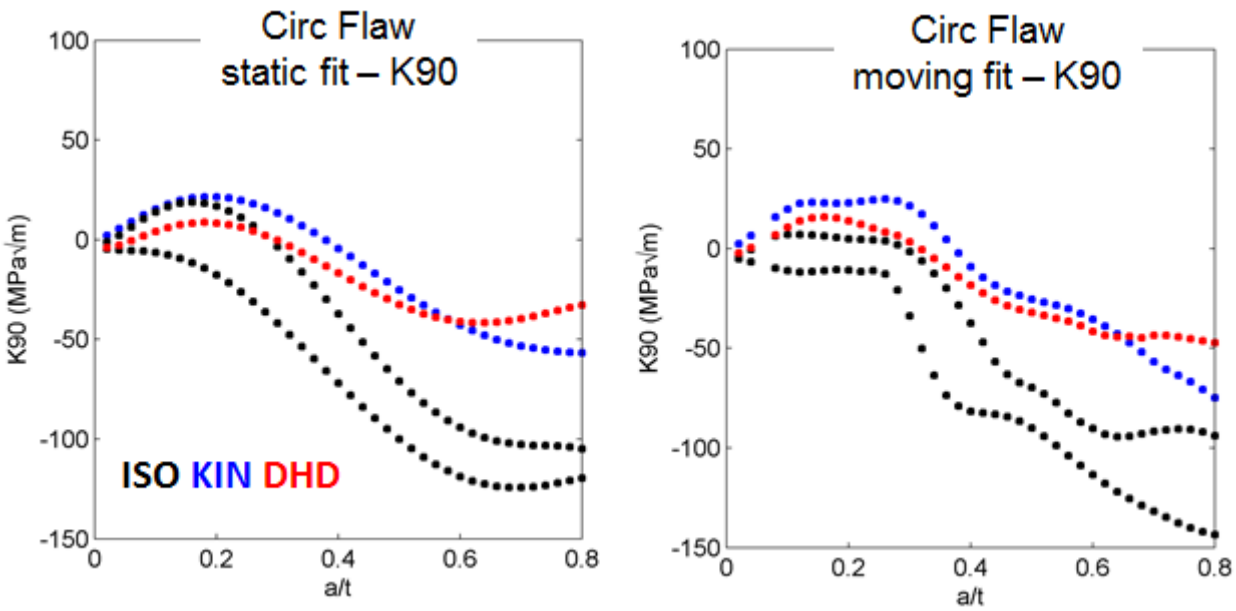

Figure 7-7 Stress Intensity Factor for Phase 4 Axial WRS

7.3.3. Phase 2a Flaw Evaluation Scoping Analysis

This Section extends the scoping analysis in Sections 7.3.1 and 7.3.2 to a flaw growth calculation to illustrate the effect of the variation in calculated weld residual stresses. Flaw growth calculations involve additional assumptions on operating loads, initial flaw geometry, and crack growth law. Table 7-1 shows the inputs used in this analysis.

Table 7-1 Inputs for Flaw Evaluation Scoping Study

Initial Flaw Geometry					
a/t	c/a	Orientation			
0.1	2	Circumferential			
Operating Loads					
σ_m [MPa]		σ_b [MPa]			
36.9		43.2			
WRS, $\sigma(x) = \sigma_0 + \sigma_1\left(\frac{x}{t}\right) + \sigma_2\left(\frac{x}{t}\right)^2 + \sigma_3\left(\frac{x}{t}\right)^3 + \sigma_4\left(\frac{x}{t}\right)^4$					
Case	σ_0 [MPa]	σ_1 [MPa]	σ_2 [MPa]	σ_3 [MPa]	σ_4 [MPa]
WRS1	550.36	1030.8	-10098	14568	-5655.5
WRS2	320.68	-481.09	-5297.4	10019	-4562.7

σ_m – axial membrane stress, σ_b – axial bending stress

The WRS curves in Table 7-1 (WRS1 and WRS2) are shown graphically in Figure 7-8. They represent an envelope of the entire pre-stainless steel closure weld Phase 2a data, rather than any single one calculated WRS curve. Flaw growth calculations were performed using the crack growth law described in MRP-115 [64]. The stress intensity factors and flaw depth are shown versus time in Figure 7-9 for three cases: WRS measurement from Phase 2a, the WRS1

curve, and the WRS2 curve. The stress intensity factor curve based upon the measurements also shows ±10 MPa√m bars, which is a validation criterion suggested in MRP-287 [27]. These upper and lower bound WRS inputs lead to very different flaw growth results. While these results are not tied to a single calculation or specific for an operating weld at a plant, Figure 7-9 clearly shows the need to address the variability in calculated weld residual stresses as identified in this program.

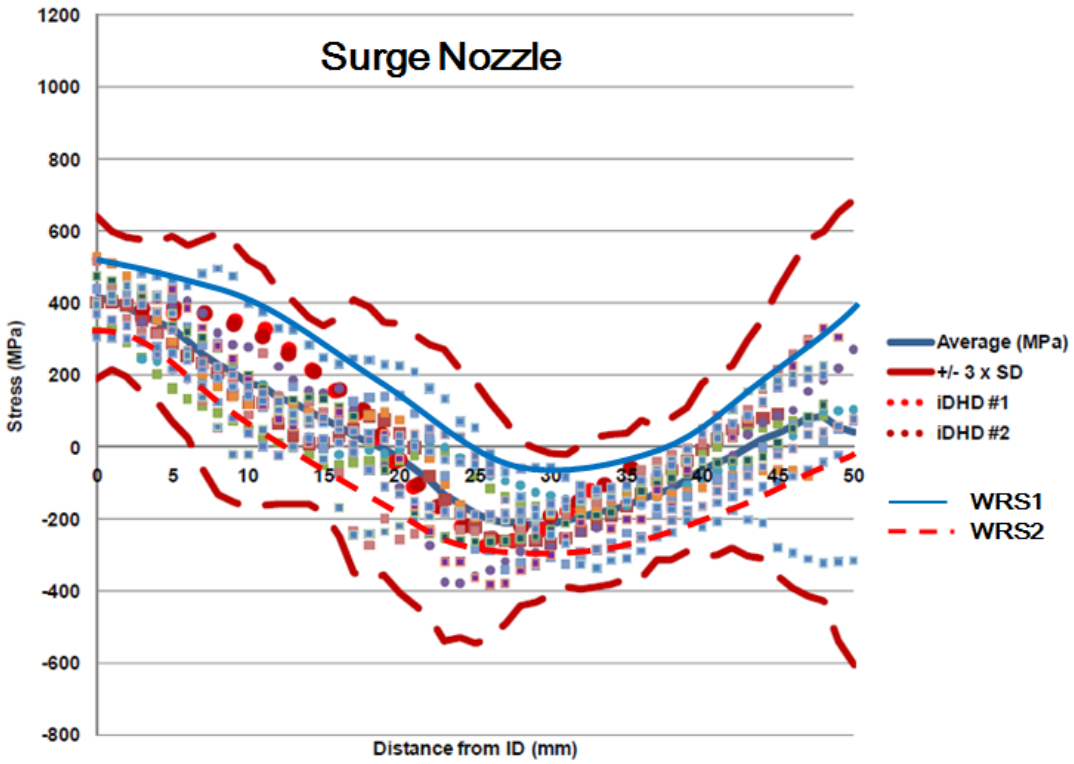

Figure 7-8 Extreme WRS Inputs

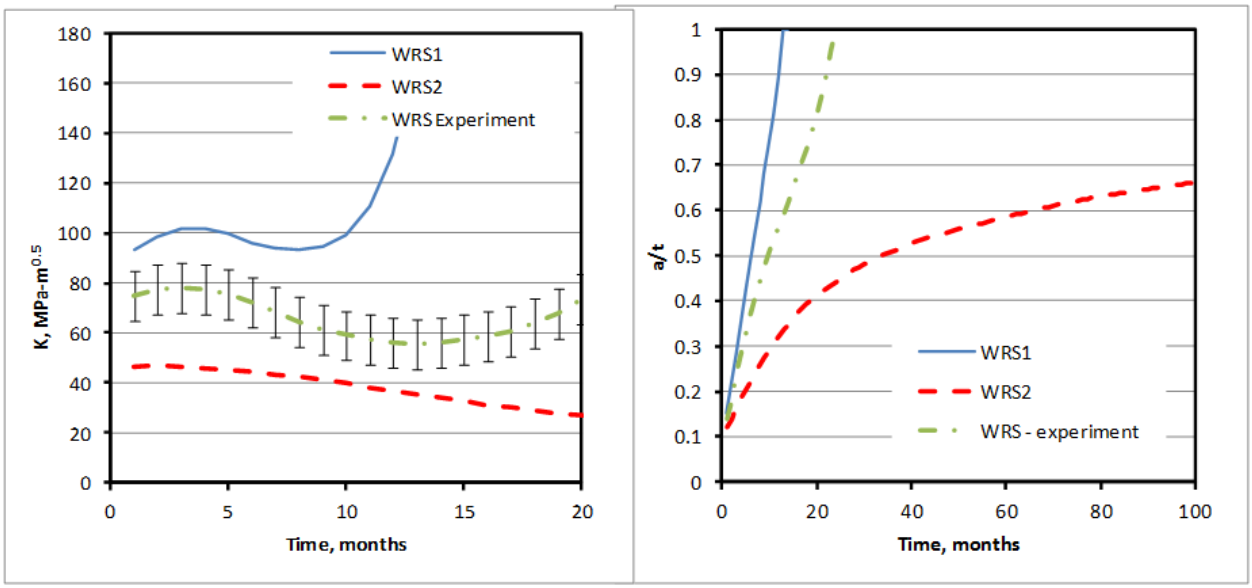

Figure 7-9 Stress Intensity Factor and Flaw Depth against Time

The flaw evaluation scoping analysis presented in Section 7.3.3 is subject to the following limitations.

- The data in Figure 7-8 includes WRS predictions with different hardening law assumptions. Formulating guidance on hardening law choice is one option for reducing modeling uncertainty.
- The WRS inputs to this analysis do not represent any single analyst's prediction.
- The data in Figure 7-8 is based upon WRS predictions made prior to the stainless steel closure weld, which is conservative for most welds of this type.

7.4 WRS Uncertainty Conclusions

The purpose of the work described in Chapter 7 was to make an initial assessment of the observed modeling uncertainty demonstrated in Chapters 4 and 6. These analyses do not evaluate the effectiveness of WRS modeling in the prediction of crack growth, but instead they illustrate the need to reduce the modeling uncertainty. This section describes the conclusions from this work.

- The WRS profiles from the FE studies can be difficult to fit with a polynomial. Literature studies have suggested that, despite the poor fit, reasonable stress intensity factors can be obtained from the polynomial-based equations. The Universal Weight Function Method [15],[16] offers an approach that does not rely on polynomial fitting and that improves the accuracy of the calculation for certain cases.
- When the stress intensity factor results in Figure 7-3 and Figure 7-4 are discriminated by the data source, the approximate spread in stress intensity factor calculations is as follows.
  - 60 MPa√m for predictions based upon isotropic hardening
  - 40 MPa√m for predictions based upon kinematic hardening, and
  - 25 MPa√m for the deep hole drilling measurements
- The fitting procedure can be executed in two ways: a static fit, where the entire WRS profile is fit for each crack depth considered, and a moving fit, where the WRS profile is fit only up to the crack tip. This work showed that stress intensity factor magnitudes were similar for each case, but that the profile shape did change depending on the method chosen.
- Model validation criteria could potentially be based upon calculation of stress intensity factor with measured and modeled WRS distributions. The extremes of the observed data in the Phase 2a results did not meet a ±10 MPa√m criterion, which is a validation criterion suggested in MRP-287 [27]. However, filtering the data by hardening law type decreases the extremes, but does not allow the data to fall within the ±10 MPa√m criterion.
- The scoping analysis presented in Chapter 7, which focused on the conservative extremes of the WRS modeling results, demonstrated a large impact on primary water stress corrosion crack growth. Continued research is needed to develop finite element modeling guidelines that reduce modeling uncertainty to acceptable limits and to develop quantitative acceptance criteria for model validation.

8 CONCLUSIONS

The work in this report represents first-of-a-kind, double-blind weld residual stress WRS modeling and measurement campaigns on prototypic safety-related nuclear component mockups. While a variety of measurement techniques were initially considered for this work, strain-relief techniques proved to be the most reliable for the materials of interest. Application of diffraction techniques is possible, but the complicating effects of large grain size, crystallographic texture, and chemical concentration gradients present in these welds must be overcome to obtain reasonable results.

The finite element models considered in the modeling round robin studies were predominately 2-D axisymmetric models. The model results did not always agree perfectly in trend and magnitude with the experimental data. However, there were cases where the average of the modeling results showed reasonable agreement with the experiments. A relatively large degree of analyst-to-analyst scatter was observed in this work. The effect of the observed scatter was evaluated in Chapter 7 by considering stress intensity factor calculations and flaw growth calculations. This work demonstrated the need to develop appropriate modeling guidelines to reduce uncertainty in WRS prediction.

Since plastic deformation is expected during the thermal cycles associated with welding, an appropriate strain hardening law must be chosen to predict the change in the yield surface due to plastic strain history. The choice of hardening law had a large effect on the modeling results. While the mixed hardening law provides the most accurate description of material behavior, the experimentation required to develop the material parameters is resource intensive. Developing guidelines for dealing with the hardening law issue will be important in future efforts. Post processing of FE results presents another potential source of uncertainty. For instance, no guidelines for extracting results were provided to the round robin participants in each research phase. This led to data massaging after the fact to promote reasonable comparisons among the various submissions. Other sources of uncertainty, such as process sequence, were identified through modeling sensitivity studies in this work.

The concept of quantitative validation of WRS models or modeling procedures is not straight forward. The European R6 code and the Electric Power Research Institute's Materials Reliability Program-287 report have suggested criteria for model validation (see Chapter 2), but this report does not endorse those criteria. Nor does this report define alternative criteria for model validation. The data found in this report, along with data collected in future efforts, may help to define validation criteria going forward. The work in Chapter 7 demonstrated the difficulties of developing quantitative, objective acceptance criteria with such large uncertainties in WRS prediction. Therefore, development of modeling guidelines to minimize analyst-to-analyst uncertainty will also be important for establishing acceptance criteria.

9 KNOWLEDGE GAPS

The following lists the six U.S. Nuclear Regulatory Commission (NRC) objectives for the Weld Residual Stress Validation Program identified in Chapter 1.

- Validate axisymmetric finite element modeling as a predictive tool for WRS, using robust experimental methods.
- Support the NRC's Office of Nuclear Reactor Regulation in development of appropriate WRS/flaw evaluation review guidelines.
- Perform independent confirmatory research on industry guidance for executing WRS analysis.
- Assess and evaluate the near-term adequacy of industry's mitigation activities where WRS minimization is necessary.
- Improve WRS finite element analysis predictive methodologies.
- Determine estimates for WRS uncertainty distributions, which are needed in probabilistic analyses (e.g., xLPR Code–eXtremely Low Probability of Rupture [25],[26]).

Development of flaw evaluation guidelines for NRC reviewers is linked to an informed judgment of expected modeling uncertainty. Knowledge gaps to address this objective include a lack of validation criteria, a large degree of modeling uncertainty, and a lack of guidance for FE modeling of WRS. Future efforts should focus on resolving these open issues. One avenue for addressing these concerns is producing ASME Code guidance for WRS input development, which NRC staff has been actively engaged in.

An accurate description of WRS uncertainty distributions for probabilistic assessments has not been formulated. Preliminary work in the xLPR project has applied more rigorous statistical tools than considered in this report to quantify uncertainty of WRS profiles. Lessons learned in modeling practices from this work, including choice of hardening law and post processing, were applied to the xLPR project. Additional modeling efforts specific to the xLPR project were an ongoing effort as of publication of this document.

10 FUTURE WORK

The U.S. Nuclear Regulatory Commission should focus future weld residual stress research on addressing the knowledge gaps developed in the previous section. Suggestions for future work are as follows.

- Develop specific validation criteria for comparing WRS measurement and modeling results.
- Establish guidelines for WRS input development for deterministic flaw evaluations, including finite element best practices, should be established.
- Develop additional guidance for accounting for uncertainty in WRS inputs for flaw evaluations.
- Focus future finite element round robin studies on reducing model-to-model variability, given lessons learned in FE modeling best practices.
- Apply more robust methods to quantify modeling uncertainty in future round robin efforts.

11 REFERENCES

[1] W. J. Shack, “Measurement of Throughwall Residual Stresses in Large Diameter Type 304 Stainless Steel Piping Butt Weldments,” ANL-82-15, Argonne National Laboratory, March 1982.

[2] D. J. Shim, S. Kalyanam, E. Punch, T. Zhang, F. W. Brust, G. Wilkowski, A. Goodfellow, and M. Smith, “Advanced Finite Element Analysis (AFEA) Evaluation for Circumferential and Axial PWSCC Defects”, Proceedings of the 2010 ASME Pressure Vessel Piping Conference, Seattle, WA, PVP2010-25162, July 2010.

[3] D. Rudland, T. Zhang, G. Wilkowski, and A. Csontos, “Welding Residual Stress Solutions for Dissimilar Metal Surge Line Nozzles Welds,” Proceedings of the ASME Pressure Vessels and Piping Conference, Chicago, IL, PVP2008-61285, July 2008.

[4] A. T. Howell, “Degradation of the Davis-Besse Nuclear Power Station Reactor Pressure Vessel Head Lessons Learned Report,” U.S. Nuclear Regulatory Commission Memorandum, September 2002 [ML022740211].

[5] A. T. Howell, “Davis-Besse Reactor Vessel Head Degradation Lessons-Learned Task Force Report,” U.S. Nuclear Regulatory Commission Technical Report, September 2002 [ML022760172].

[6] NUREG/BR-0353, Rev. 1, “Davis-Besse Reactor Pressure Vessel Head Degradation,” U.S. Nuclear Regulatory Commission, August 2008

[7] D. Rudland, Y. Chen, T. Zhang, G. Wilkowski, J. Broussard, and G. White, “Comparison of Welding Residual Stress Solutions for Control Rod Drive Mechanism Nozzles,” Proceedings of the ASME Pressure Vessels and Piping Conference, San Antonio, TX, PVP2007-26045, 2007.

[8] M. T. Anderson, T. Zhan, D. Rudland, and G. Wilkowski, “Final Report – Inspection Limit Confirmation for Upper Head Penetration Nozzle Cracking,” PNNL-17763, U.S. Department of Energy, August 2008.

[9] E. J. Sullivan, A. A. Csontos, T. R. Lupold, and C.-F. Sheng, “Regulatory Perspective on Advanced Finite Element Flaw Growth of Alloy 82/182 Butt Welds,” Proceedings of the ASME Pressure Vessels and Piping Conference, Chicago, IL, PVP2008-61485, 2008.

[10] G. A. White and J. E. Broussard, MRP-216, “Materials Reliability Program: Advance FEA Evaluation of Growth of Postulated Circumferential PWSCC Flaws in Pressurizer Nozzle Dissimilar Metal Welds,” Electric Power Research Institute, Report 1015400, August 2007.

[11] P. Donavin, G. G. Elder, and W. H. Bamford, “Technical Basis Document for Alloy 82/182 Weld Inspection Code Case N-770,” ASME International, BC 07-514, August 2008.

[12] Case N-770, “Alternative Examination Requirements and Acceptance Standards for Class 1 PWR Piping and Vessel Nozzle Butt Welds Fabricated with UNS N06082 or UNS W86182 Weld Filler Material with or without Application of Listed Mitigation Activities,” ASME International, June 2011.

[13] ASME Boiler & Pressure Vessel Code, Section XI (2008a), “Rules for Inservice Inspection of Nuclear Power Plant Components,” ASME International, New York, NY, July 2008.

[14] T. L. Anderson, Fracture Mechanics: Fundamentals and Applications, 3rd Edition, Taylor & Francis Group, LLC, Boca Raton, FL, 2005.

[15] S. X. Xu, D. A. Scarth, and R. C. Cipolla, “Technical Basis for Proposed Weight Function Method for Calculation of Stress Intensity Factor for Surface Flaws in ASME Section XI Appendix A,” Proceedings of the 2011 ASME Pressure Vessel Piping Conference, Baltimore, MD, PVP2011-57911, July 2011.

[16] S. X. Xu, D. A. Scarth, and R. C. Cipolla, “Calculation of Stress Intensity Factor for Surface Flaws using Universal Weight Functions with Piece-Wise Cubic Stress Interpolation,”

Proceedings of the ASME Pressure Vessels and Piping Conference, Toronto, Canada, PVP2012-78236, July 2012.
[17] API 579-1/ASME FFS-1, Fitness-for-Service, API Publishing Services, Washington, DC, 2007.
[18] Letter from J. E. Dyer to Jay K. Thayer dated March 5, 2007, U. S. Nuclear Regulatory Commission (ML070640401).
[19] Letter from William J. Shack to Luis Reyes, "Proposed NRC Staff and Industry Activities for Addressing Dissimilar Metal Weld Issues Resulting from the Wolf Creek Pressurizer Weld Inspection Results," March 22, 2007 (ML070240140).
[20] N. Taylor, C. Faidy, and P. Gilles, Eds, "Assessment of Dissimilar Weld Integrity: Final Report of the NESC-III Project," European Communities, Luxembourg, EUR 22510 EN, 2006.
[21] R6 Revision 4, "Assessment of the Integrity of Structures Containing Defects," British Energy, April 2001.
[22] H. J. Rathbun, L. F. Fredette, P. M. Scott, A. A. Csontos, and D. L. Rudland, "NRC Welding Residual Stress Validation Program International Round Robin Program and Findings," Proceedings of the ASME Pressure Vessels and Piping Conference, Baltimore, MD, PVP2011-57642, July 2011.
[23] L. F. Fredette, M. Kerr, H. J. Rathbun, and J. E. Broussard, "NRC/EPRI Welding Residual Stress Validation Program: Phase III - Details and Findings," Proceedings of the ASME Pressure Vessels and Piping Conference, Baltimore, MD, PVP2011-57645, July 2011.
[24] T. Zhang, F. W. Brust, and G. Wilkowski, "Weld Residual Stress in Large Diameter Nuclear Nozzles," Proceedings of the ASME Pressure Vessels and Piping Conference, Baltimore, MD, PVP2011-57959, July 2011.
[25] C. Harrington and D. Rudland, NUREG-2110/EPRI 1022860, "xLPR Pilot Study Report," U.S. Nuclear Regulatory Commission/Electric Power Research Institute, Washington, DC, February 2012.
[26] D. Rudland and C. Harrington, "Initial Development of the Extremely Low Probability of Rupture (xLPR) Version 2.0 Code," Proceedings of the ASME Pressure Vessels and Piping Conference, Toronto, Canada, PVP2012-78186, July 2012.
[27] C. Harrington, 'Materials Reliability Program: Primary Water Stress Corrosion Cracking Flaw Evaluation Guidance (MRP-287)," Report 1021023, Electric Power Research Institute, Palo Alto, CA, December 2010.
[28] B. D. Cullity and S. R. Stock, Elements of X-Ray Diffraction, 3rd Edition, Prentice Hall, Upper Saddle River, New Jersey, 2001.
[29] X-L. Wang, Z. Feng, S. Spooner, C. R. Hubbard, and B. Taljat, "Characterization of Welding Residual Stresses with Neutron Diffraction," Proc. Taiwan Int. Welding Conf., 155-161, 1998.
[30] I. C. Noyan and J. B. Cohen, Residual Stress Measurement by Diffraction and Interpretation, Springer-Verlag, New York, New York, 1987.
[31] Aaron D. Krawitz, Introduction to Diffraction in Materials Science and Engineering, John Wiley & Sons, Inc. New York, NY, 2001.
[32] E. J. Kingston, D. Stefanescu, A. H. Mahmoudi, C. E. Truman, and D. J. Smith, "Novel Applications of the Deep-Hole Drilling Technique for Measuring Through-Thickness Residual Stress Distributions," Journal of ASTM International, Vol. 3, No. 4, April 2006.
[33] A. H. Mahmoudi, S. Hossain, C. E. Truman, D. J. Smith, and M. J. Pavier, "A New Procedure to Measure Near Yield Residual Stresses using the Deep Hole Drilling Technique," Journal of Experimental Mechanics, Vol. 49, No. 4, August 2009.
[34] A. H. Mahmoudi, D. J. Smith, C. E. Truman, and M. J. Pavier, "Application of the Modified Deep Hole Drilling Technique (iDHD) for Measuring Near Yield Non-Axisymmetric

Residual Stresses," Proceedings of the ASME Pressure Vessels and Piping Conference, Prague, Czech Republic, PVP2009-77940, July 2009.
[35] M. B. Prime, "Cross-Sectional Mapping of Residual Stresses by Measuring the Surface Contour after a Cut," Journal of Engineering Materials and Technology, Vol. 123, April 2001, pp. 162-168.
[36] A. T. DeWald, J. E. Rankin, M. R. Hill, M. J. Lee, and H.-L. Chen, "Assessment of Tensile Residual Stress Mitigation in Alloy 22 Welds Due to Laser Peening," Journal of Engineering Materials and Technology, Vol. 126, October 2004, pp. 465-473.
[37] A. T. DeWald, M. R. Hill, and E. Willis, "Measurement of Welding Residual Stress in Dissimilar Metal Welds Using the Contour Method," Proceedings of the ASME 2011 Pressure Vessels & Piping Division Conference, Baltimore, MD, PVP2011-57720, 2011.
[38] M. B. Prime, R. J. Sebring, J. M. Edwards, D. J. Hughes, and P. J. Webster, "Laser Surface-Contouring and Spline Data-Smoothing for Residual-Stress Measurement, Experimental Mechanics, Vol. 44, No. 2, 2004, pp. 176-184.
[39] J. Broussard, "Materials Reliability Program: Welding Residual Stress Dissimilar Metal Butt-Weld Finite Element Modeling Handbook (MRP-317)," Report 1022862, Electric Power Research Institute, Palo Alto, CA, December 2011.
[40] J. Goldak, A. Chakravarti, and M. Bibby, "A New Finite Element Model for Welding Heat Sources," Metallurgical Transactions B, Vol. 15B, 1984, pp. 299-305.
[41] Z. Feng, K. Wolfe, and E. Willis, "A Computational Modeling Tool for Welding Repair of Irradiated Materials," 19th International Conference on Nuclear Engineering, May 16-19, 2011, Chiba, Japan, ICONE19-44103.
[42] B. Taljat, T. Zacharia, X.-L. Wang, J. R. Keiser, R. W. Swinderman, Z. Feng, and M. J. Jirinec, "Numerical Analysis of Residual Stress Distribution in Tubes with Spiral Weld Overlay," Welding Journal, Vol. 77, 1998, pp. 328s-335.
[43] Z. Feng, "A Computational Analysis of Thermal and Mechanical Conditions for Weld Metal Solidification Cracking," Welding in the World, Vol. 33, 1994, pp. 340-347.
[44] D. Rudland, R. Kurth, B. Bishop, P. Mattie, H. Klasky, and D. Harris, "Development of Computational Framework and Architecture for Extremely Low Probability of Rupture (xLPR) Code," Proceedings of the ASME Pressure Vessels and Piping Conference, Seattle, WA, PVP2010-25963, July 2012.
[45] J. Broussard, "Materials Reliability Program: Finite-Element Model Validation for Dissimilar Metal Butt-Welds (MRP-316)," Electric Power Research Institute, EPRI 1022861, December 2011.
[46] 2010 ASME Boiler & Pressure Vessel Code, Section II Part A, "Ferrous Materials Specification," SA-240/SA-240M, ASME International, New York, NY, July 2011.
[47] 2010 ASME Boiler & Pressure Vessel Code, Section II Part C, "Specifications for Welding Rods, Electrodes, and Filler Metals," SFA-5.14/SFA5.14M, ASME International, New York, NY, July 2011.ASME II
[48] D.W. Brown, T. M. Holden, B. Clausen, M. B. Prime, T. A. Sisneros, H. Swenson, and J. Vaja, "Critical Comparison of Two Independent Measurements of Residual Stress in an Electron-Beam Welded Uranium Cylinder: Neutron Diffraction and the Contour Method," Acta Materialia, Vol. 59, No. 3, 2011, pp. 864-873.
[49] M. Kerr, D. L. Rudland, M. B. Prime, H. Swenson, M. A. Buechler, and B. Clausen, "Characterization of a Plate Specimen from Phase I of the NRC/EPRI, Weld Residual Stress Program," Proceedings of the ASME Pressure Vessels and Piping Conference, Baltimore, MD, PVP2011-57687, July 2011.
[50] D. L. Rudland, A. Csontos, F. W. Brust, and T. Zhang, "Welding Residual Stress and Flaw Evaluation for Dissimilar Metal Welds with Alloy 52 Inlays," Proceedings of the ASME Pressure Vessels and Piping Conference, Prague, Czech Republic, PVP2009-77167, July 2009.

[51] L. Fredette and P. Scott, “Evaluation of Full Structural and Optimized Weld Overlays As Mitigation Strategies for Primary Water Stress Corrosion Cracking in Pressurized Water Reactors,” US Nuclear Regulatory Commission Report, U.S. NRC Agencywide Data Access and Management System (ADAMS) Accession Number ML101260540, April 2010.
[52] L. Fredette and P. Scott, “Evaluation of the Mechanical Stress Improvement Process (MSIP) as a Mitigation Strategy for Primary Water Stress Corrosion Cracking in Pressurized Water Reactors,” US Nuclear Regulatory Commission Report, U.S. NRC Agencywide Data Access and Management System (ADAMS) Accession Number ML092990646, September, 2009.
[53] C. King and G. Frederick, “Non-Proprietary Version, Materials Reliability Program: Technical Basis for Preemptive Weld Overlays for Alloy 82/182 Butt Welds in PWRs (MRP-169),” EPRI Report Number 1012843, Electric Power Research Institute, Palo Alto, CA, 2005.
[54] ASME Code Case N-504-4, “Alternative Rules for Repair of Classes 1, 2, and 3 Austenitic Stainless Steel Piping,” Section XI, Division I, July 2006.
[55] ASME Code Case N-754, “Optimized Structural Dissimilar Metal Weld Overlay for Mitigation of Class 1, 2, and 3 Items,” Section XI, Division I, January 2009.
[56] ABAQUS User Manual, Simulia, Dassault Systems, version 6.10, 2010.
[57] F.W. Brust, T. Zhang, D.-J.Shim, S. Kalyanam, G. Wilkowski, M. Smith, and A. Goodfellow, “Summary of Weld Residual Stress Analyses for Dissimilar Metal Weld Nozzles,” Proceedings of the 2010 ASME Pressure Vessel Piping Conference, Seattle, WA, PVP2010-25162, July 2010.
[58] L. Fredette, P. Scott, and F. W. Brust, “An Analytical Evaluation of the Efficacy of the Mechanical Stress Improvement Process in Pressurized Water Reactor Primary Cooling Piping,” Proceedings of the 2008 ASME Pressure Vessels and Piping Conference, Chicago, IL, PVP2008-61484, July 2008.
[59] L. Fredette, P. Scott, F. W. Brust, and A. Csontos, “An Analytical Evaluation of the Efficacy of the Mechanical Stress Improvement Process in Pressurized Water Reactor Primary Cooling Piping,” Proceedings of the 2009 ASME Pressure Vessels and Piping Conference, Prague, Czech Republic, PVP2009-77327, July 2009.
[60] K. Ogawa, L. A. Chidwick, E. J. Kingston, I. Muroya, Y. Iwamoto, and D. J. Smith, “Measurement of Residual Stresses in the Dissimilar Metal Weld Joint of a Safe-End Nozzle Component,” Proceedings of the 2009 ASME Pressure Vessels and Piping Conference, Prague, Czech Republic, PVP2009-77830, July 2009.
[61] D. Rudland, T. Zhang, G. Wilkowski, and A. Csontos, “Welding Residual Stress Solutions for Dissimilar Metal Surge Line Nozzles Welds,” Proceedings of the 2008 ASME Pressure Vessels and Piping Conference, Chicago, Illinois, PVP2008-61285, July 2008.
[62] D. A. Scarth and S. Xu, “Closed-Form Calculation of Stress Intensity Factor for an Axial ID Surface Flaw in Cylinder Subjected to Weld Residual Stresses,” Proceedings of the 2013 ASME Pressure Vessels and Piping Conference, Chicago, Illinois, PVP2013-97522, July 2013.
[63] D. J. Shim, M. Kerr, and S. Xu, “Effect of Weld Residual Stress Fitting on Stress Intensity Factor for Circumferential Surface Cracks in Pipe,” Proceedings of the 2012 ASME Pressure Vessels and Piping Conference, Toronto, Ontario, Canada, PVP2012-78180, July 2012.
[64] J. Hickling, “Materials Reliability Program: Crack Growth Rates for Evaluating Primary Water Stress Corrosion Cracking of Alloy 82, 182, and 132 Welds (MRP-115),” Electric Power Research Institute, EPRI 1006696, November 2004.

NRC FORM 335
(12-2010)
NRCMD 3.7

U.S. NUCLEAR REGULATORY COMMISSION

BIBLIOGRAPHIC DATA SHEET

(See instructions on the reverse)

1. REPORT NUMBER
(Assigned by NRC, Add Vol., Supp., Rev., and Addendum Numbers, if any.)

NUREG-2162

2. TITLE AND SUBTITLE

Weld Residual Stress Finite Element Analysis Validation: Part 1 - Data Development Effort

3. DATE REPORT PUBLISHED

MONTH	YEAR
March	2014

4. FIN OR GRANT NUMBER

5. AUTHOR(S)

Michael L. Benson, David L. Rudland, and Aladar A. Csontos

6. TYPE OF REPORT

Technical

7. PERIOD COVERED (Inclusive Dates)

2009-2012

8. PERFORMING ORGANIZATION - NAME AND ADDRESS (If NRC, provide Division, Office or Region, U. S. Nuclear Regulatory Commission, and mailing address; if contractor, provide name and mailing address.)

Division of Engineering
Office of Nuclear Regulatory Research
U.S. Nuclear Regulatory Commission
Washington, DC 20555-0001

9. SPONSORING ORGANIZATION - NAME AND ADDRESS (If NRC, type "Same as above", if contractor, provide NRC Division, Office or Region, U. S. Nuclear Regulatory Commission, and mailing address.)

Same as above.

10. SUPPLEMENTARY NOTES

11. ABSTRACT (200 words or less)

This report is aimed at prediction of weld residual stress (WRS) in safety-related nuclear components. WRS is a significant driving force for primary water stress corrosion cracking. As such, it is an important input to deterministic and probabilistic flaw growth calculations.

NRC's objectives for this work include: validate axisymmetric finite element modeling as a predictive tool for WRS, using robust experimental methods; support the development of appropriate WRS/flaw evaluation review guidelines; perform independent confirmatory research on industry guidance for executing WRS analysis; assess and evaluate the adequacy of industry's mitigation activities where WRS minimization is necessary; improve WRS finite element analysis predictive methodologies; determine estimates for WRS uncertainty distributions, which are needed in probabilistic analyses.

This report describes WRS measurement methods and finite element modeling techniques for predicting WRS. The measurement and modeling efforts were performed on both small-scale scientific specimens and on large-scale prototypic mockups of in-service nuclear plant components. For example, Chapter 4 describes results from a double-blind finite element round robin, where international participants completed finite element models of a prototype pressurizer surge nozzle without access to the measurement data. Validation criteria for WRS models will be developed in future research efforts.

12. KEY WORDS/DESCRIPTORS (List words or phrases that will assist researchers in locating the report.)

dissimilar metal welds, primary water stress corrosion cracking, weld residual stress, finite element analysis, model validation

13. AVAILABILITY STATEMENT

unlimited

14. SECURITY CLASSIFICATION

(This Page)
unclassified

(This Report)
unclassified

15. NUMBER OF PAGES

16. PRICE

Federal Recycling Program

UNITED STATES
NUCLEAR REGULATORY COMMISSION
WASHINGTON, DC 20555-0001

OFFICIAL BUSINESS

NUREG-2162

Weld Residual Stress Finite Element Analysis Validation: Part 1 – Data Development Effort

March 2014